

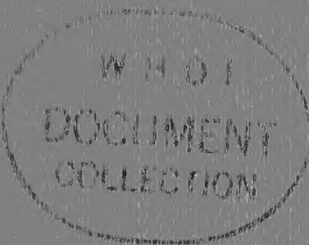
International Workshop on Low-Frequency Propagation and Noise

Volume 2

Woods Hole, Massachusetts

14-19 October, 1974

1977



Sponsored by CNO (OP-095)

Supported by CNR

**Coordinated at the
Maury Center for Ocean Science
Department of the Navy
Washington, D.C.**

DATA LIBRARY & ARCHIVES
Woods Hole Oceanographic Institution



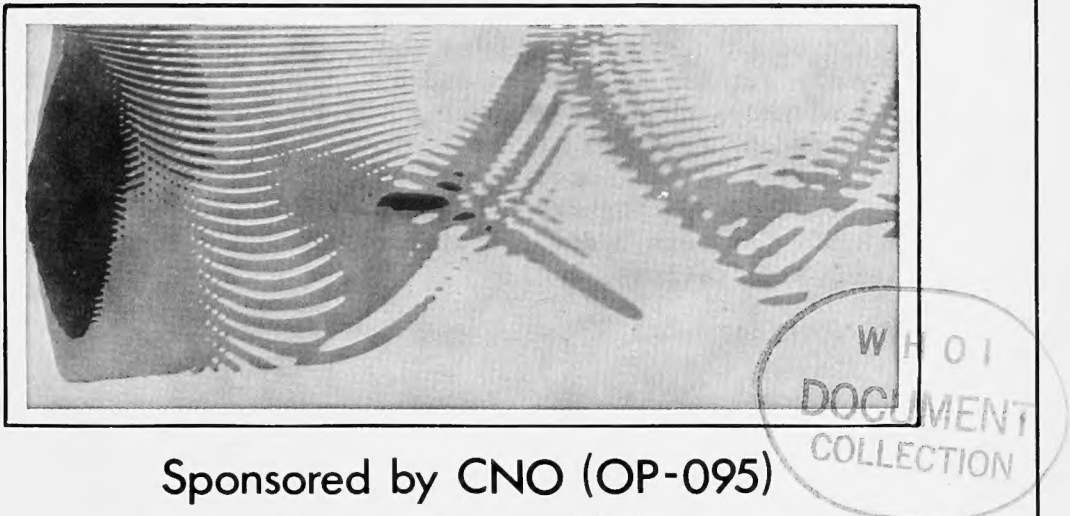
0 0301 0076023 7

International Workshop on Low-Frequency Propagation and Noise

Volume 2

Woods Hole, Massachusetts

14-19 October, 1974



Sponsored by CNO (OP-095)

Supported by CNR

**Coordinated at the
Maury Center for Ocean Science
Department of the Navy
Washington, D.C.**

WHOI
DOCUMENT
COLLECTION

ACKNOWLEDGEMENTS

These proceedings record the first plenary session of the International Workshop on Low Frequency Propagation and Noise, sponsored by the Director, Antisubmarine Warfare Programs of the U. S. Navy Chief of Naval Operations staff. Scientists from six nations--Australia, Canada, New Zealand, Norway, the United Kingdom, and the United States--participated. The Workshop was conducted by the Chief of Naval Research. The executing agency was the Maury Center for Ocean Science; Director, Dr. J. B. Hersey. Commander A. G. Brookes, Jr., USN, coordinated the conduct of the symposium which was held at the Woods Hole Oceanographic Institution, Quisset Campus, Woods Hole, Massachusetts. The Office of Naval Research is indebted to the Institution for its excellent hosting of this meeting and in particular to Mr. Charles S. Innis for his conspicuous efficiency and skill in making all local arrangements. All participants in the Workshop made substantial contributions either by preparing the papers listed in the Table of Contents or by chairing various sessions. These proceedings were recorded in detail by Ace Federal Reporters, Inc. The completeness and quality with which the proceedings were recorded are much appreciated and have made possible the level of detail these proceedings contain. The proceedings were edited primarily by the authors themselves and by Mr. F. P. Diemer in the Office of Naval Research and Commander A. G. Brookes, Jr., USN. The final editing and preparation of these proceedings were performed by Science Applications, Inc., under contract to the Office of Naval Research. Technical editing was performed by Drs. J. Czika, J. S. Hanna, and R. C. Cavanagh under the direction of C. W. Spofford, all of Science Applications, Inc.

The illustration on the title page displays iso-loss contours in range and depth generated by the Parabolic Equation Model of Dr. F.D. Tappert. Regions of heaviest shading correspond to losses of less than 80 dB re 1 yard, lighter shading to losses between 80 and 90 dB, and lightest shading to losses greater than 90 dB. The calculation is for a constant (pressure) gradient sound-speed profile in water 16,000-feet deep overlying a highly absorbing bottom. The source is at a depth of 8,000 feet, the acoustic frequency is 50 Hertz, and the maximum range is 50 nautical miles.

Details on the technique and more examples are contained in Dr. Tappert's paper entitled "Selected Applications of the Parabolic-Equation Method in Underwater Acoustics" found in Volume I of these Proceedings.

Title page was designed by Frank Varcolik, SAI.

PREFACE

The International Workshop on Low-Frequency Propagation and Noise was held at the Woods Hole Oceanographic Institution, Woods Hole, Massachusetts, from October 15 to 19, 1974. These Proceedings consist of either author-supplied texts or edited versions of the oral presentations and edited condensations of the discussions. In the edited sections, the editors have made every effort to render faithfully the essential content of the oral presentation or discussion.

These Proceedings are presented in two volumes, each consisting of 2 days of presented papers. Several of the original presentations have been superceded by a published version, which the authors also have submitted for publication here. In these cases, with the permission of the authors and the publishers, the published articles are reproduced here in facsimile. The presentations so rendered are the following:

- i) Dr. Weinberg's paper appeared as NUSC Technical Report 4867.
- ii) The presentation of Drs. Flatté and Munk contained some of the information presented in the three articles published in the *Journal of the Acoustical Society of America*.
- iii) Dr. Raisbeck's paper appeared in the *U. S. Navy Journal of Underwater Acoustics*.

INTERNATIONAL WORKSHOP
ON LOW-FREQUENCY PROPAGATION AND NOISE

VOLUME II

TABLE OF CONTENTS

	<u>Page</u>
V. SPECIAL EFFECTS (<i>R. H. Nichols, Session Chairman</i>)	
SURFACE DECOUPLING EFFECTS, <i>M. A. Pedersen, D. F. Gordon, and D. White</i>	559
A THEORETICAL APPROACH TO THE PREDICTION OF SIGNAL FLUCTUATIONS DUE TO ROUGH-SURFACE SCATTERING, <i>F. M. Labianca and E. Y. Harper</i>	583
SOFAR PROPAGATION OF WIDE-BAND SIGNALS TO LONG RANGES, <i>R. P. Porter</i>	633
CONVERGENCE ZONE DEPENDENCE ON FREQUENCY, <i>R. M. Fitzgerald</i>	667
VI. GEOGRAPHIC EFFECTS (<i>E. E. Hays, Session Chairman</i>)	
LOW-FREQUENCY PROPAGATION IN THE ICE-COVERED ARCTIC OCEAN, <i>Henry W. Kutschale</i>	683
ARCTIC ENVIRONMENTAL LF ACOUSTICS MEASUREMENTS, MODELS AND PLANS, <i>Beaumont M. Buck</i>	725
ENVIRONMENTAL FACTORS AFFECTING LOW-FREQUENCY PROPAGATION IN THE OCEAN, <i>David G. Browning</i>	769

VOLUME II

TABLE OF CONTENTS (Cont'd)

	<u>Page</u>
VII. NOISE MECHANISMS (<i>I. Dyer, Session Chairman</i>)	
AMBIENT-NOISE MODELS, <i>R. C. Cavanagh</i>	801
GEOGRAPHICAL VARIATION OF AMBIENT NOISE IN THE OCEAN FOR THE FREQUENCY RANGE FROM 1 HERTZ TO 5 KILOHERTZ, <i>Robert L. Martin and Anthony J. Perrone</i>	817
STATISTICAL ANALYSIS OF SHIP-GENERATED NOISE, <i>S. C. Daubin</i>	843
VIII. NOISE MEASUREMENTS (<i>W. A. Von Winkle, Session Chairman</i>)	
VERTICAL NOISE DISTRIBUTION, <i>V. C. Anderson</i>	859
DIRECTIONAL NOISE AMBIGUITY RESOLUTION WITH LINEAR ARRAYS, <i>Gordon Raisbeck</i>	887

INTERNATIONAL WORKSHOP
ON LOW-FREQUENCY PROPAGATION AND NOISE

VOLUME I

TABLE OF CONTENTS

	<u>Page</u>
I. ENVIRONMENTAL MEASUREMENTS (<i>J. B. Hersey, Session Chairman</i>)	
INTRODUCTION, <i>Dr. J. B. Hersey</i>	1
TIME VARIATIONS OF SOUND SPEED OVER LONG PATHS IN THE OCEAN, <i>G. R. Hamilton</i>	7
THE ACOUSTIC OUTPUT OF EXPLOSIVE CHARGES, <i>Ermine A. Christian</i>	31
EXPLOSIVE SOUND-SOURCE STANDARDS, <i>M. S. Weinstein</i>	61
APPLICATION OF RAY THEORY TO LOW-FREQUENCY PROPAGATION, <i>Henry Weinberg</i>	93
II. PROPAGATION THEORY (<i>R. R. Goodman, Session Chairman</i>)	
NORMAL MODES IN OCEAN ACOUSTICS, <i>D. C. Stickler</i>	125
SELECTED APPLICATIONS OF THE PARABOLIC-EQUATION METHOD IN UNDERWATER ACOUSTICS, <i>Frederick Tappert</i>	155
CALCULATION OF THE EFFECT OF INTERNAL WAVES ON OCEANIC SOUND TRANSMISSION, <i>Stanley M. Flatté and</i> <i>Frederick D. Tappert</i>	201
SOUND PROPAGATION THROUGH A FLUCTUATING STRATIFIED OCEAN: THEORY AND OBSERVATION, <i>W. H. Munk and F. Zachariasen</i> . .	211
INTERPRETATION OF MULTIPATH SCINTILLATIONS ELEUTHERA TO BERMUDA IN TERMS OF INTERNAL WAVES AND TIDES, <i>Freeman Dyson, W. H. Munk and B. Zetler</i>	233

VOLUME I

TABLE OF CONTENTS (Cont'd)

	<u>Page</u>
III. EFFECTS OF BOUNDARIES (<i>M. Schulkin, Session Chairman</i>)	
ACOUSTIC PROPERTIES OF THE SEA FLOOR, <i>John Ewing</i>	249
THE EFFECT OF ROUGH INTERFACES ON SIGNALS THAT PENETRATE THE BOTTOM, <i>C. W. Horton, Sr.</i>	275
BOTTOM PROPERTIES FOR LONG-RANGE PROPAGATION PREDICTION, <i>Aubrey L. Anderson</i>	297
FORWARD SCATTERED LOW-FREQUENCY SOUND, <i>W. I. Roderick</i> . . .	325
IV. SIGNAL CHARACTERISTICS (<i>T. G. Birdsall, Session Chairman</i>)	
COHERENCE, <i>Theodore G. Birdsall</i>	357
FLUCTUATIONS: AN OVERVIEW, <i>Ira Dyer</i>	365
SOUND PROPAGATION IN A RANDOM MEDIUM, <i>Robert H. Mellen</i> . .	387
PHASE FLUCTUATIONS, COHERENCE AND INTERNAL WAVES, <i>R. C. Spindel</i>	423
FIXED-SYSTEM MEASUREMENTS OF TIME-VARYING MULTIPATH AND DOPPLER SPREADING, <i>H. A. DeFerrari</i>	465
DESIGN OF TRANSMISSION LOSS EXPERIMENTS, <i>J. S. Hanna</i> . . .	509

SURFACE DECOUPLING EFFECTS

M. A. Pedersen, D. F. Gordon, and D. White
Naval Undersea Center

This paper presents recent theoretical progress on the surface decoupling effect, which produced high propagation loss for source or receiver near the ocean surface. The effect is greatest at low frequencies where ray theory is most suspect. Thus, the effect is approached from the more accurate normal mode standpoint. These normal mode investigations have provided some significant new results. They predict that the highest levels for distant shipping noise should occur just below the surface decoupling region. They also predict that under conditions of severe near-surface gradients, ray theory computations for near-surface sources and receivers are in serious error in that the maximum convergence zone intensities of mode theory can occur in the ray theory shadow zones. Two new ray theory approximations to surface decoupling loss have been developed and are compared with normal mode results. These new approximations represent a significant improvement over the old iso-speed approximation available in the past.

The work reported here is part of a continuing NUC effort to utilize normal mode theory to investigate low-frequency propagation in the deep ocean. Starting in 1954 we applied this mode theory to propagation in surface channels (Pedersen and Gordon, 1966). In the late 1960s this model was extended to examine propagation in the deep ocean. A computer program was developed by Dave Gordon and is referred to as the NUC n-layer normal mode program (Gordon, 1971A). This program has been used in a variety of applications (Gordon, 1971B, and Gordon, 1972). Detailed acoustic fields as calculated by this program have exhibited a number of new characteristics of importance in the understanding of low-frequency propagation. Some of these characteristics have ray theory analogs. Others are in complete variance with ray theory and the mechanisms are not

understood. We plan a systematic investigation of those acoustic characteristics that appear to be important from the standpoint of application to sonar systems. This paper presents results of our investigation of one of these characteristics, which we refer to as the surface decoupling effect.

This presentation is based on a project sponsored by NAVELEX Code 320. This project is to make a definitive theoretical investigation of the surface decoupling effect, which can be of vital significance in low-frequency underwater sound propagation. The results of this project are contained in an NUC technical publication (Pedersen, Gordon, and White, 1976). About 10 percent of the material in this publication has been extracted for presentation here.

The surface decoupling effect is also referred to as the surface-image effect or pressure-release effect. The effect produces high propagation losses for a source or receiver near the ocean surface. This effect is greatest at low frequencies, where ray theory is most suspect. It is logical then to explore the concept of surface decoupling from the standpoint of the more accurate normal mode theory.

Here the surface decoupling effect is inherent in the theory and enters as the boundary condition that the acoustic pressure be zero at the ocean surface. Although the mode theory is more accurate than ray theory, it is difficult to extract the functional dependence on such parameters as frequency, depth, profile characteristics, etc. Using the approach of two interfering ray paths, the surface-decoupling effect can also be developed by ray theory. Here the functional dependence on the parameters is much more explicit.

Both the mode and ray theory approaches play an important role. The mode theory serves as a control to indicate the accuracy of the ray theory, while the ray theory approach yields results which are easier to interpret and to apply.

This paper will always present the surface-decoupling effect as a function of receiver depth for a fixed source depth. However, since reciprocity holds, one may reverse the roles of source and receiver. Hence, any result presented here for receiver depth may be interpreted also as a result for source depth.

Unless stated to the contrary, all numerical computations of this paper are based on a fixed source depth of 100 yards and an acoustic frequency of 10 Hz.

Most of the computations are based on a sound speed profile for the Atlantic presented by Tolstoy and May (1960).

In the mode computations, only trapped modes are considered; these are the modes with negligible damping and which propagate to long range. The present study suppresses bottom bounce propagation. At short ranges, where bottom bounce propagation is important, the surface decoupling effect will be range dependent and is much more complicated than the case treated here.

Features of the remainder of this presentation are as follows:

- 1) Examples of how the surface decoupling effect appears in the detailed propagation loss computations of mode theory
- 2) Theory and examples which illustrate the concept of surface decoupling from the mode theory standpoint
- 3) Various ray theory approximations to surface decoupling

- 4) Comparison between these ray theory approximations and mode theory
- 5) Functional dependence of surface decoupling on important parameters as determined by ray theory.

Figure 1 presents iso-propagation loss contours in the range-receiver depth plane. The receiver depth is shown from the surface to 1,000 yard depth and the range interval from 1,000 to 1,080 kyd. At this range the convergence zones overlap, although there still remains a structure which is cyclical with range. The important feature is the marked increase in loss near the surface, i.e., at receiver depths shallower than 200 yards. All normal mode contour plots show this increased loss near the surface at short as well as long range.

Figure 2 presents plots of propagation loss versus range for various receiver depths. The shallowest receiver depth is 5 yards and the receiver depths are progressively doubled to 320 yards. The region to the left represents the direct field. The region centered at about 65 kyd range is the first convergence zone. The high loss region centered at about 30 kyd represents the "shadow-zone" region. Since bottom bounce propagation is not included in this computation, this high loss region is ensonified by various diffraction mechanisms.

For the conditions of Figure 2, the surface decoupling region is shallower than 206 yards. Consider the six solid curves of Figure 2 for receivers in this region. The surface decoupling effect can be seen as a monotonic decrease in propagation loss with increasing depth and also as a repetitive shape in the loss curve. This repetitive shape can be explained by normal mode theory, but is too involved for this presentation. For the near-surface receivers doubling the depth decreases the propagation loss by 6 dB. This will be explained later.

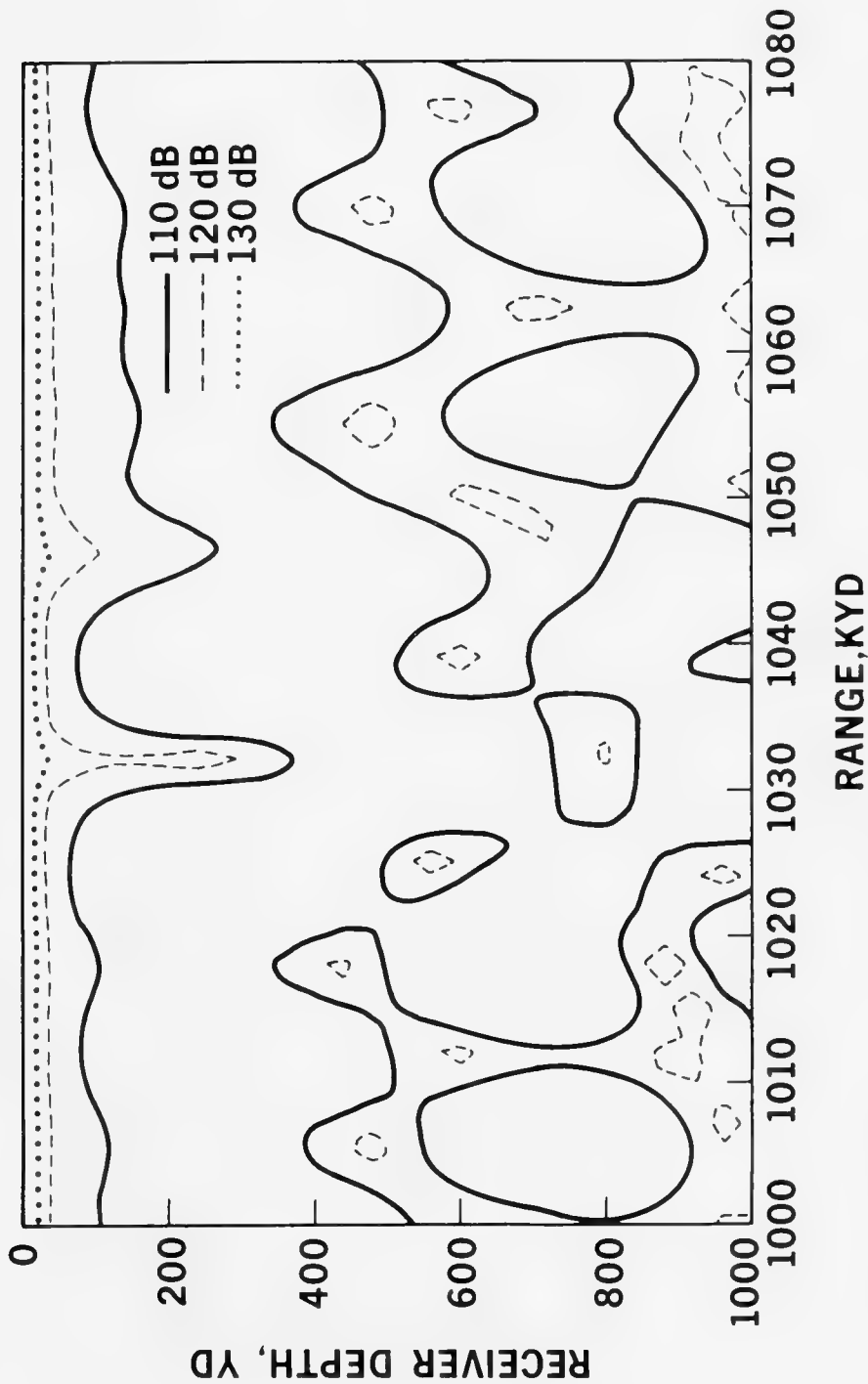


Figure 1. LONG-RANGE PROPAGATION LOSS CONTOURS

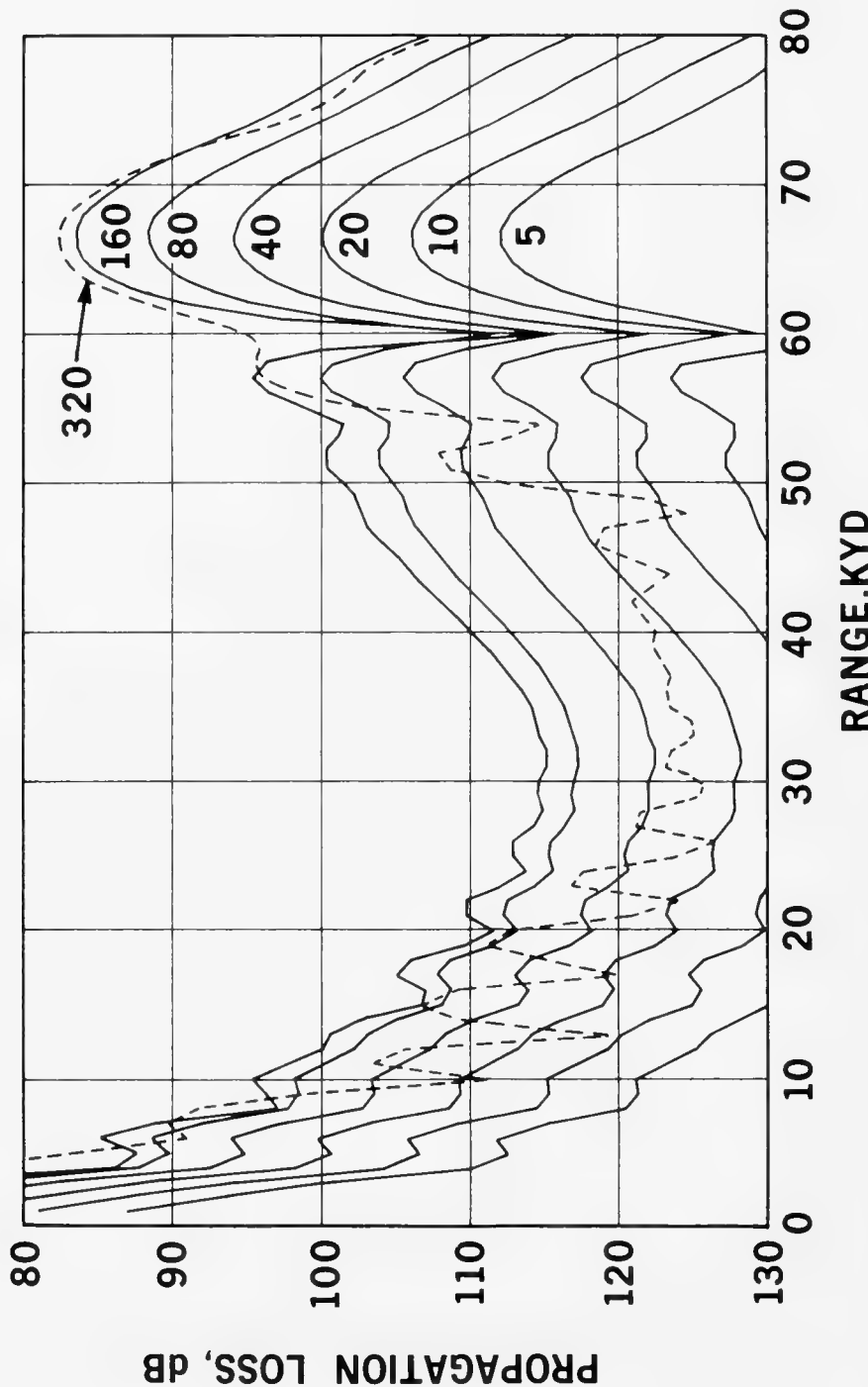


Figure 2. SHORT-RANGE PROPAGATION LOSS PLOTS

The receiver depth of 320 feet, as illustrated by the dashed curve, is below the surface decoupling region and has an entirely different character.

The repetitive shape of the propagation loss curves in the surface decoupling region points up a newly found deficiency in ray theory. We have observed pronounced disagreements between ray and mode theory in cases where the caustic structure of the convergence zones varies markedly with depth in the surface decoupling region. These disagreements occur under conditions of severe near-surface gradients. In this case ray theory predicts a marked difference in convergence zone structure with near-surface depth, whereas the more accurate mode theory predicts no change in shape at all, but only in amplitude. We have found cases for near-surface receivers where the region of minimum propagation loss in mode theory convergence zones lies in the shadow zones of ray theory.

Figure 3 presents normal mode expressions pertaining to the surface decoupling effect. Equation 1 is an expression for the propagation loss associated with the random phase or power addition of modes. This process smoothes out the detailed interference beats between modes and enables one to distinguish between the basic range and depth effects. The H_0 term in Equation 1 is independent of range. The second term represents cylindrical spreading while the third term represents an attenuation loss.

Our interest is in the H_0 term of Equation 2. This term contains the dependence of the smoothed propagation loss on frequency, sound speed profile, and source and receiver depths. In Equation 2, C_a is the mean phase velocity of the trapped modes and f is the acoustic frequency in Hz.

1. $H_R = H_0 + 10 \log r + \alpha_A r.$
2. $H_0 = -10 \log (C_a S^2/f).$
3. $S^2 = \sum_{n=1}^N |U_n(z) U_n(z_o)|^2.$
4. $H_N(z) = -10 \log \left[C_N |U_N(z) U_N(z_o)|^{2/f} \right].$
5. $Z_{SD} = \text{DEPTH OF FIRST MINIMUM IN } H_N(z).$
6. $H_S = H_N(z) - H_N(Z_{SD}).$
7. $H_S = -10 \log |U_N(z)|^2 + 10 \log |U_N(z_{SD})|^2.$

Figure 3. MODE APPROACH TO SURFACE DECOUPLING

Equation 3 represents the power addition of the mode amplitude functions. Here n is the mode number and N is the number of trapped modes. Z is the receiver depth and Z_o is the source depth. The U functions are the solutions to the Helmholtz equation. We need not discuss the detailed form of these functions. The boundary conditions require that the U functions go to zero at the ocean surface. Thus, H_o goes to plus infinity as the source or receiver depth approaches the ocean surface. The source and receiver depth enter the U functions in exactly the same manner. This is consistent with the acoustic property of reciprocity.

In regions where the surface decoupling effect is the controlling feature, the dominant contribution to the mode sum is often that of the last trapped mode. Equation 4 defines $H_N(Z)$. This is the counterpart of H_o for the last trapped mode. Here the mode sum of Equation 3 is replaced by the contribution of the dominant mode. We shall presently see an example of H_o and $H_N(Z)$. This example will demonstrate the relationship more clearly.

Now $H_N(Z)$ will have N maxima and N minima as Z varies from the ocean surface to the ocean bottom. Equation 5 defines the surface decoupling depth, Z_{SD} , as the depth of the first minimum in $H_N(Z)$. The surface decoupling depth is the depth of the shallowest antinode in the standing wave pattern of the last trapped mode.

Equation 6 defines the surface decoupling loss, H_s . It is the difference between $H_N(Z)$ and H_N evaluated at the decoupling depth, Z_{SD} . H_s is infinite at the surface and decreases monotonically to zero value at the decoupling depth.

Equation 7 follows immediately from Equations 4 and 6. We present Equation 7 to demonstrate that H_s is independent of the source depth, Z_o .

Figure 4 illustrates the important mode theory quantities, which were introduced in Figure 3. The computations are for the conditions of Figures 1 and 2.

The dashed curve is H_o which indicates how the smoothed propagation loss varies with depth. Ideally, one would like a simple theory which describes H_o in terms of dependence on various parameters. Unfortunately, H_o is a very complicated function which depends on source depth as well as profile parameters. The problem of approximating H_o is under consideration, but for now we must be content to treat the surface decoupling effect as characterized by $H_N(z)$.

The solid curve $H_N(z)$ represents the standing wave pattern of mode 14, which is the last trapped mode. The first node occurs at the surface. The first antinode occurs at a depth of 206 yards. According to our previous definition, this is the surface decoupling depth, z_{SD} . Also shown are a second node at 410 yards and a second antinode at 590 yards.

The relative maximum in the loss for H_o at 480 yards is associated with the second node in $H_N(z)$. It is not as pronounced as a node because of the contribution of lower order modes which have nodes at different depths. However, at the surface, all modes have nodes. Thus, the major depth dependence of H_o will occur near the surface with relatively minor changes below the surface decoupling region.

Note that in the near surface region the shape of H_o is very similar to the shape of $H_N(z)$. This similarity results because N is not only the dominant mode, but also because other modes which contribute to H_o have similar shapes in the surface decoupling region.

Observe that the minimum loss in H_o occurs at a depth of 259 yards. One can demonstrate from mode theory that for any source

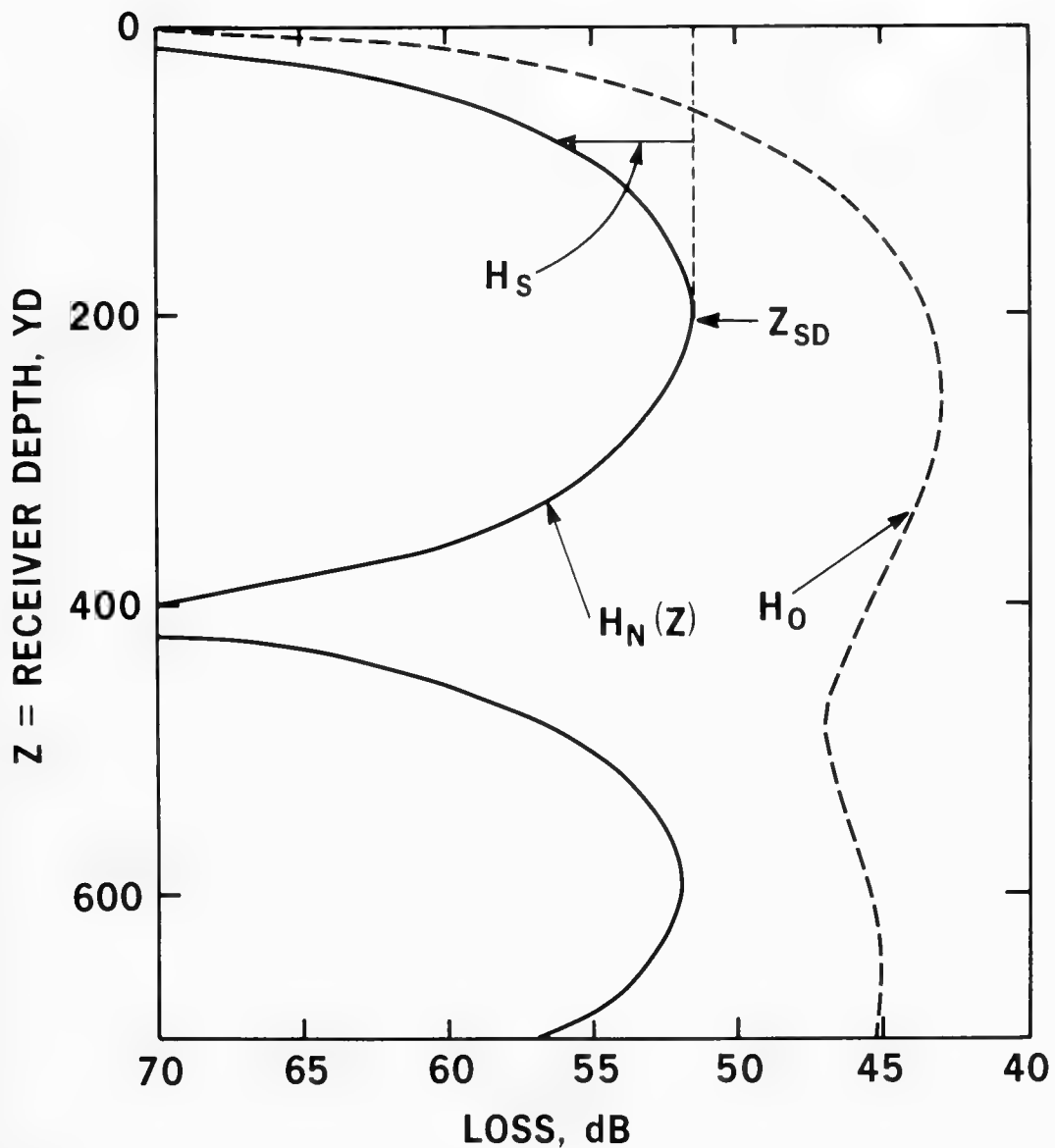


Figure 4. ILLUSTRATION OF MODE APPROACH

depth in the surface decoupling region, the minimum H_o (minimum average propagation loss) occurs for a receiver depth somewhat below the surface decoupling depth. In this example the source depth is 100 yards and the minimum in H_o occurs 53 yards below the decoupling depth. This feature yields an interesting prediction about sea noise from distant shipping. Here the source of the noise is in the surface decoupling region. Hence, the noisiest receiver depth should be somewhat deeper than the decoupling depth. Since decoupling depth depends on frequency, the noisiest receiver depth should tend to increase with decreasing frequency, other factors being equal.

The surface decoupling loss, H_S , is also illustrated in Figure 4. Note that H_S is a measure of the shape of $H_N(Z)$ in the surface decoupling region. As such, it is also a reasonable measure of the shape of H_o .

The big advantage in the use of H_S and Z_{SD} to characterize the surface decoupling effect is that these quantities can be approximated by ray theory. These approximations exhibit the dependence on various parameters and allow us to obtain a quantitative feel for the surface decoupling effect. We now will consider ray approximations to H_S and Z_{SD} .

Figure 5 presents three ray theory approximations to the surface decoupling effect. Equations 1 and 2 apply to all approximations. In Equation 2, ω is the angular frequency and Δt is the travel time difference between the two ray paths which interfere to cause the surface decoupling effect. The three approximations are obtained by the use of various expressions for Δt and hence for χ . In all approximations the surface decoupling depth, Z_{SD} , is that depth for which $\chi = \pi/2$. At this depth, $\sin \chi = 1$ and the surface decoupling loss, H_S , equals zero.

1. $H_S = -20 \log (\sin \chi)$, where
2. $\chi = \omega \Delta T / 2.$
3. $\chi = \omega Z \sin \Theta_0 / C_0.$ ISOSPEED
4. $Z_{SD} = C_0 / 4 f \sin \Theta_0.$
5. $\chi = \omega C_m^{-1} \int_0^Z \tan \Theta \, dz.$
6. $Z_{SD} = \text{solution of } \int_0^{Z_{SD}} \tan \Theta \, dz = C_m / 4f.$ CHI
7. $\chi = (Z/Z_{SD}) \pi / 2.$ LINEAR

Figure 5. RAY APPROXIMATIONS TO SURFACE DECOUPLING

Equations 3 and 4 give χ and Z_{SD} for the isospeed approximation. Here the sound speed is assumed to be a constant value, C_0 . Z represents the depth of the receiver, θ_0 the ray angle, and f the acoustic frequency in Hertz. Equations 3 and 4 are old results. These expressions are essentially the same as those developed by C. Spofford of AESD and used by him in the original FACT model (Spofford, 1974, and Baker and Spofford, 1974).

Equations 5 through 7 describe two new approximations developed by D. Gordon of NUC. The CHI approximation is given by Equations 5 and 6. Here Δt is evaluated by a ray theory integral which takes into account the structure of the sound speed profile. For this method the tangent of the ray angle is integrated from the surface down to the receiver depth Z . The ray parameter is C_m , which is the phase velocity of the ray. It is the sound speed at which the ray becomes horizontal. Equation 6 is the mathematical way of expressing that Z_{SD} is the value of depth for which $\chi = \pi/2$.

The linear approximation is given by Equations 6 and 7. Here Z_{SD} is determined by Equation 6 as in the CHI method. However, χ is determined by Equation 7, in which χ varies linearly with Z . The structure of the sound speed profile determines Z_{SD} as in the CHI method. However, once Z_{SD} has been determined, the dependence of the profile on Z is ignored and χ is determined by a single linear relationship. Note that in the CHI method χ depends only on the profile from surface down to depth Z , whereas in the linear method χ depends on the profile from the surface down to the decoupling depth no matter how shallow the receiver depth is.

Figure 6 compares the decoupling loss of mode theory with those of the three ray approximations. The difference between the loss of mode theory, H_s , and the particular approximation is shown as a

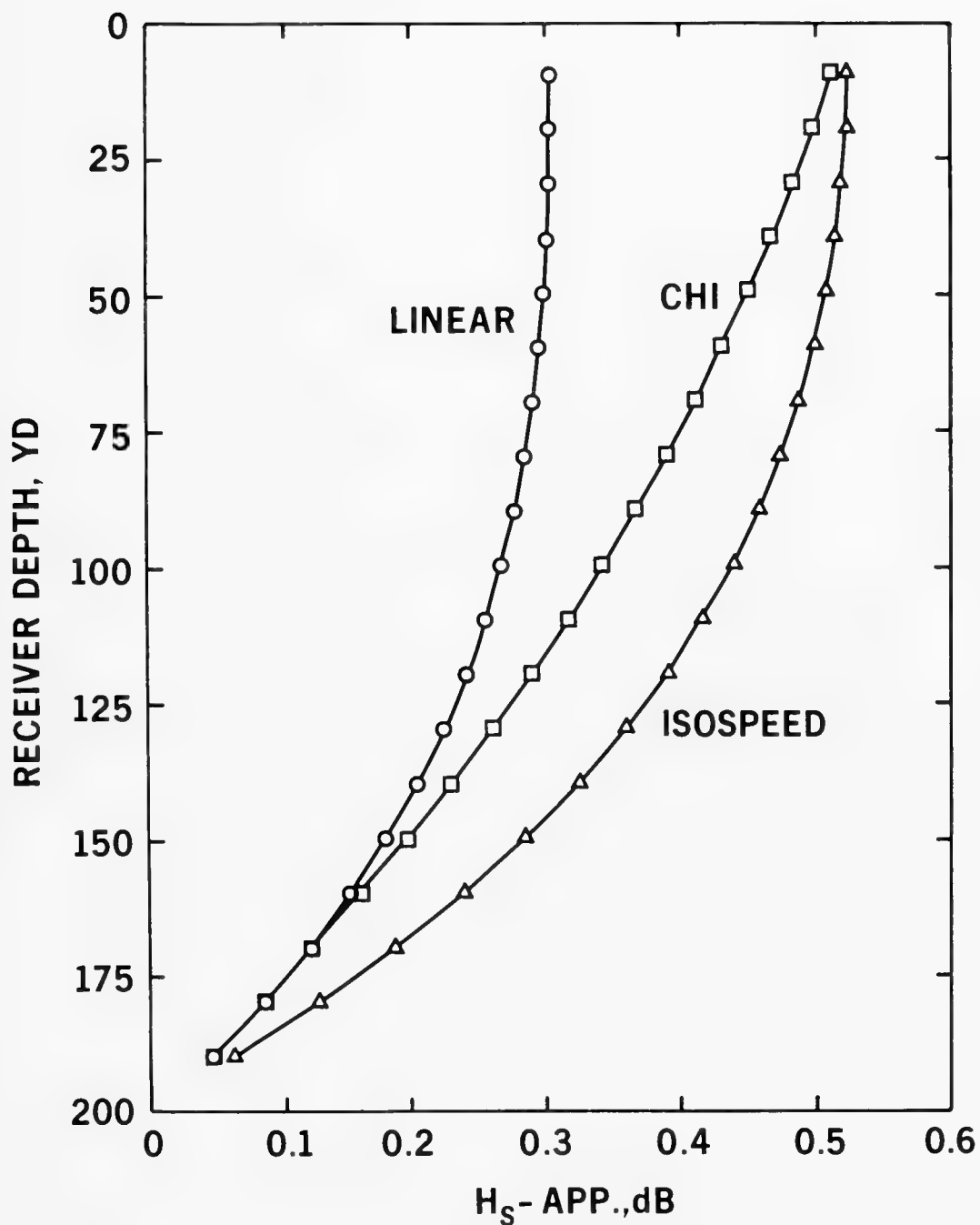


Figure 6. COMPARISON FOR MILD GRADIENTS

function of receiver depth. These computations are for the conditions of Figures 1, 2, and 4, i.e., the Atlantic profile and 10 Hz frequency. The linear approximation agrees with the mode theory to within 0.3 dB, while the CHI and isospeed approximation agree to within 0.6 dB. Although not shown here, the surface decoupling depth of the isospeed approximation is 6.4 percent shallower than that of mode theory. The corresponding value for the linear and CHI approximation is 4.0 percent shallower than that of mode theory.

For this profile the CHI and linear approximations are only slightly better than the isospeed computation. The reason is that the Atlantic profile has a surface layer down to 460 foot depth. Thus the profile is essentially isospeed (gradient of 0.02 sec^{-1}) for the upper 75 percent of the decoupling depth.

Figure 7 is similar to Figure 6 except the computations are made for a sound speed profile for the Sea of Japan, in the month of July. This profile is characterized by severe negative gradients starting at the surface. This gradient is -1.2 sec^{-1} for the first 67 yards.

The isospeed approximation is very poor. As can be seen in Figure 7, this approximation to the decoupling loss can be off by more than 9 dB. Moreover, this approximation to the surface decoupling depth is 191 percent too deep. This depth is then off by a factor of three.

In contrast, the linear approximation is very good. As can be seen in Figure 7, this approximation to the decoupling loss is off at most only 0.3 dB. Moreover, this approximation to the surface decoupling depth is only 6 percent too deep. The accuracy of the linear approximation then is essentially the same here as it was for Figure 6.

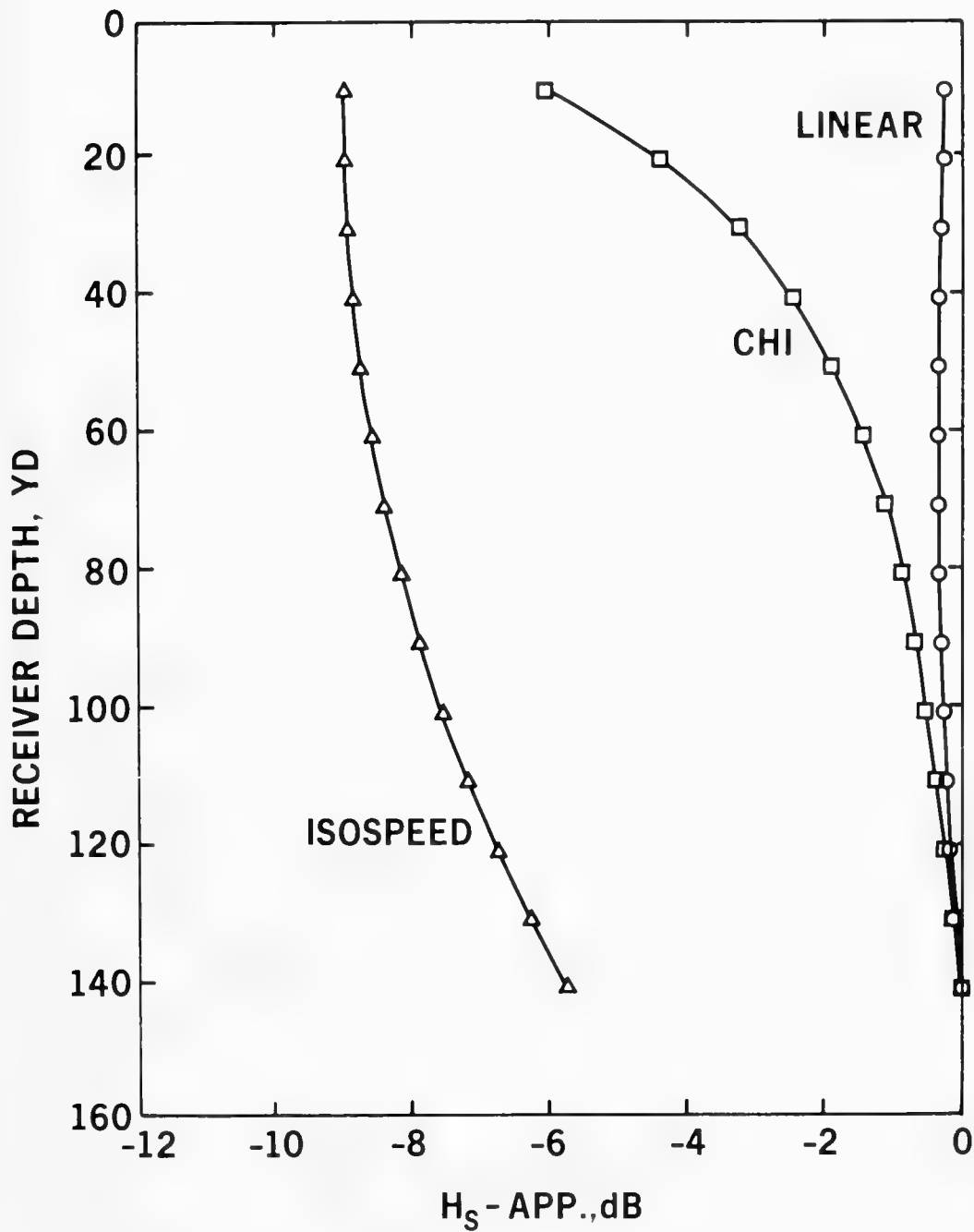


Figure 7. COMPARISON FOR SEVERE GRADIENTS

The accuracy of the CHI approximation lies between that of the linear and isospeed approximations. However, the linear method is a significant improvement over the CHI approximation as well as the isospeed approximation.

For the case of negative near-surface gradients, the isospeed method will always predict too large a decoupling loss and too large a decoupling depth.

Frequencies of 10, 31, and 104 Hz have been investigated for three different ocean profiles. For all of these conditions the decoupling loss of the linear method agrees with the mode result to within 0.4 dB. At lower frequencies this ray approximation eventually breaks down. The frequency of this breakdown depends on the depth excess in the sound speed profile. When only a few modes are trapped, one encounters the situation where the ray corresponding to the last trapped mode does not intersect the surface. For this case a completely different approach will have to be developed. At a frequency of 1.4 Hz for the Sea of Japan profile, the linear method was off by 3.3 dB.

Figure 8 presents the surface decoupling depth for the isospeed approximation. In this approximation the depth may be expressed in terms of acoustic wave length. Values are given as a function of the ray angle at the surface which is plotted here on a two-cycle logarithmic scale.

Although the isospeed approximation can degrade by as much as a factor of 3 in extreme cases, it does provide a simple and useful guide. For example, the horizontal lines in the figure designate the surface angles involved for various ray paths for two typical deep ocean profiles. The upper line represents a Pacific profile with a 100-foot surface layer, while the lower line represents the Atlantic

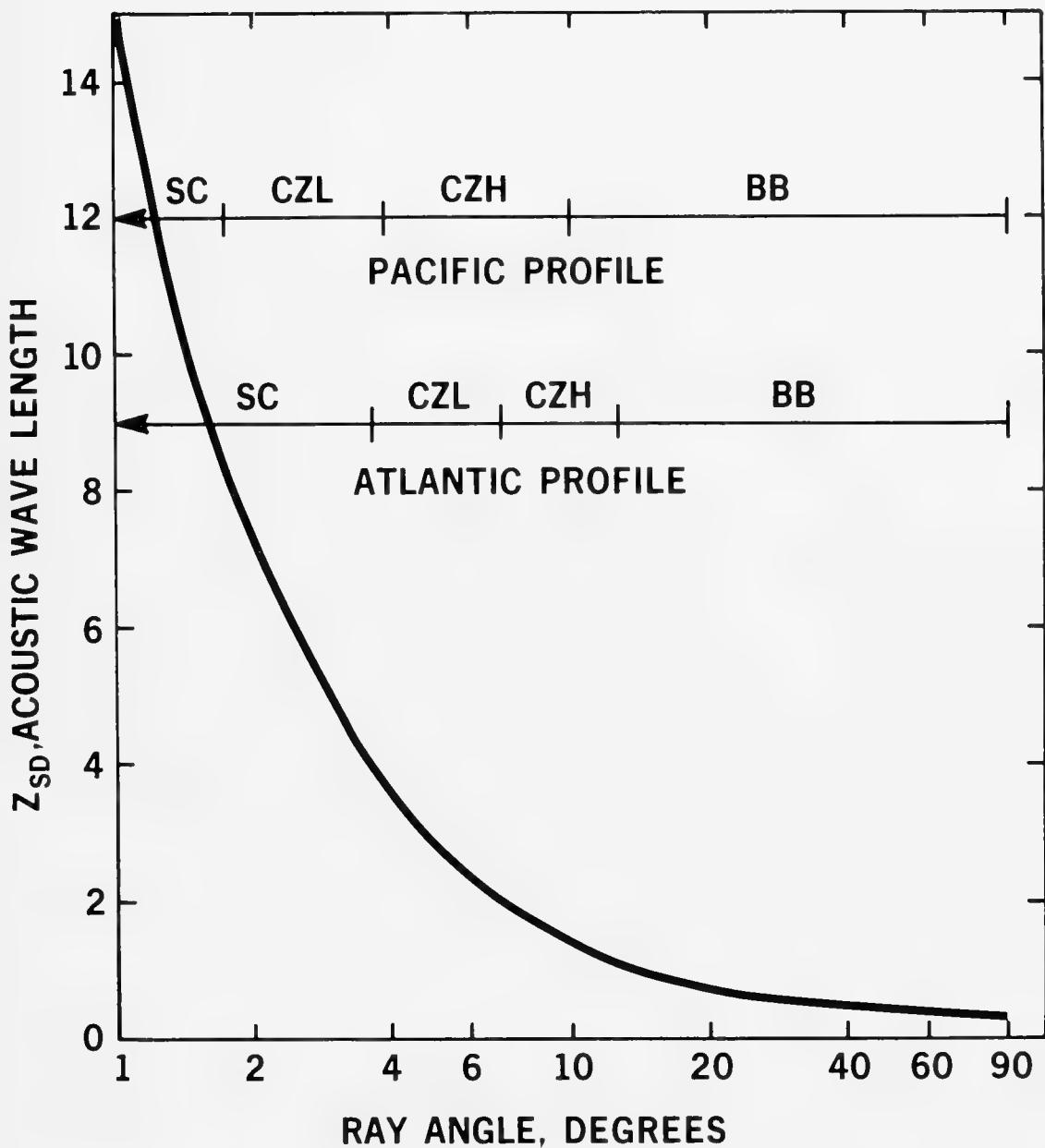


Figure 8. DECOUPLING DEPTH FOR ISOPEED APPROXIMATION

profile of this paper with a 460-foot surface layer. The region to the right, labeled BB, represents the bottom bounce region. For these two profiles, the corresponding surface decoupling depths lie between 1.5 and 0.25 wave lengths.

The region in the middle of the figure labeled CZL and CZH represents the convergence zone region. The rays in a convergence zone are folded at the caustic into two branches. Here CZL represents the lower-angle branch and CZH represents the higher-angle branch. For most cases the higher-angle branch will be more important than the lower-angle branch. For the two profiles, the higher-angle branch spans values of decoupling depth from 3.7 to 1.3 wavelengths. This span may be regarded as typical for convergence zone propagation.

The region to the left of the figure, labeled SC, is the surface channel region. Here the decoupling depth exceeds 4 wavelengths. Although the decoupling depths expressed as number of wavelengths can be huge for surface channel propagation, the physical decoupling depths are limited because only high frequencies propagate in surface channels. For example, on the basis of normal mode theory, one can demonstrate that the surface decoupling depth can never exceed 56.4 percent of the layer depth. This limit corresponds to the onset of trapping for the first mode. If two modes are trapped, then the surface decoupling depth cannot exceed 20.5 percent of the layer depth.

Figure 9 presents the surface decoupling loss for the linear approximation expressed in terms of the dimensionless ratio Z/Z_{SD} . For small values of χ , $\sin \chi$ is proportional to χ . Thus, for small ratios halving the depth increases the loss by 6 dB. This rule does not hold for large values. For example, a 50 percent ratio corresponds to 3 dB loss — not 6 dB loss.

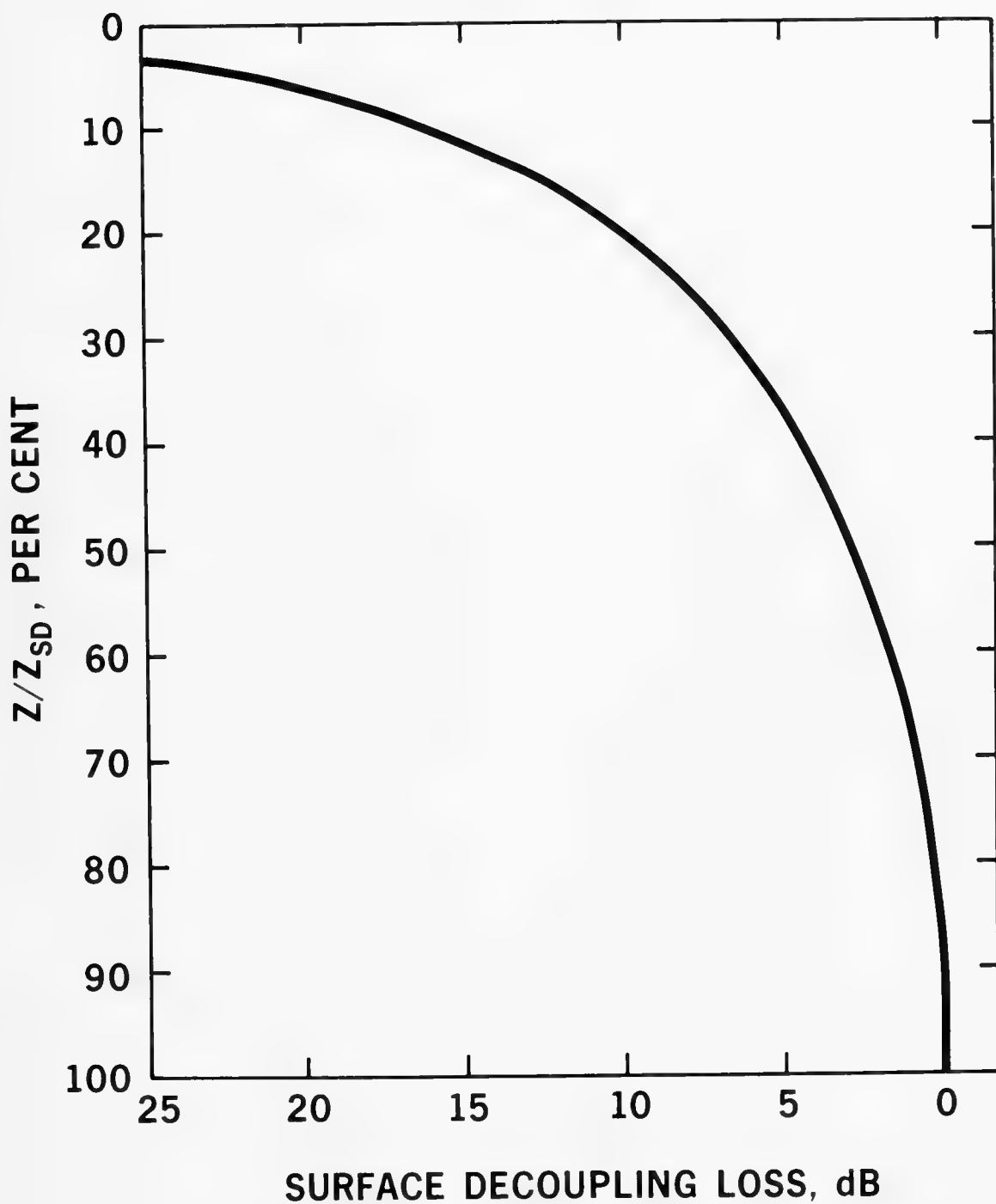


Figure 9. DECOUPLING LOSS FOR LINEAR APPROXIMATION

This curve provides some practical "rule of thumb" values. One-half the decoupling depth is 3 dB loss. One-third depth is 6 dB loss. One-fifth depth is 10 dB loss. One-tenth depth is 16 dB loss.

Observe that for a given receiver depth the loss will decrease with increasing frequency because the surface decoupling depth decreases with increasing frequency. This phenomenon is believed to be the controlling factor which causes the ambient noise in the ocean to increase in the region from about 10 Hz to 80 Hz.

In summary, a new ray theory model of surface decoupling loss has been developed which is adequate for frequencies above 10 Hz. Investigation of the surface decoupling phenomena by mode theory has resulted in several new conclusions: The highest levels for shipping noise are predicted to occur at receiver depths somewhat in excess of the decoupling depth. Under conditions of severe near-surface gradients, there is marked disagreement between convergence propagation losses in the decoupling region as calculated by the ray theory and by normal mode theory.

An exercise known as CAPER was conducted in late August 1974 by NUC, MPL, and HIG under LRAPP sponsorship. Part of this exercise consisted of measuring convergence zone propagation loss at 104 Hz on five receivers distributed from 10-foot to 150-foot depth and covering the surface decoupling region. These data will be analyzed to determine if they confirm the theory presented here.

REFERENCES

Baker, C. L., and C. W. Spofford, "The FACT Model," Volume 2, AESD Technical Note TN-74-04, December 1974.

Gordon, D. V., "Normal Mode Computation of Propagation Loss for an Arbitrary Number of Layers (U)," Naval Undersea Center Technical Publication 236, July 1971A (CONFIDENTIAL).

Gordon, D. F., "Investigation of Low Frequency Acoustic Propagation in the Deep Ocean by Normal Mode Theory," USN *J. Underwater Acoustics* 21, 4, 603-624, October 1971B (CONFIDENTIAL).

Gordon, D. F., "Comparison of Low-Frequency Acoustic Propagation in Deep Water with Normal-Mode Computations(U)," USN *J. Underwater Acoustics* 22, 4, 325-346, October 1972 (CONFIDENTIAL).

Pedersen, M. A., and D. F. Gordon, "A Normal Mode Approach to Underwater Sound Propagation (U)," Naval Electronics Laboratory Report 1407, September 1966 (CONFIDENTIAL).

Pedersen, M. A., D. F. Gordon, and D. White, "Low Frequency Propagation Effects for Sources and Receivers Near the Ocean Surface," Naval Undersea Center Technical Publication (1976 in publication).

Spofford, C. W., "The FACT Model," Volume 1, Maury Center Report 109, November 1974.

Tolstoy, I., and J. May, "A Numerical Solution for the Problem of Long-Range Sound Propagation in Continuously Stratified Media, with Applications to the Deep Ocean," *J. Acoustic Soc. Am.* 32: 655-660, June 1960.

A THEORETICAL APPROACH TO THE PREDICTION
OF SIGNAL FLUCTUATIONS
DUE TO ROUGH-SURFACE SCATTERING

F. M. Labianca and E. Y. Harper
Bell Telephone Laboratories, Inc.

A research program, the purpose of which is the rational prediction of signal fluctuations in a physically realistic ocean environment, has been initiated. An initial scattering model is adopted which accounts for fluctuations on the time scale of the random ocean surface. Some applications of this model to current problems in signal processing are presented.

A perturbation procedure is presented which allows for a fully three-dimensional treatment of the scattering from a stochastic ocean surface, and which includes the effects of refraction.

The perturbation procedure is applied to the problem of scattering in the region of surface-image interference for a deterministic nonrefractive ocean surface. The results, which are original, have a useful ray-theoretic interpretation in terms of multipath effects and energy conservation. The extension of these results to the case of a random ocean surface is discussed. The latter results are relevant to such problems as noise suppression in towed-array operation.

INTRODUCTION

Our interest in signal fluctuations and their prediction has been motivated by the need for realistic simulated data to support the signal processing activities at Bell Laboratories. Accordingly, I would like to make a few preliminary remarks before describing our model and what we have been able to achieve with it. Later on, I will describe what research efforts will be needed to develop it further.

One example of the application of the model is the current interest in the stability of the relative phase between two receiver points. A number of researchers, see Grube (1974), Gerlach (1973), and Mangano (1969), have reported apparently conflicting empirical results, sometimes from the same experiment. For example, my Figure 1 shows the violent relative phase fluctuations observed by Mangano (1969) for two hydrophones spaced only 22 feet apart. Figure 2 shows the more coherent behavior observed during a different period of the same experiment for the same hydrophones.* On the other hand, good long-term relative phase coherence has been observed between arrays spaced many miles apart [Grube (1974), and Gerlach (1974)].

Various attempts [for example, Brock (1973)] have been made at explaining such fluctuations. Hirsch (1974) has given a particularly satisfying phenomenological explanation which is in agreement with the predictions our model can make on a regular basis. Basically, Hirsch comes to three main conclusions. First, for the closely spaced elements, coherence is high when the energy is high and the carrier dominates the Doppler shifted energy. Second, also for closely spaced elements, when the carrier fades the Doppler shifted energy is no longer negligible and the coherence decreases. Figure 3 shows the power spectrum associated with the violent fluctuation illustrated in Figure 1. The spectrum within half of a Hertz of the carrier (here labeled DC value) is typical of the type of acoustic spectrum arising from rough-surface interaction. When the sideband energy is comparable to the carrier energy, as it turns out to be in this case, the relative phase coherence decreases giving rise to the

* Both of these phase plots were recorded for a 115-Hz source drifting at approximately 1 knot at broadside to the elements.

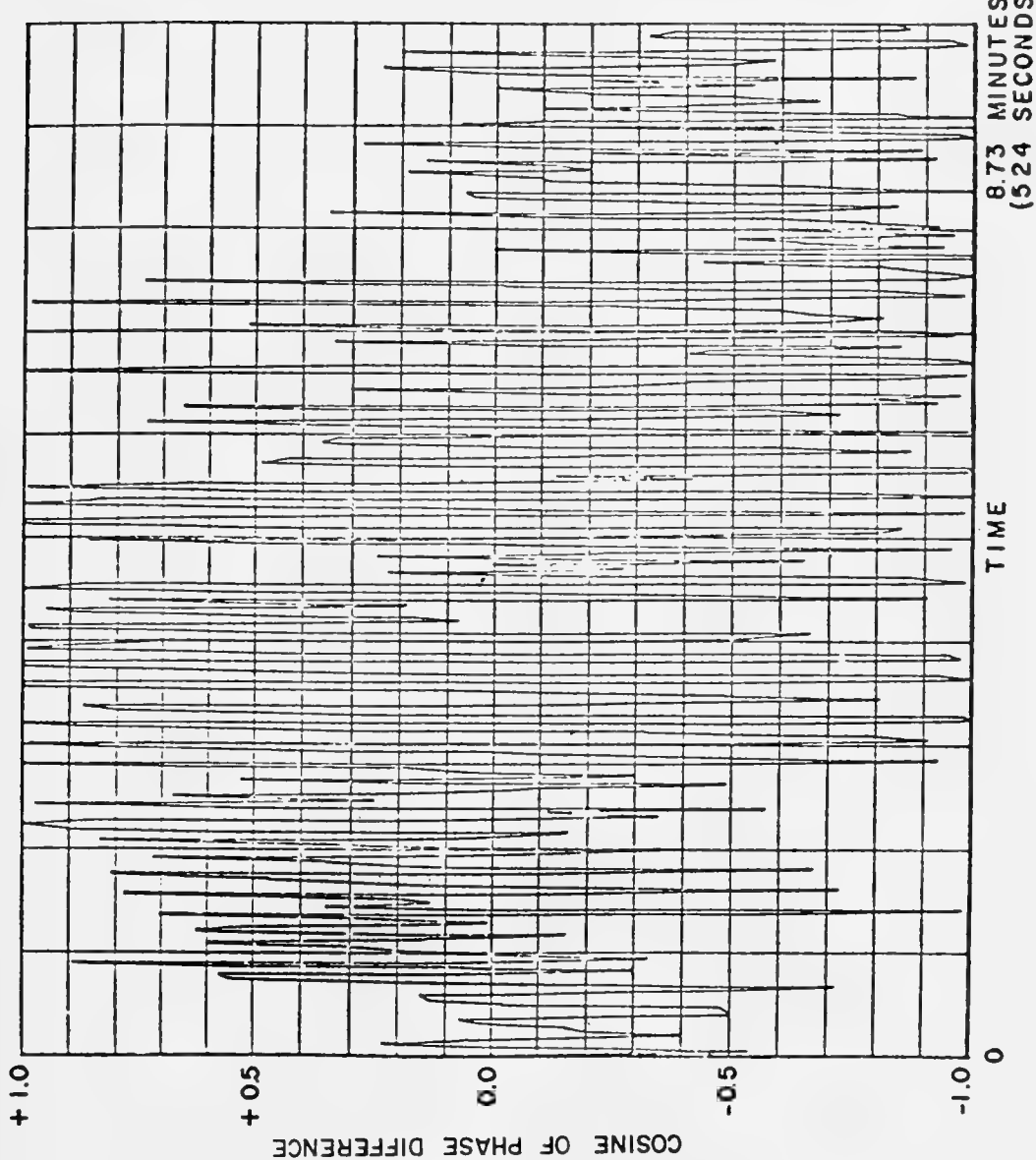


Figure 1. PHASE FLUCTUATION VERSUS TIME, RECORD A

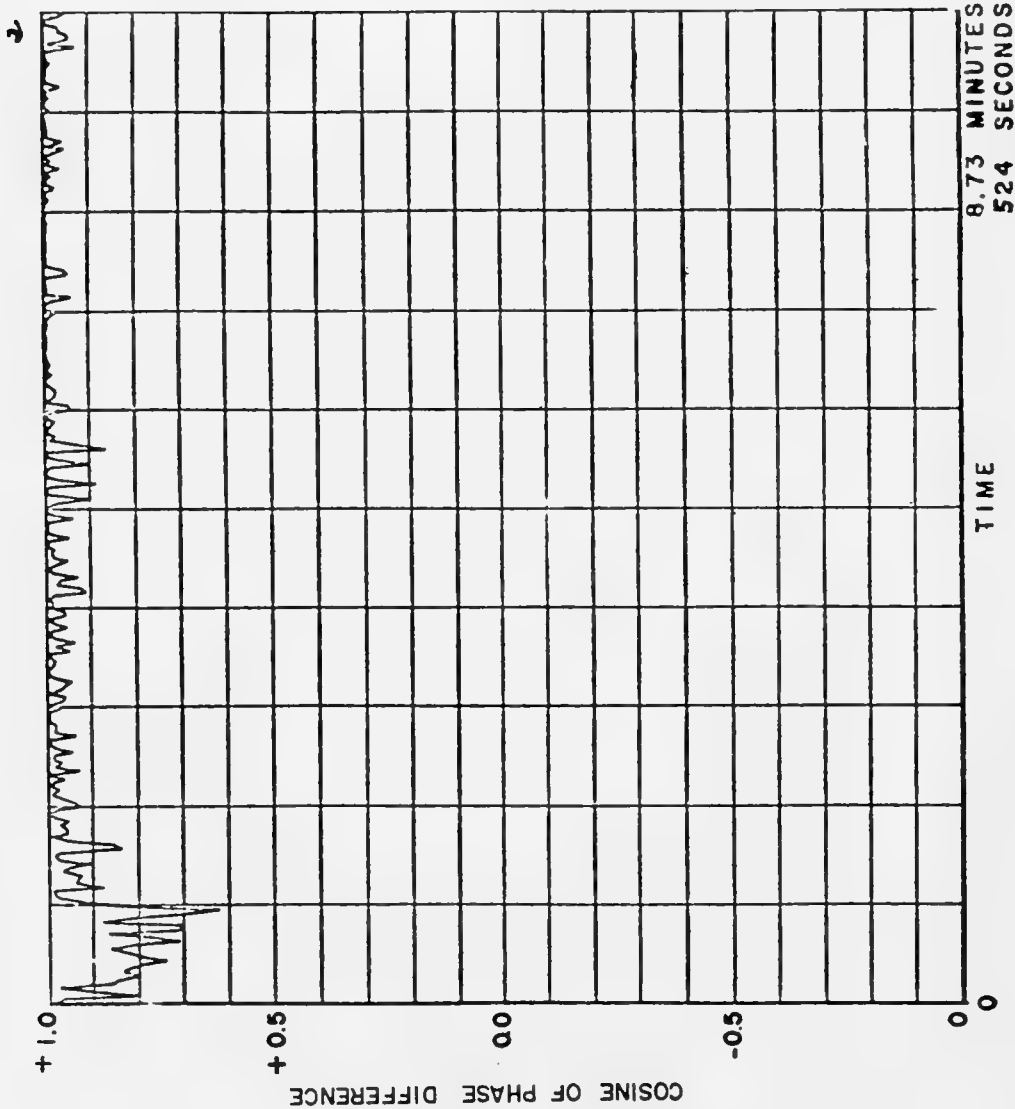


Figure 2. PHASE FLUCTUATIONS VERSUS TIME, RECORD B

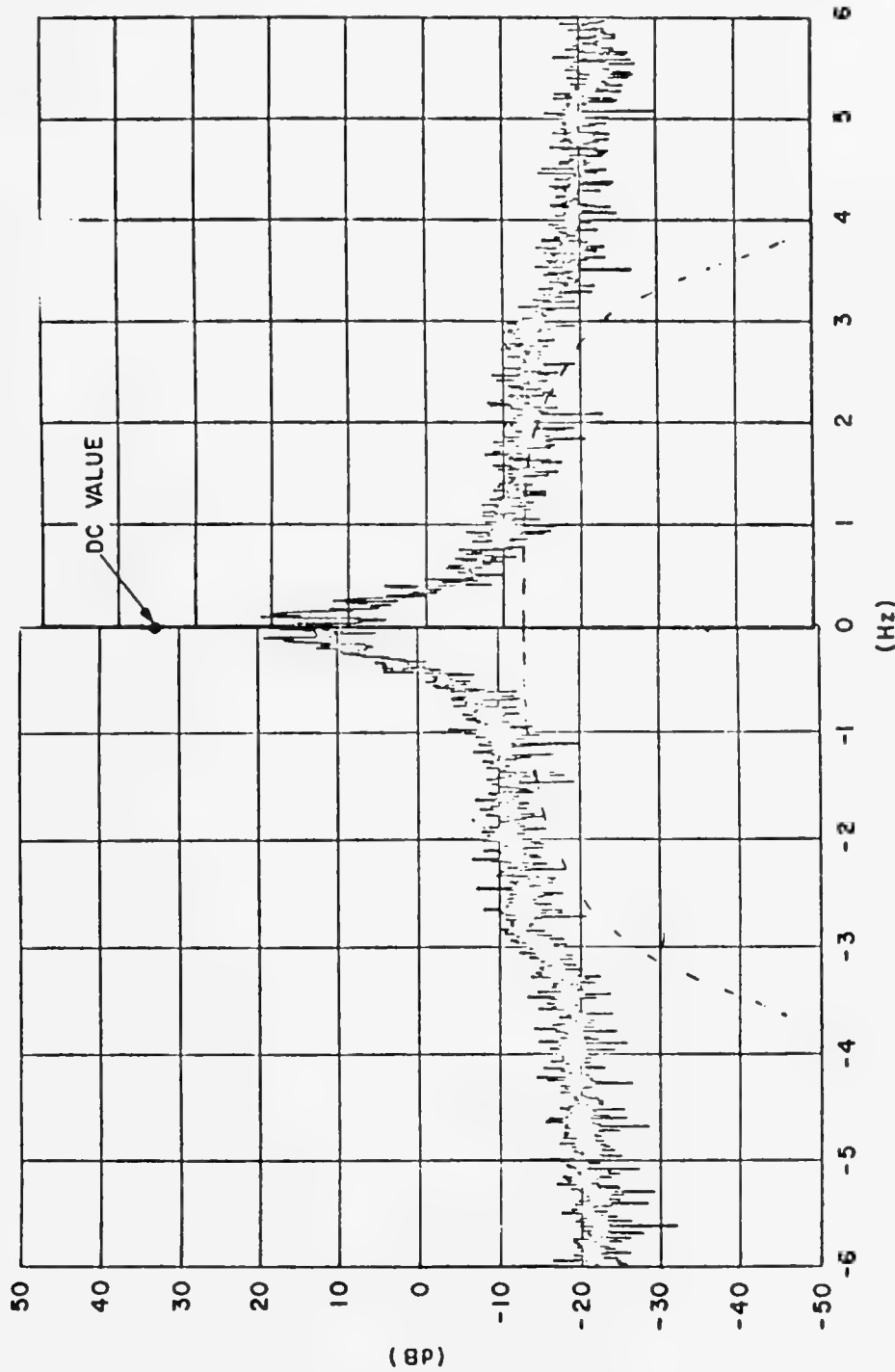


Figure 3. POWER SPECTRUM OF PHASE FLUCTUATIONS IN RECORD A

violent fluctuations illustrated earlier. We will show subsequently that nearly equal carrier and sideband energy occurs at the nulls in the carrier due to surface-image interference in a nonrefracting ocean. Mangano's (1969) results indicate that in regions of refractive interference at greater range, a similar reduction of the carrier relative to the sideband energy occurs. Finally, Hirsch's third conclusion is that in the case of widely spaced arrays, high coherence is achieved when the skewed Doppler arrivals are rejected by narrow beams.

The qualitative conclusions drawn by Hirsch are correct in their gross features but the reasoning does not permit detailed prediction of fluctuations on a regular basis. This is the reason why we have developed our model. We will first describe the model and later present numerical results. We will indicate some possible improvements.

PERTURBATION MODEL

The perturbation method utilized in our model is ideally suited to situations where the acoustic wavelength is the order of the ocean surface wavelength. This is in contrast to cases where the acoustic wavelength is small compared to the surface irregularities, in which case the Kirchoff or physical-optics approximation becomes suitable (see Holford). Figure 4 outlines the procedure for setting up the scattering formalism. Part A is a mathematical statement of the boundary-value problem. The pressure P satisfies the wave equation with a depth-dependent sound speed, a time-harmonic point-source forcing function and the usual boundary conditions. The function ζ gives the spatial behavior of the surface (deterministic or random) and a can be thought of as an rms surface waveheight. Part B shows

A. The Boundary-Value Problem

$$\left[\nabla^2 - \frac{1}{c^2(z)} \frac{\partial^2}{\partial t^2} \right] P(\underline{r}, \underline{r}', t) = -\delta(\underline{r} - \underline{r}') e^{-i\omega t}$$

$$P = 0 \quad \text{on} \quad z = z_{\text{surface}}$$

$$P \rightarrow 0 \quad \text{as} \quad |\underline{r}| \rightarrow \infty$$

$$z_{\text{surface}} = a\zeta(\rho, t)$$

B. The Perturbation Procedure

$$P \sim P_0 + aP_1 + a^2P_2 + O(a^3)$$

$$P_{z=z_{\text{surface}}} \sim \left[P_0 + aP_1 + a^2P_2 + O(a^3) \right]_{z=0}$$

$$+ a \left[\frac{\partial P_0}{\partial z} + a \frac{\partial P_1}{\partial z} + O(a^2) \right]_{z=0} \zeta(\rho, t)$$

$$+ a^2 \left[\frac{\partial^2 P_0}{\partial z^2} + O(a) \right] \frac{\zeta^2(\rho, t)}{2} = O(a^3)$$

Figure 4. THE SCATTERING FORMALISM

the perturbation expansion of the pressure and the surface boundary condition. The perturbation parameter, a , is the rms waveheight, which is taken to be small compared to all other lengths in the problem, e.g., the acoustic and surface-wave wavelengths. Implicit in the assumption of small a is also an assumption of small ocean surface slopes. This presents no serious limitation and is generally valid except in a very rough sea where the waves are breaking and the surface correlation length is the order of a few meters.

When the expansions are substituted into the equations of Part A and coefficients of like-powers of a are matched, there results the sequence of boundary value problems in Figure 5. The $O(1)$ problem is the smooth surface problem, while the higher order problems contain the effects of the surface through the boundary conditions. For example, in the $O(a)$ problem, the surface boundary condition is made up of the product of the surface function ζ and the z -derivative of the $O(1)$ pressure. In the $O(a^2)$ problem, the complexity of the boundary condition increases in a similar fashion and in general the surface boundary condition of a higher order problem depends on the solution of all the lower order problems. Further, since each boundary condition is made up of a sum of products of time-variable functions, it is clear that new frequencies will be generated. This is, of course, a consequence of the fact that the complete boundary value problem is nonlinear in time. But the important point is that the bandwidth of the acoustic spectrum increases with the addition of higher order corrections.

A formal procedure can be used in the solution of the sequence of boundary value problems. Since in each case the surface boundary condition has been reduced to the $z = 0$ plane and since the sound speed depth dependence is the same for each problem, the solutions

$$O(1): \quad \left[\nabla^2 - \frac{1}{c^2(z)} \frac{\partial^2}{\partial t^2} \right] P_0(\underline{r}, \underline{r}', t) = -\delta(\underline{r} - \underline{r}') e^{-i\omega t}$$

$$P_0(\underline{r}, \underline{r}', t) = 0 \quad \text{on} \quad z = 0$$

$$O(a): \quad \left[\nabla^2 - \frac{1}{c^2(z)} \frac{\partial^2}{\partial t^2} \right] P_1(\underline{r}, \underline{r}', t) = 0$$

$$\left[P_1(\underline{r}, \underline{r}', t) \right]_{z=0} = - \left[\frac{\partial P_0}{\partial z} \quad \zeta(\underline{\rho}, t) \right]_{z=0}$$

$$O(a^2): \quad \left[\nabla^2 - \frac{1}{c^2(z)} \frac{\partial^2}{\partial t^2} \right] P_2(\underline{r}, \underline{r}', t) = 0$$

$$\left[P_2(\underline{r}, \underline{r}', t) \right]_{z=0} = - \left[\frac{\partial P_1}{\partial z} \quad \zeta(\underline{\rho}, t) + \frac{\partial^2 P_0}{\partial z^2} \quad \frac{\zeta^2(\underline{\rho}, t)}{2} \right]_{z=0}$$

Figure 5. THE SEQUENCE OF BOUNDARY-VALUE PROBLEMS

can be represented by a combination of Fourier transforms for the horizontal spatial coordinates and an expansion in terms of the eigenfunctions (or normal modes) characteristic of the sound-speed depth dependence. We have developed this procedure and as a first application of it we have applied it to a semi-infinite isovelocity ocean. The approach has been utilized by Fessenden (1973) for this geometry, but in a limited way and for different application. We present the application of the theory both for a sinusoidal deterministic surface, and for a random surface composed of a sum of sinusoids with random phases and frequencies and possessing a typical Pierson-Neumann frequency spectrum.

The geometry for the isovelocity case is illustrated in Figure 6. The surface is a moving sinusoid traveling in the positive x direction and the excitation is a point source located on the z axis. This treatment is completely three-dimensional. The procedure for deriving the field expressions at a particular field point, here characterized by the polar coordinates (ρ , β , z) is to evaluate the integral representations by the method of stationary phase. The stationary phase equations were solved numerically. As Figure 6 implies, the field expressions are amenable to ray-theoretic interpretation. There are four contributions to a field point when the analysis is carried to second order consistent with conservation of energy: the direct contribution, the specularly reflected carrier and the up and down Doppler-shifted sidebands. The first order correction yields the two sidebands, while the portion of the second order contribution which is retained corrects for the energy removed from the carrier in establishing the first-order sidebands. The solution of the second-order boundary value problem also yields up and down Doppler sidebands at twice the surface frequency. However, these would require fourth-order corrections for conservation of energy and hence are discarded.

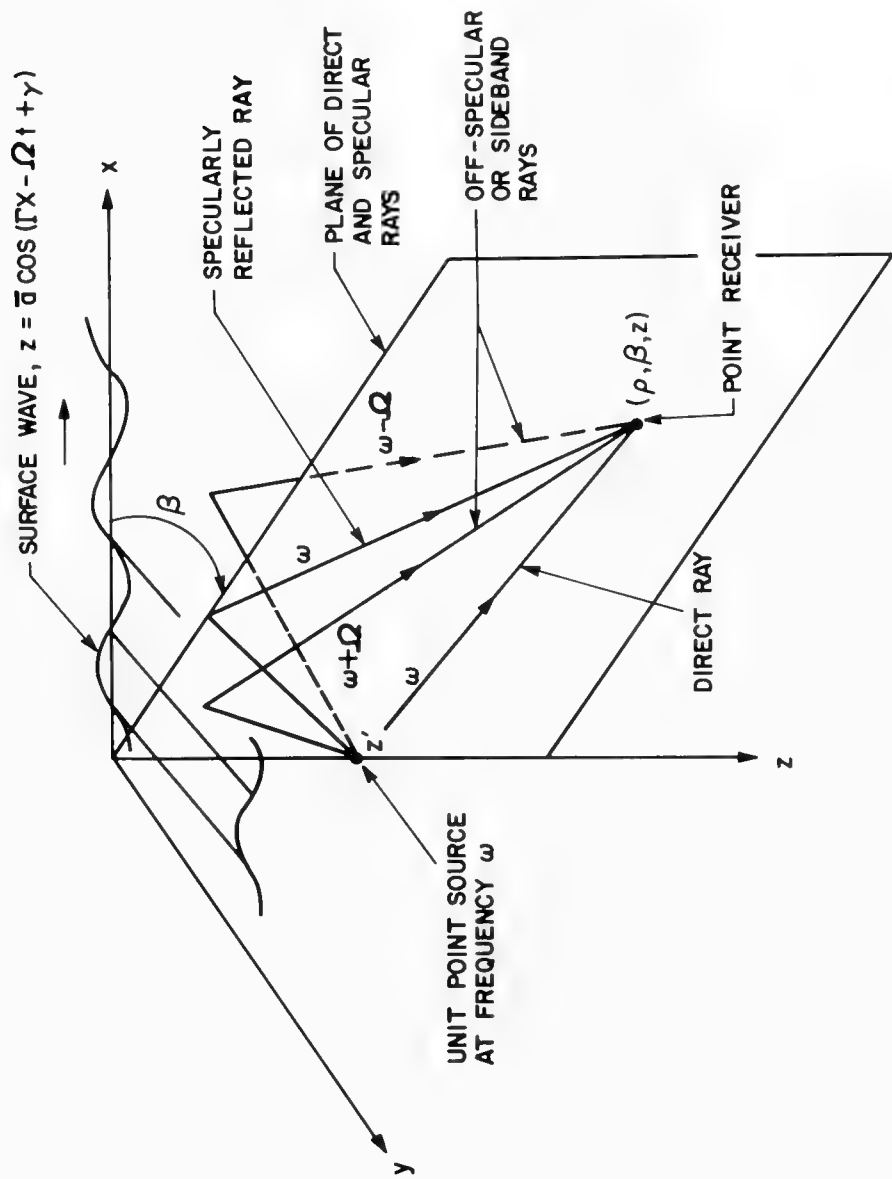


Figure 6. GEOMETRY OF SURFACE-IMAGE INTERFERENCE (LLOYD'S-MIRROR) REGION

Figure 7 illustrates the ray-theoretic interpretation from a different point of view, that of the generation of the first-order sidebands at the point of impact of the surface-reflected carrier ray. Given the angle of incidence of the carrier, the angles of the sideband rays can be determined. It is clear from this diagram that each of the two sidebands which contributes to a given field point must have been generated by separate carrier rays impinging on the surface at different points. Energy conservation is illustrated in Figure 8. We have, in fact, established that to second order, the energy which impinges on the surface is conserved in a ray-tube sense. The energy which traverses a cross section of the incident ray tube is equal to the sum of the energies which traverse cross sections of the sideband and carrier ray tubes.

The field-point contribution to the time series for the sinusoidal surface case is illustrated in Figure 9. The first term corresponds to the direct field and R_1 is the distance between source and receiver. The second term is the specularly reflected carrier. Here R_2 is the distance between the image and receiver and the term involving Q_0 is the energy-conservation correction to the carrier. The remaining terms are the up and down Doppler-shifted sidebands. It is clear from this form of the time series that the surface-scattering process can be regarded as a narrowband FM process, a fact of some significance in signal-processing applications.

NUMERICAL RESULTS

A description of some numerical results for the sinusoidal surface case is given below. Noteworthy features are the asymmetry in the sideband structure and the planes of symmetry in which the sidebands become equal. The results for the sinusoidal surface case

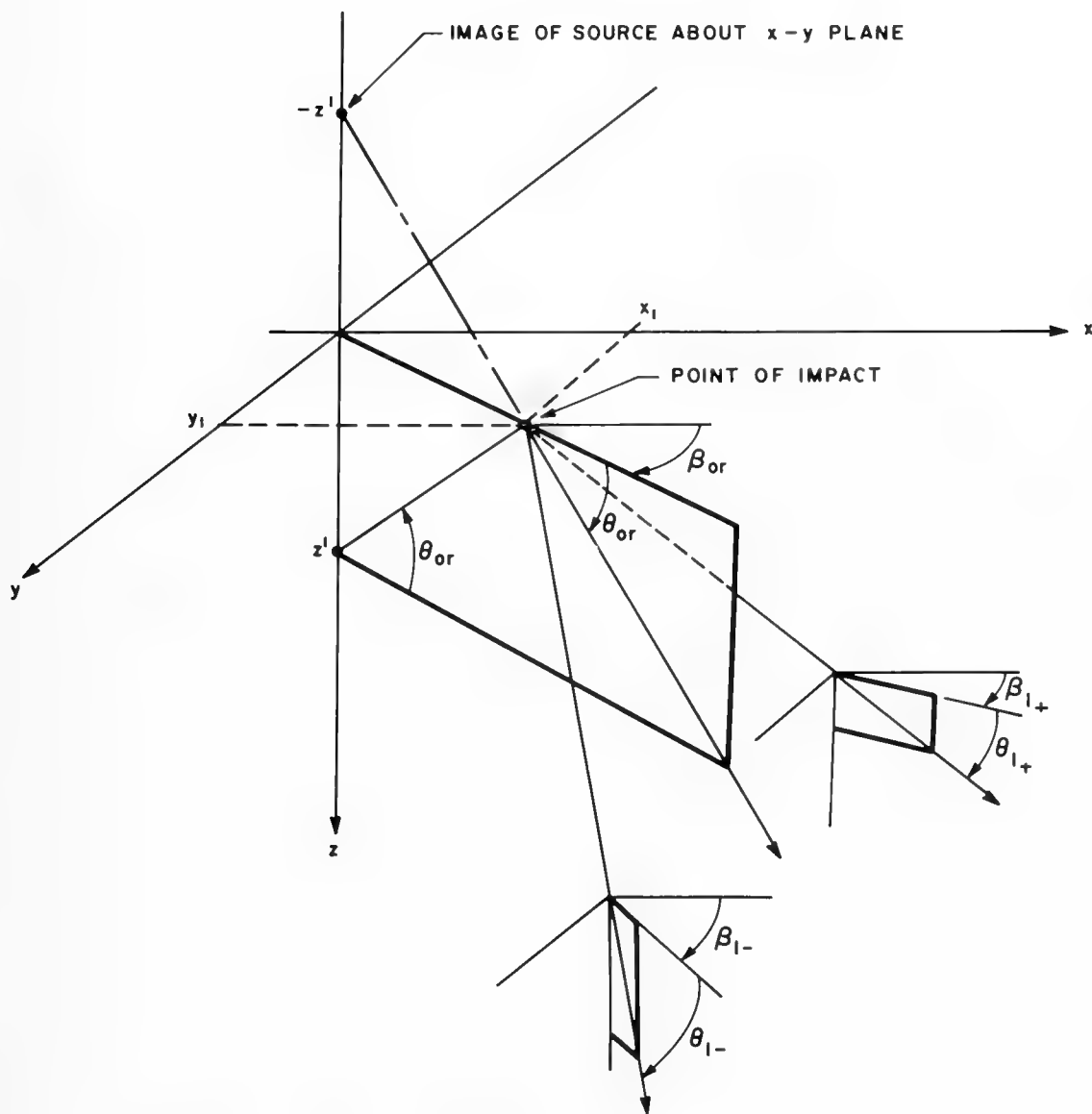


Figure 7. RAY DIAGRAM SHOWING THE GENERATION OF THE FIRST-ORDER SIDEBANDS AT THE POINT OF IMPACT OF THE SURFACE-REFLECTED CARRIER RAY.

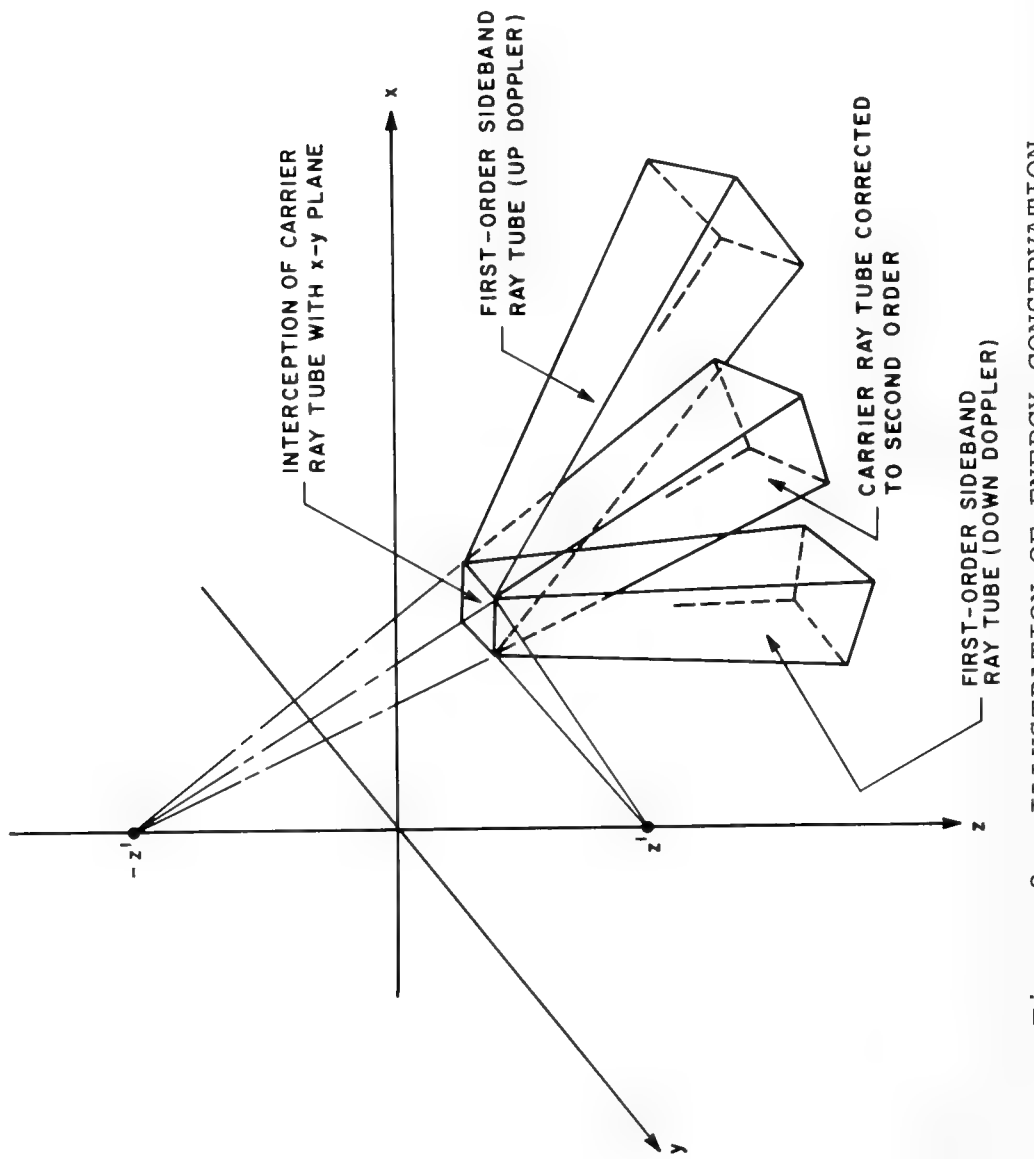


Figure 8. ILLUSTRATION OF ENERGY CONSERVATION

$$1/\sqrt{2} \zeta(x,t) = \cos(\Gamma x - \Omega t + \gamma)$$

$$P(\underline{r}, \underline{r}', t) \sim (4\pi R_1)^{-1} \cos(kR_1 - \omega t)$$

$$+ \left[-(4\pi R_2)^{-1} + (ak)^2 Q_0(\underline{r}, \underline{r}') \right] \cos(kR_2 - \omega t)$$

$$- (ak) Q_{1+}(\underline{r}, \underline{r}') \sin \left(kS_{1+}(\underline{r}, \underline{r}') + \gamma - (\omega + \Omega)t \right)$$

$$- (ak) Q_{1-}(\underline{r}, \underline{r}') \sin \left(kS_{1-}(\underline{r}, \underline{r}') - \gamma - (\omega - \Omega)t \right)$$

Figure 9. TIME SERIES FOR A SINUSOIDAL SURFACE

are for an acoustic frequency of 100 Hz and a surface-wave frequency of 0.1 Hertz (surface wavelength $\Lambda = 129$ m). Figure 10 shows the total power in the acoustic signal as a function of range superimposed on the corresponding smooth surface transmission-loss function. The essential feature in this figure is the smoothing out of the power curve because of the redistribution of energy. The receiver at $z = 1,000$ m is located well below the source at $z' = 50$ m and the radial direction, $\beta = 0^\circ$, coincides with the direction in which the surface wave is traveling. The computations were made for a surface waveheight $\bar{a} = 2$ m. Figure 11 displays the spectral decomposition of the total power curve into the carrier and sideband curves. The sideband curves are seen to be asymmetric with the down Doppler-shifted sideband decreasing more rapidly with range.

The azimuthal dependence of the sideband structure is illustrated in the next two figures. In Figure 12, $\beta = 45^\circ$ and the sidebands begin to spread apart further out in range. In Figure 13, $\beta = 90^\circ$ and the sidebands are equal. The smoothing effect on the total power in this plane of symmetry is greater than in any of the other directions by as much as 3 dB at the longer ranges. This is, of course, because the equality of the sidebands doubles their contribution to the total power. Finally, Figure 14 shows how the sidebands have reversed in the $\beta = 180^\circ$ direction.

There is another plane of symmetry across which the sideband structure reverses and that is the plane where the receiver depth equals the source depth. In this plane, regardless of the direction specified by the angle β , the sidebands are always equal. Figure 15 shows the total power curves for a source and receiver depth of 50 m at an angle $\beta = 45^\circ$. The corresponding spectral breakdown is illustrated in Figure 16 and the sidebands are seen to be equal.

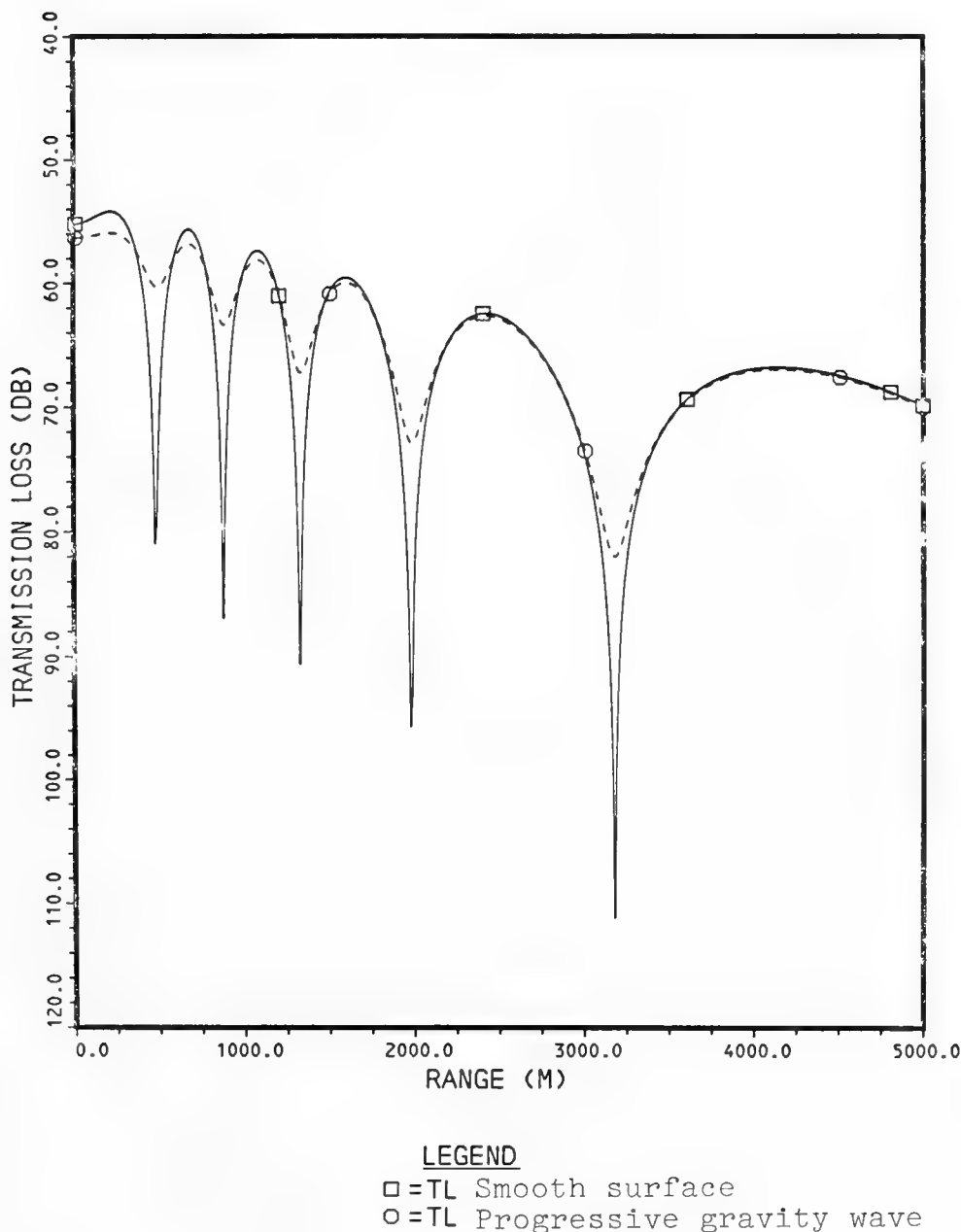


Figure 10. TRANSMISSION LOSS VS RANGE FOR $\beta = 0.0^\circ$,
 $f = 100.0$ Hz, $z = 1000.0$ m, $z' = 50.0$ m,
 $\bar{a} = 2.0$ m and $A = 128.9$ m

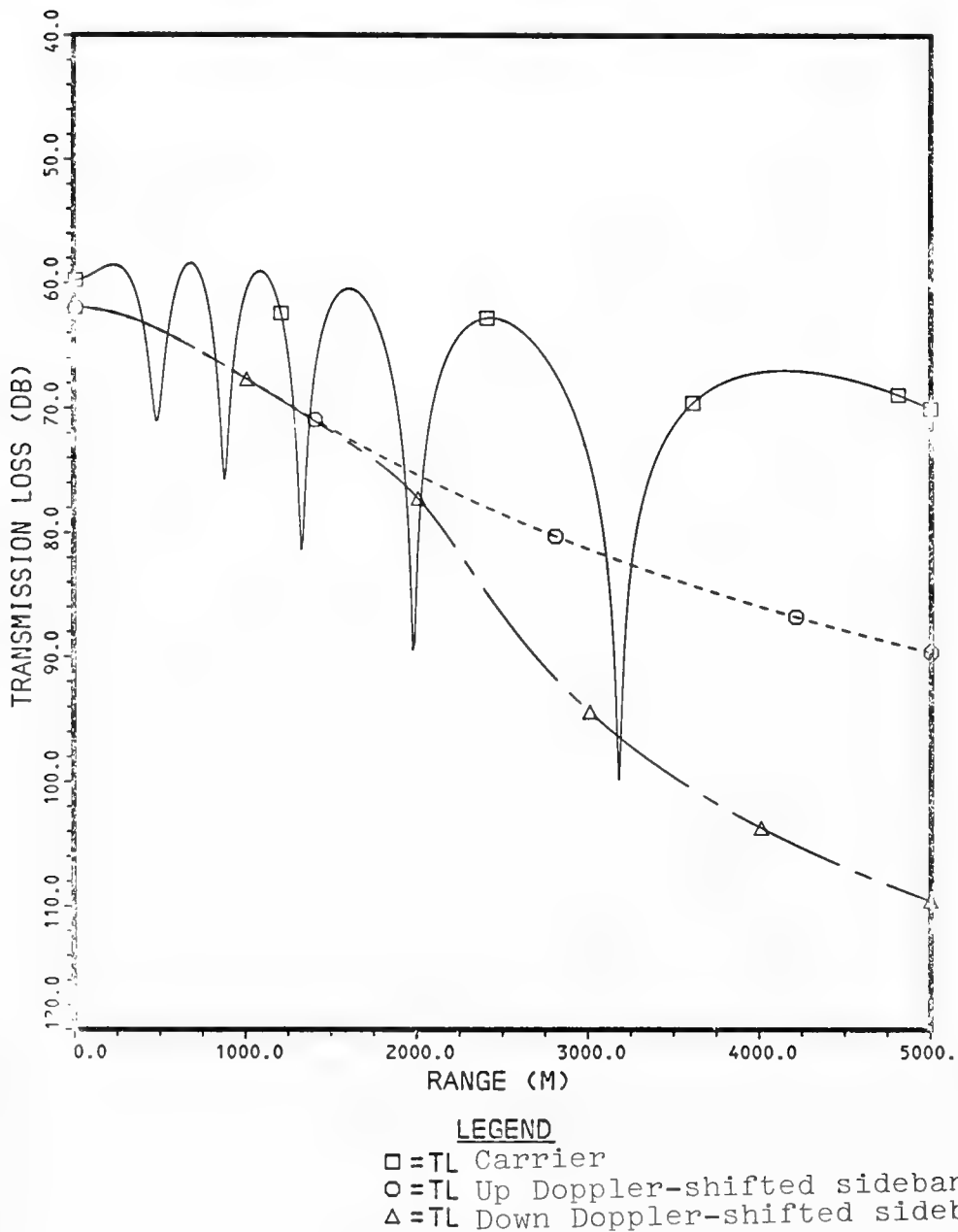


Figure 11. TRANSMISSION LOSS VS RANGE
A SPECTRAL DECOMPOSITION OF SIGNAL
INTENSITY FOR $\beta = 0.0^\circ$, $f = 100.0$ Hz,
 $z = 1000.0$ m, $z' = 50.0$ m, $\bar{a} = 2.0$ m
and $A = 128.9$ m

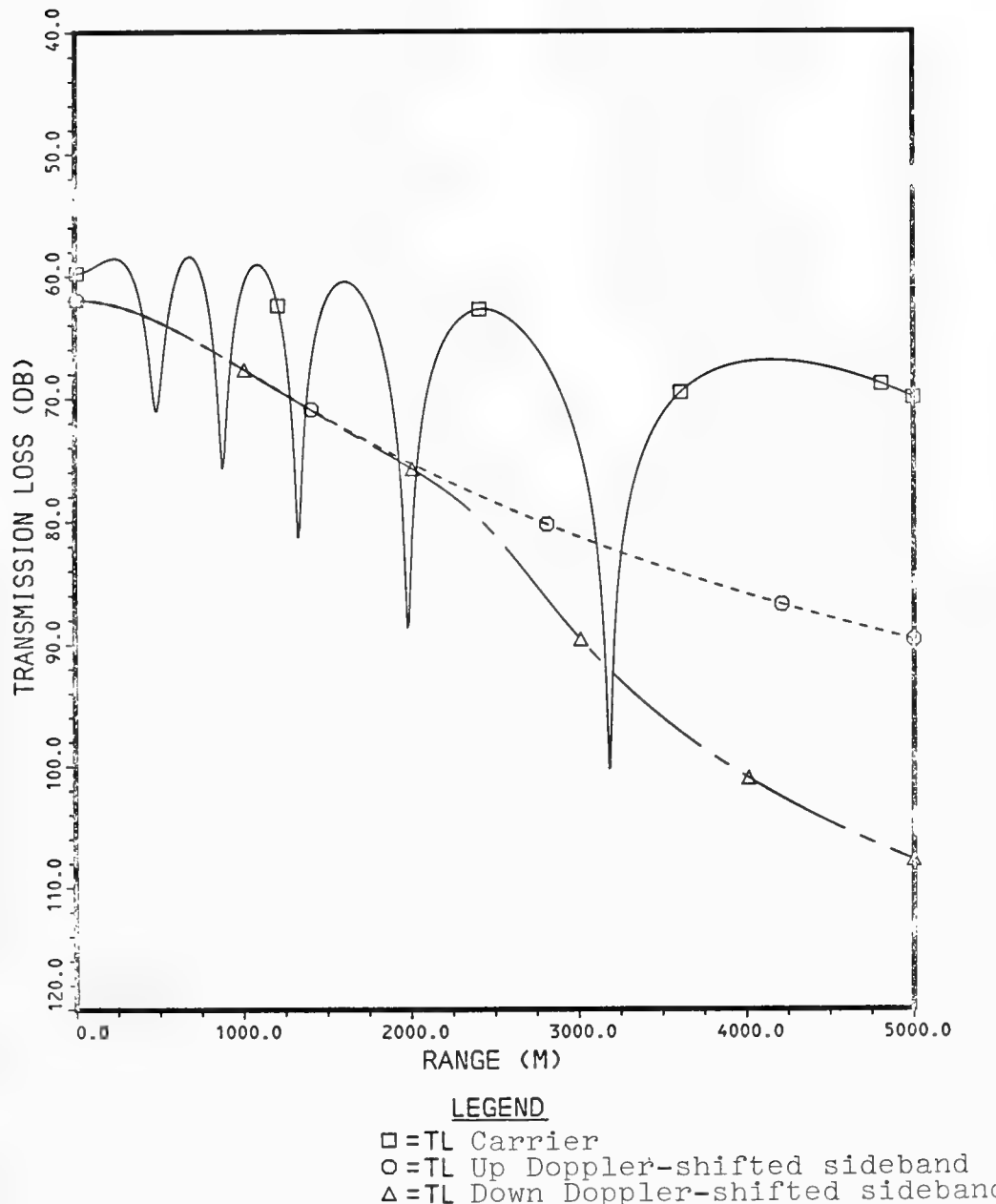
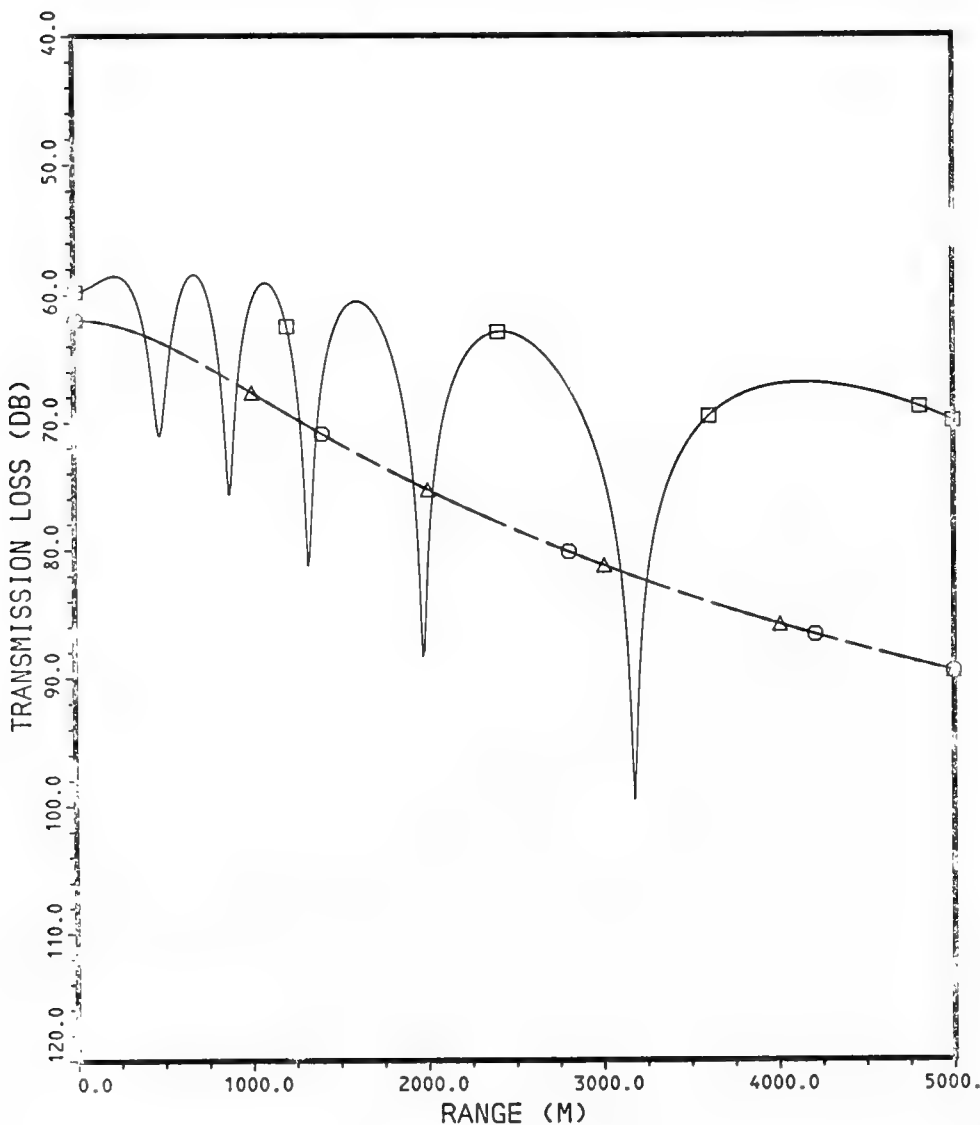


Figure 12. TRANSMISSION LOSS VS RANGE FOR A SPECTRAL DECOMPOSITION OF SIGNAL INTENSITY FOR $\beta = 45.0^\circ$, $f = 100.0$ Hz $z = 1000.0$ m, $z' = 50.0$ m, $\bar{a} = 2.0$ m and $A = 128.9$ m



LEGEND

- = TL Carrier
- = TL Up Doppler-shifted sideband
- △ = TL Down Doppler-shifted sideband

Figure 13. TRANSMISSION LOSS VS RANGE
A SPECTRAL DECOMPOSITION OF SIGNAL
INTENSITY FOR $\beta = 90.0^\circ$, $f = 100.0$ Hz,
 $z = 1000.0$ m, $z' = 50.0$ m, $\bar{a} = 2.0$ m
and $A = 129.9$ m

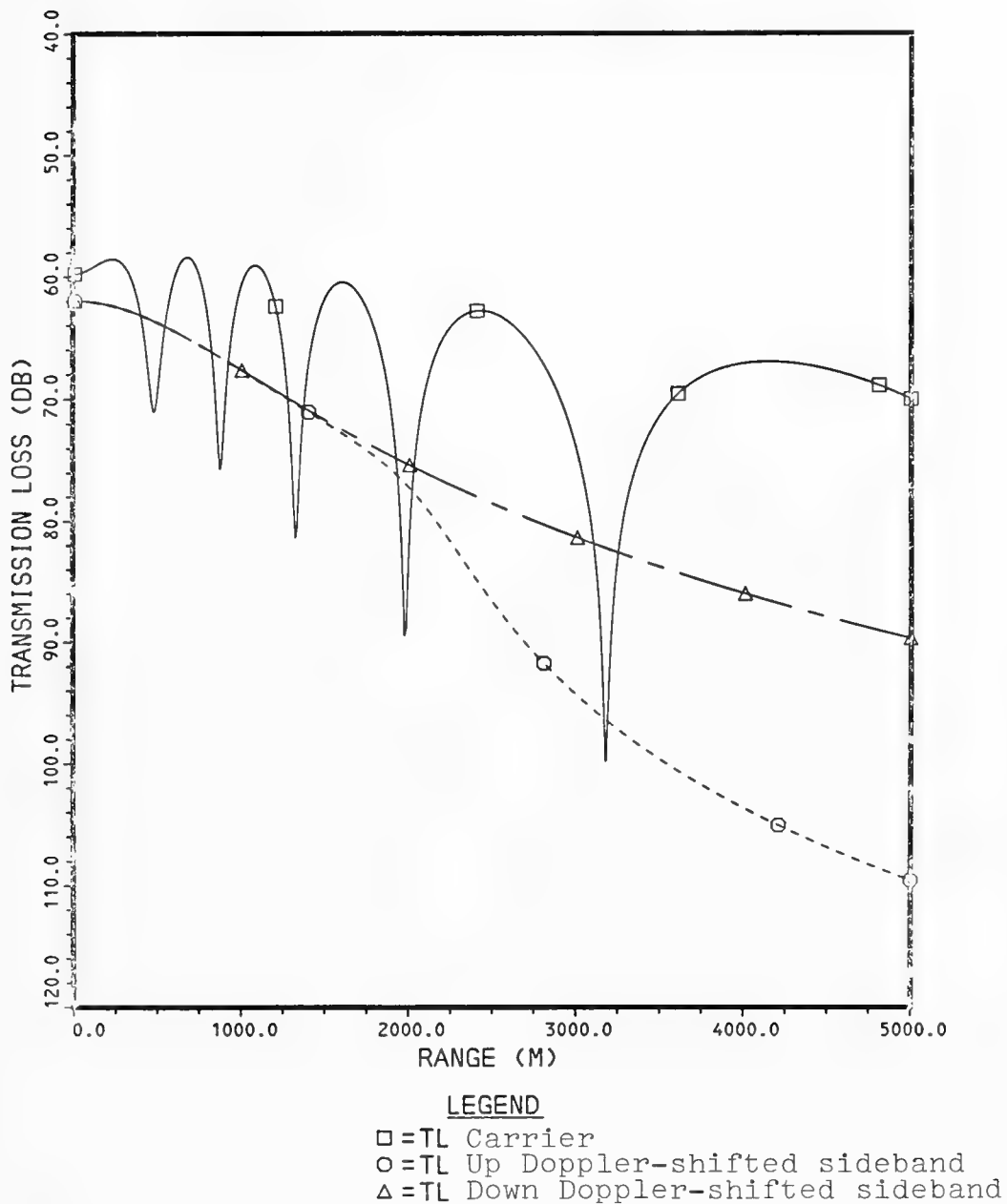


Figure 14. TRANSMISSION LOSS VS RANGE FOR A SPECTRAL DECOMPOSITION OF SIGNAL INTENSITY for $\beta = 180.0^\circ$, $f = 100.0$ Hz, $z = 1000.0$ m, $z' = 50.0$ m, $\bar{a} = 2.0$ m and $A = 128.9$ m

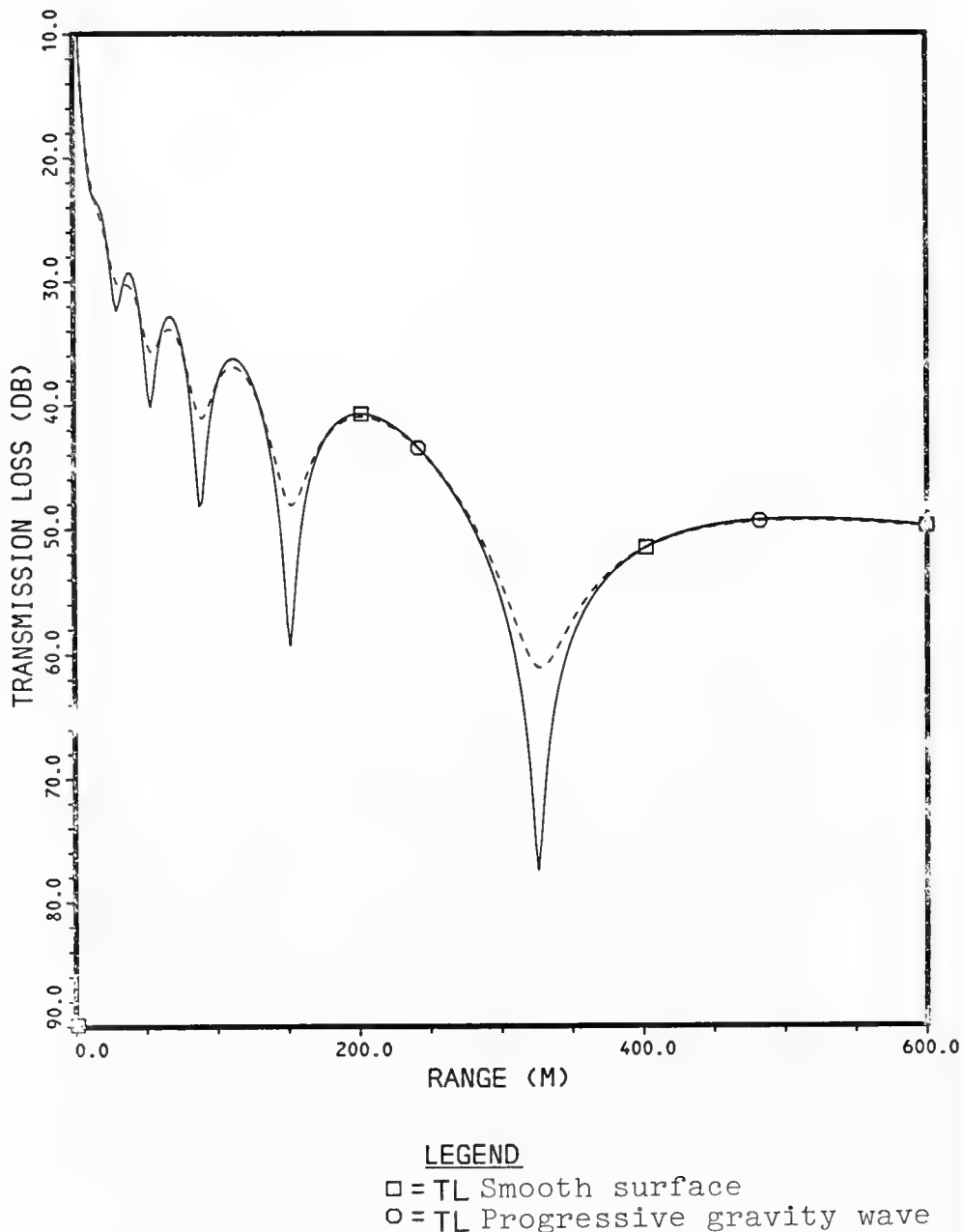


Figure 15. TRANSMISSION LOSS VS RANGE
TOTAL SIGNAL INTENSITY FOR
 $\beta = 45.0^\circ$, $f = 100.0$ Hz, $z = 50.0$ m,
 $z' = 50.0$ m, $\bar{a} = 2.0$ m and $A = 128.9$ m

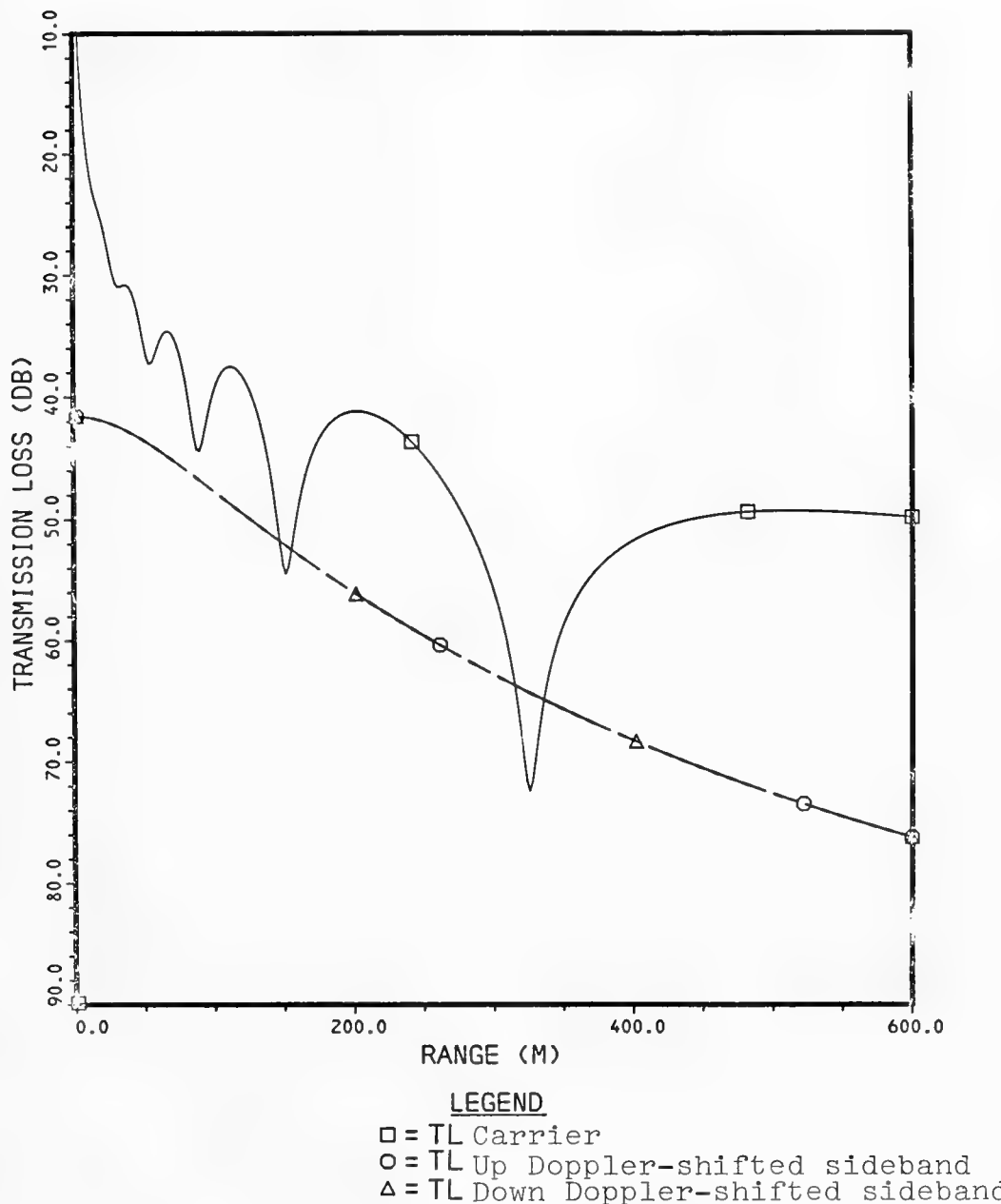


Figure 16. TRANSMISSION LOSS VS RANGE
A SPECTRAL DECOMPOSITION OF SIGNAL
INTENSITY FOR $\beta = 45.0^\circ$, $f = 100.0$ Hz,
 $z = 50.0$ m, $z' = 50.0$ m, $\bar{a} = 2.0$ m,
and $A = 128.9$ m

The reversal of the sidebands is illustrated in Figure 17 where the receiver is now above the source. Here the direction of the three power curves is that of the surface wave ($\beta = 0^\circ$) and the up Doppler-shifted sideband is seen to die out more rapidly than the down Doppler-shifted one.

The planes of symmetry which I have just illustrated can be predicted mathematically, and indeed we have done this in the two cases of $\beta = 90^\circ$ and $z = z'$. The $\beta = 90^\circ$ symmetry is perhaps intuitively acceptable, but there is no *a priori* reason to expect the $z = z'$ symmetry to exist. In fact, although we can describe all of the geometric consequences of the latter symmetry, there does not appear to be an obvious physical explanation for it. And as far as the reversal in the amplitudes of the sidebands about this plane is concerned, we have not been able to assign a simple physical explanation to it either. Perhaps the complicated geometrical structure precludes this.

The generalization of the isovelocity half space problem to the case of a random surface is now presented. Figure 18 shows the time series for the surface simulation, as well as the resulting pressure. Following Shinozuka and Jan (1972), we simulate the surface as a sum of sinusoids. Here the phases γ_j are random and uniformly distributed between 0 and 2π , and the frequencies Ω_j have a small random part about a mean value. The means are equally spaced over some band and the random part prevents the process from being periodic. The amplitudes h_j are deterministic, being determined from the height of the power spectrum at the mean value of Ω_j . The power spectrum can be a measured spectrum or a typical Pierson-Neumann distribution. In any case, the simulated process is ergodic with respect to its mean and auto-correlation. For large samples (i.e., large M), the process becomes Gaussian.

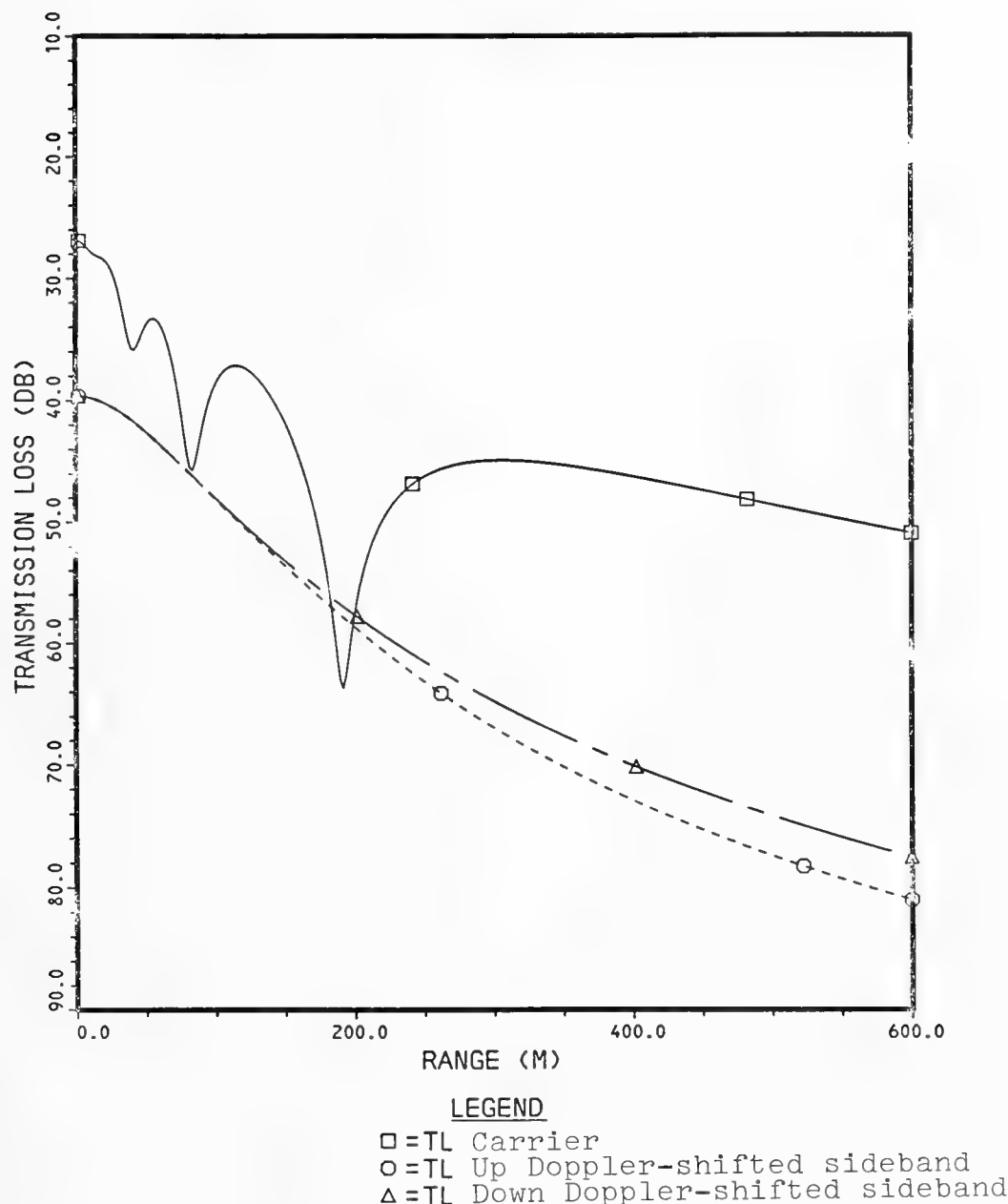


Figure 17. TRANSMISSION LOSS VS RANGE
A SPECTRAL DECOMPOSITION OF SIGNAL
INTENSITY FOR $\beta = 0.0^\circ$, $f = 100.0$ Hz,
 $z = 30.0$ m, $z' = 50.0$ m, $\bar{a} = 2.0$ m
and $A = 128.9$ m

$$z_{\text{surface}}(x, t) = \sum_{j=1}^M h_j \cos(\Gamma_j x - \Omega_j t + \gamma_j)$$

$$P(\underline{r}, \underline{r'}, t) \sim (4\pi R_1)^{-1} \cos(kR_1 - \omega t)$$

$$+ \left[-(4\pi R_2)^{-1} + (ak)^2 \sum_{j=1}^M \frac{h_j^2}{a^2} Q_{j20}(\underline{r}, \underline{r'}) \right] \cos(kR_2 - \omega t)$$

$$- (ak) \sum_{j=1}^M \frac{h_j}{a} Q_{1j+}(\underline{r}, \underline{r'}) \sin \left[kS_{j1+}(\underline{r}, \underline{r'}) + \gamma_j - (\omega + \Omega_j)t \right]$$

$$- (ak) \sum_{j=1}^M \frac{h_j}{a} Q_{1j-}(\underline{r}, \underline{r'}) \sin \left[kS_{j1-}(\underline{r}, \underline{r'}) - \gamma_j - (\omega - \Omega_j)t \right]$$

Figure 18. TIME SERIES FOR A RANDOM SURFACE

The essential feature to notice about the pressure time series is that it has basically the same form as in the single sinusoid case, except that now there are contributions from all frequencies in the spectrum. To second order in the perturbation there are still four contributions to a field point: the direct field, the corrected specular reflection, and the up and down Doppler-shifted sidebands.

Figure 19 displays the form of the power spectrum, the Fourier transform of the autocorrelation function, for the pressure process. The sideband spectra are seen to be linear combinations of the average value of the square of the sideband amplitude functions $Q_{1j\pm}^2$. The weighting factors are the squared amplitudes of the surface sinusoids. Thus, the quantities $Q_{1j\pm}^2$ can be regarded as the squared magnitude of a sideband system function evaluated at the mean values of Ω_j .

The value of the carrier spectrum is not as simple to describe. There is no simple linear relationship between it and the surface spectrum. About all that can be said for it is that it is a complicated function of the square of the amplitudes of the surface sinusoids.

We have been able to generate a large number of numerical results for the random surface case and we will show a selected few of them. All the following plots are computer generated for an acoustic frequency of f (F on the plots) = 50 Hz, and an rms wave-height a (A on the plots) = 2.48 m. The latter is computed from a Pierson-Moskowitz spectrum which is illustrated below. Again note the asymmetry of the sidebands and the planes of symmetry $\beta = 90^\circ$ and z (Z on the plots) = z' (ZP on the plots).

$$R_P(\tau) = E [P(\underline{r}, \underline{r}', t) P(\underline{r}, \underline{r}', t + \tau)]$$

$$S_P(\sigma) = \frac{1}{2\pi} \int_{-\infty}^{\infty} R_P(\tau) e^{i\sigma\tau} d\tau$$

Sideband Spectra:

$$S_{P+}(\sigma) = \sum_{j=1}^M h_j^2 \left\langle Q_{1j+}^2 \right\rangle \delta(|\sigma| - (\omega + \Omega j))$$

$$S_{P-}(\sigma) = \sum_{j=1}^M h_j^2 \left\langle Q_{1j-}^2 \right\rangle \delta(|\sigma| - (\omega - \Omega j))$$

Carrier Spectrum:

$$S_{PC}(\sigma) = F(h_j^2) \delta(|\sigma| - \omega)$$

Figure 19. POWER SPECTRUM

Figure 20 is a transmission loss plot for $\beta = 0^\circ$ displaying the total power distribution for a smooth (deep nulls) surface and a random (smooth plot) surface. The source and receiver are located at 50 m and 1,000 m, respectively. The redistribution of energy is readily apparent. Figure 21 shows the corrected carrier against the smoothed surface. Of course, the carrier nulls are deeper than for the total transmission loss. Note the two numbers, $R = 2,000$ m and $R = 3,200$ m, at which a peak and a null occur because a later figure displays the sideband system function and the acoustic frequency spectrum at those points for purposes of comparison.

Figure 22 shows the spectral breakdown into carrier and sidebands. The sidebands are seen to start out together at short range with the down Doppler-shifted one (IM) falling off more readily at long range.

The asymmetry in the sidebands is even more readily apparent in plots of the sideband system function as a function of surface frequency. Figure 23 displays this function (Q1P and Q1M on the plots) at the range 2,000 m, a peak in the transmission loss. For a Pierson-Moskowitz spectrum giving rise to an rms waveheight of 2.48 m, as displayed in Figure 24, the acoustic spectrum, normalized to the carrier, appears as in Figure 25. The asymmetry in the sidebands and the fact that the receiver point is at a peak in the surface-image interference is readily apparent. For the same surface spectrum, the system function and the acoustic spectrum at a null in the surface-image interference ($R = 3,200$ m) are displayed, respectively, in Figures 26 and 27. In this last figure, the dominance of the sidebands is apparent.

The next five figures display the various curves showing the $\beta = 90^\circ$ plane of symmetry. Figure 28 shows the spectral breakdown.

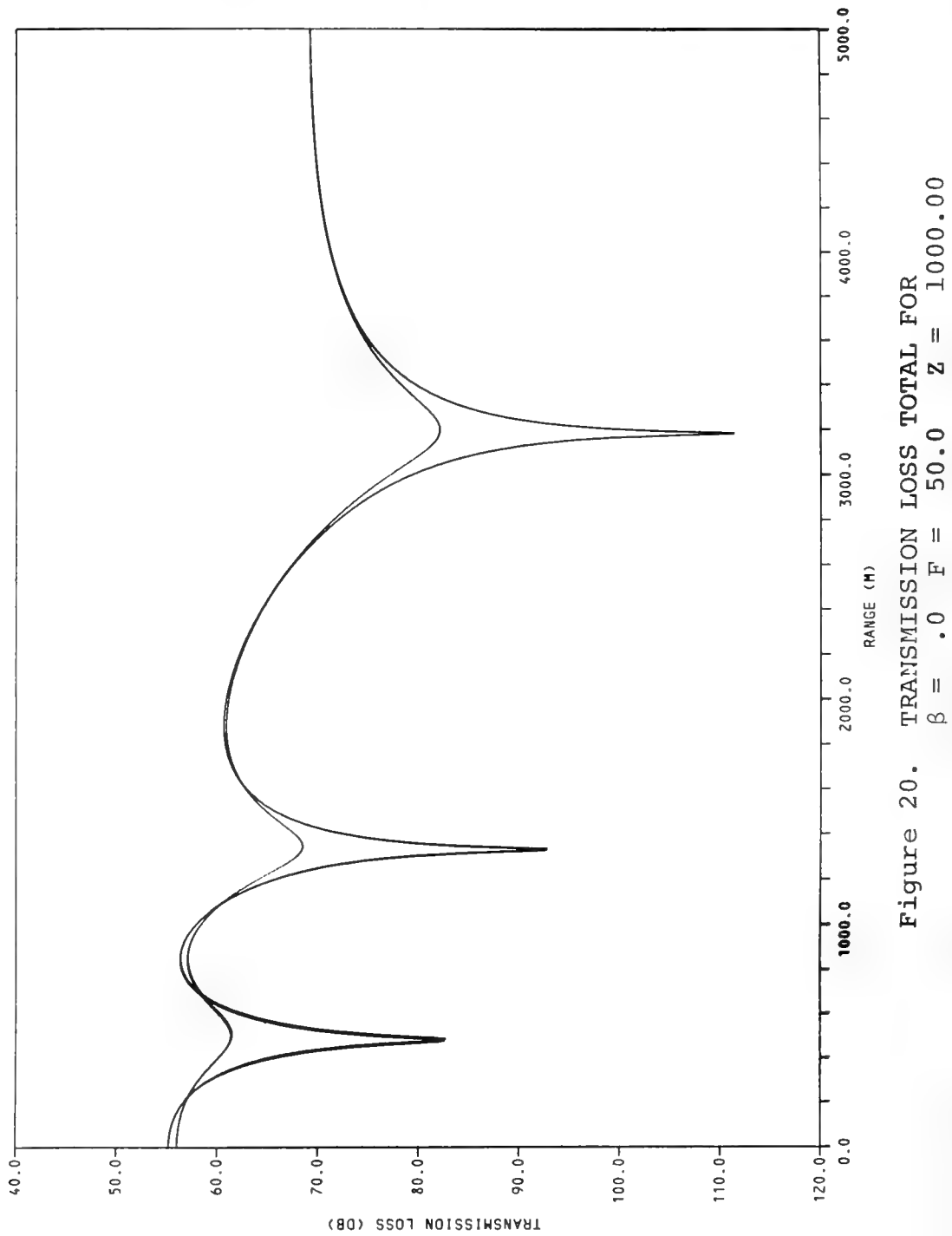


Figure 20. TRANSMISSION LOSS TOTAL FOR
 $\beta = .0$ $F = 50.0$ $Z = 1000.00$
 $ZP = 50.00$ $A = .24807+.01$

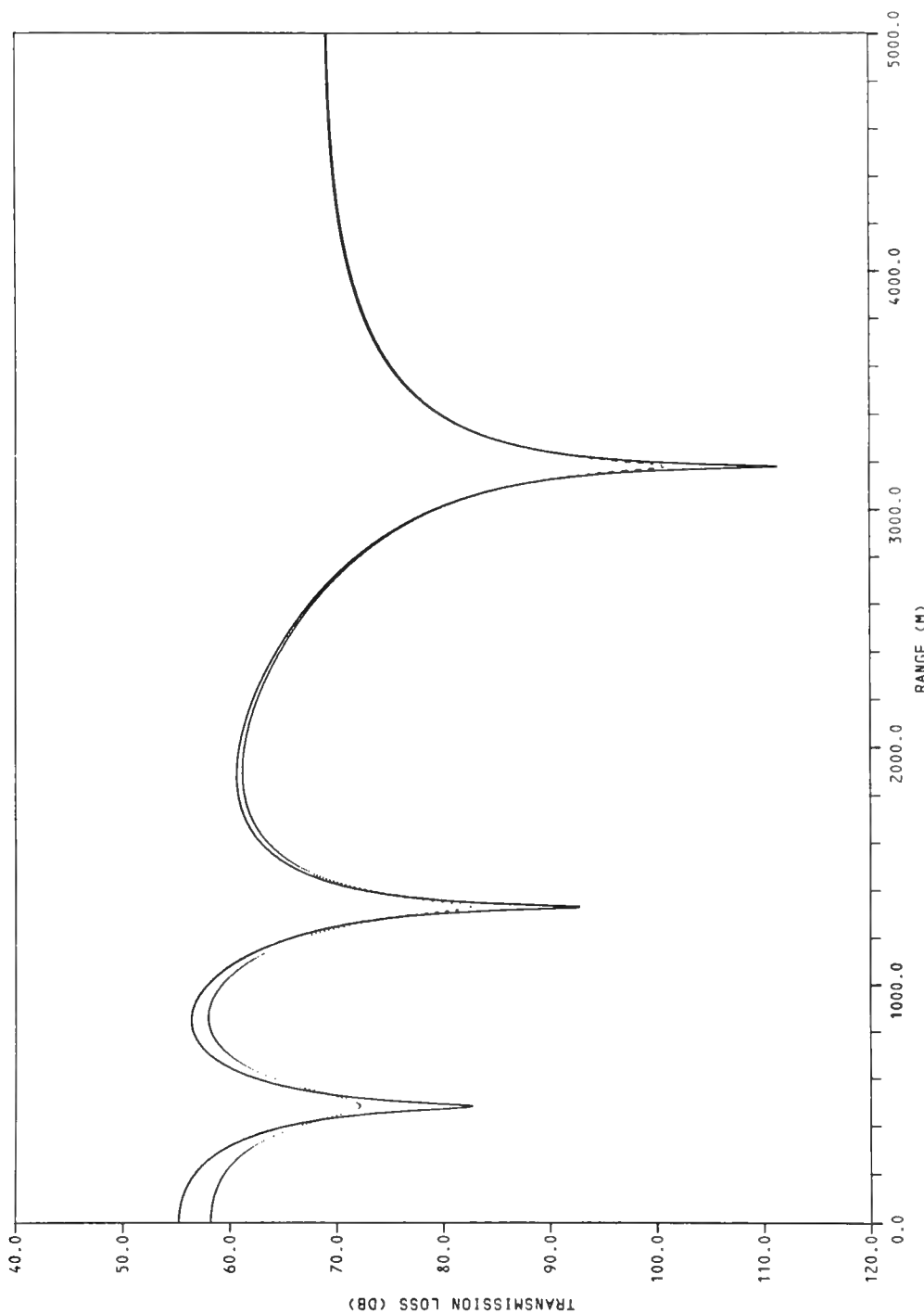


Figure 21. TRANSMISSION LOSS CARRIER FOR
 $\beta = .0$ $F = 50.0$ $Z = 1000.00$
 $Z_P = 50.00$ $A = .24807+01$

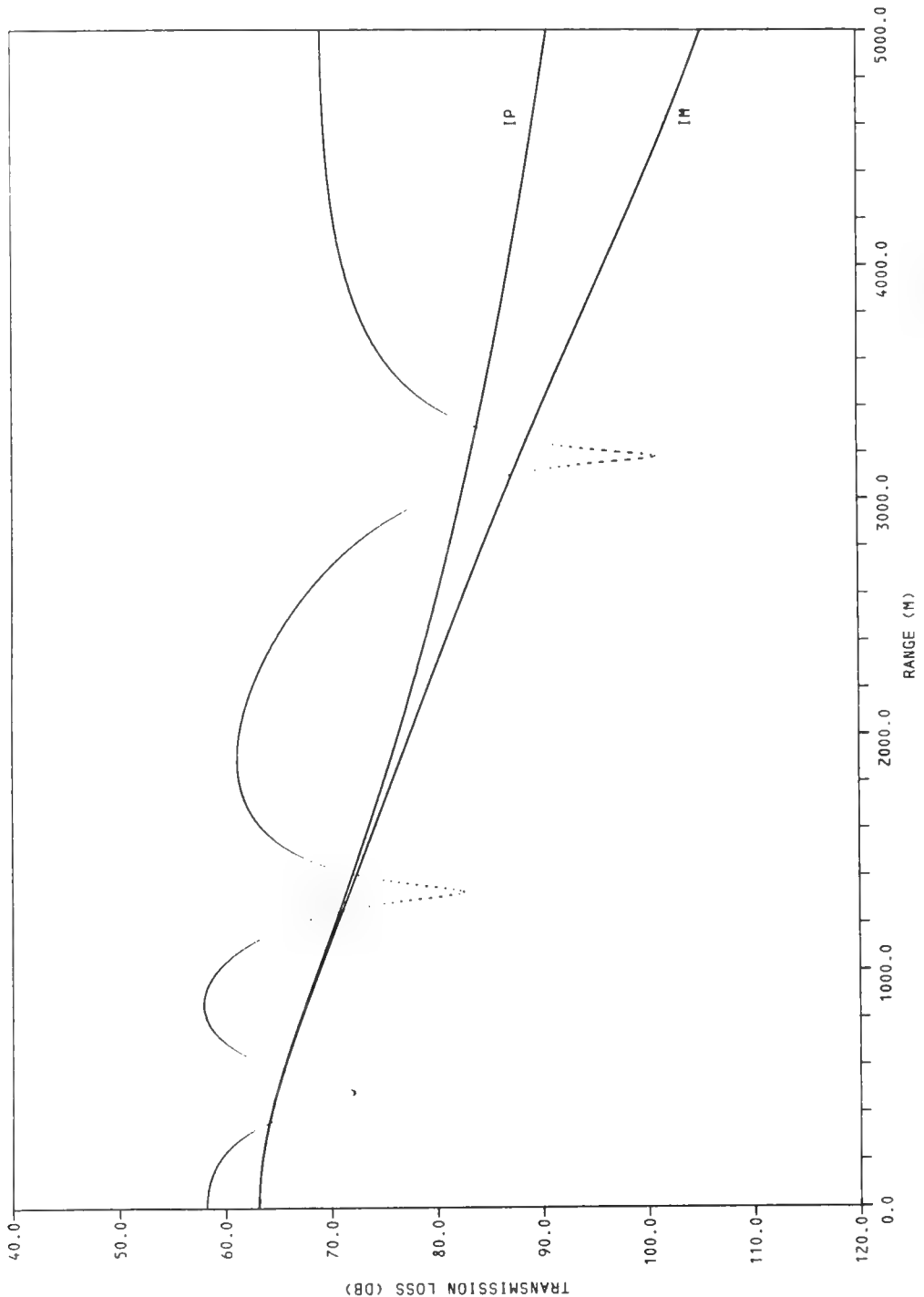


Figure 22. TRANSMISSION LOSS CARRIER AND SIDEBANDS FOR
 $\beta = 0$ $F = 50.0$ $Z = 1000.00$ $Z_P = 50.00$
 $A = .24807+01$

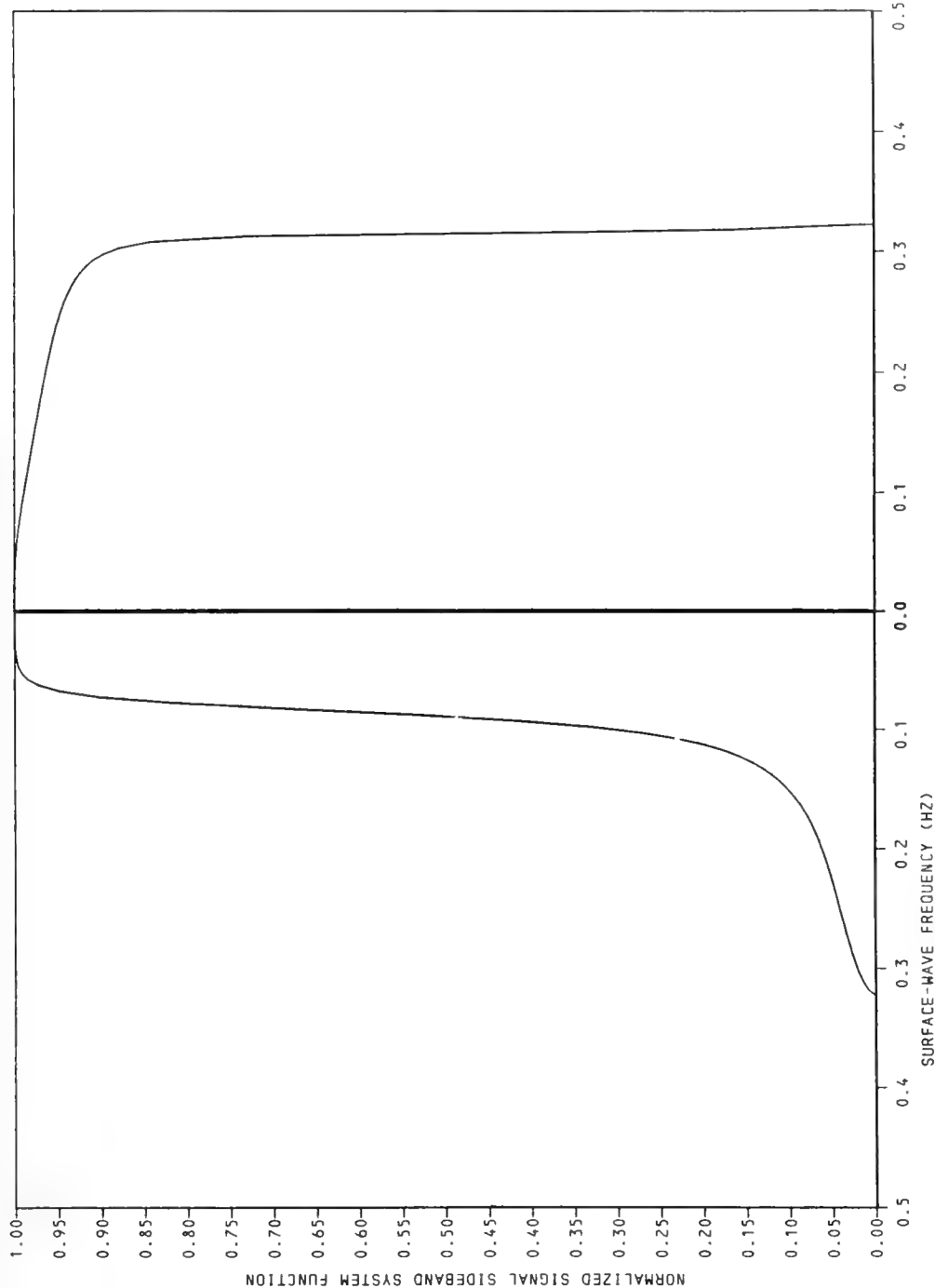


Figure 23. SIDEBAND SYSTEM FUNCTION VS SURFACE WAVE FREQUENCY
FOR $\beta = .0$ $F = 50.0$ $Z = 1000.00$ $ZP = 50.00$
 $R = 2000.0$ $QIM = .43099-04$ $QIP = .43099-04$ (MIN.FREQ.)

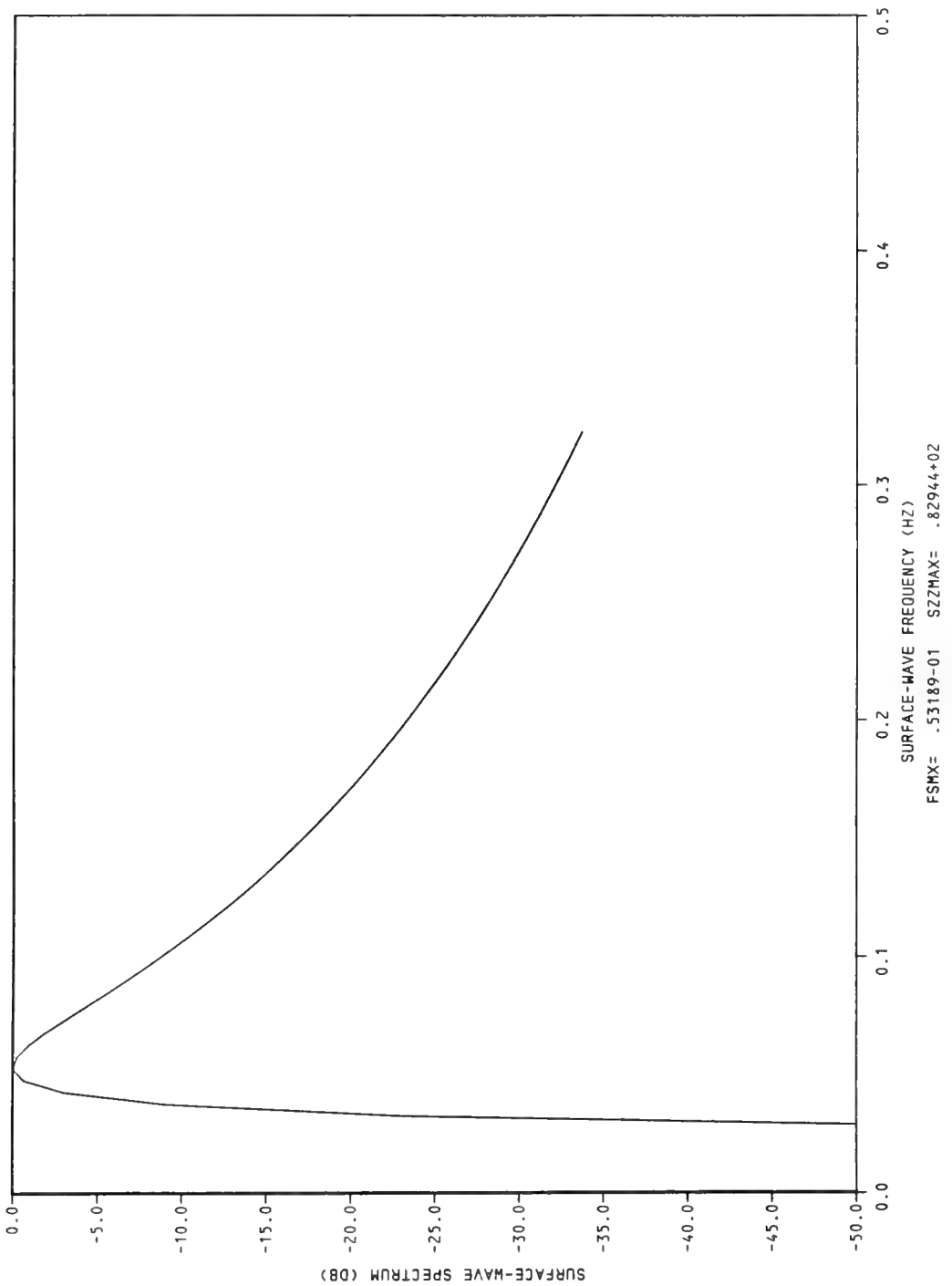


Figure 24. PIERSON-MOSKOWITZ SPECTRUM

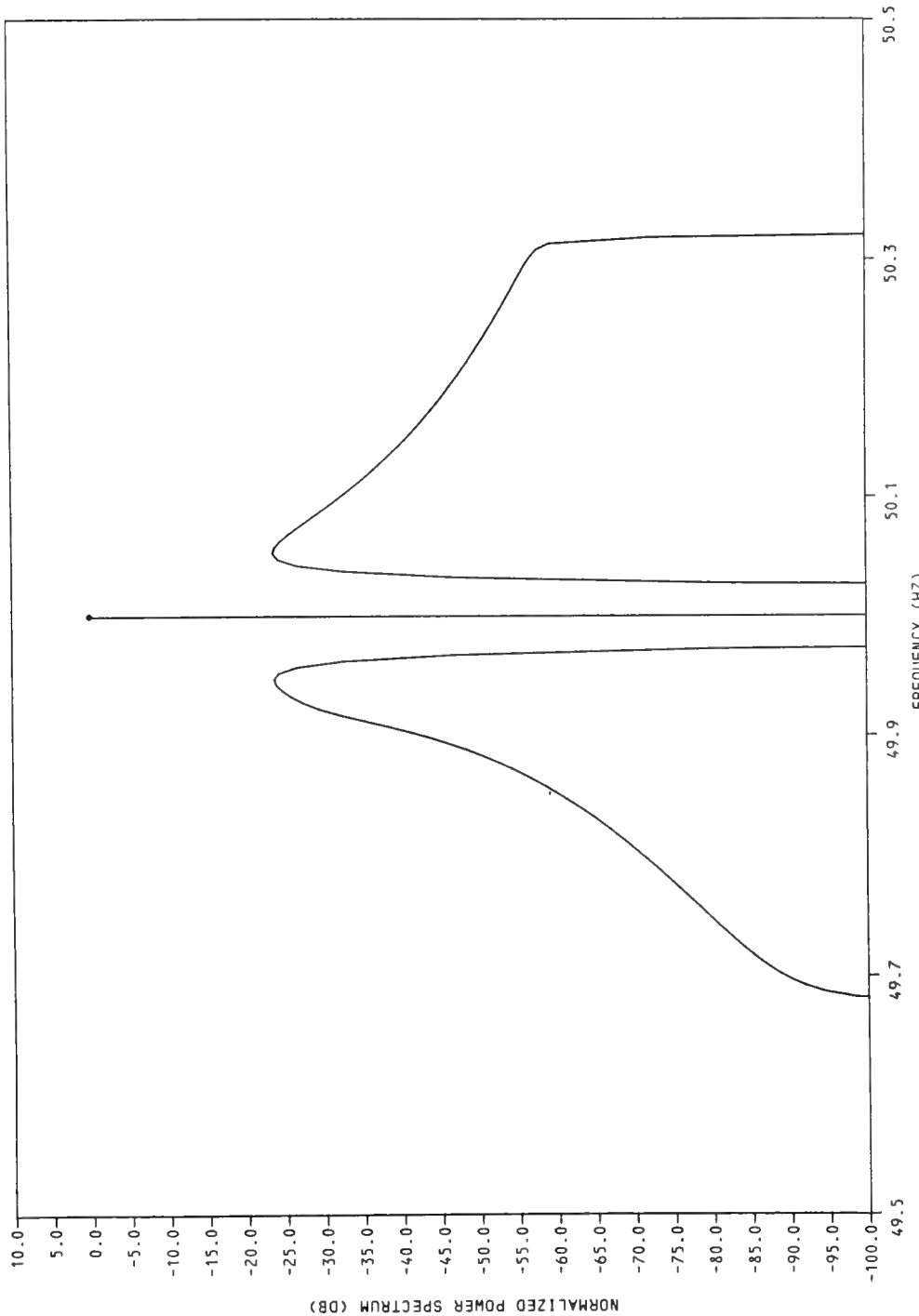


Figure 25. ACOUSTIC SPECTRUM FOR $\beta = 0$ $F = 50.0$ $Z = 1000.00$
 $ZP = 50.00$ $R = 2000.0$ $SP(2\pi F) = .11341-08$
 $\Delta FSHZ = .50000-02$

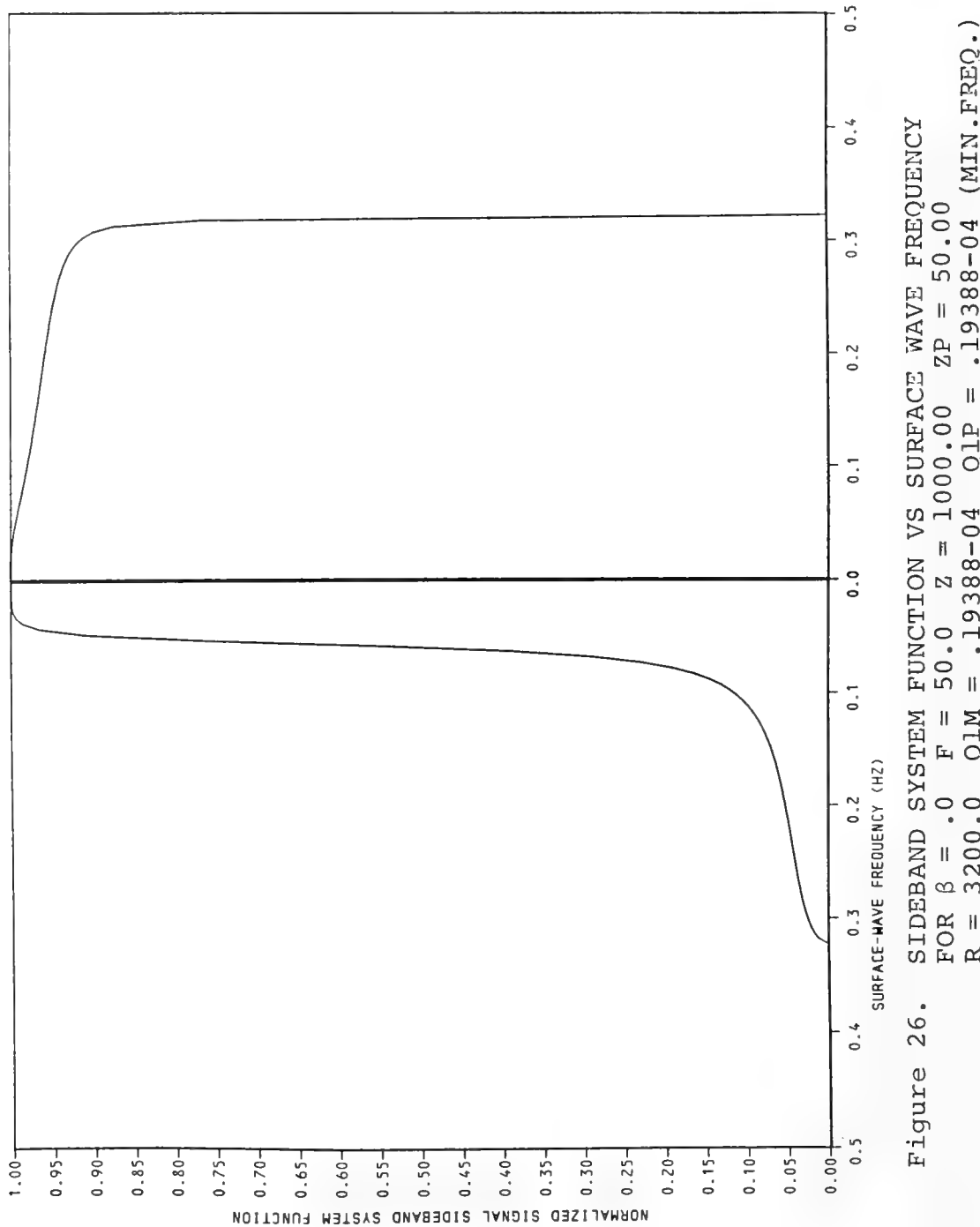


Figure 26. SIDEBAND SYSTEM FUNCTION VS SURFACE WAVE FREQUENCY

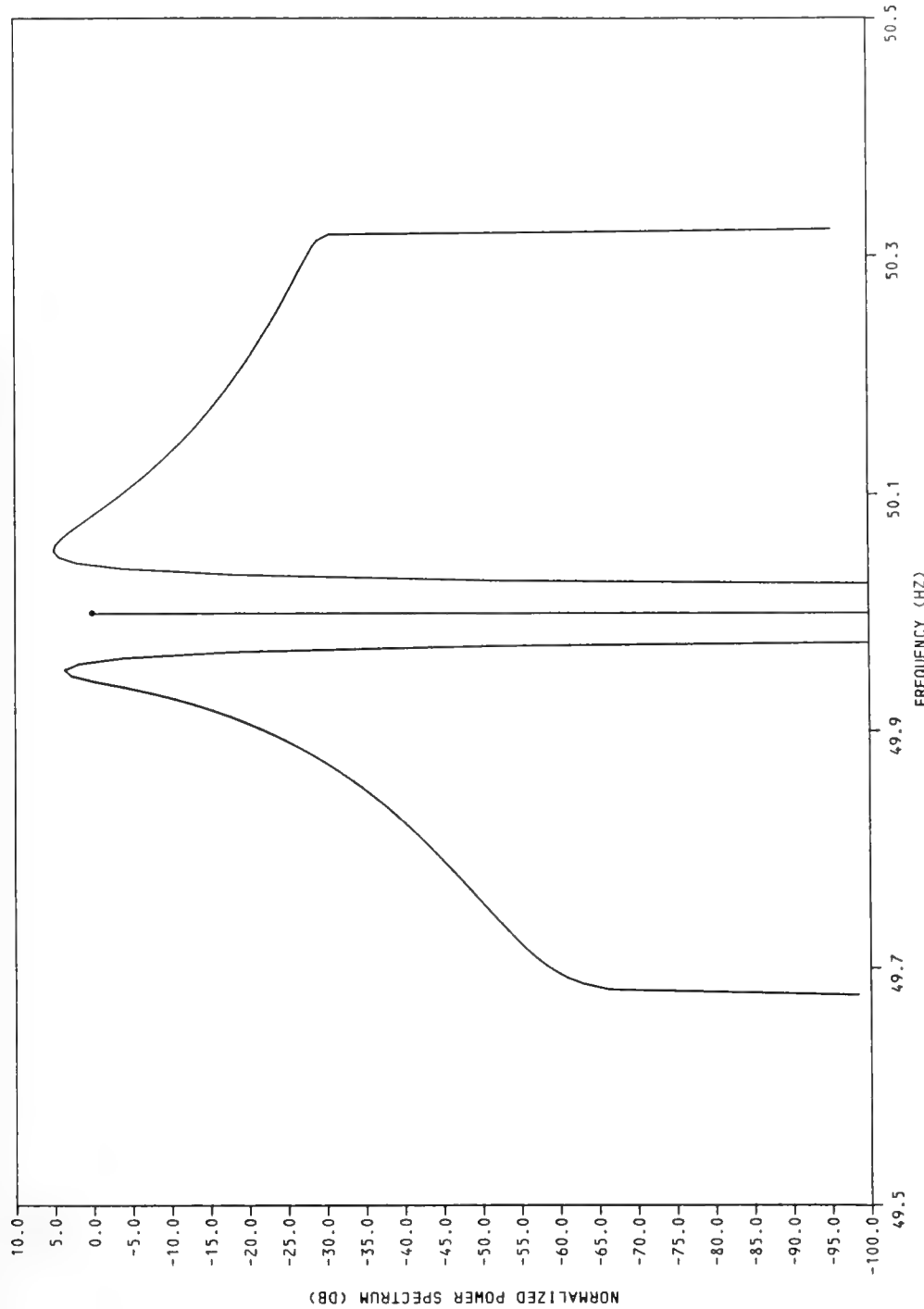


Figure 27. ACOUSTIC SPECTRUM FOR $\beta = 0$ $F = 50.0$ $Z = 1000.00$
 $ZP = 50.00$ $R = 3200.0$ $SP(2\pi F) = .30593-12$
 $\Delta F_{SHZ} = .500000-02$

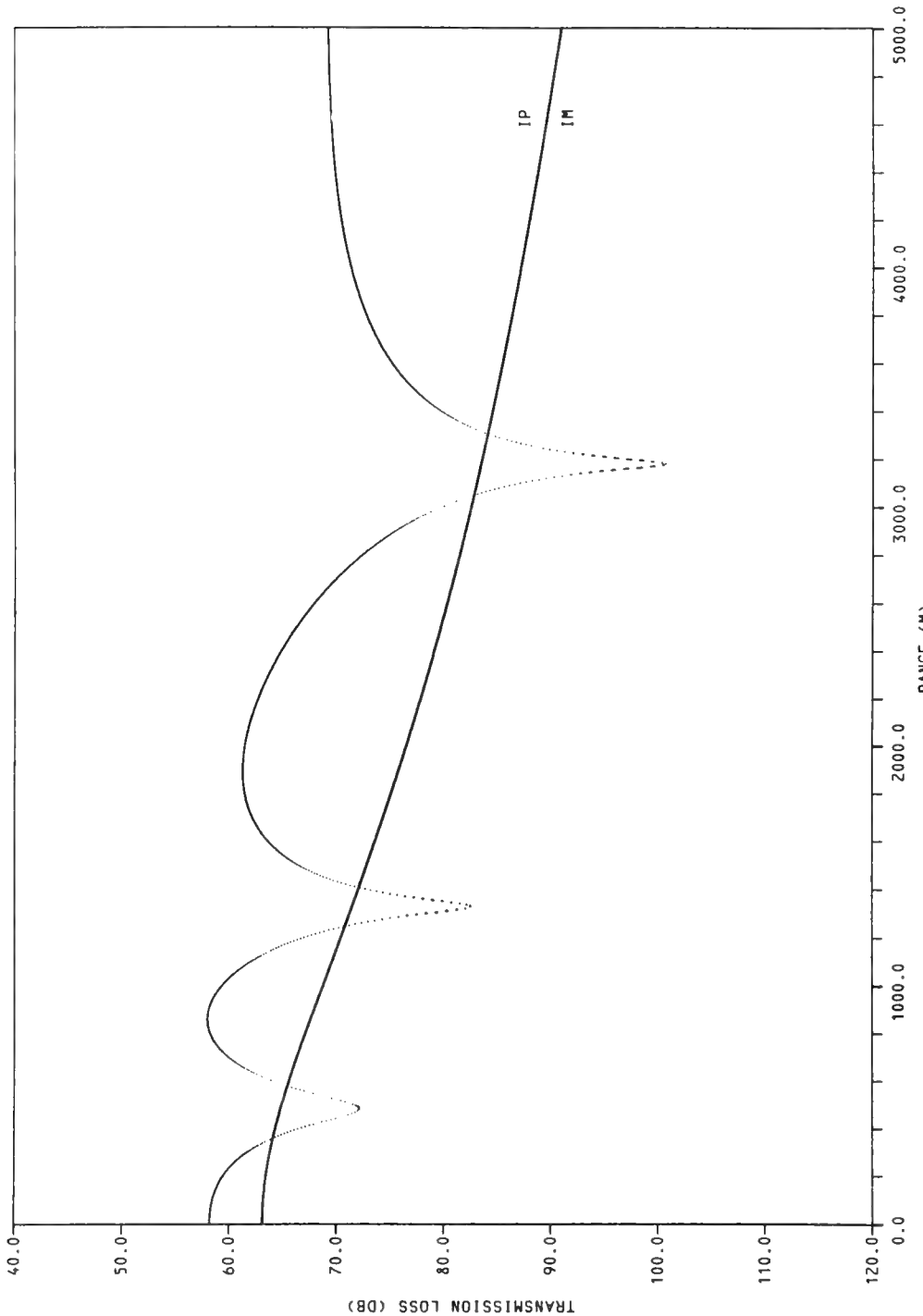


Figure 28. TRANSMISSION LOSS CARRIER AND SIDEBANDS FOR
 $\beta = 90.0$ $F = 50.0$ $Z = 1000.00$ $ZP = 50.00$
 $A = .24807+01$

The sideband curves are on top of one another. Figure 29 displays the symmetric system function at the interference peak, while Figure 30 shows the corresponding acoustic spectrum. Figure 31 is a plot of the symmetric system function at the null and Figure 32 is the corresponding acoustic spectrum.

The final set of results which I would like to display is that of the $z = z'$ symmetry. These were computed for the same surface spectrum and a source and receiver depth of 50 m. The curves illustrate the case $\beta = 45^\circ$ at a range of 2,000 m. This range is beyond the surface-image interference region, the 12 dB per-double-distance region. Figure 33 shows the spectral breakdown with the equal sidebands. Figure 34 shows the symmetric system function and Figure 35 shows the corresponding acoustic spectrum. It is interesting to note that the $z = z'$ symmetry which we have been predicting theoretically has been observed experimentally. Figure 36 shows a typical set of spectral plots from a recent paper by Brown and Frisk (1974). These plots show the acoustic spectrum superimposed on the surface spectrum for a one-bounce configuration where the source and receiver depths were equal. They display a marked symmetry.

In the future, we intend to explore the model's usefulness in situations with refraction, with immediate emphasis on a deep surface duct.

REFERENCES

- Brock, H. W., "Coherence of Multipath Transmission (U)," Bell Laboratories Ocean Systems Technology Paper, OSTP-3HWB, September 1, 1973 (CONFIDENTIAL).

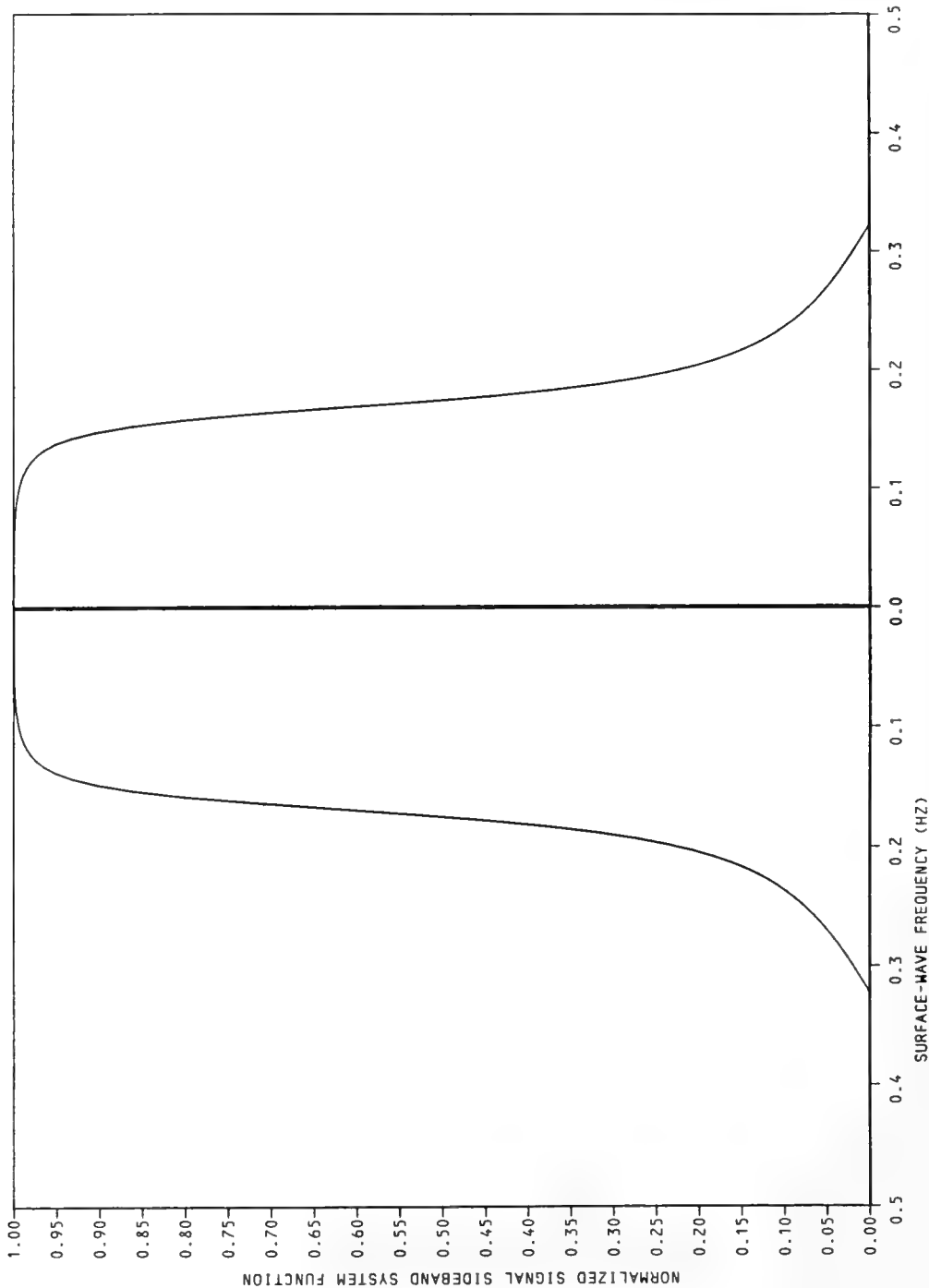


Figure 29. SIDEBAND SYSTEM FUNCTION VS SURFACE WAVE FREQUENCY
FOR $\beta = 90.0$ $F = 50.0$ $Z = 1000.00$ $Z_P = 50.00$
 $R = 2000.0$ $Q_{LM} = .43099-04$ $Q_{LP} = 43099-04$ (MIN.FREQ2.)

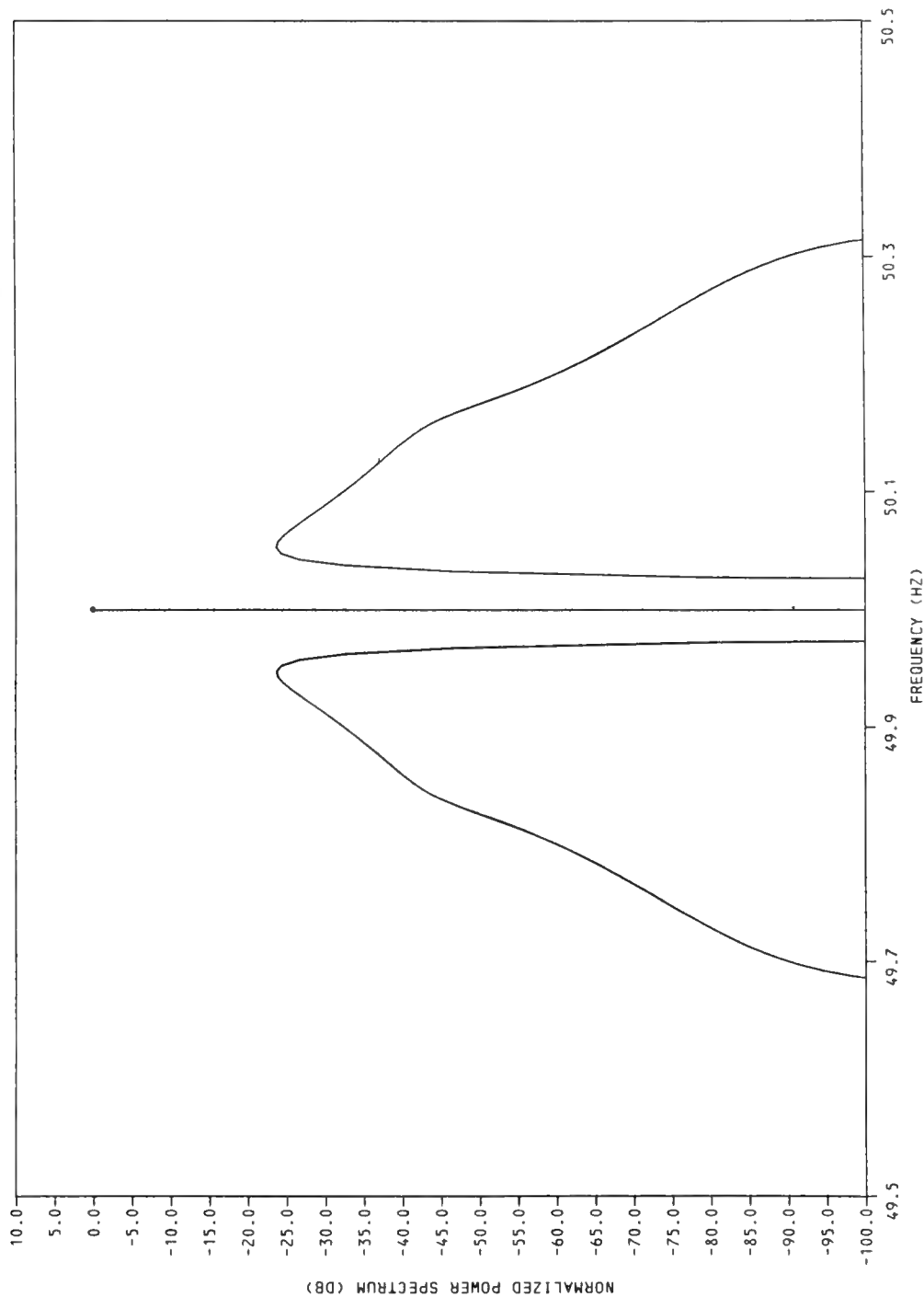


Figure 30. ACOUSTIC SPECTRUM FOR $\beta = 90.0$ $F = 50.0$
 $Z = 1000.00$ $ZP = 50.00$ $R = 2000.0$ $SP(2\pi F =$
.11262-08 $\Delta F_{SHZ} = .50000-02$

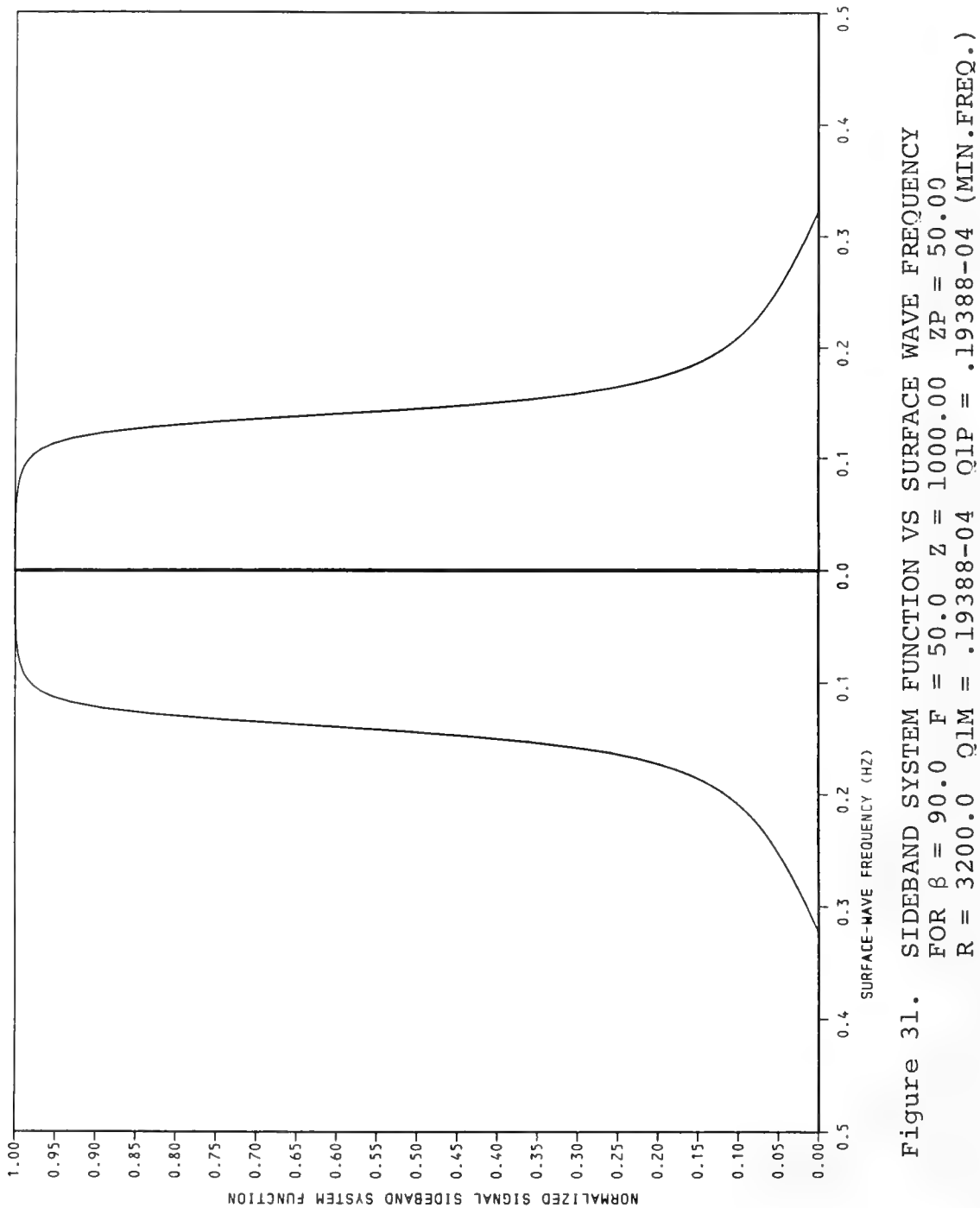


Figure 31. SIDEBAND SYSTEM FUNCTION VS SURFACE WAVE FREQUENCY

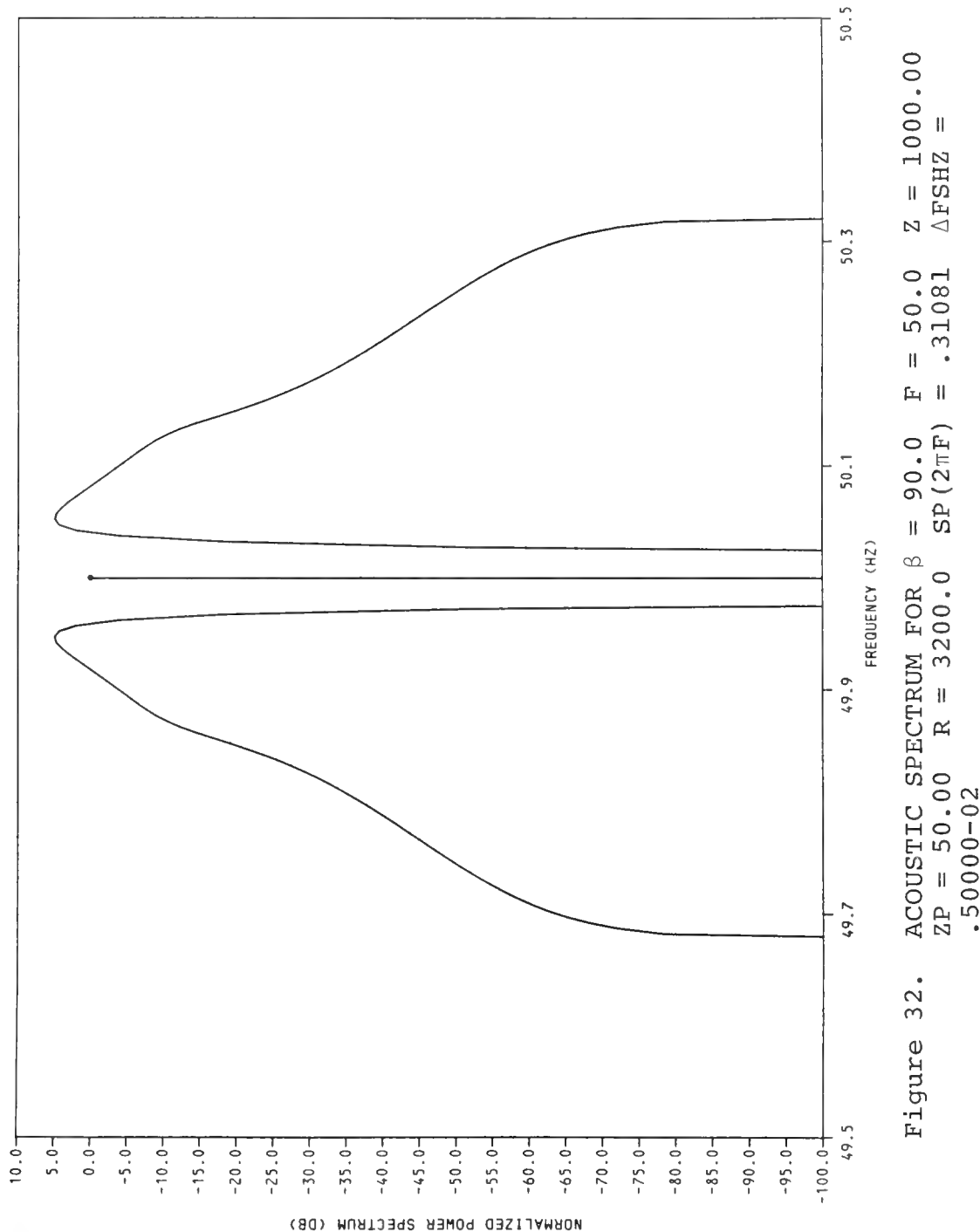


Figure 32.

ACOUSTIC SPECTRUM FOR $\beta = 90.0$ $F = 50.0$ $Z = 1000.00$

$Z_P = 50.00$ $R = 3200.0$ $SP(2\pi F) = .31081$ $\Delta F_{SHZ} =$

$.50000-02$

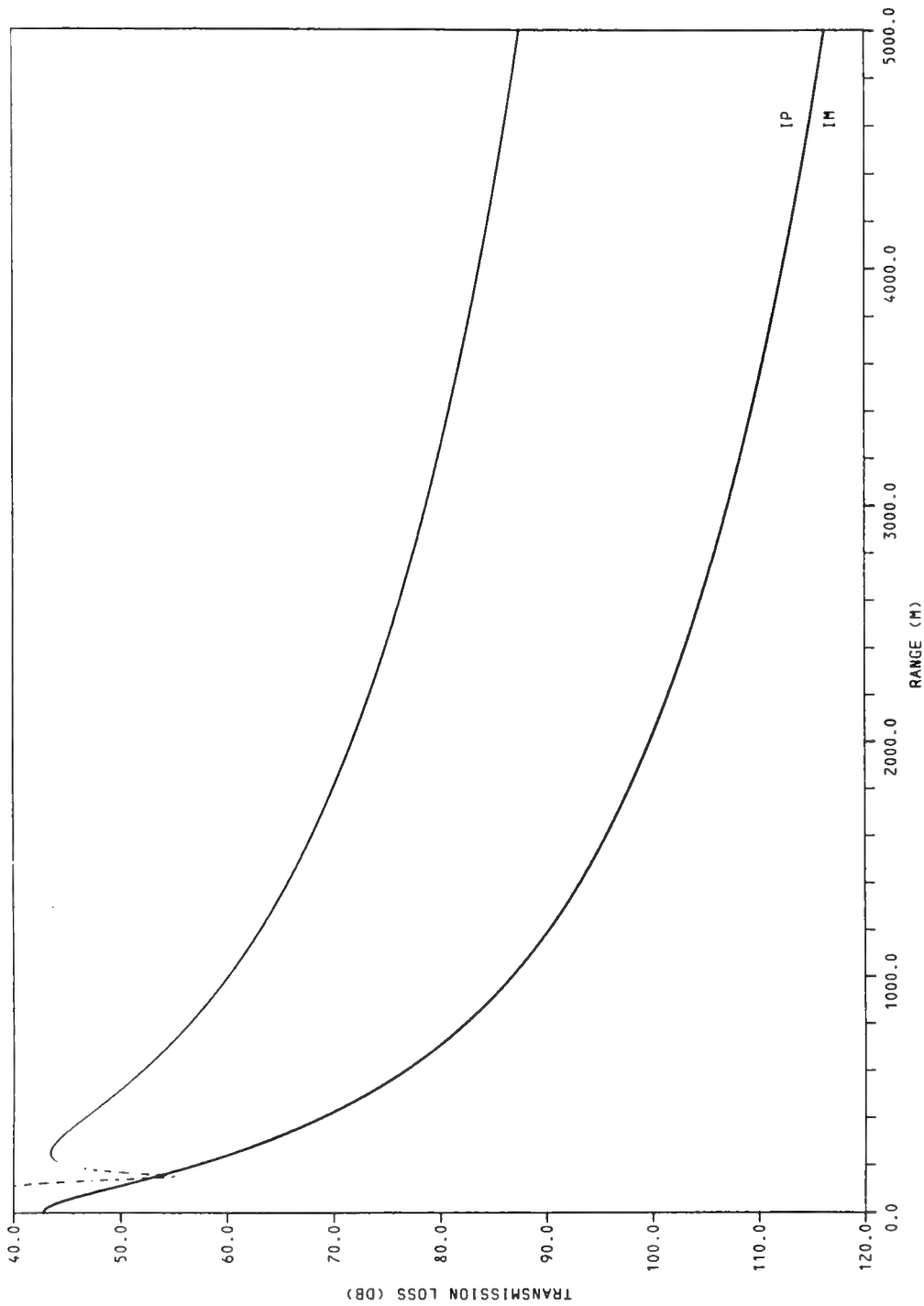


Figure 33. TRANSMISSION LOSS CARRIER AND SIDEBANDS FOR
 $\beta = 45.0$ $F = 50.0$ $Z = 50.00$ $Z_P = 50.00$
 $A_1 = .24807+01$

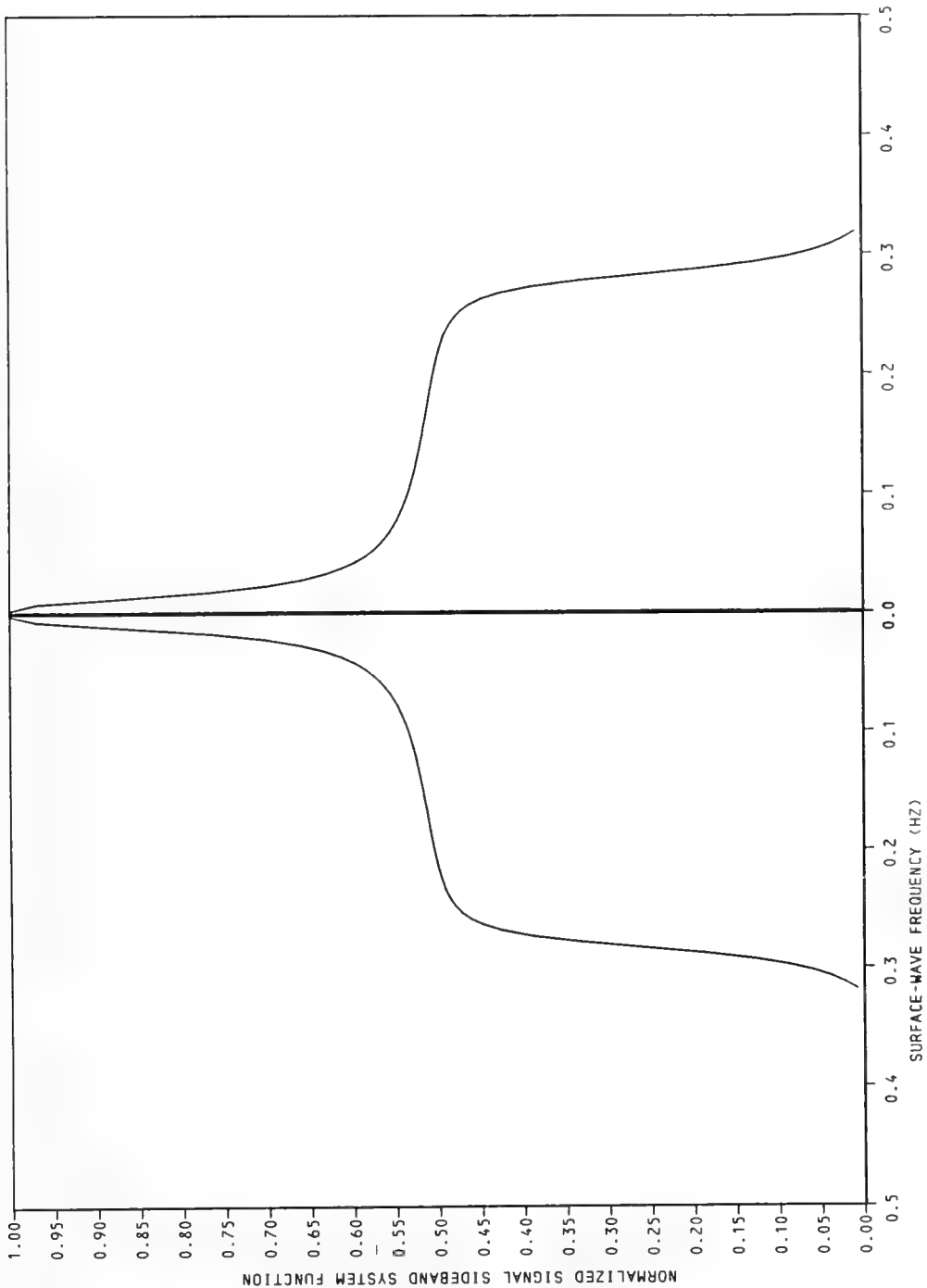
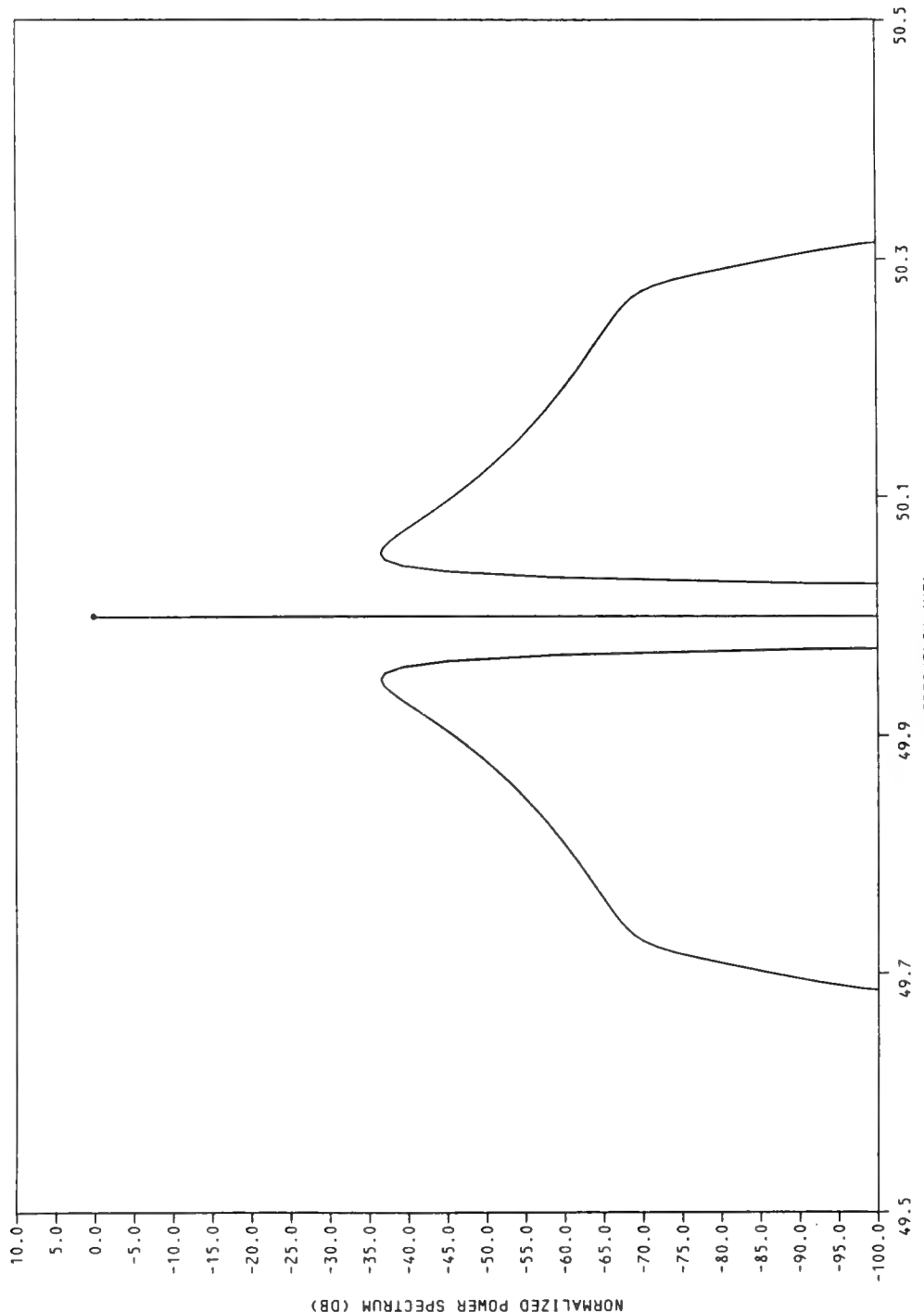


Figure 34. SIDEBAND SYSTEM FUNCTION VS SURFACE WAVE FREQUENCY

FOR $\beta = 45.0$ $F = 50.0$ $Z = 50.0$ $ZP = 50.00$
 $R = 2000.0$ $QIM = .52207-05$ $QIP = .52207-05$ (MIN. FREQ.)



LABIANCA/HARPER: A THEORETICAL APPROACH TO THE PREDICTION OF SIGNAL FLUCTUATIONS DUE TO ROUGH-SURFACE SCATTERING

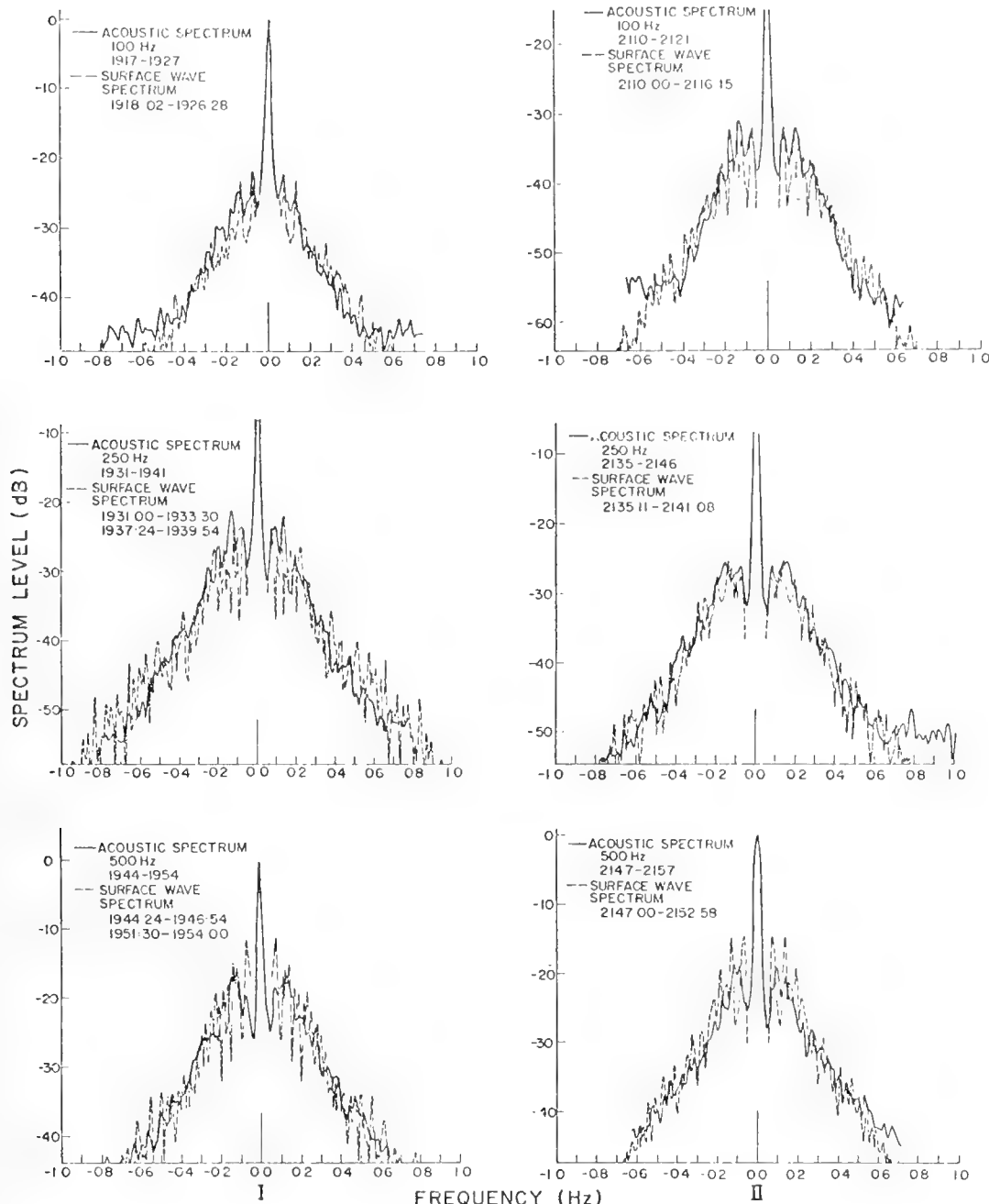


Figure 36. EXPERIMENTAL POWER SPECTRUM SHOWING CARRIER AND SIDEBANDS FOR A RANDOM OCEAN SURFACE

LABIANCA/HARPER: A THEORETICAL APPROACH TO THE PREDICTION OF SIGNAL FLUCTUATIONS DUE TO ROUGH-SURFACE SCATTERING

Brown, M. V., and G. V. Frisk, "Frequency Smearing of Sound Forward-Scattered from the Ocean Surface," *JASA* 55, 4:744-749, April 1974.

Fessenden, D. E., "Space Wave Field Produced by a Vertical Electric Dipole above a Perfectly Conducting Sinusoidal Ocean Surface," *IEEE Trans. Ant. and Prop.* AP 21:32-37, 1972.

Gerlach, A., Private communication to Bell Laboratories personnel from the Naval Research Laboratory, 1973.

Grube, G. W., "Phase Received on Several Arrays — One Experiment (U)," Bell Laboratories Ocean Systems Technology Paper, OSTP-21 GWG, March 19, 1974 (CONFIDENTIAL).

Hirsch, P., "Phase Fluctuations (U)," Bell Laboratories Ocean Systems Technology Paper, OSTP-20PH, March 4, 1974 (CONFIDENTIAL).

Holford, R. L., "Validity of the Method of Physical Optics in Rough-Surface Scattering," to be published.

Mangano, D. T., "Low Frequency, Narrowband, Multipath Phase and Amplitude Fluctuations at Closely Spaced Hydrophones: Part II — The Relationship Between Amplitude and Phase Fluctuations (U)," Internal Bell Laboratories Memorandum, December 1, 1969 (CONFIDENTIAL).

Shinozuka, M., and C. M. Jan, "Digital Simulation of Random Processes and Its Applications," *J. of Sound and Vibration*, 25:111-128, 1972.

DISCUSSION

Mr. C. W. Spofford (Office of Naval Research): Were their measurements in the direct path kind of region?

Dr. F. M. Labianca (Bell Telephone Laboratories, Inc.): Yes. One single bounce.

Dr. W. H. Munk (Institute of Geophysics and Planetary Physics, University of California at San Diego): Your stochastic model is still one-directional?

LABIANCA/HARPER: A THEORETICAL APPROACH TO THE PREDICTION OF SIGNAL FLUCTUATIONS DUE TO ROUGH-SURFACE SCATTERING

Dr. Labianca: Yes.

Dr. Munk: Since the observed beam width of a sea is plus or minus 60 degrees, it would be awfully nice if you could generalize once more and allow for the (direction) of the waves.

Dr. Labianca: I think we can do that. Right now we know how to do that, at least for the sidebands, to first order. We haven't figured out a way to generalize it for arbitrary direction to all orders.

Dr. P. W. Smith (Bolt, Beranek, and Newman, Inc.): Would you guess that you would have symmetry of the Doppler spectrum if you had plane wave incidence? Thinking of the image situation.

Dr. Labianca: I don't know. I'll have to think about that.

SOFAR PROPAGATION OF WIDE-BAND SIGNALS
TO LONG RANGES

R. P. Porter

Woods Hole Oceanographic Institution
Woods Hole, Massachusetts

A fundamental shortcoming is evident in low-frequency acoustics investigations being carried out today. Since operational surveillance systems must cope with extremely narrow-band sources, nearly all transmission assessment programs are based on continuous-tone analytical models. These models do not agree in detail with shot data — nonetheless, wide-band sources are usually preferred for measurement of long-range transmission in a SOFAR channel because it is then possible to sort out the arrival structure of the signal. Thus, the propagation along individual paths can be assessed. Understanding of the relationship between continuous-tone loss models and wide-band data is necessary if we are to have confidence in our transmission assessment programs.

In this paper we review the basic phenomena encountered in propagating wide-band signals to long range. We show that there is a well defined arrival structure in frequency as well as time. Some theoretical ideas are presented that allow efficient estimation of transmission loss. We argue that wide-band loss estimates need not take longer to carry out than narrow-band estimates. Some loss calculations are presented for the Mediterranean Sea that show reasonable agreement with measurements. Finally, we suggest future experiments that will further development of wide-band models and should reveal presently unobserved phenomena.

INTRODUCTION

Detonated charges or other wide-band signals are the usual means employed to sort out long-range sound transmission for the simple reason that they provide the only practical way to evaluate sound transmission

along several different paths. In contrast, surveillance systems, and the propagation models designed to analyze them, are based on the reception of narrow-band components. We need to know more about the interrelationships of these very different signals after they have traveled through the ocean.

The acoustic field at a long range from a localized source is a strong function of the time dependence of the projected pulse. For example, the propagation loss estimated from shot data does not reveal the semi-periodic variation with range that is observed with single tone or CW sources. As most calculations of transmission loss are based on the transmission of a single harmonic, we should not be surprised when such models fail to accurately predict sound levels from shots. Clearly, predictions of signal level should be based on models that include the spectral characteristics of the source and receiver as well as the channel propagation.

In this paper, we illustrate some of the observed phenomena found in wide-band propagation, discuss a propagation model, and present the results of some simple loss calculations. We have investigated wide-band propagation in the Mediterranean Sea and have found clearly delineated mode and ray arrival structures. Dispersed high-order modes have been observed at frequencies as high as 300 Hz and at ranges of 600 km. Spectrum analysis of shot records has revealed as many as five identifiable group-velocity profiles (modal dispersion curves) that correlate with propagation modes as high as 70. It is typical of these records that the highest frequencies arrive last. These group velocity profiles can be identified because only a few high-order modes are received. This quite unexpected result is a consequence of interference between the upward and downward traveling waves that constitute each mode.

The data discussed here were taken in the western Mediterranean during July 1968 on the cruise CHAIN 82. One-pound charges were dropped and received once per hour at the sound channel axis depth of 100 m. Precise STD lowerings were made permitting detailed correlation of analytical and experimental results.

ANALYSIS OF SIGNAL STRUCTURE

Propagation conditions during July are such that there is an extremely sharp SOFAR channel at a depth of 100 m in the western Mediterranean. The ray trace of Figure 1 shows that ray angles between $\pm 10^\circ$ are wholly refracted when the source and receiver are on the channel axis. Since nearly all surface reflected energy is also bottom reflected, the signal structure at long range exhibits classic SOFAR arrival structure. Note that as the ray angle increases, the ray cycle length is longer and that the ray turning points are in higher sound-velocity water. Thus, rays with long cycle lengths will arrive sooner.

Figure 2 shows graphic recordings of the arrival structure of four shots at ranges between 250 and 380 km. At T_o , the axial arrival time, most of the energy has arrived; afterwards the signal level drops abruptly to the noise level. It should be noted that the axial arrival is actually much more intense. Some clipping by the graphic recorder has been permitted so that the early arrivals can be easily seen. For arrival time $t < T_o$, it is possible to resolve the records into multiple arrivals. Each of these arrival times is characteristic of a particular eigenray defined as a ray leaving the source at such an angle that it crosses the channel axis at the receiver. For the Mediterranean sound-velocity profile, the larger the exit angle from the source, the earlier an eigenray arrives at the receiver. It is evident from both the short records and the ray trace (Figure 1),

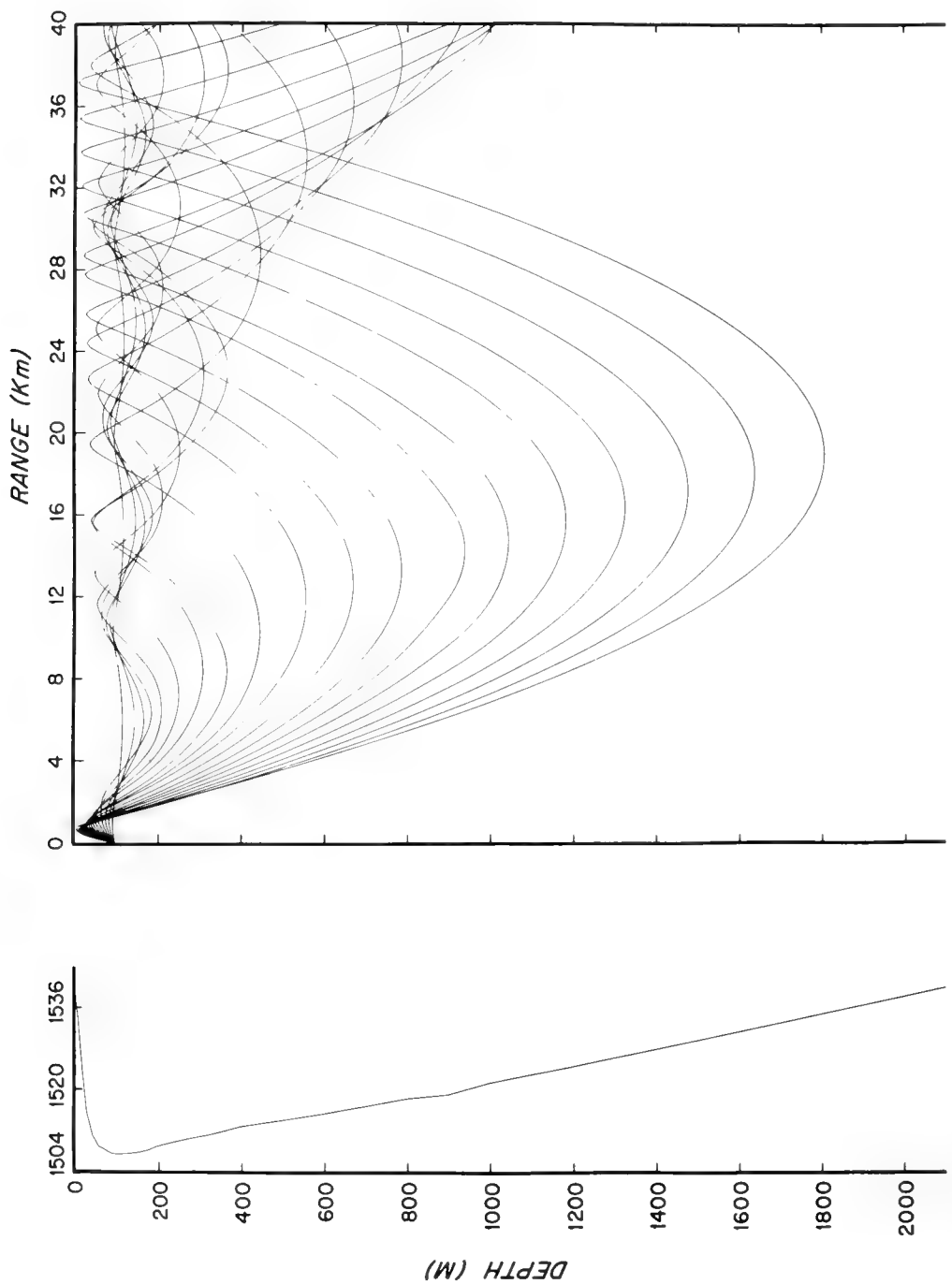


Figure 1. SOUND VELOCITY PROFILE AND RAY TRACE
FOR THE MEDITERRANEAN

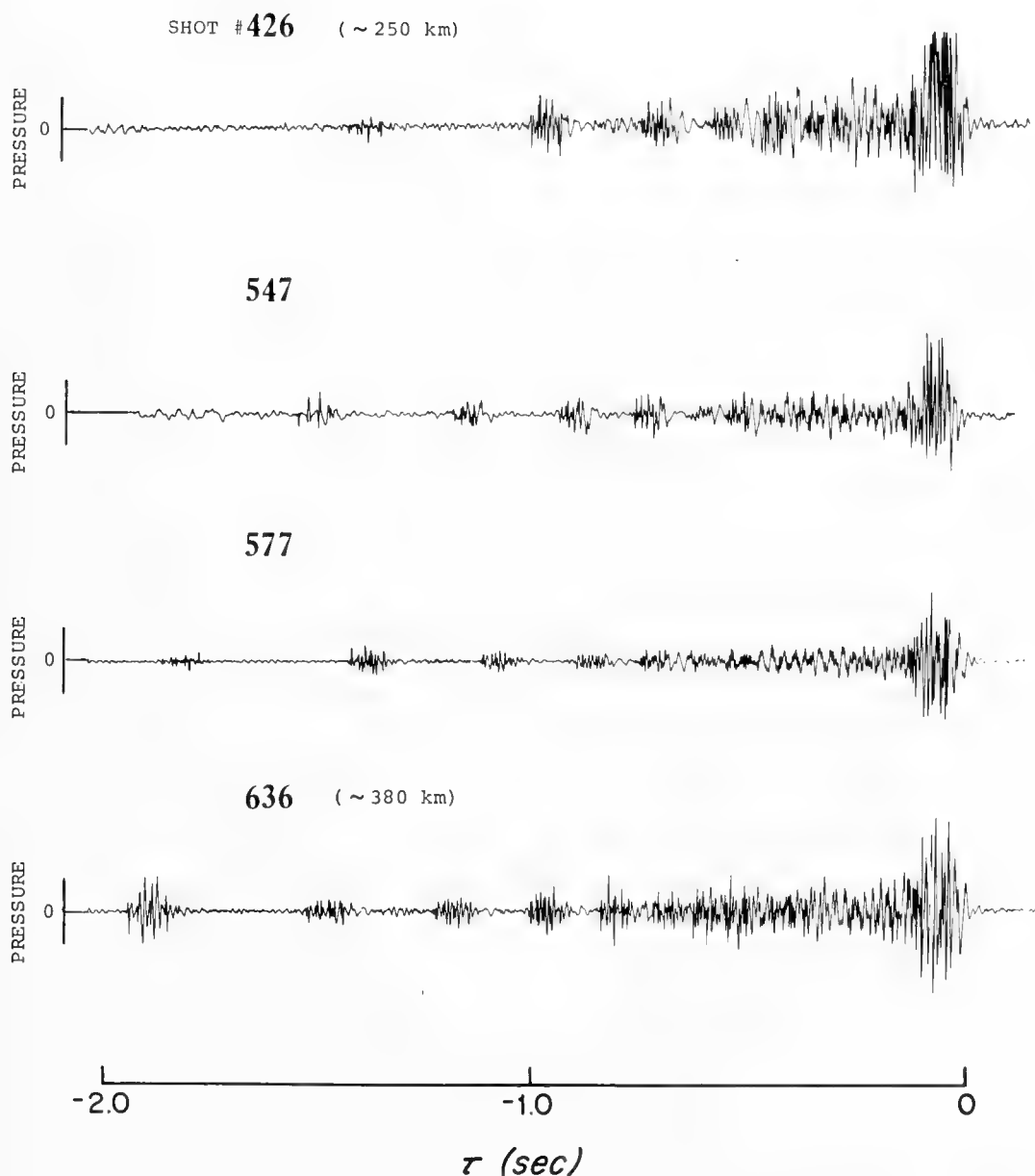


Figure 2. SIGNAL STRUCTURE VERSUS RELATIVE ARRIVAL TIME

that many eigenrays exist for each source and receiver location. We define an eigenray of order n as having n ray cycles between source and receiver. To be more precise, we should talk of an eigenray family consisting of four rays, each with slightly different travel times, corresponding to rays which reach the receiver after traveling $n - 1$, n , $n + 1$ upper half cycles and n lower half cycles. A ray traveling $n - 1$ lower half cycles is said to be an eigenray of order $n - 1$.

The arrival time τ , relative to the axial arrival time, of each of the resolved arrivals of the shot records is plotted in Figure 3. The vertical width of the bar is a measure of the spread in arrival time (see Figure 2) due to the spread of the transmitted pulse as well as diffraction along the ray path. Individual eigenrays can actually be identified and tracked through successive shots. A given eigenray arrives earlier as the receiving ship moves further away. An eigenray of order n must have an increasing cycle length implying that it travels through relatively fast sound-velocity regimes. Calculations of eigenray arrival times for this sound-velocity profile agree very well with the measured arrival times.

It gradually became clear to us that the CHAIN 82 data exhibit all the features of classic SOFAR propagation. We decided that we ought to study the frequency arrival structure — the hope being that we would observe mode dispersion. Actually, we expected nothing dramatic because many modes were expected to be present between frequencies of 100 to 300 Hz.

The very first sonogram made with a graphic spectrum analyzer showed us that we were very wrong. We were presented with simultaneously observable group-velocity profiles, characteristic of mode dispersion, and resolved ray arrivals. Figure 4 shows several

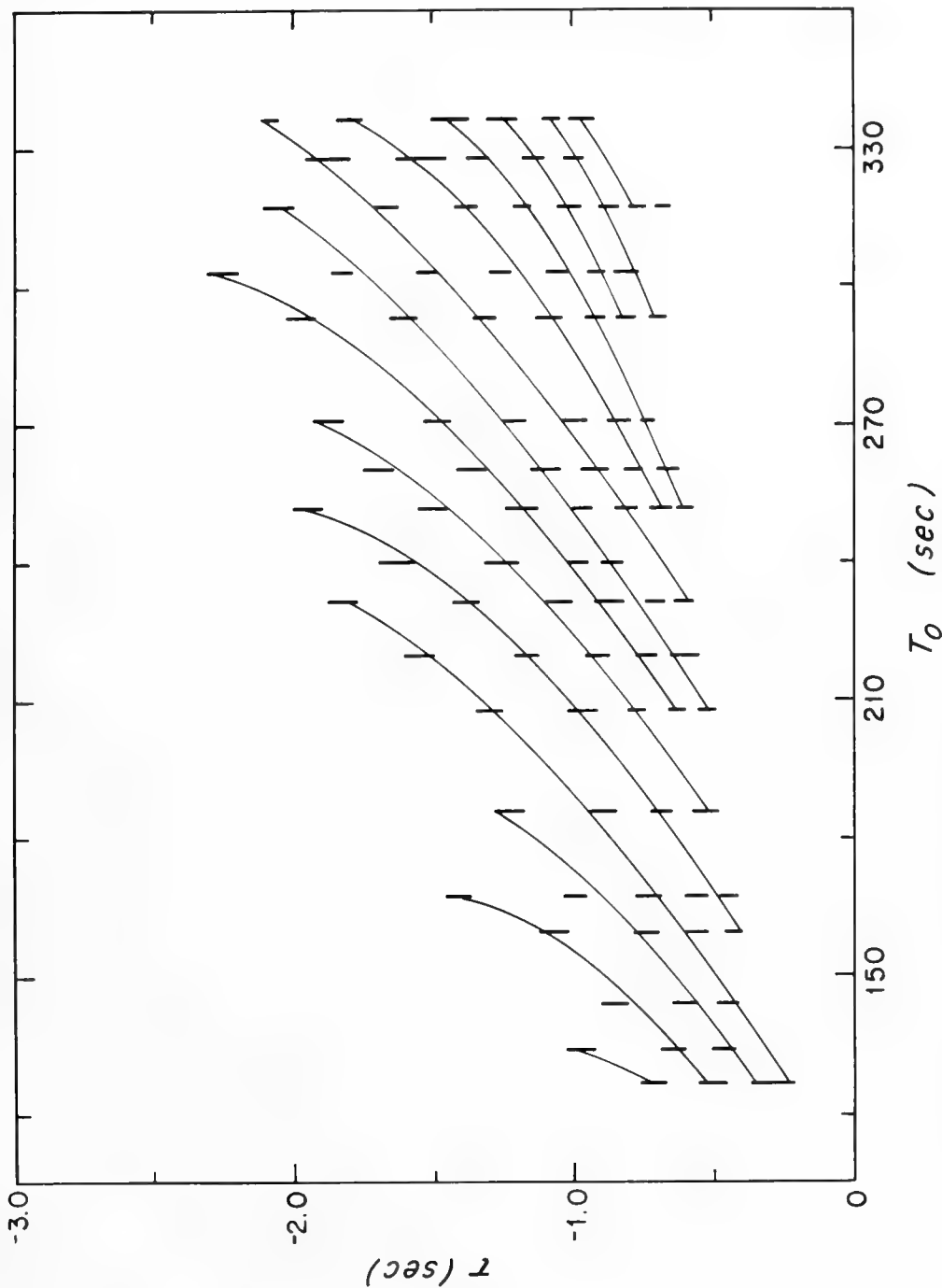


Figure 3. RELATIVE ARRIVAL TIME VERSUS AXIAL ARRIVAL TIME

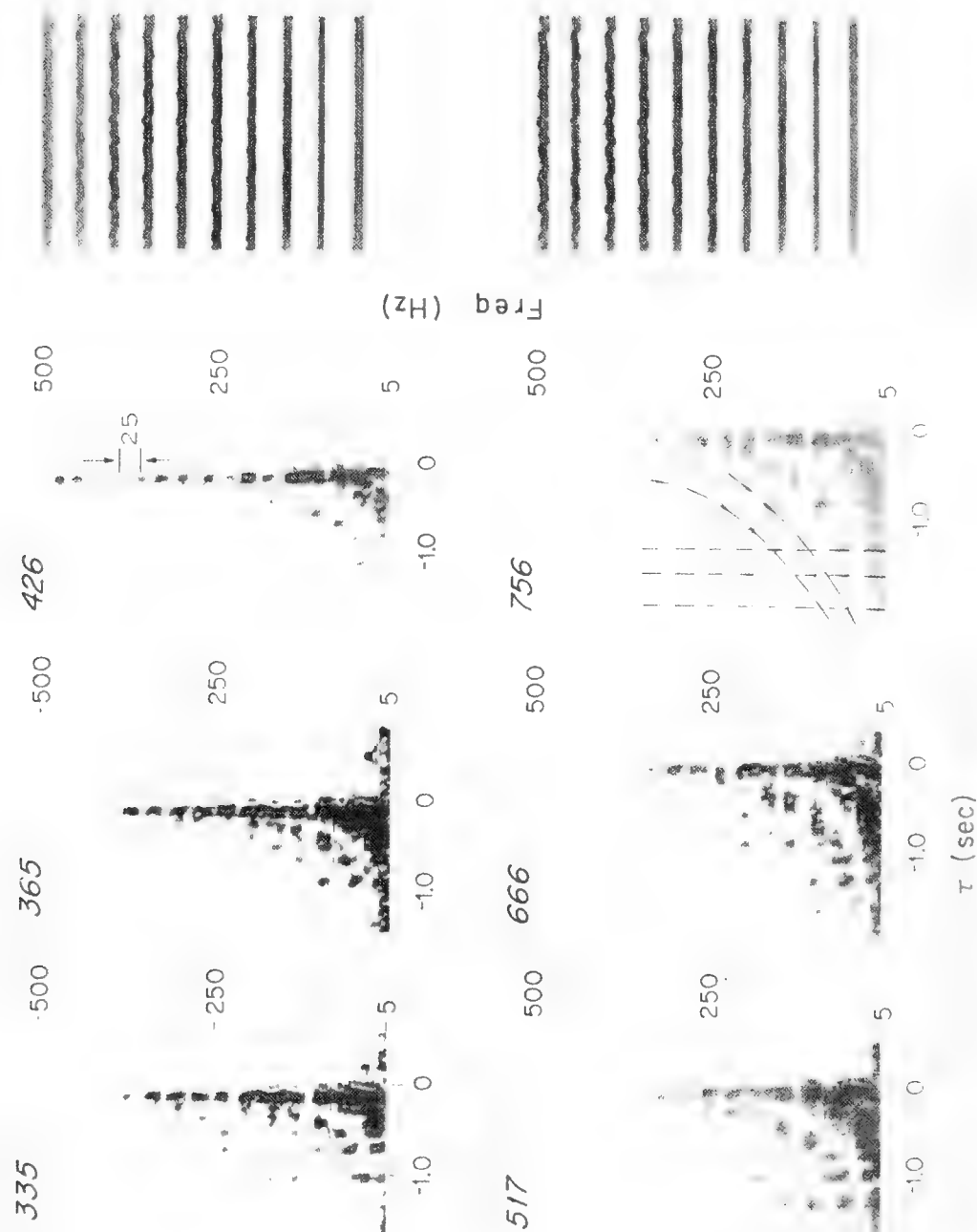


Figure 4. SONOGRAMS OF SHOTS BETWEEN 100 KM AND 600 KM

sonograms of shots at increasing ranges between 100 and 600 km. Shot 756 shows seven individually observable ray arrivals and four well-defined mode dispersion curves. It was quickly realized that the mode curves were not the first four, lowest order modes; the frequencies were much too high for the observed arrival-time delays. For example, mode $m = 4$ should arrive with frequencies of a few Hz not 200 Hz as observed. The inevitable conclusion was that the mode-dispersion curves (or group-velocity profiles) belonged to high-order modes and that most of the high-order modes were among the missing.

Where are they? It turns out that the modes actually observed result from an interference mechanism. Figure 5 shows the upward and downward traveling waves that combine to make the standing wave we identify as the field of a single mode. These two waves interfere constructively or destructively, depending on the depth z and the sound-velocity profile. In other words, the receiver can be at a null for a particular mode and then that mode will not appear in the shot arrival. Constructive reinforcement depends on the receiver depth, not the range.

It can be shown for a bilinear profile that the modes that interfere constructively are directly dependent on the skew of the sound-velocity profile. The skew of the Mediterranean profile is 20 to 1. As a consequence, only one out of every 20 modes interferes with maximum constructive interference. In the North Atlantic the skew is 6 to 1; one would expect 1 out of every 6 modes to interfere constructively.

It is well known that a given frequency, for a given mode, travels with a unique group velocity. Further, we have argued that the modes actually received depend only on the receiver depth and not the range. Thus, plots of arrival frequency versus fractional

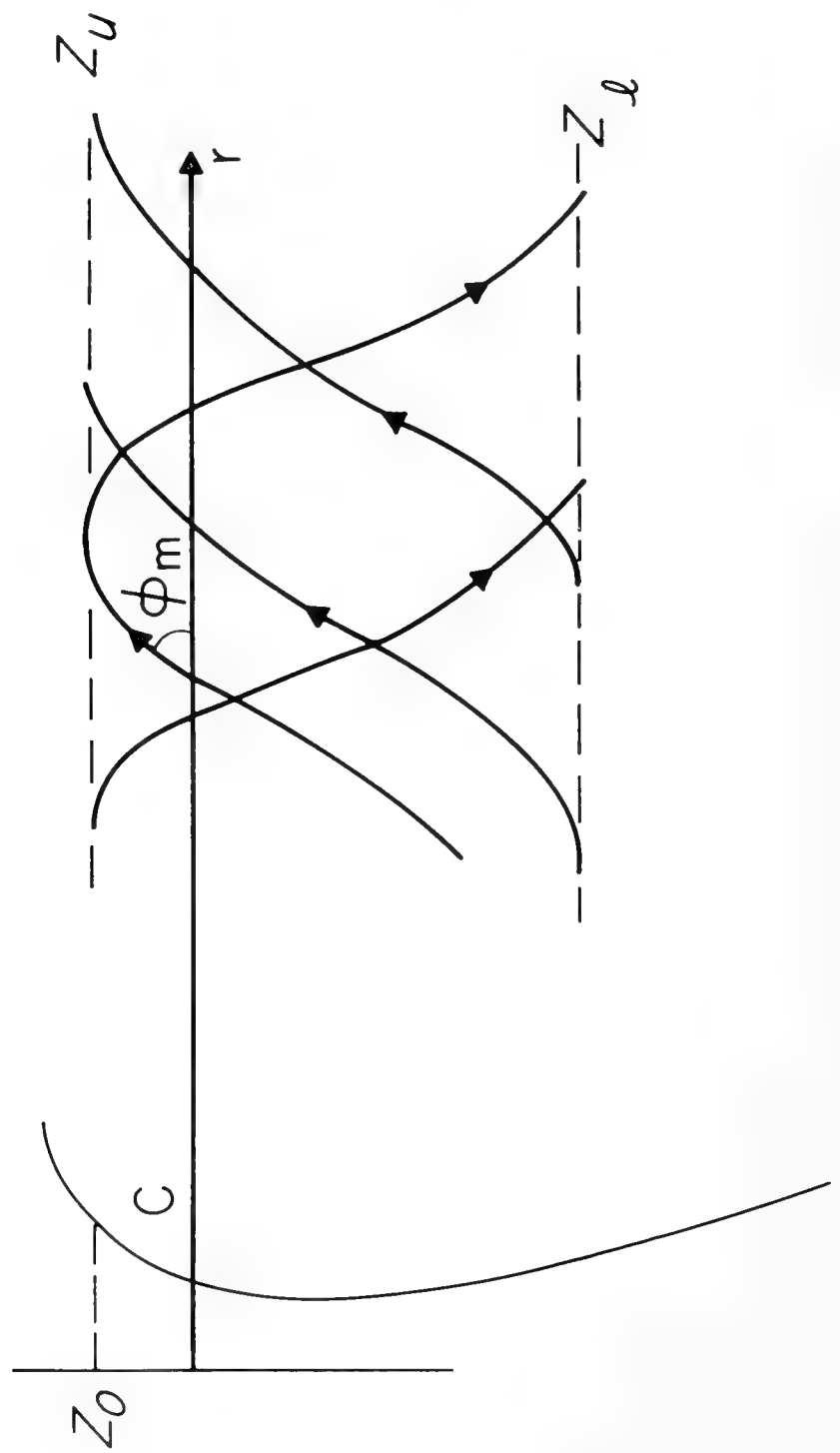


Figure 5. SCHEMATIC OF VELOCITY PROFILE AND RAY TRACE OF A MODE

arrival time (delay from the axial arrival divided by the axial arrival time) for all shots should group along the same dispersion curves. Note that the fractional arrival time is directly proportional to the group velocity. Figure 6 is a plot of the arrival frequencies for seven shots at ranges from 100 km to 600 km. The curves drawn through the symbols are not fits to the data; they are calculated group-velocity profiles for those modes predicted to have maximum constructive interference. The horizontal axis is fractional arrival time.

The theoretical curves are calculated only for wholly refracted modes. All energy arriving earlier than $\tau_r = -0.65 \times 10^{-2}$ is felt to be surface reflected. We feel that there is observed surface reflected energy on only three pulses.

MODE EXPANSIONS AND THE WKB APPROXIMATION

One of the more dramatic of the phenomena observed in these sonograms is the simultaneous appearance of resolved modes and rays. Nowhere in the literature do references to this combined behavior appear. There is evidence of lower order modes at long ranges in the Arctic, and there is also evidence of resolved arrivals in most of the early papers on SOFAR propagation. However, the mode and ray viewpoints are thought to be separate. That is, one can observe either modes or rays but not both together. We have seen that both phenomena appear together and are observable, at least in the Mediterranean, with the appropriate spectrum analysis.

We have developed a simple theory based on the WKB approximation and combined with a stationary phase integration over the spectrum of the transmitted pulse. The results are summarized in Figures 7 and 8. The spectrum of the received signal is a sum over the normal modes Φ_m .

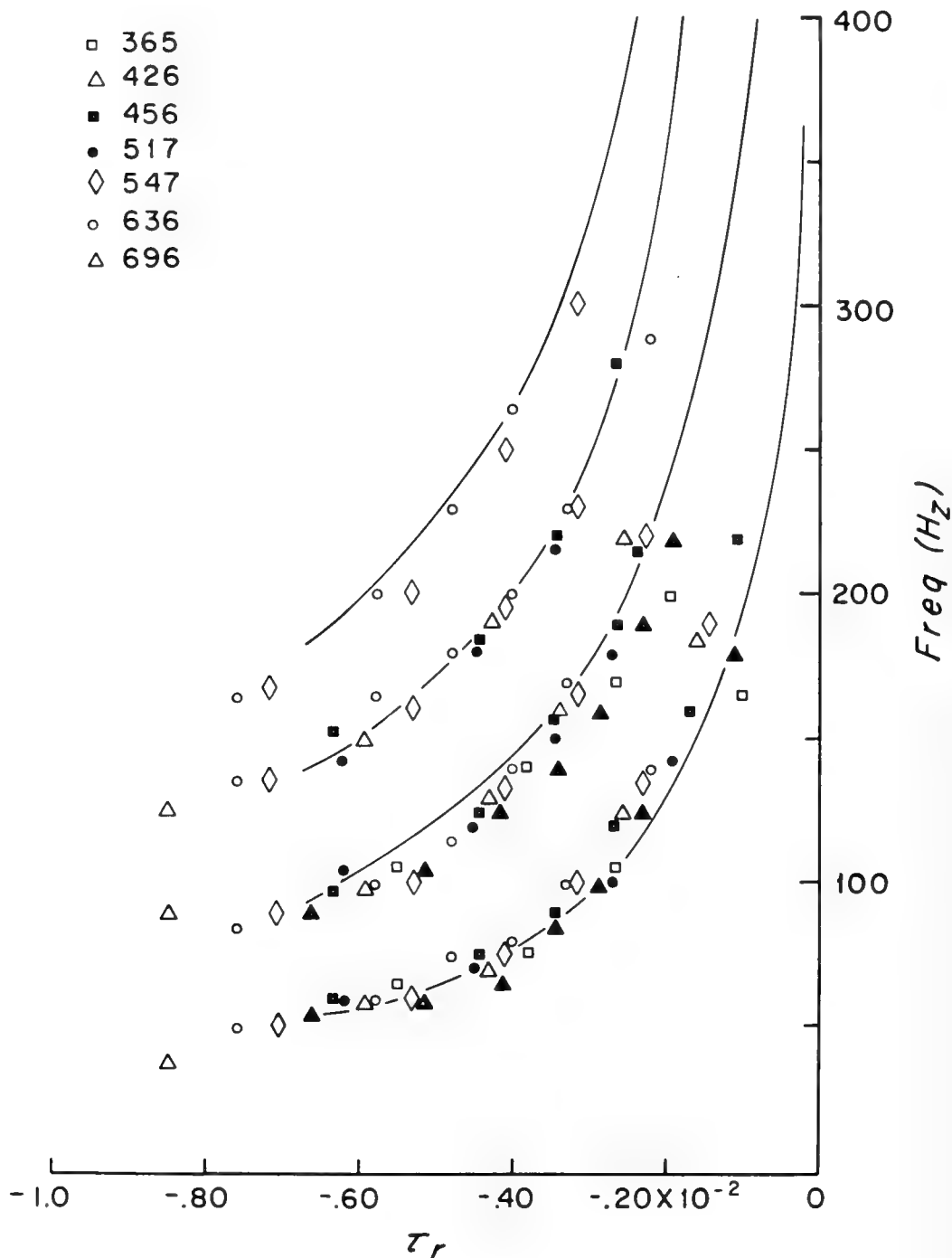


Figure 6. ARRIVAL FREQUENCY VERSUS FRACTIONAL ARRIVAL TIME

$$\Psi(r, z, \omega) = i F(\omega) \sum_{m=0}^{\infty} A_m \Phi_m(z) \bar{\Phi}_m(z_o) \exp[i(k_0 r \cos \phi_m - \pi/4)]$$

NORMAL MODE EXPANSION

$$\Phi_m(z) = \gamma_m^{-1/2} \cos[\theta_m(z_u, z) - \pi/4]$$

PHASE INTEGRAL
EIGENFUNCTION

$$\Psi_m(r, z, t) = \int_{-\infty}^{\infty} F(\omega) B_m(\omega) M_m(z, z_o) \exp[i(k_0 r \cos \phi_m - \omega t)] d\omega$$

ACOUSTIC FIELD OF PULSE (PROPAGATION INTEGRAL)

$$M_m(0, 0) = [\cos^2[\theta_m(z_u, 0) - \pi/4]]$$

MODE INTERFERENCE

EVALUATE BY METHOD OF STATIONARY PHASE

Figure 7. SUMMARY OF THEORY

$$\theta_m(z_u, z_x) = (m+1/2)\pi \quad \text{RESONANCE CONDITION}$$

$$t/r = U_m^{-1} = d(k_o \cos \phi_m)/d\omega \quad \text{GROUP VELOCITY}$$

$$\omega_m = g_m(r/t) \quad \text{DISPERSION CURVE}$$

$$1/2 \Delta\omega^2 dt/d\omega |_{\omega_m} \gg 1 \quad \text{TIME-BANDWIDTH PRODUCT}$$

$$\psi(r, z, t) = \sum_{m=0} F(\omega_m) C_m M_m(z, z_o) \exp[-i2(m+1/2)\pi r/h(\phi_m)]$$

$$h(\phi_m) \quad \text{RAY CYCLE LENGTH}$$

Figure 8. SUMMARY OF THEORY (Continued)

$F(\omega)$ is the spectrum of the transmitted pulse or shot, A_m is a weighting term containing the cylindrical spreading factor for each mode as well as some normalization terms, and the exponent contains the horizontal propagation constant for each mode. ϕ_m is the angle the propagation vector makes with channel axis. The eigenfunction Φ is found from the WKB approximation where θ is the phase integral from depth z to the turning point z_u . γ_m is the vertical propagation constant. The cos term expresses the mode interference and its dependence on z . It is zero when the argument is $(2n + 1) \pi/2$ and largest when the argument is $m\pi$. The acoustic field is found by integrating the normal mode expansion over all ω . The interference terms from the eigenfunctions are lumped together into an interference factor M ; remaining terms have been placed in B_m .

The integral over frequency is evaluated by the method of stationary phase. The group velocity of speed at which energy of frequency ω and mode m travels is found by minimizing the exponent of the propagation integral subject to the constraint that the characteristic equation or resonance condition for the normal modes be obeyed.

The resonance condition is simply the requirement that the phase of a mode vary by $m\pi$ between the upper and lower turning points. The dispersion curve of relationship between frequency and group velocity is found by combining the first two equations in Figure 8. In order that the major contribution to the phase integral comes from the vicinity of the stationary phase point, the product of the time spread of the channel and the bandwidth of the pulse must be large.

The next-to-last equation in Figure 8 results from evaluating the propagation integral at the stationary phase point. It is clearly a summation over all modes with each mode weighted by the interference

factor M . Somewhat less obviously, all modes constructively interfere when $r/h(\phi)$ is an integer, that is, when there is an integer number of ray cycles between source and receiver. Since ϕ is a function of the group velocity (because of the resonance condition), the signal is reinforced only for those arrival times that correspond to the reception of an eigenray.

Figure 9 shows the received signal structure when an impulse is transmitted. There are resolved arrivals corresponding to individual eigenrays. Each arrival has a spectrum determined by those modes for which the interference factor is greatest.

The previous analysis holds with slight modification if a dispersive pulse is transmitted. From Figure 10, if α is rapidly varying the arrival time is a sum of the channel plus the pulse dispersion. To illustrate the effect of pulse dispersion, consider a linear FM pulse from 0 to 400 Hz with a time spread of 1 sec received at 300 km. The pulse sweeps up with higher frequencies transmitted later. Since higher frequencies are delayed due to channel dispersion, the net effect of the swept pulse is to increase the dispersion. The left side of Figure 11 is the dispersion curves for the CHAIN 82 profile; the right side is the resulting dispersion curves for the FM transmitted pulse.

PROPAGATION LOSS FOR WIDE-BAND SOFAR TRANSMISSIONS

All of this suggests that simplifications can be achieved in the calculation of wide-band transmission loss. Intuitively, if the received signal bunches into energy packets that are resolved in time and frequency, the total energy is the sum of the energy of the individual packets. More precisely, we have shown that the received energy is the sum of the energies transmitted in each mode and

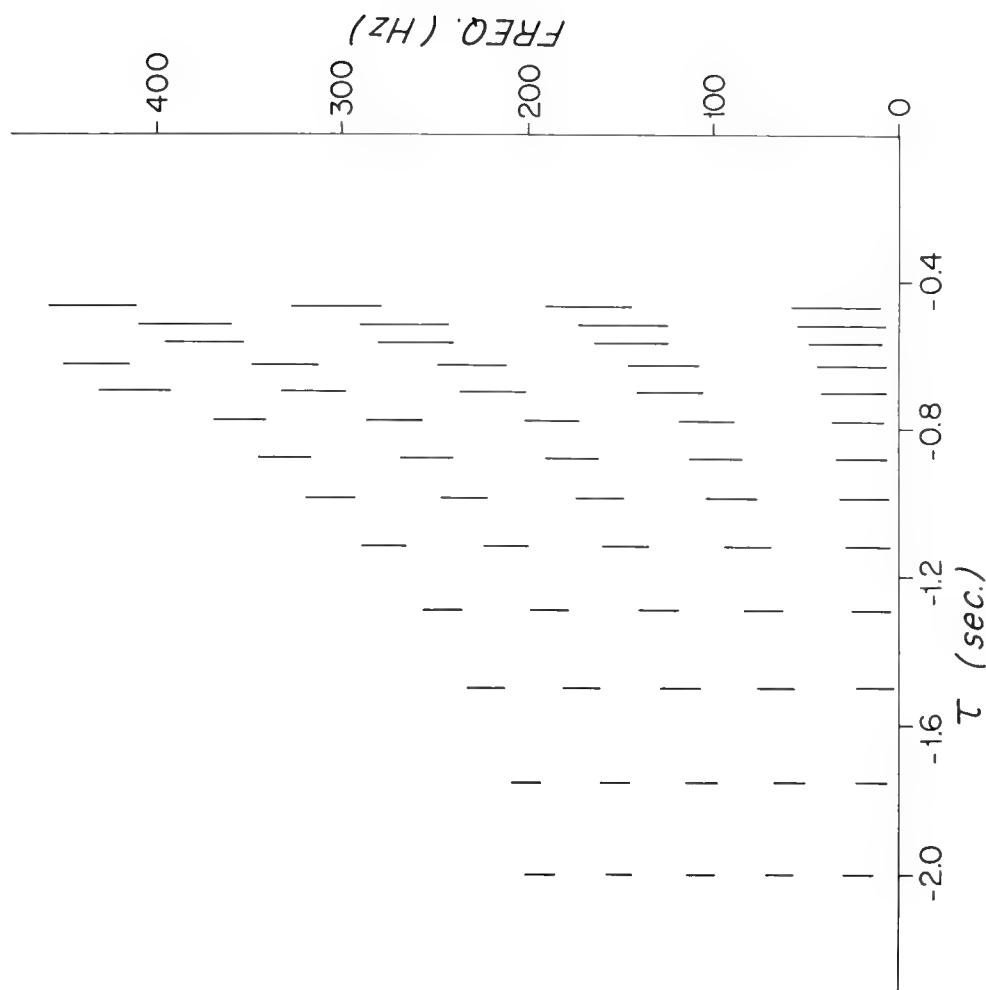


Figure 9. SIGNAL STRUCTURE FOR AN IMPULSE

DISPERSIVE PULSE

$$F(\omega) = |F(\omega)| \exp[i\alpha(\omega)] \quad \alpha(\omega) \text{ RAPIDLY VARYING}$$

$$\alpha = [rd(k_0 \cos \phi_m)/d\omega + d\alpha/d\omega]$$

$$\tau_r = -(1 - c_o/U_m) \quad \text{RELATIVE ARRIVAL TIME}$$

CONSIDER LINEAR FM PULSE

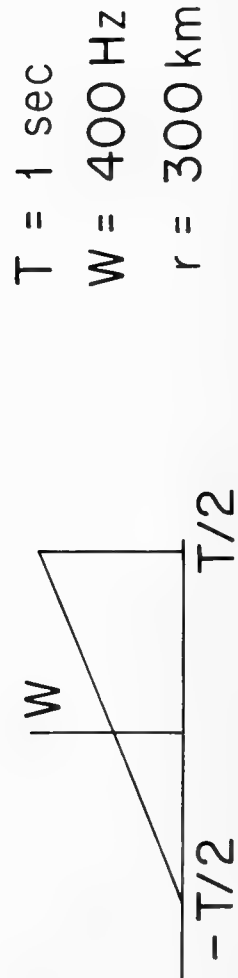


Figure 10. OUTLINE OF PULSE DISPERSION EFFECTS

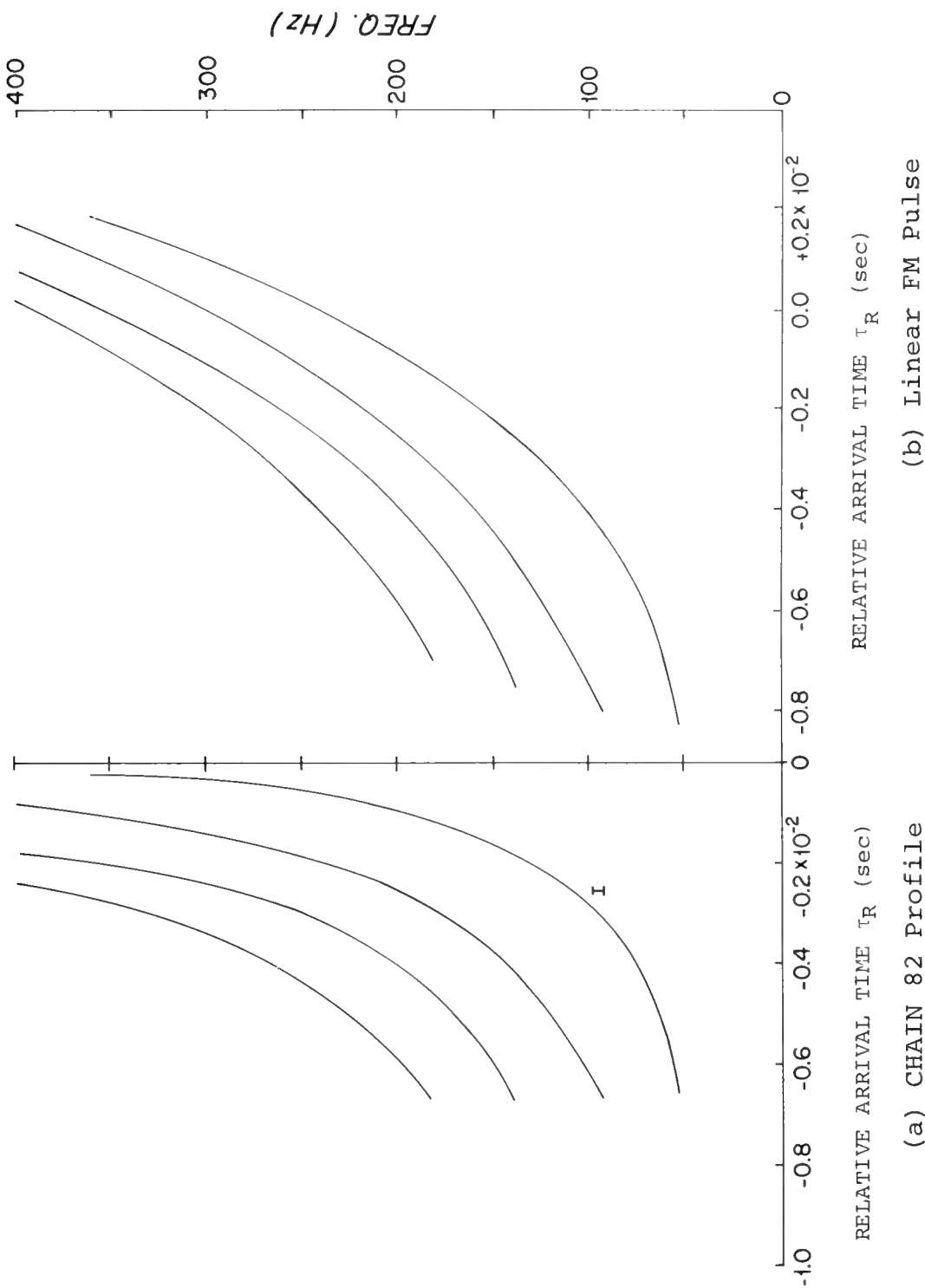


Figure 11. DISPERSION CURVES

eigenray. Contrast this with narrow-band propagation loss where the modes must be combined coherently. Those using mode theory have generally observed that incoherent mode summation is a better fit to data measured with shots, a result that confirms wide-band theory.

Software has been developed to calculate the loss. The program is based on the WKB approximation to the normal modes, and the stationary phase approximation to the propagation integral. Loss estimation proceeds first by estimating the eigenrays for a given range. This is done by calculating the cycle length and requiring that there be an integer number of cycles between source and receiver. Then the resonance condition and group velocity relation are combined to determine the received frequency for each mode. The interference factor M is then calculated to find the energy distribution among the modes.

The main difficulty with the method is that the WKB solution diverges near ray turning points. Thus, as we vary the source and receiver depths, we observe a rapidly varying and erroneous propagation loss. We have attempted to correct this by applying a diffraction correction, based on Airy functions, to the field of each mode when z is near the turning point.

Figures 12 and 13 show propagation loss as a function of depth for two ranges at 100 Hz. Figure 12 is for the sound velocity profile measured on CHAIN 82, while Figure 13 is the N^2 - bilinear approximation to that profile. The diffraction correction significantly smooths the loss curves for both profiles. This is expected because the introduction of diffraction reduces the effect of the WKB turning points. It should also be noted that the N^2 - bilinear loss curve is significantly smoother than that for the actual CHAIN 82 profile. This is a consequence of the changing slope of dc/dz of the actual data.

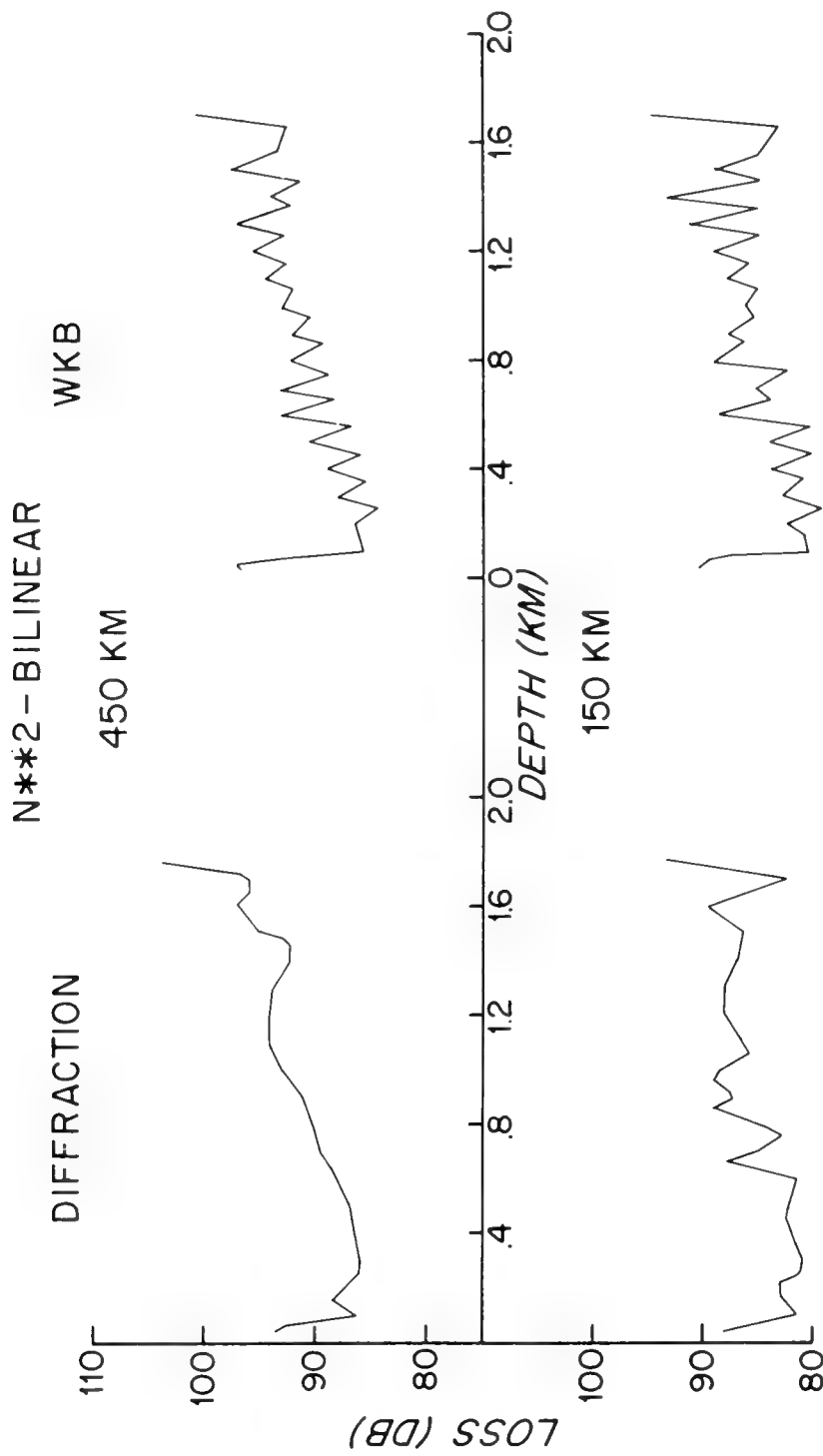


Figure 12. PROPAGATION LOSS CURVES FOR CHAIN 82 PROFILE

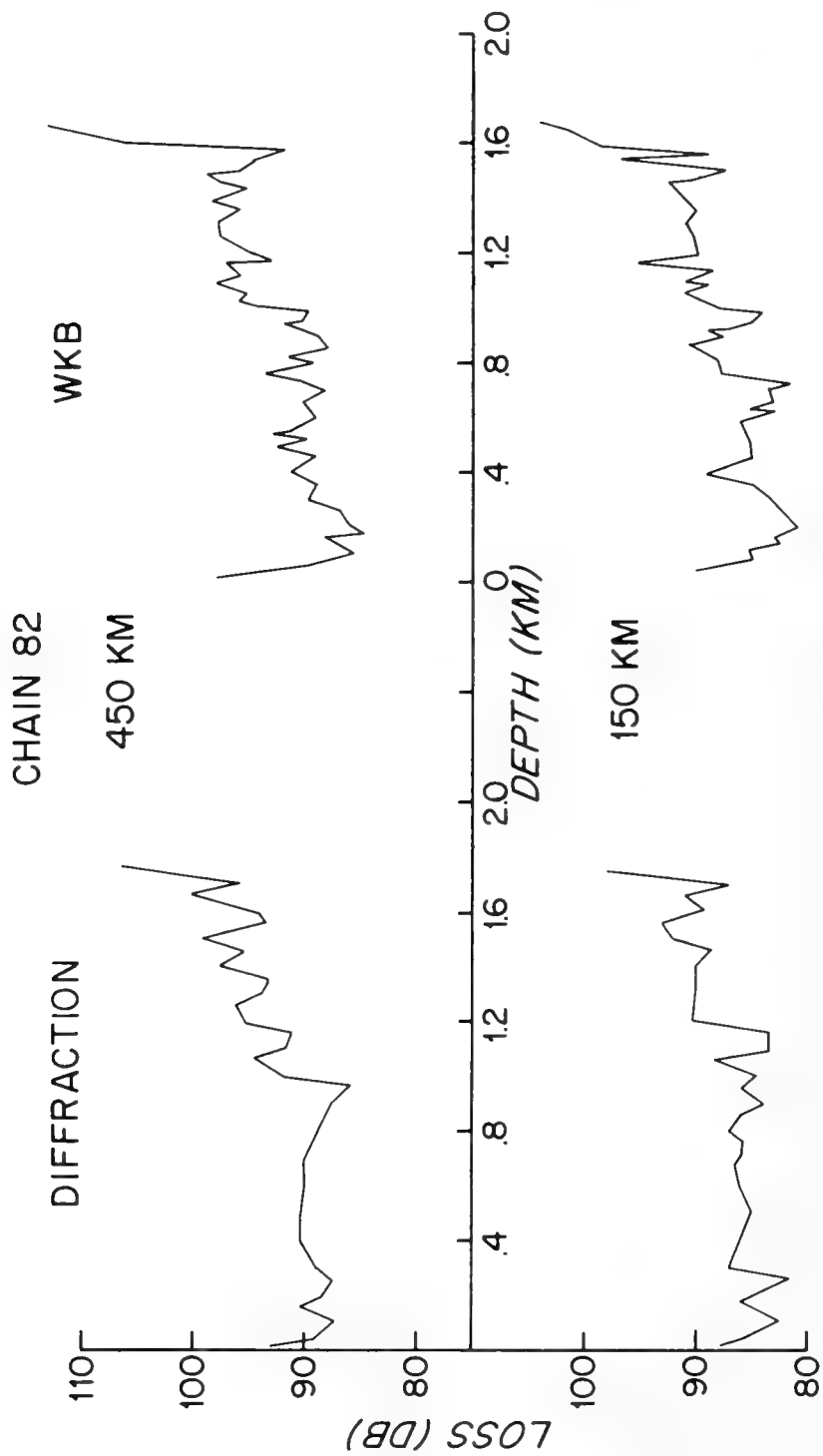


Figure 13. PROPAGATION LOSS CURVES FOR APPROXIMATION TO CHAIN 82 PROFILE

Figure 14 shows the propagation loss as a function of range for the N^2 - bilinear profile. The source and receiver are both on the axis of the sound channel. For this profile, the WKB and diffraction-corrected losses are nearly identical. On the other hand, Figure 15 for the CHAIN 82 profile shows as much as 5 dB difference between the WKB and diffraction-corrected loss curves. The two curves agree pretty well for ranges less than 100 km and greater than 350 km. Also shown is experimental data for CHAIN 82, source and receiver both on the channel axis. The frequency is 100 Hz. Interestingly, the WKB loss calculations are within 2 dB of the experimental data, while the diffraction-corrected theory overestimates the loss by as much as 5 dB.

Nonetheless, the agreement between theory and experiment appears to us to be pretty good. We have been able to estimate the loss without any artificial assumptions of mode incoherence. Further, the wide-band loss calculations have about the same computation requirements as do narrow-band mode calculations.

SUMMARY

We have illustrated phenomena present in wide-band, long-range transmissions. Group-velocity versus frequency (dispersion) curves are revealed by spectrum analysis of shot records. Dispersion is observed at frequencies as high as 300 Hz and for mode numbers as high as 70. It has been shown that at frequencies between 25 and 300 Hz that both ray and mode structure is apparent in the pulse signature. An analysis based on the WKB approximation shows that this combined structure should appear in the data and, further, predicts the field at long ranges from the source. Good agreement between theoretical and experimental dispersion curves has been obtained with the WKB approximation to mode theory.

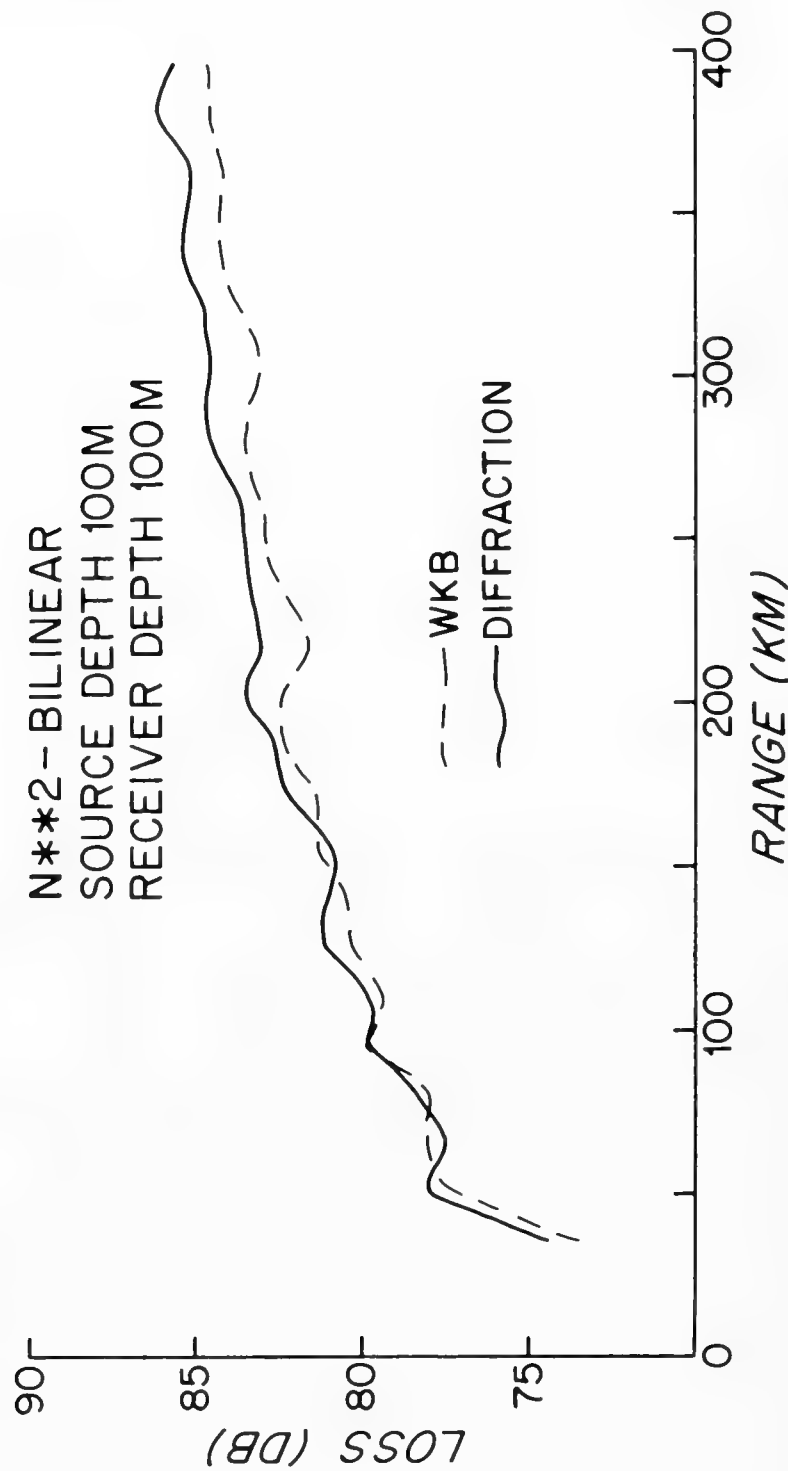


Figure 14. PROPAGATION LOSS FOR BILINEAR PROFILE

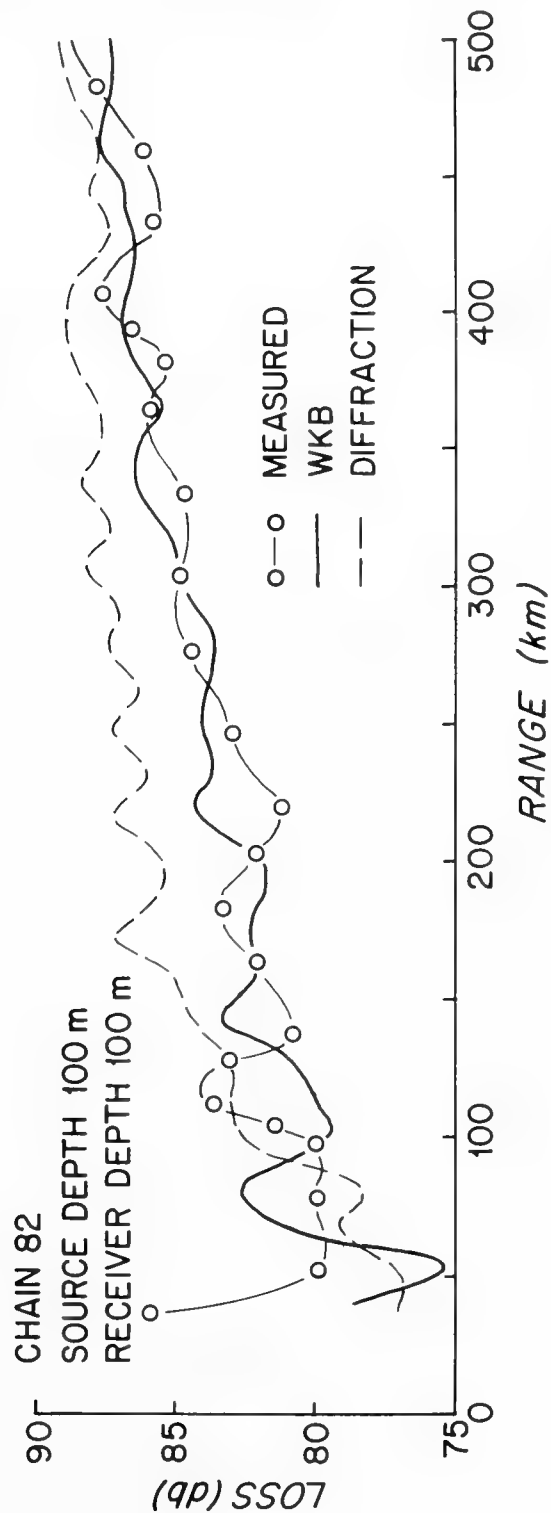


Figure 15. PROPAGATION LOSS VERSUS RANGE:
AND MODEL CALCULATIONS
MEASUREMENTS

Propagation loss estimates based on dispersive propagation have been presented. A diffraction correction to WKB theory has been necessary to prevent divergence of the energy calculations near the ray turning points. Reasonably good agreement has been obtained between this theory and loss data obtained in the western Mediterranean.

Future work should include both experimental and analytical effort. Wide-band data, with sources and receivers on the channel axis, are needed for other areas besides the Mediterranean. It is important to know if simultaneous ray and mode resolution is possible elsewhere. It would be very interesting to see wide-band data obtained with a swept frequency source. The ability to alter the dispersion of the received signal has interesting ramifications for future experiments. More detailed development of the propagation-loss software package is required. It should be based on more exact mode theory or a better diffraction correction. We should also study the possible generalization of the parabolic-equation technique to include wide-band signals.

DISCUSSION

Dr. P. W. Smith (Bolt, Beranek, and Newman, Inc.): Dr. Porter's pictures are the most fascinating, stimulating ones I have seen for a long while. They represent a frequency-time decomposition of the energy transmitted from an explosive sound. I guess this is a situation where one can see what he looks for, in a certain sense, and you were lucky to see both rays and modes at the same time.

It seems to me that there is a certain fundamental limitation on the product of resolution time and resolution bandwidth, but you can arrange that area in any shape you want. You could, for example, try to get more resolution in time, in which case you would have to have

wider bandwidth and you would see rays. You could, in principle, even arrange your resolution window to be parallel to the mode dispersion curves and see only modes.

So that it is in a sense gratuitous, and I think a very happy fortune, that you happened to pick proportions that showed both at once.

Dr. Porter: To my mind the fundamental result is that the energy in a wideband signal is the sum of the energy in each mode at each eigenray arrival. That's another way of saying it is the sum of the energy in each frequency, each eigenray arrival, if the signal bandwidth times the dispersion of the channel is large.

That is quite a different statement than for narrowband signals where you have to add the pressure in each mode.

Dr. H. Weinberg (New London Laboratory, Naval Underwater Systems Center): I'd like to make a statement that is really directed toward the entire group, and I hope it is taken more as constructive criticism. Now seems like a good time to bring it up.

Very often somebody will discuss a method, a program, or a technique and then almost the very next speaker will get up and say that that method does not exist. In particular, a statement was made a couple of times, for example, that there aren't any computer programs taking account of shots, the broadband; in fact, a couple of programs can do precisely just that.

It is unfortunate that so little information flows between the various labs with respect to the different models actually available. I hope that something can be done to increase the speed of flow between people who have use for such programs.

Dr. W. H. Munk (Institute of Geophysics and Planetary Physics, University of California at San Diego): He just volunteered for the Steering Committee, didn't he? (Laughter)

Dr. J. B. Hersey (Office of Naval Research): Let me make this comment. One of the functions of the AESD, which they perform periodically, is to get the community together in a smaller workshop than this to exchange views and present background papers specifically on models. And I guess I need to know how this device is working.

Mr. Spofford: Okay. In terms of ray programs, about 3 years ago, LRAPP actually sponsored a ray tracing workshop that was followed up about 6 months later by some strong recommendations on what the next Navy standard ray tracing model should be. More recently, AESD hosted a normal mode wave program kind of workshop. Now, the program that Dr. Weinberg referred to, the latest CONGRATS program, is more recent than these workshops.

Dr. Weinberg: I'm not talking about that program.

Mr. Spofford: Well, it's a ray program, I guess, in a sense. I'm not sure; maybe I've missed the program he's referring to. Basically, ray programs can construct this kind of arrival structure in as much detail as you choose. It's the relation between the modes and the rays that I'm having difficulty in interpreting. It's kind of new to me. I don't know of any programs that do that.

Dr. Hersey: I know of one isolated experiment, which was a very elaborate one, on bottom bounce by Hastrup at La Spezia, in which he worked out the impulse response for explosive shots of reflections from the bottom. But, if you have ever tried to read that paper, really read it, it is a rather confusing thing to interpret.

I, too, regret that there isn't more of that type of presentation in this workshop. There may be before we get through. But I wondered if you could give us a thumbnail sketch of what the models that you refer to will do, because I think we ought to get a description of them as an important key part of this workshop.

Dr. Weinberg: The particular program I was talking about is a couple of years old and is called PEAK or PASSIVE, I don't know which. It was designed by Howard Newman of our lab and Jeff Colling. It's really just a "brute force" model. It allows you to input various characteristics. It tries to take into account various characteristics of systems rather than an explosive source. But I'm sure it could do that as well. It's not a very elegant program, but it does allow you to do broadband analysis.

My point wasn't that we had a ray program. Just the fact that nobody is really aware of the type of programs that we do have.

Dr. Hersey: Well, I guess I have to say that that is the responsibility of the people who do know about the program. The attendance at the workshops has been broad. Don't you agree? It may not be a very serious mistake, but it is a defect that we have to correct.

Dr. Weinberg: The type of program that we were talking about really didn't come up in any of the workshops so far. The first workshop was basically a ray tracing workshop. The second one was

a non-ray tracing. This program realizes the fact that there are discrepancies among various propagation loss models, which is the basis of these types of programs. It sort of allows you to choose what type of propagation loss model you want to use. It's just a bookkeeping system. It just didn't seem to fall into any of the workshop discussions that we have had.

Dr. Hersey: Possibly what we need, I know there's been some discussion of this within the Maury Center, is to focus on what we can do with broadband programs. Does anyone feel any great enthusiasm for that?

Dr. F. D. Tappert (Courant Institute of Mathematical Sciences of New York University): This issue actually came up at the last AESD workshop in the form of how one would write programs to get impulse response functions. On one level it was a trivial thing. You take any normal mode program or parabolic-equation program and run it at a thousand frequencies and get out the impulse response. It just takes an enormous amount of computer time.

I think what we have to learn is how to use the most modern computers. For example, the Illiac computer is especially designed to process in parallel 64 different frequencies and I think there is a need to get access to computers like this. If we had time on these machines, we could, by very straightforward methods, get impulse response curves.

Dr. Hersey: I think you have brought up a great point,
Dr. Weinberg.

Dr. Smith: Excuse me. May I demur on principle? No matter what computer you had, there will always be something that you can't compute with it. You will want a stronger one. I think we have to

decide what we want to compute. Do we want this structure or not? That requires us to consider the uses of our output.

Dr. Hersey: Preston, I agree with that very strongly, and so far our decision has been to opt for guessing at broadband results on the basis of CW programs in order to save money. That is implicit. I think there isn't anyone in the room who wouldn't have done the other if it had been cheap. Our whole field, going back 30 years, is a study in taking advantage of high-powered methods that have become cheap in money. We have been able to address problems that we simply couldn't address before. We'd just better keep our eyes open for the time, the moment even, when a new high-powered computer or a clever device of some other sort becomes available to us.

Mr. Spofford: I have one more comment. I think I would take exception to the final question about going out and attempting to verify this model with a measurement. I feel that probably the best way to verify an approximation which could be very powerful if it checks out and saves us from making all those normal mode runs would be some very careful numerical experiments, if you will, to determine the range of validity of this technique.

Unless I'm missing something in the technique, unless there's something about it which says that the wave equation which we use and which we solve for in normal mode programs is not the correct equation for these broadband signals — and I don't think you were saying that.

Dr. Porter: No. Of course I agree with the wave equation. The reason that I am interested in seeing some experiments is to look at some data from other oceans with axial shots and axial receivers. I'm not interested *per se* in going out and running more experiments if some already exist. But I would like to see if you can identify the same kind of structure in some other oceans.

Now, that's more of a scientific interest than it is an operator's interest. I agree with you, Chuck, that the thing to do is to try the model and test its limitations against what we already have.

Dr. Munk: I want to ask a naive question of Bob Porter and Fred Tappert. It seems to me that if you are analyzing an initial pulse problem, there ought to be an easier way to put it on a computer than to add a million frequencies. And it seems one should go back and do the physical integration for the initial pulse rather than using our traditional dependence on Fourier synthesis and trying to make that work.

Am I mistaken on that?

Dr. Tappert: I can respond to that. It is possible to include time dependence in the parabolic equation: to keep the time variable t as another independent variable. It is simply a question of programming technique whether you prefer a million points in time or a million frequencies.

I don't think that many will be necessary. But it's just a tradeoff in the approach that you use. The Fourier space representation is equivalent mathematically to the temporal representation for linear equations.

Mr. M. A. Pedersen (Naval Undersea Center): Well, this last summer I talked to Morris Daintith and Ian Roebuck at AUWE, and they have developed what they call the impulse method which does perhaps what you are thinking about. Rather than looking at a discrete frequency, then integrating over frequencies, they do the opposite problem of picking a response function for a given time and integrate in the other direction.

Dr. H. W. Kutschale (Lamont-Doherty Geological Observatory of Columbia University): In the Arctic, dispersion is characteristic of the signal propagation. We have been computing pressure pulses for a number of years using normal mode theory. Currently, in connection with propagation loss, we have been using the FFP with considerable success. Recently Fred DiNapoli has extended the FFP to transient signals and I think his results would be of considerable interest to the community.

And one other point — the initial normal mode computations made by Pekeris for the two-layer case were subsequently done by him in the time domain using a ray theory, and this type of approach has been extended to multilayer systems in seismology. I think some of these techniques might be quite useful for the higher frequency acoustics community.

Dr. Hersey: I think one note I have to introduce is based on such things as Ira Dyer's question last night about the requirement that we really do contribute to solving the problems of people who pay us. Unfortunately, unless we can make a compelling story for any such thing as the thing we have been discussing in the last few minutes — namely, working out impulse response type methods of analyzing propagation — we will very quickly be accused with the refrain that I keep hearing in Washington, "Oh, those fellows are just doing science for science's sake." That is, they say, we have abandoned the idea of making science useful.

This simply won't be supported unless we can make a very, very cogent case for it supporting a practical end. I'm sorry, but I believe that is true in the present climate.

CONVERGENCE ZONE DEPENDENCE ON FREQUENCY

R. M. Fitzgerald

Naval Research Laboratory,
Washington, D. C.

This presentation concerns a comparison of transmission-loss curves for 13.89 Hz and 111.1 Hz. Because of the source-receiver geometry and the ocean environment of the experiment, the predominant modes of propagation were RSR-type paths. Thus, we are considering frequency effects and the formation of convergence zones. Transmission-loss calculations based on modal solutions to the wave equation compare favorably with measurements.

For a range-and azimuth-independent medium the wave equation is separable. At long ranges its solution can be approximated by a finite sum of discrete normal modes. Using the asymptotic form of the Hankel function, one obtains the solution for the acoustic pressure given in Figure 1. The reciprocal square root of range results from geometric spreading. The mode summation describes the interference effects. The quantity ω is the source frequency and K_m is a separation constant. The amplitudes P_m depend on the source and receiver depths and indicate the extent to which a mode is excited and detected.

The phase velocity, C_m^{th} , of the m^{th} mode is defined as ω divided by K_m . It is useful for a qualitative description of the eigenfunctions. The depths at which the sound speed in the medium equals the m^{th} phase velocity, C_m^{th} , correspond to the turning points of the m^{th} eigenfunction. Where the speed of sound is less than the phase velocity of an excited mode, the eigenfunction is oscillatory and the energy can be concentrated. Where the speed of sound exceeds the phase velocity, the eigenfunction is exponentially decreasing.

$$\begin{aligned}
 P &= -\frac{1}{\sqrt{r}} \sum_m P_m \cos \left(\kappa_m r - \omega t - \pi/4 \right) \\
 P &= \left[-\frac{1}{r} \sum_{mn} P_m P_n \cos \left(\kappa_m r - \kappa_n r \right) \right]^{1/2} \cos \left(\eta - \omega t - \pi/4 \right) \\
 \eta &= \arctan \left[\frac{\sum_m P_m \sin \kappa_m r}{\sum_n P_n \cos \kappa_n r} \right]
 \end{aligned}$$

Figure 1. EXPRESSIONS FOR NORMAL MODE SOLUTION TO WAVE EQUATION

Such a region corresponds to the shadow region for the associated ray. The argument of the exponential describing the decay of the eigenfunction in the shadow region is proportional to frequency. The lower the frequency, the farther the wave function extends into the shadow region. This is simply a statement that diffraction effects become more significant at lower frequencies. In the experiment to be described, the diffraction effects at 13.89 Hz appear sufficient to markedly change the character of the transmission-loss curve from that of 111.1 Hz.

In Figure 1, the pressure is rewritten on the second line in terms of phase and amplitude by using trigometric identities. The transmission loss depends on the amplitude which is the square-bracketed term. In this term we again have the geometric spreading factor, $1/r$, and an interference summation. Considering the double summation in the amplitude, we note that the convergence zone phenomenon is due to the existence of a set of modes which have the property that

$$K_m - K_{m+1} \sim \frac{2\pi}{\lambda}$$

where λ , the convergence zone interval (~ 65 km), is independent of m . Because the interference effects depend as well on the modal excitations, P_m , we shall also be looking at the products, $P_m P_{m+1}$.

Figure 2 shows a simplified sound speed profile that is typical of the North Atlantic in the sense that it exhibits a thermocline, a SOFAR axis and a depth excess. This profile was used to compute the modal parameters in Figure 3.

Figure 3 shows calculations of modal parameters for the profile of Figure 2 for frequencies 13.89 Hz and 111.1 Hz. The lower frequency points are marked with an X. The higher frequency points are marked with a circle. Source depths are 104 m (13.89 Hz) and 21 m

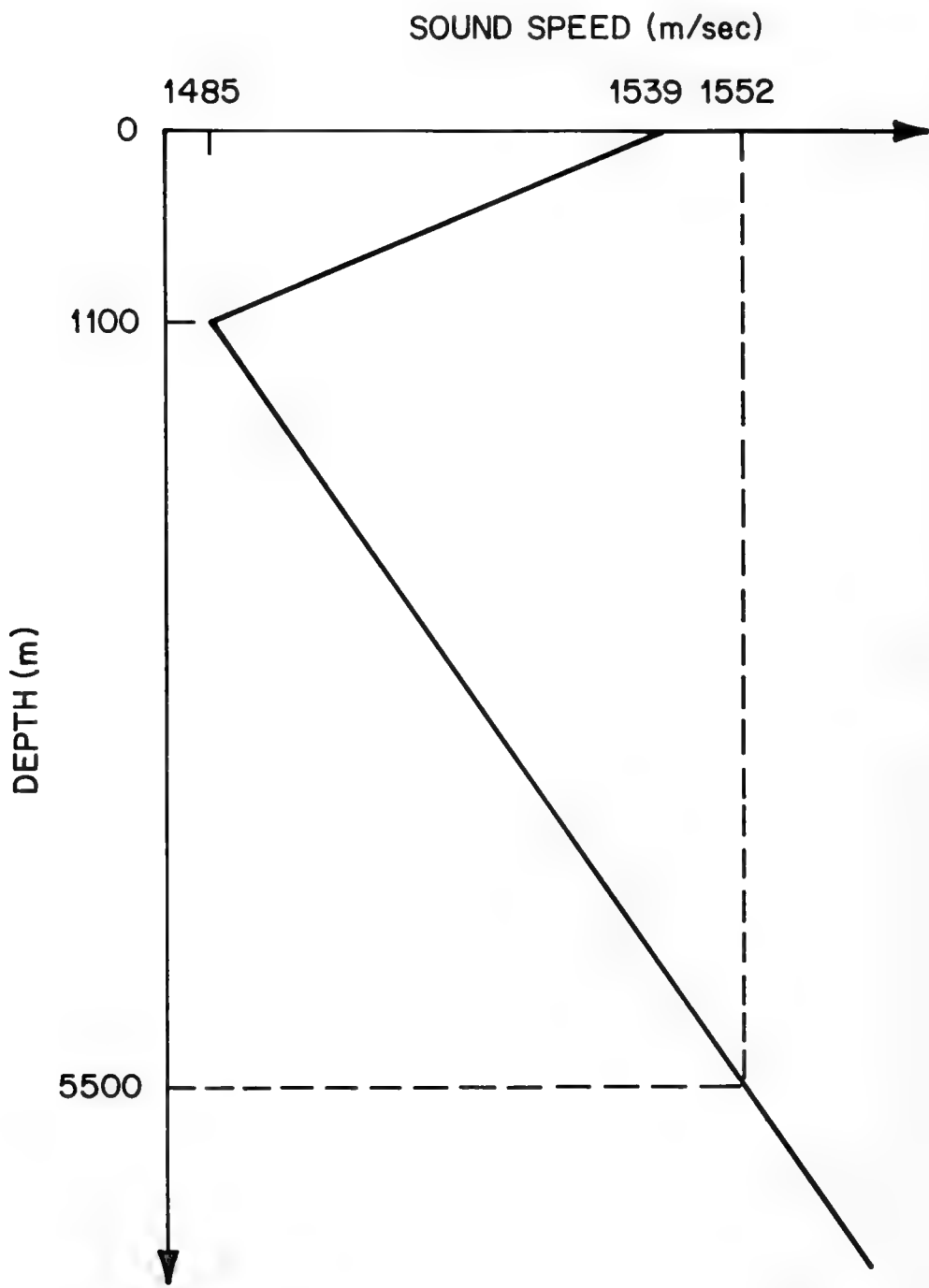


Figure 2. SIMPLIFIED SOUND SPEED PROFILE

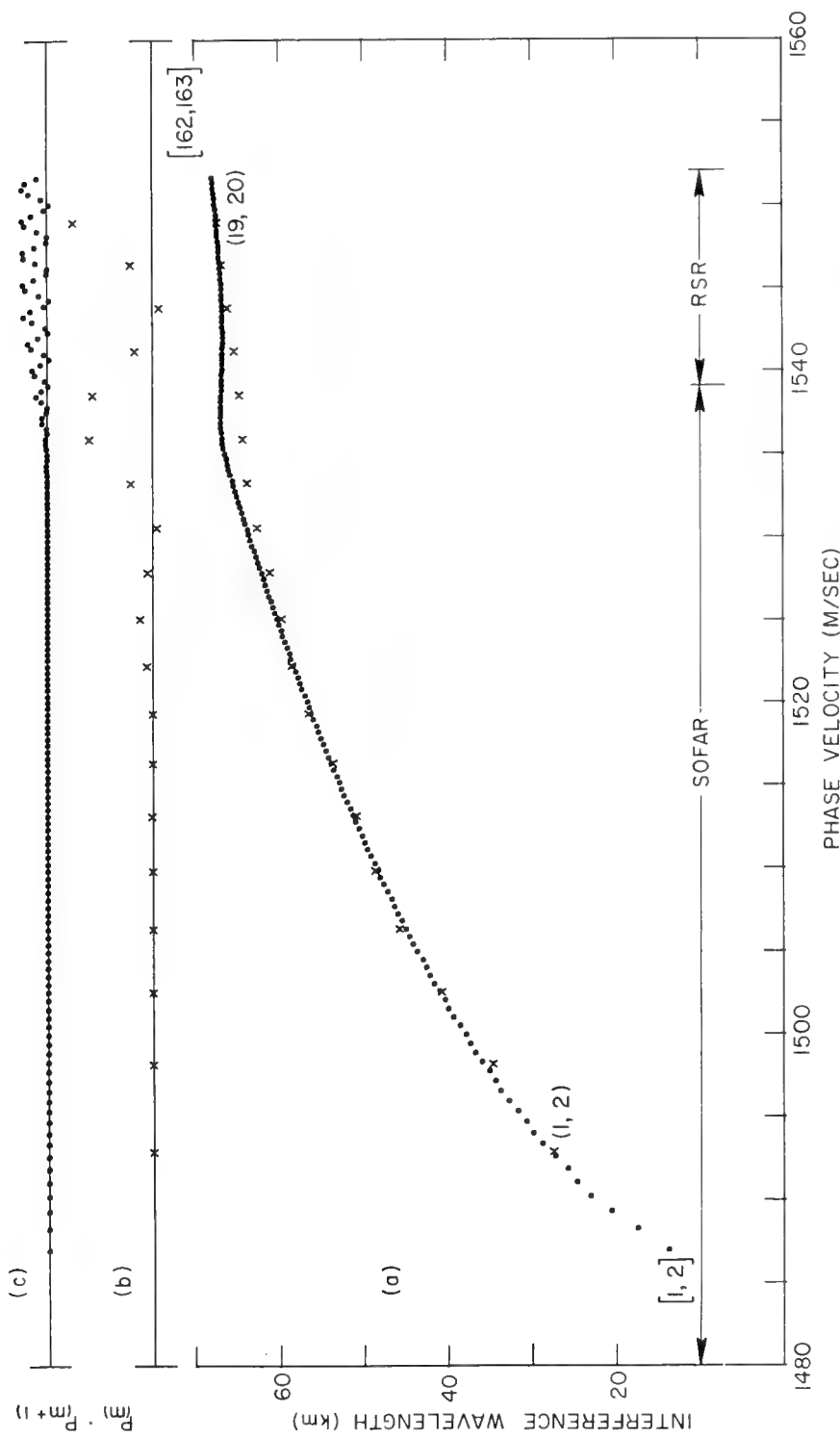


Figure 3. CALCULATIONS OF MODAL PARAMETERS

(111.1 Hz). Receiver depth is 1100 m. This Figure contains plots of $P_m P_{m+1}$ + 1 and interference wave length

$$\left(\lambda_{m, m+1} = \frac{2\pi}{K_m - K_{m+1}} \right) \text{ versus average phase velocity } \left(C_{m, m+1} = \frac{C_m + C_{m+1}}{2} \right)$$

for the two source frequencies.

The plots of $P_m P_{m+1}$ + 1 indicate that the principal modes of propagation are the RSR and highest phase velocity SOFAR modes, an expected feature for these source depths. The lower plot shows that the interference wavelengths for adjacent modes follow the same trends except for phase velocities slightly less than the speed of sound at the surface. The 111.1 Hz modes, which have a turning point just below the ocean surface, rapidly decay above that turning point and do not sense the surface. The 13.89 Hz modes, however, decay more slowly, sense the surface, and are affected by it.

Looking again at the low-frequency excitation, it appears that the excited low-frequency modes can be divided into two groups. The group with the lower phase velocities has an average interference wavelength of about 62 km. The other group has an average interference wavelength of about 65 km. The high-frequency modes can be divided into several groups based on the excitation plot but all groups have an interference wavelength of about 65 km.

Figure 4 shows the calculated transmission loss curves for the two frequencies. As anticipated, the high-frequency curve is composed of sharply defined convergence zones having an average spacing of 65 km. At the low frequency, the first convergence zone is composed of two peaks having different interference wavelengths. As range increases, these two peaks gradually move apart. By about the 20th

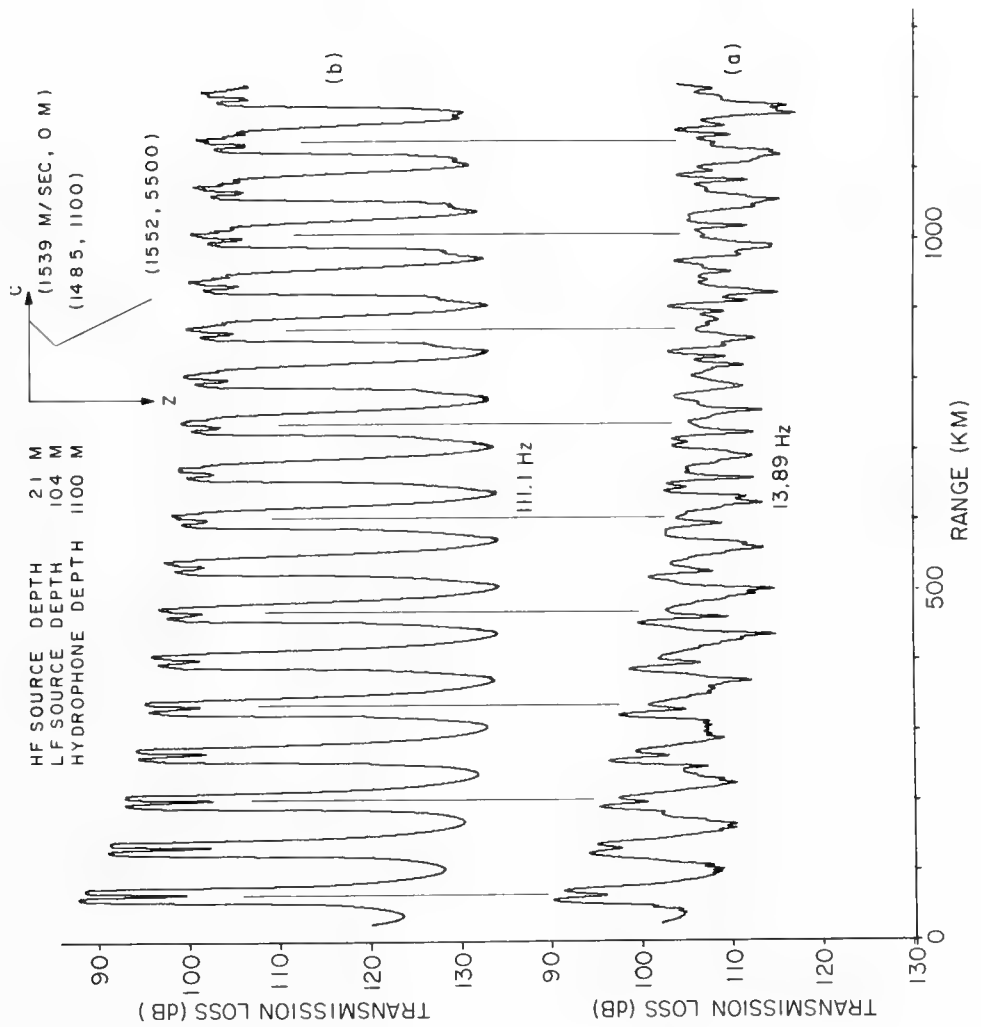


Figure 4. CALCULATED TRANSMISSION LOSS

high-frequency convergence zone, the low-frequency peaks have moved sufficiently far apart to overlay the peaks of other convergence zones.

These calculations will be compared with some experimental data in the next three Figures. Figure 5 shows the location of an experiment in which two cw sources were towed in a northerly direction away from a hydrophone located near the West Indies. Source frequencies and depths correspond to those of the preceding calculation. The receiver was located on the SOFAR axis. The sound-velocity profiles measured at ranges less than 1085 km from the receiver are superimposed in the leftmost box in Figure 6. The average of these profiles corresponds roughly to the bilinear profile of the calculation.

Figure 7 shows the experimental transmission-loss data. Curves (a) and (c) are the transmission-loss curves for the 13.89-Hz and 111.1-Hz signals, respectively. Curves (b) and (d) are 7-km running averages of intensity for curves (a) and (c). In curve (b) we see a double peak in the low-frequency convergence zone which opens with increasing range until the lefthand peak of one zone has moved over to the righthand peak of the previous zone. Figure 8 shows the detail of Figure 7 for ranges less than 1000 km.

Profile 1 in Figure 9 was used by Gordon to calculate the modal parameters of the next Figure. The profile continues into the bottom depths as a steep negative gradient. As a result, higher modes (BRSR) are very leaky and do not influence the field at long ranges.

Figure 10 is a plot by Gordon of interference wavelength, $\lambda_{m, m+1}$, versus average phase velocity, $\bar{\lambda}_{m, m+1}$, for frequencies of 31 Hz and 200 Hz. The plotted points for the two frequencies follow each other closely except in the region of the higher SOFAR

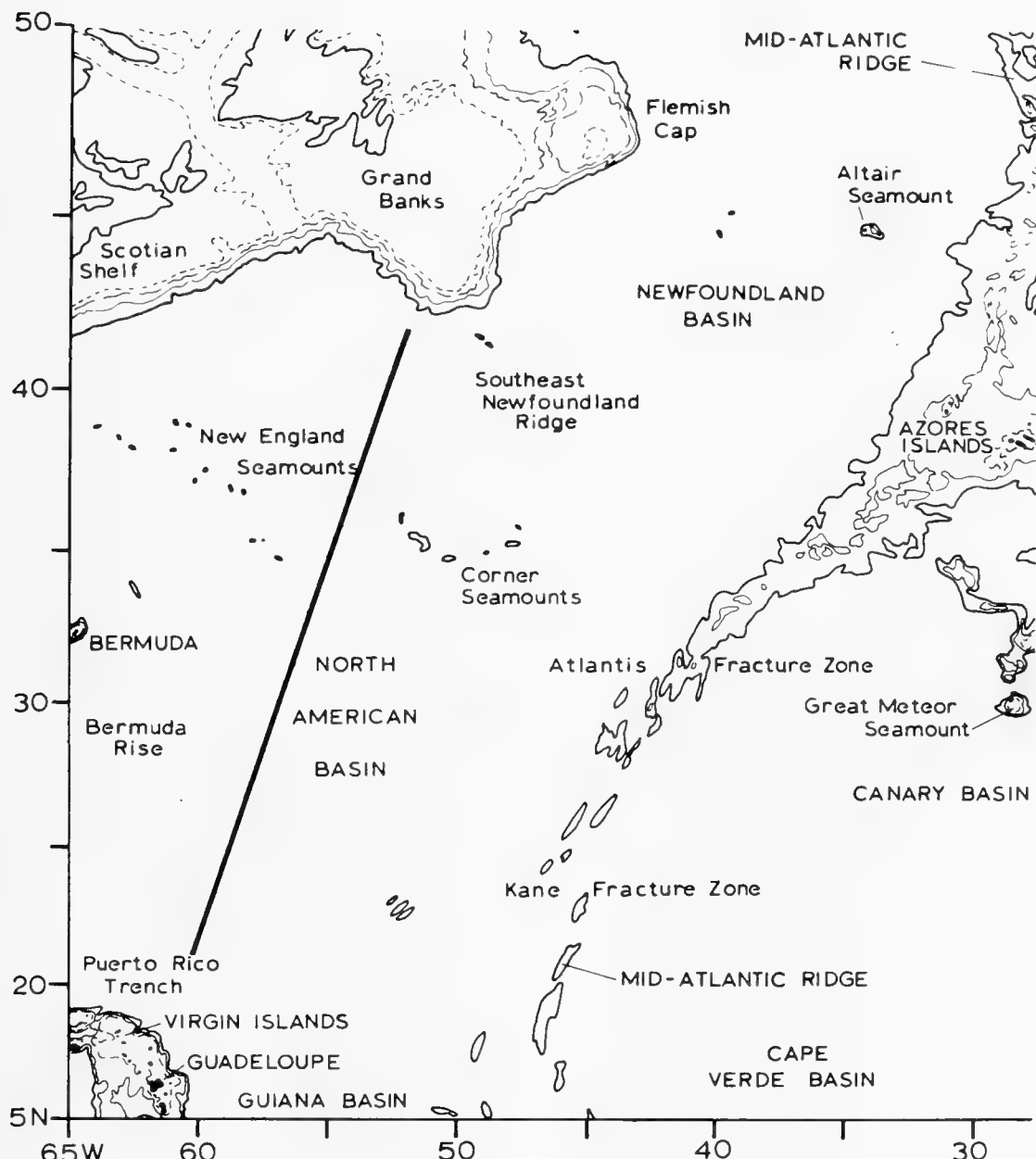


Figure 5. LOCATIONS OF EXPERIMENT

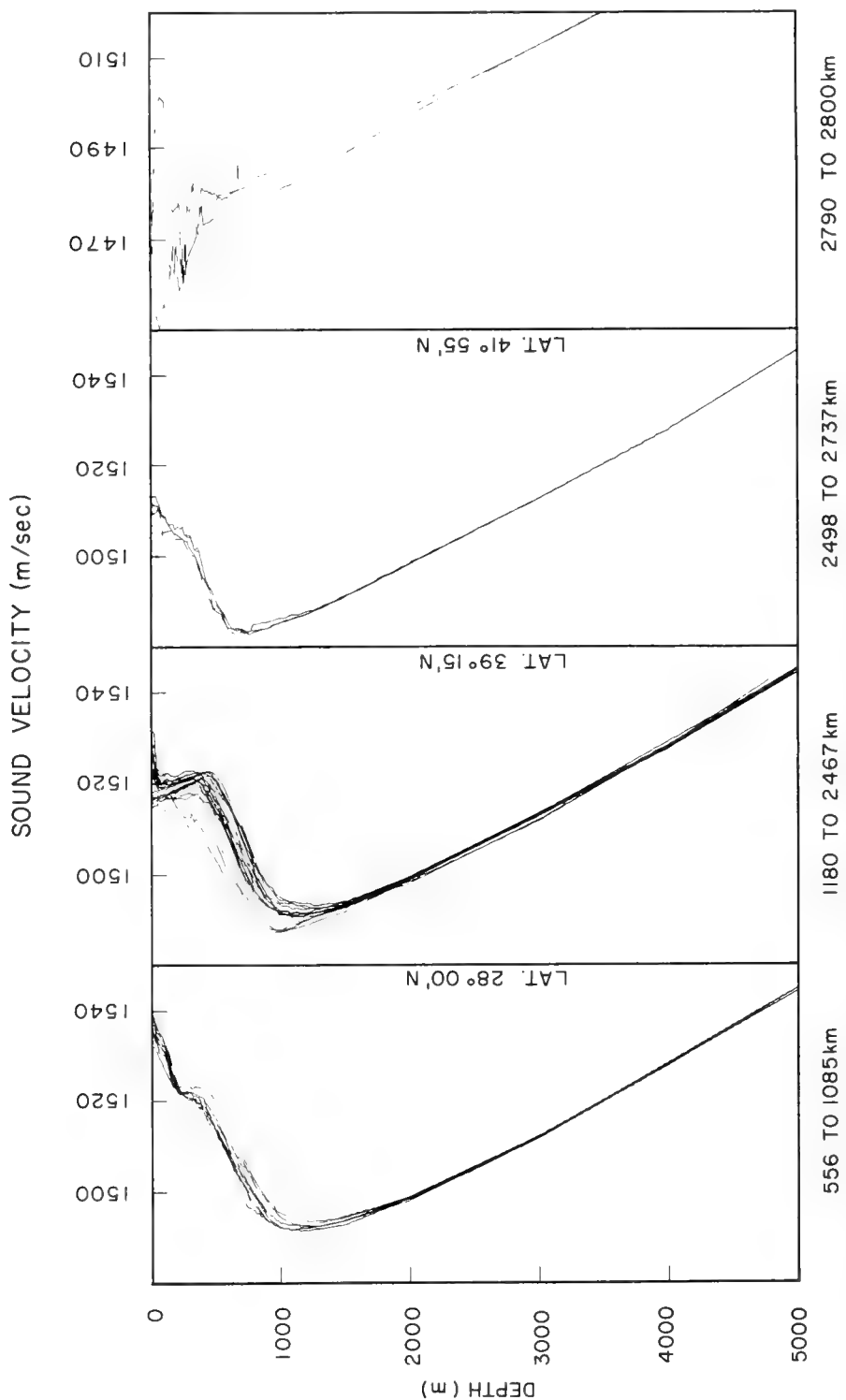


Figure 6. SOUND VELOCITY PROFILES ALONG THE TRACK

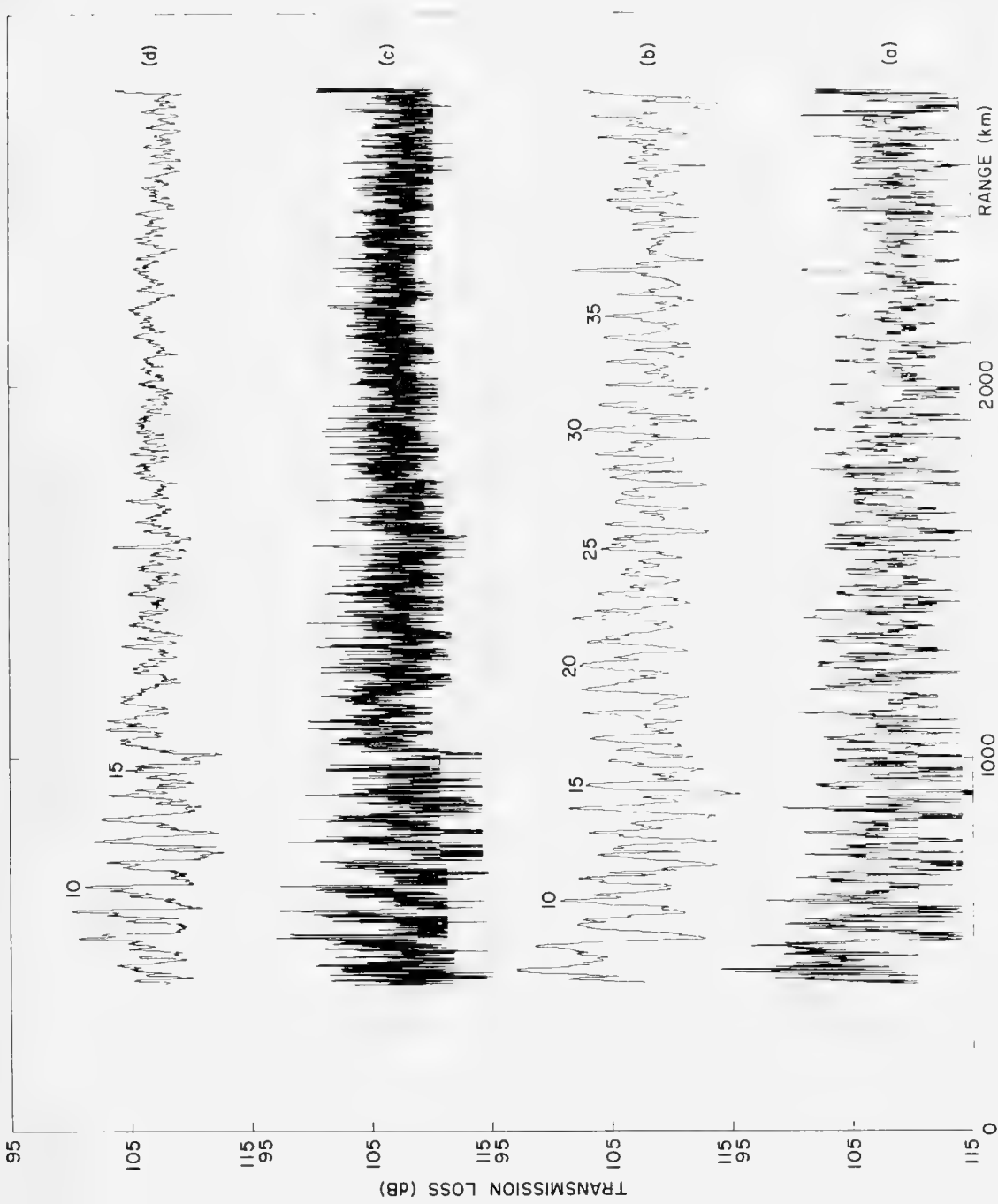


Figure 7. EXPERIMENTAL TRANSMISSION LOSS CURVES

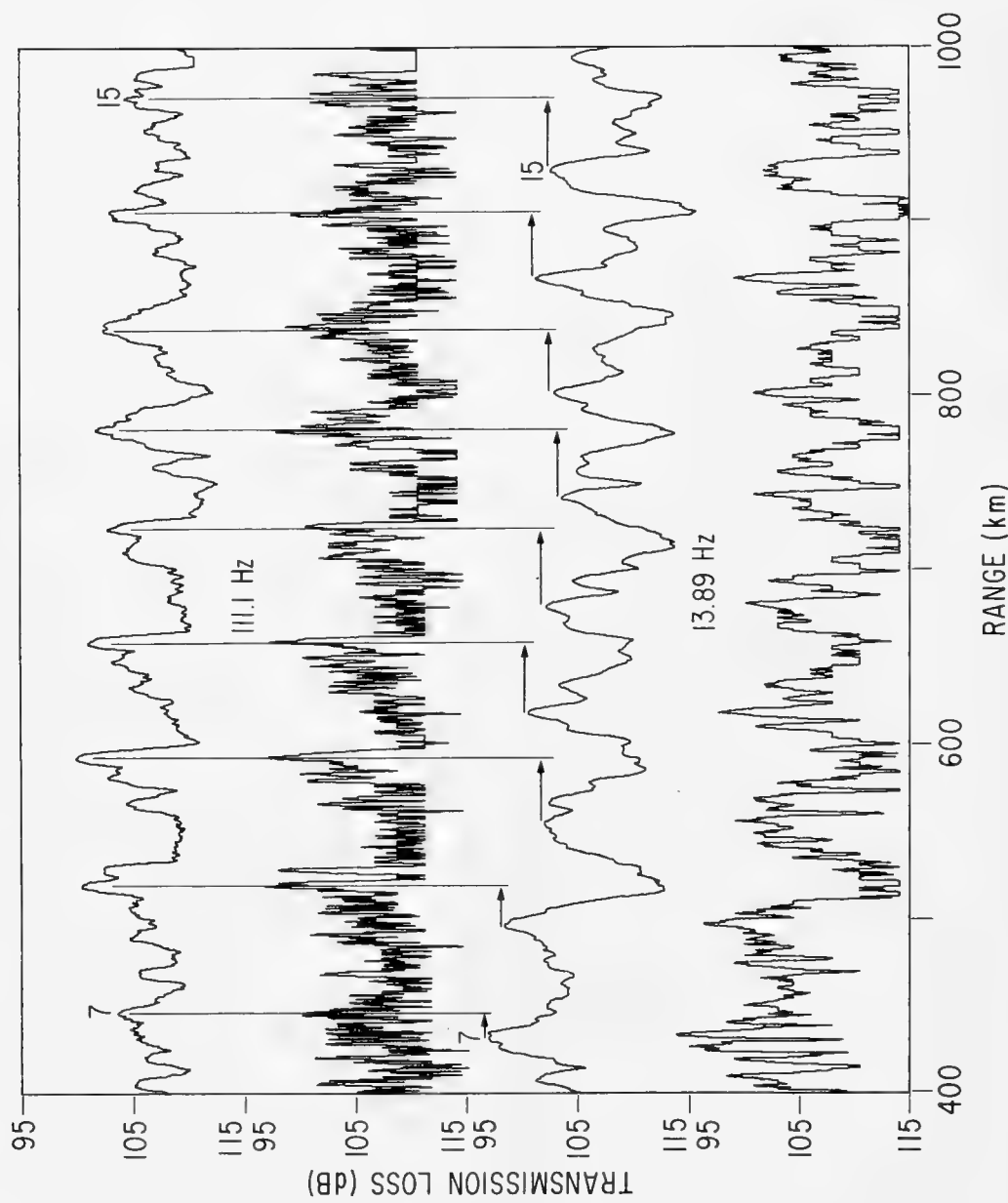


Figure 8. TRANSMISSION LOSS DETAIL

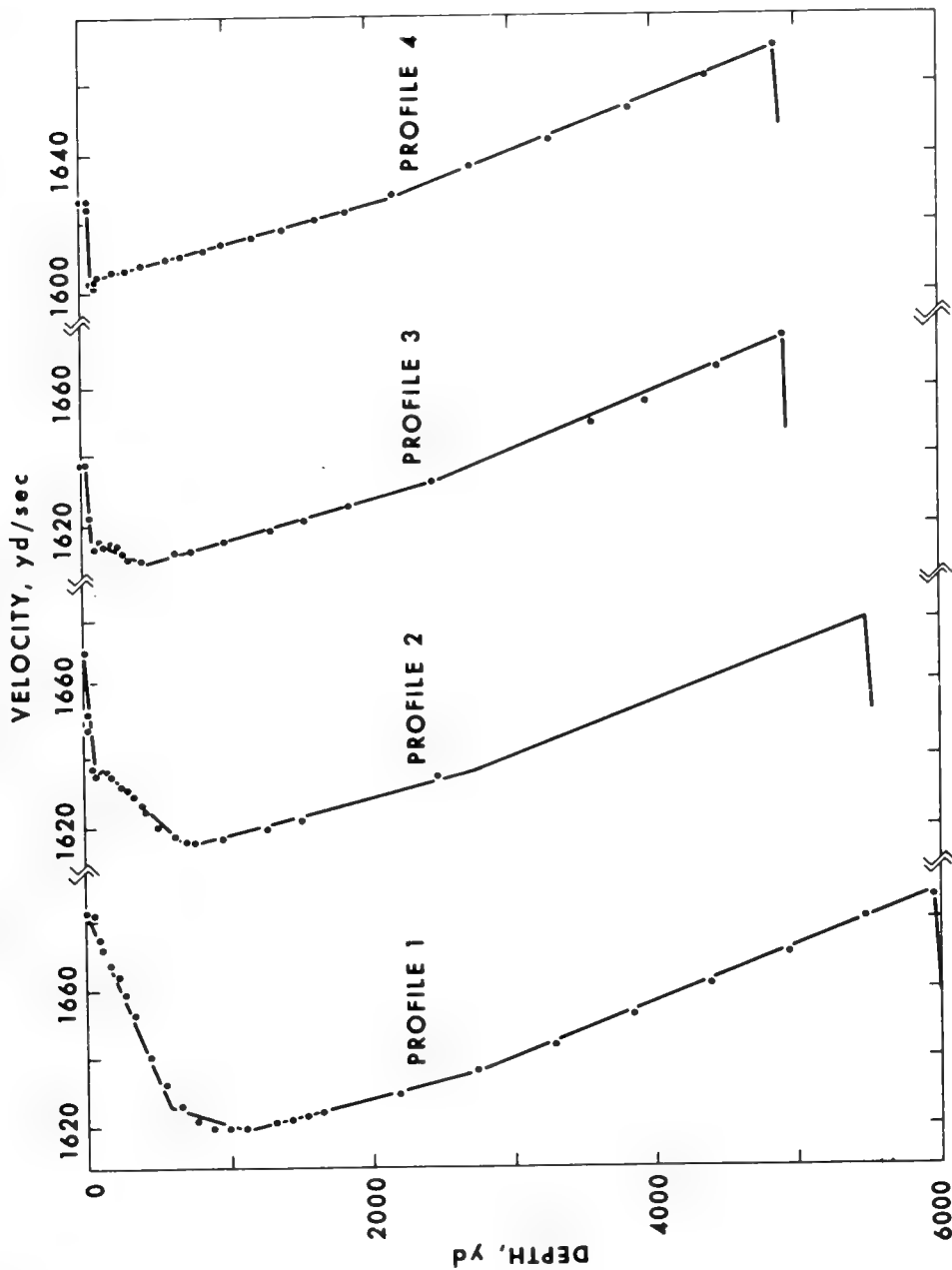


Figure 9. SOUND VELOCITY PROFILES

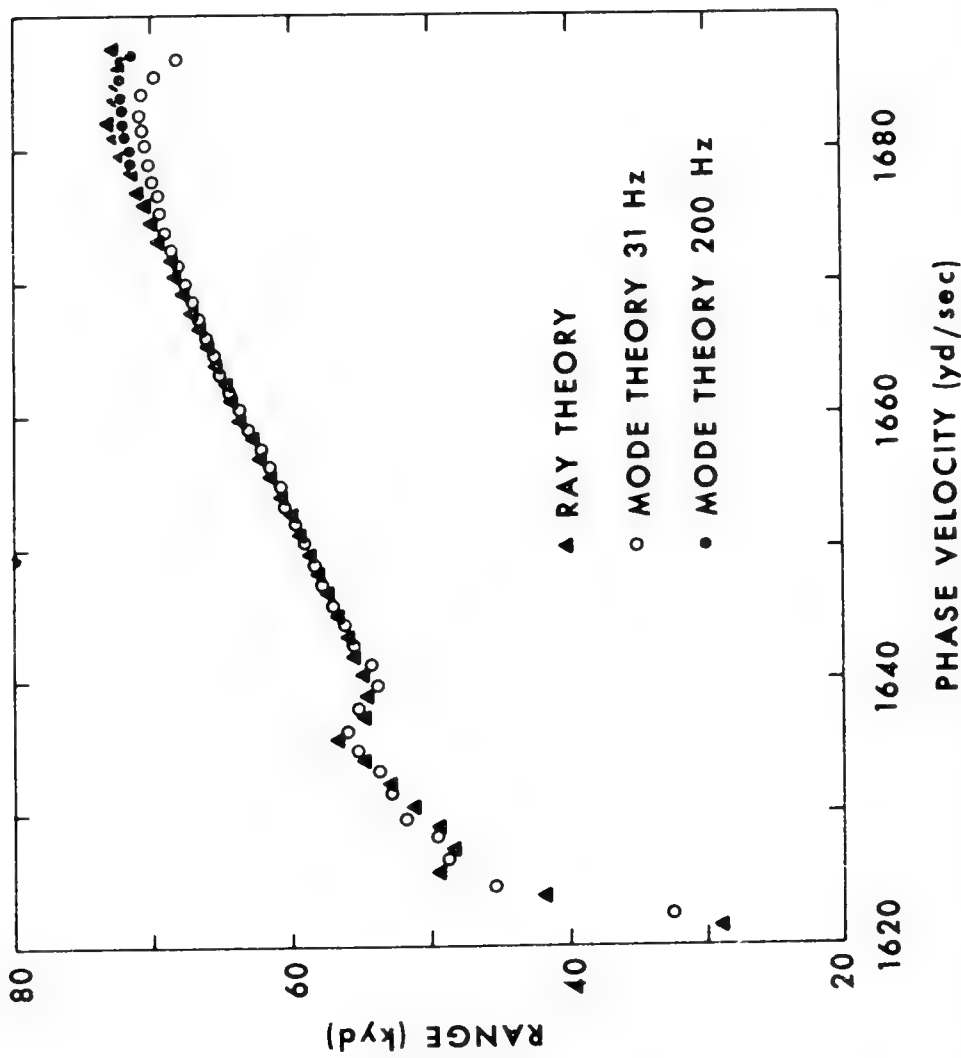


Figure 10. INTERFERENCE WAVELENGTH VERSUS PHASE VELOCITY (FROM GORDON)

and RSR type modes. This effect is again produced by the slow decay of the lower-frequency eigenfunction in the shadow region of the associated ray. The 31-Hz SOFAR modes with phase velocities slightly less than the speed of sound at the surface decay slowly into the upper thermocline and sense the pressure-release surface. The corresponding 200-Hz modes decay rapidly and do not sense the surface. The same effect occurs for modes with phase velocities slightly less than the speed of sound at the bottom. The higher 31-Hz RSR modes sense the profile's steep negative gradient in the bottom. The 200-Hz modes do not.

DISCUSSION

Dr. Gordon Raisbeck (Arthur D. Little, Inc.): You showed that the convergence-zone length when plotted against a certain mode parameter was different for two different frequencies only over part of the range of the argument.

You also showed that the amplitudes of the modes were far from uniform. It happens in the examples you showed that the amplitudes are large just in the same range of the parameter where they diverge.

You failed to say that there was a common cause. Was this accidental or is this a general rule that the amplitudes will be high just in the range of parameter where there is a difference between the two frequencies?

Dr. Fitzgerald: The plot of interference wavelength versus average phase velocity is independent of mode excitation. That plot comes only from the calculation of the separation constants, the eigenvalues. So it's totally independent of the excitation. The excitation is determined by the location of the source and receiver.

Dr. Raisbeck: There are possible excitations in which all the energy would fall in the range where the convergence zones had the same length for the two frequencies.

Dr. Fitzgerald: That's right. Yes.

Dr. John S. Hanna (Office of Naval Research): I'd like to make a comment. I think if I could adopt a ray-tracing point of view for just a moment, at the low frequency the two different periods that you observed in the convergence zone correspond respectively to the RR propagating rays and the RSR propagating rays. The only reason for making that observation is that I would invite some of you to take a look at the PARKA data, particularly for the 500-foot source and 50 Hz center frequency. You can see quite clearly those two different periods and the way they change the function of range in-exactly the same way you showed.

Dr. Fitzgerald: As I indicated, the region in which the interference wavelength was different was the region in which the phase velocity of the mode was less than the speed of sound at the surface, which indicates it's an RR.

LOW-FREQUENCY PROPAGATION IN THE ICE-COVERED ARCTIC OCEAN

Henry W. Kutschale

Lamont-Doherty Geological Observatory
Columbia University
Palisades, New York

The two features peculiar to the polar environment that most strongly influence underwater sound are the permanent ice cover, which averages about 12 feet in thickness in the central Arctic Ocean, and the velocity structure in the water. Ice movement generates ambient noise, and the ice modifies propagation, particularly at high frequencies, by scattering waves from the rough ice boundaries. Signals are detected by hydrophones at water depth and geophones in the ice. In deep water of the central Arctic Ocean, sound velocity is generally an increasing function of depth from the surface to the bottom. Such a velocity profile is found only in polar waters. The sound velocity structure is remarkably uniform as a function of both location and time of year. Sounds are transmitted to great ranges in this sound channel by upward refraction in the water and repeated reflection from the ice canopy. The surface sound channel of the Arctic is the polar extension of the deep sound channel or SOFAR channel of the nonpolar oceans, but the Arctic signals often differ markedly in character from those observed in the deep channel, largely because of the predominance of low-frequency waves (6 to 40 Hz) in the Arctic. The Arctic signals are dispersive with low-frequency waves traveling faster than high-frequency waves in each normal mode. At a range of 350 nautical miles from an explosion up to eight normal modes are commonly observed with a suggestion of still higher modes. In contrast to the uniformity of the velocity structure in the water, the bottom and surface topography of the ice is highly variable in both space and time. This variability of the ice cover is the major cause of corresponding variations of propagation loss observed in different areas during nearly simultaneous experiments over deep water. Recent experiments conducted in cooperation with O. I. Diachok of the Naval Oceanographic Office are described to illustrate recent advances in experimental techniques. Surface ice roughness was measured continuously by laser

from an aircraft with simultaneous measurements of propagation loss from air-dropped SUS charges.

The purpose of this paper is to present a summary of the important aspects of long-range, low-frequency propagation in deep water of the central Arctic Ocean. The emphasis is on a comparison of field data with theory. Generally good agreement is found between experiment and theory employing ray theory, WKB mode approximation, normal-mode theory and the Fast Field Program (FFP), provided the approximate nature of the former two methods is kept in mind. The normal-mode formulation and the FFP technique are derived from the exact integral solution of the wave equation for sources in a multi-layered, interbedded liquid-solid half space. The FFP, introduced by Marsh and DiNapoli, is a fast, convenient method for computing propagation loss as a function of range and source and detector depth. The FFP integrates directly the exact integral solution of the wave equation employing the Fast Fourier Transform and is particularly well suited for Arctic propagation because of the uniformity of the vertical sound velocity structure. Reflection loss by the rough ice boundaries is easily incorporated in the integral solution. Computed propagation loss is in close agreement with field data. For computations of dispersion and signal waveforms, normal-mode theory is in good agreement with field data.

Field data strongly suggest that reliable estimates of propagation loss as a function of range in deep water can be obtained from measurements by aircraft of surface ice roughness combined with computer modeling of loss. The FFP seems most useful for frequencies below 100 Hz, while at higher frequencies both ray theory and the FFP yield results in close agreement.

A characteristic feature of long-range explosive sound propagation in deep water of the central Arctic Ocean is that the signals are dispersive; that is, waves of each frequency travel with different phase and group velocities. Dispersion of explosion sounds in shallow water was discovered and extensively investigated by Worzel and Ewing (1948) during World War II. These observations of Worzel and Ewing in shallow water were explained by Pekeris (1948) who had developed

the normal-mode theory of shallow-water propagation. There is a close analogy between propagation in shallow water and propagation to long ranges in deep water of the central Arctic Ocean. In the central Arctic Ocean, the dispersion is different from that in shallow water because the Arctic propagation is controlled by the velocity structure in the water; but the methods of analyzing the Arctic signals parallels closely the methods employed by these early workers.

For many applications, it is convenient to consider the propagation in terms of ray theory. The connection between ray and normal-mode theory is conveniently done in terms of the WKB approximation (Kutschale, 1971). In other words, we sometimes deal with modes, sometimes with ray theory, and we connect these two methods using the WKB approximation.

This paper is divided into two parts. The first part deals with the character and analysis of Arctic SOFAR signals. The second part deals with propagation loss as a function of range: measurements, computations, and methods of estimating loss as a function of range employing data from airborne measurements of surface ice roughness. The band of frequencies of interest is from 2 to 350 Hz. The emphasis is on a comparison of measurements made over deep water with theory to arrive at an understanding of the causes of strong variations of signal amplitudes and propagation loss dependent upon source and detector depth, ice roughness, and bathymetry.

The measurements span nearly a 17-year period beginning in 1958 with the first experiments initiated at NUSC on long-range explosive sound transmission between floating ice stations. From these early experiments, many of the unique features of the Arctic signals were explained by Hecht (1960, 1961), Kutschale (1961), Marsh and Mellen

(1963), and Mellen and Marsh (1965) in terms of ray and normal-mode theory. An unexplained feature of the early experiments was the large variations (up to 40 dB) observed at each frequency of propagation loss as a function of range. Experiments made during the past 6 years by Buck, Diachok and Kutschale, combined with computer modeling by Weinstein, Chow and Kutschale, have gone a long way to unscramble the causes of these variations. The recent investigations strongly suggest that reliable estimates of propagation loss as a function of range for fixed source and detector depths can be obtained from airborne measurements of surface ice roughness combined with computer modeling of loss. An important test of prediction of loss will come when the data are analyzed from large-scale experiments conducted by Diachok and Kutschale during May 1974. These experiments will be described briefly to illustrate the airborne techniques presently in use to obtain coincident data of propagation loss as a function of range and surface ice roughness.

The central Arctic Ocean is covered by ice the year round. The pack ice averages about 10 feet thick. The ice is in continual, very slow motion under the influence of winds and currents. The pack ice is not of uniform thickness, but it is broken by leads of open water and pressure ridges. The irregularity of the pack ice boundaries is strongly dependent upon location and time of year. This seasonal and spatial dependence of ice roughness is of great importance for long-range sound propagation because of scattering of waves impinging upon the ice. Figure 1 shows a photograph of the pack ice taken from a plane.

In contrast to the variability of the ice cover, the sound speed structure in the water is very uniform as a function of location and season. Sound speed is generally an increasing function of depth from the surface to the bottom. Sounds are transmitted to long



Figure 1. PHOTOGRAPH TAKEN FROM AN AIRCRAFT OF PACK ICE.
ESTIMATED AREA ABOUT 20 SQUARE km

ranges in this sound channel by upward refraction in the water and repeated reflection from the ice. Figure 2 compares the Arctic profile with a profile of the temperate Atlantic. The Arctic sound channel is the polar extension of the deep sound channel or SOFAR channel of the nonpolar oceans. Figure 3 shows typical ray paths computed at one-degree intervals from a source at depth in the Arctic channel. The deep penetrating waves arrive first, and the waves traveling near the axis last.

The Arctic SOFAR signals are often quite different in character from those signals observed in the deep channel, largely because of the predominance of low-frequency waves in the Arctic. Waves above 40 Hz are strongly scattered by the rough ice boundaries so that at ranges beyond 700 nautical miles (1200 km), waves in the band from 8 to 40 Hz generally predominate in the signal. The dispersion observed in the Arctic signals shows that the waves are coherent over long distances. In each normal mode, both phase and group velocity decrease with increasing frequency.

Figure 4 shows the major bathymetric features of the central Arctic Ocean. Three submarine ridges are separated by deep abyssal plains. It is apparent that the Soviet Union borders on a major portion of the central Arctic Ocean. The Siberian continental shelf is the widest in the world. Certainly shallow-water propagation is of great importance, not only to the Navy but also to the oil industry, but time will not permit me to discuss this important area of under-ice acoustics.

Some sample propagation paths are shown on the map of Figure 4, and the corresponding signals will be shown on the next two figures. Signals for paths 1 to 4 were transmitted between three manned floating ice stations: ARLIS II, T-3, and Polar Pack I. Path

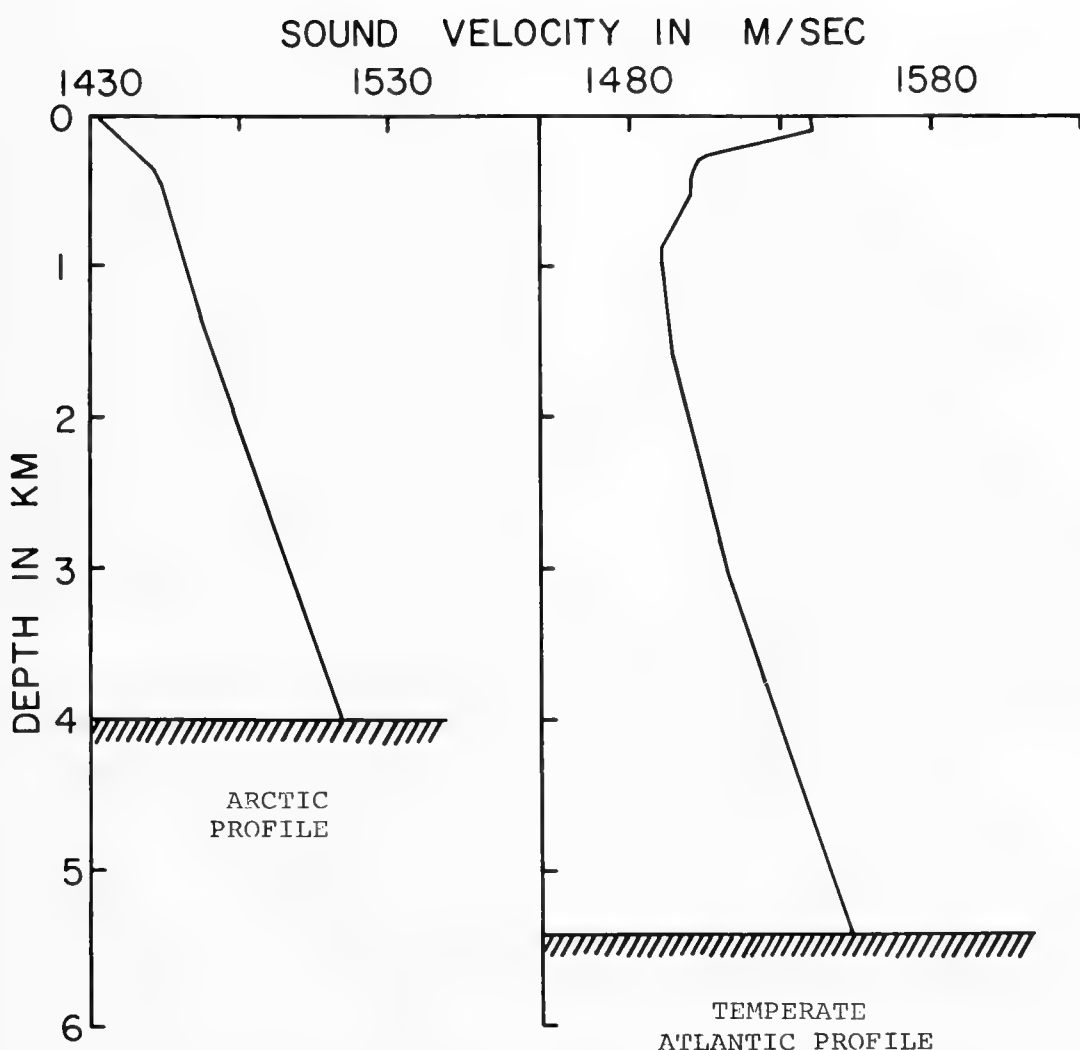


Figure 2. SOUND VELOCITY PROFILE OF CENTRAL ARCTIC OCEAN COMPARED WITH PROFILE OF TEMPERATE ATLANTIC

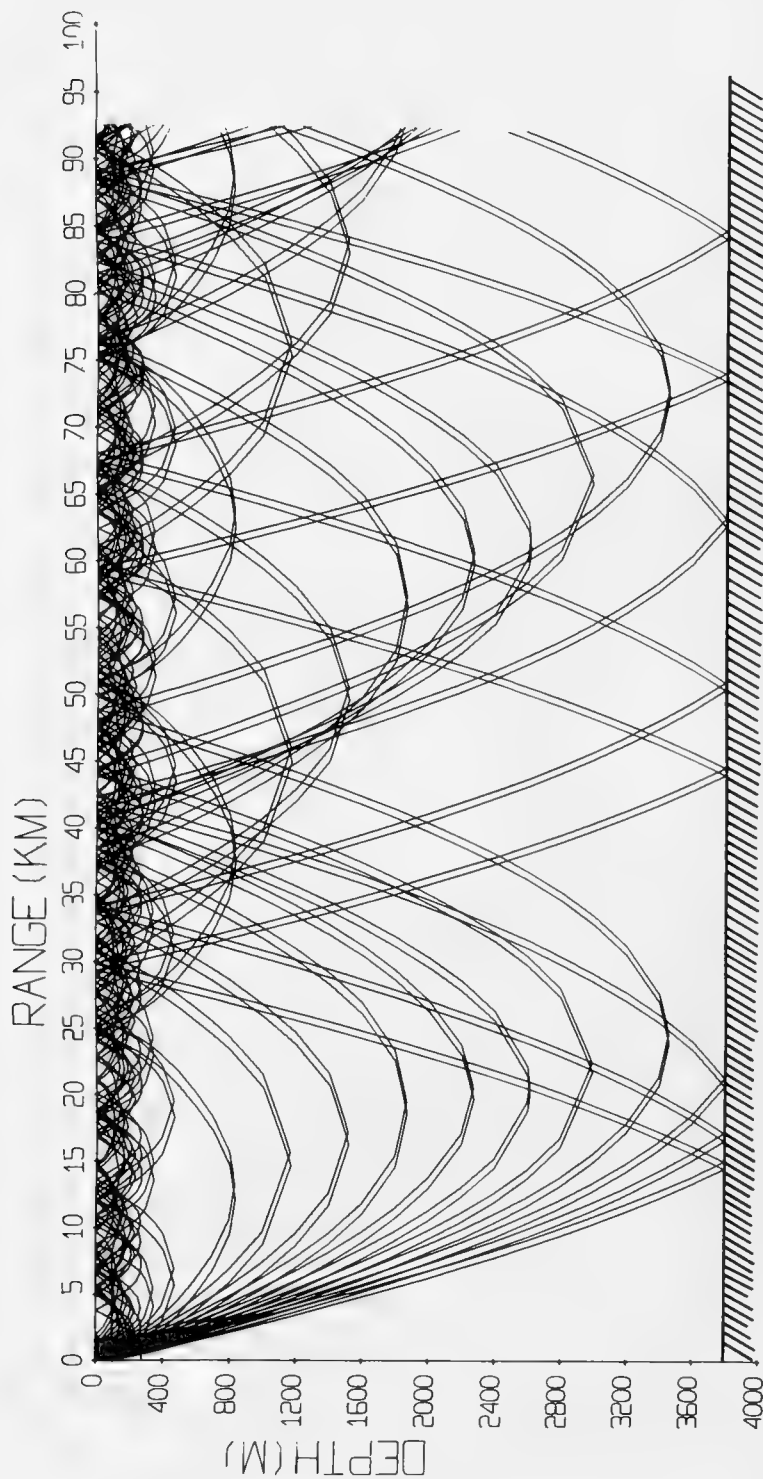


Figure 3. RAY PATHS IN ARCTIC SOUND CHANNEL COMPUTED AT
10 INTERVALS. SOURCE DEPTH 100 m

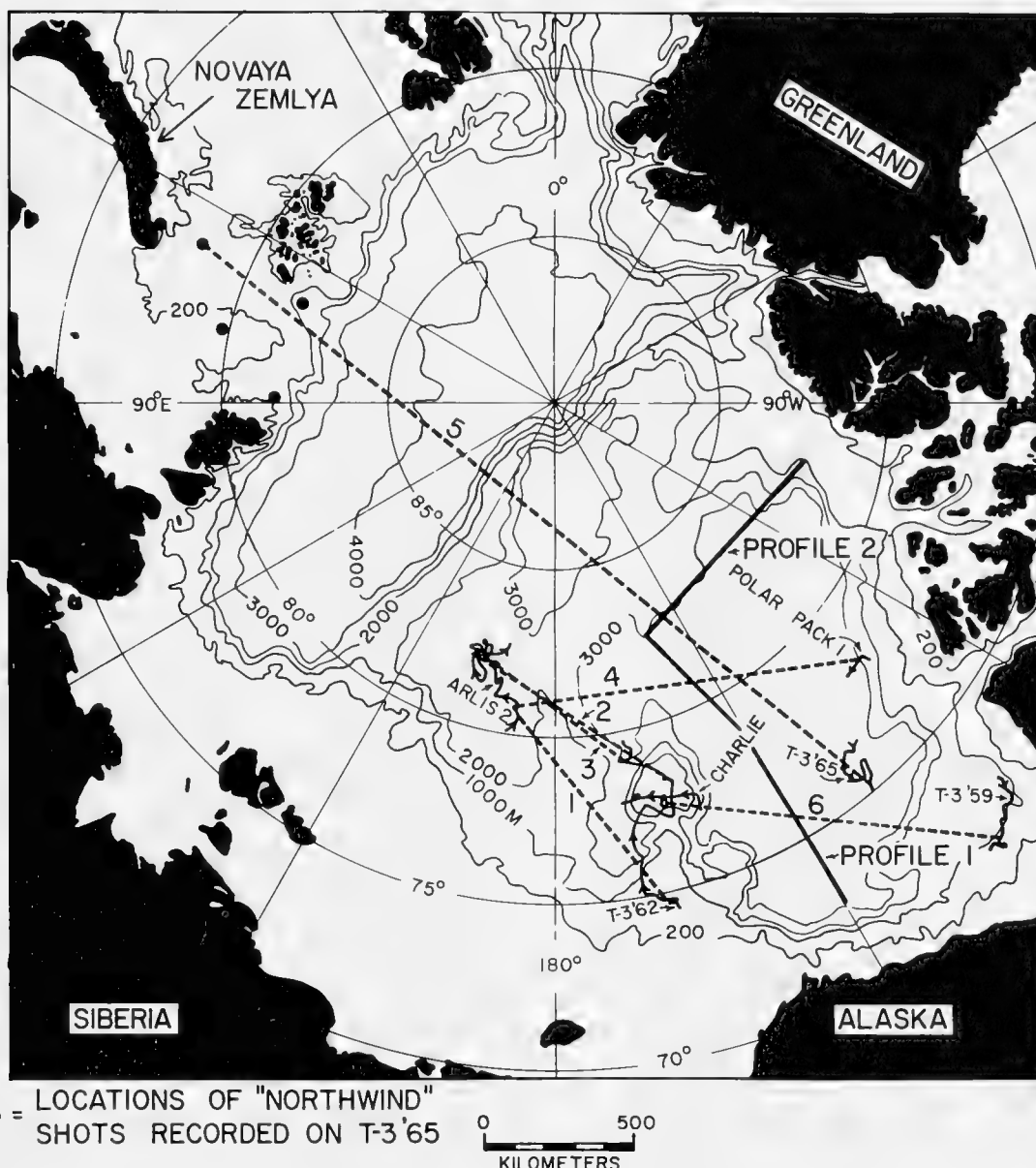


Figure 4. BATHYMETRIC MAP OF THE CENTRAL ARCTIC OCEAN. PROPAGATION PATHS ARE NUMBERED 1 TO 6. PROFILES 1 AND 2 RECORDED ON FLETCHER'S ICE ISLAND (T-3) DURING MAY 1968. CONTOURS BASED ON GEOLOGIC MAP OF THE ARCTIC (1960)

5 and the solid circles correspond to shot points occupied by the ice breaker "Northwind." The signals were recorded aboard T-3. A signal along Path 6 will show the dispersion of waves of the first two normal modes. Profiles 1 and 2 correspond to flight lines for air-dropped SUS charges recorded on T-3 in 1968. Peak signal intensities for these profiles will be shown later, but let me point out here that the signal strengths as a function of range are considerably weaker along Profile 2 than along Profile 1 because of a corresponding difference of ice roughness.

Figure 5 shows typical signals detected by hydrophones at depth and geophones on the ice surface. The signals often begin with a series of pulse-like waves corresponding to the deep penetrating RSR sounds. These waves may have the largest amplitudes. If shallow water intervenes, these waves are weak or absent. Sound spectrograms show that these waves consist of a superposition of a number of normal modes. Following these pulse-like waves, a train of nearly sinusoidal waves arrives in which frequency clearly increases with time. This dispersion is characteristic of Arctic SOFAR propagation, and it is useful for identifying weak signals by ear from high-speed playbacks of tape recordings: the signals give a tone of increasing frequency.

Figure 6 shows the nearly sinusoidal waves corresponding to the first two normal modes at a range of about 650 nautical miles from the shot.

Figure 7 shows a sound spectrogram of waves corresponding to the first two normal modes. The signal was detected on the ice by a geophone as part of a special infrasonic listening system capable of responding to waves over the frequency band from 0.1 to 30 Hz. This spectrogram illustrates clearly the spectrum of waves in the extremely low-frequency band from about 2 to 30 Hz. The reverberation

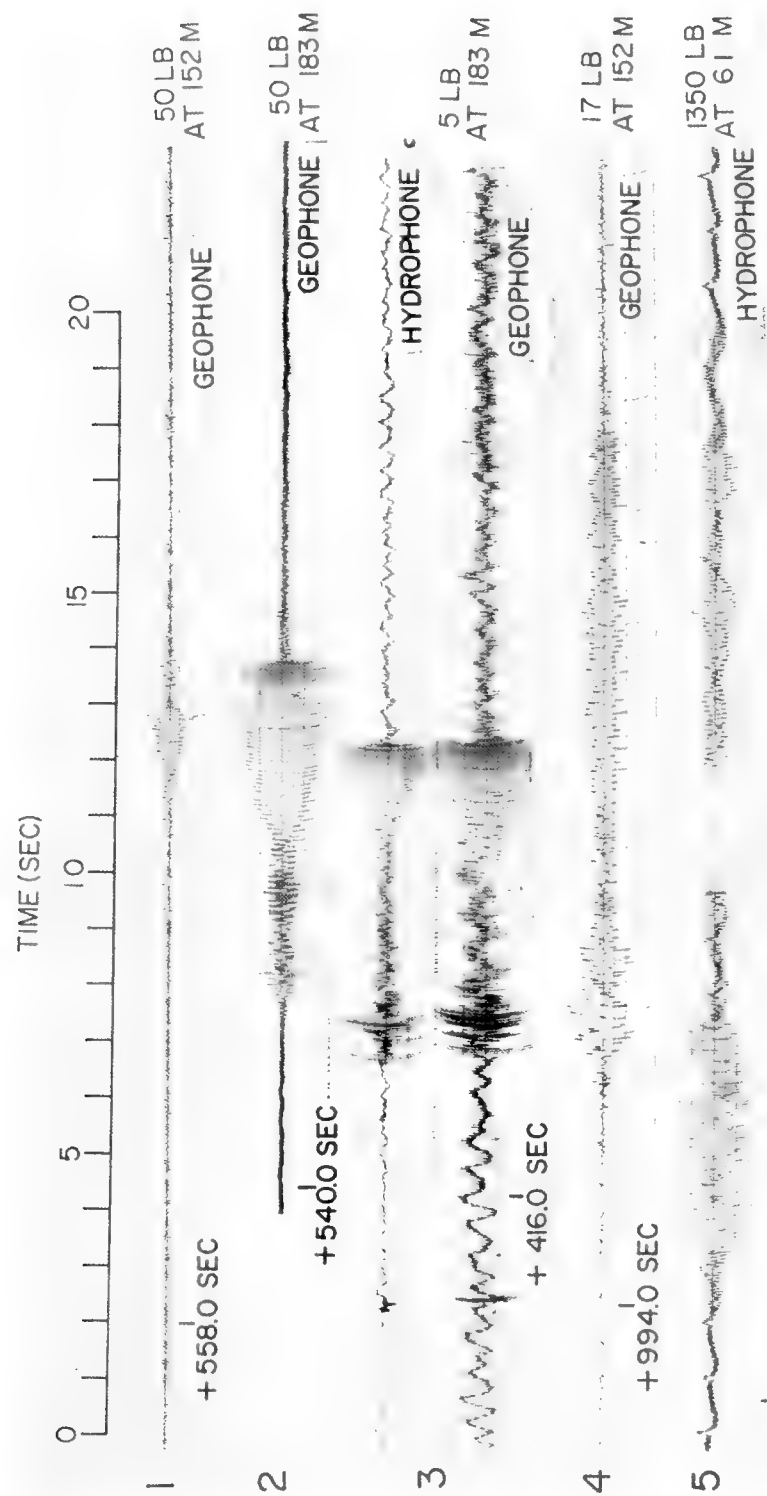


Figure 5. TYPICAL SIGNALS TRANSMITTED ALONG PATHS 1 TO 5 OF FIGURE 4. TIME AFTER SHOT SHOWN ON RECORDINGS. RANGES EXTEND FROM ABOUT 600 km UP TO 2800 km.

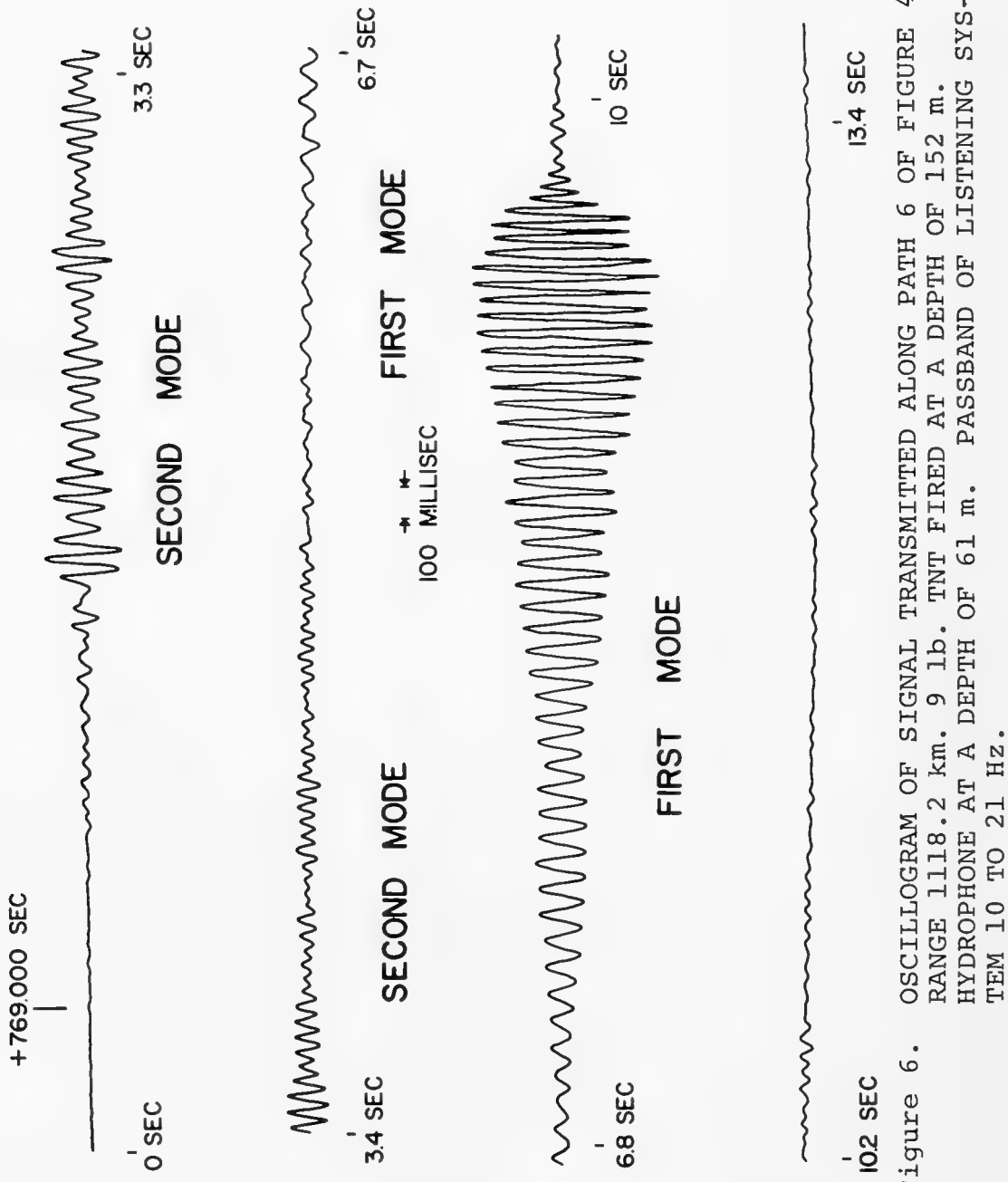


Figure 6. OSCILLOGRAM OF SIGNAL TRANSMITTED ALONG PATH 6 OF FIGURE 4.
RANGE 1118.2 km. 9 lb. TNT FIRED AT A DEPTH OF 152 m.
HYDROPHONE AT A DEPTH OF 61 m. PASSBAND OF LISTENING SYSTEM 10 TO 21 Hz.

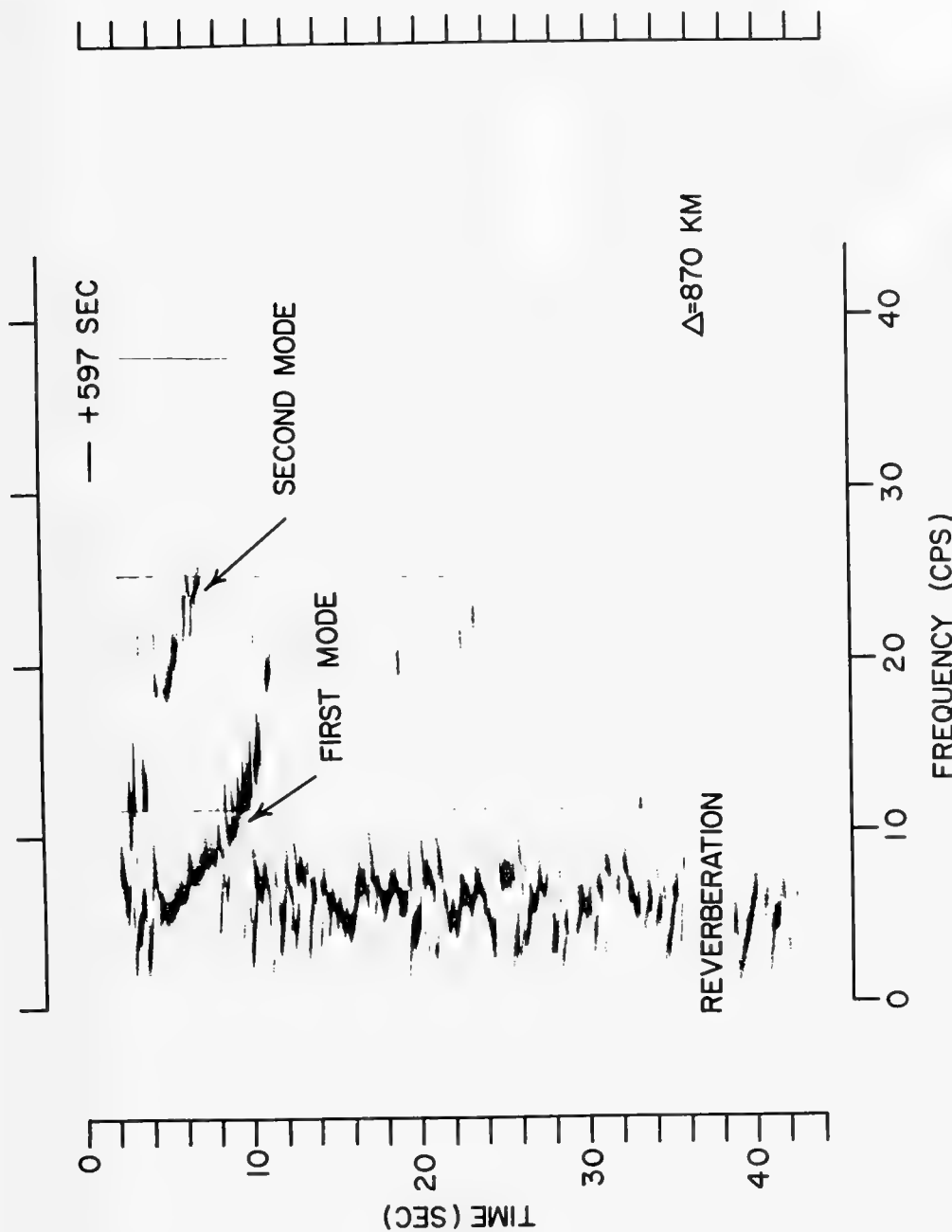


Figure 7. SOUND SPECTROGRAM OF SIGNAL DETECTED ON THE ICE BY A GEOPHONE. FREQUENCY RESPONSE OF LISTENING SYSTEM .1 TO 30 Hz. FIRST TWO NORMAL MODES CLEARLY SHOWN. BAND OF ENERGY CENTERED AT ABOUT 3 Hz. CORRESPONDS TO REVERBERATION.

corresponds to incoherent waves reflected from the ocean floor. An important point here is that the effects of ice roughness on propagation loss appear to be nearly negligible for waves below 10 Hz so that these waves will travel to very great ranges in deep water.

Figures 8 to 11 will show the effects of shot depth on the signals. The hydrophone depth and charge size were kept constant and there is only a small variation of range.

Figure 8 in this sequence shows oscilloscopes. Note that waves corresponding to the first normal mode are weak for the 366-meter shot. This is due to the pressure distribution with depth of the first normal mode or, in terms of ray theory, the lack of waves traveling along shallow-penetrating rays.

Figures 9 and 10 show sound spectrograms for this series of experiments. Up to seven normal modes are observed, but for the deep shots the first normal mode is weak compared to the shallower shots. The apparent cutoff for waves at 10 Hz is largely caused by a drop-off of response of the listening system.

Figure 11 shows the amplitude spectra of this series of shots for the total signal (of duration 6 seconds) followed immediately by 6 seconds of reverberation. Peaks at the bubble-pulse frequency and harmonics are apparent on the narrow-band spectra.

The effect of bathymetry on the signals is shown in Figure 12. For this series of experiments, shots of identical size and depth were launched from T-3 and recorded aboard ARLIS II employing a hydrophone at a fixed depth. Note the weakening of the deep penetrating sounds as the amount of shallow-water along the path increases. What this experiment shows is that the onset of a signal is largely

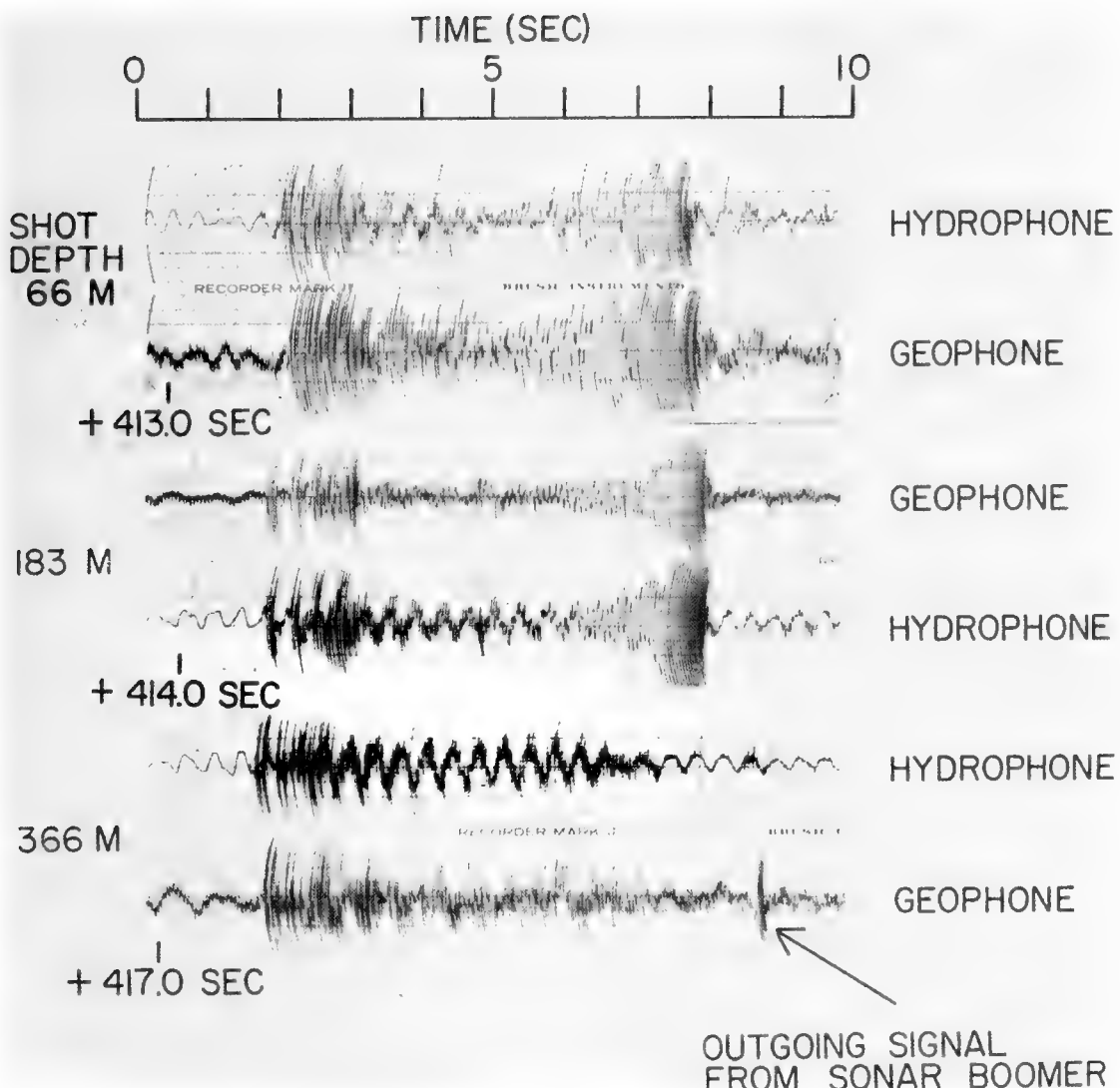


Figure 8. SEQUENCE OF OSCILLOGRAMS OF 5 lb. TNT CHARGES FIRED AT DEPTHS OF 66, 183 AND 366 m. HYDROPHONE DEPTH 46 m. SIGNALS TRAVELED ABOUT 600 km APPROXIMATELY ALONG PATH 3 OF FIGURE 4

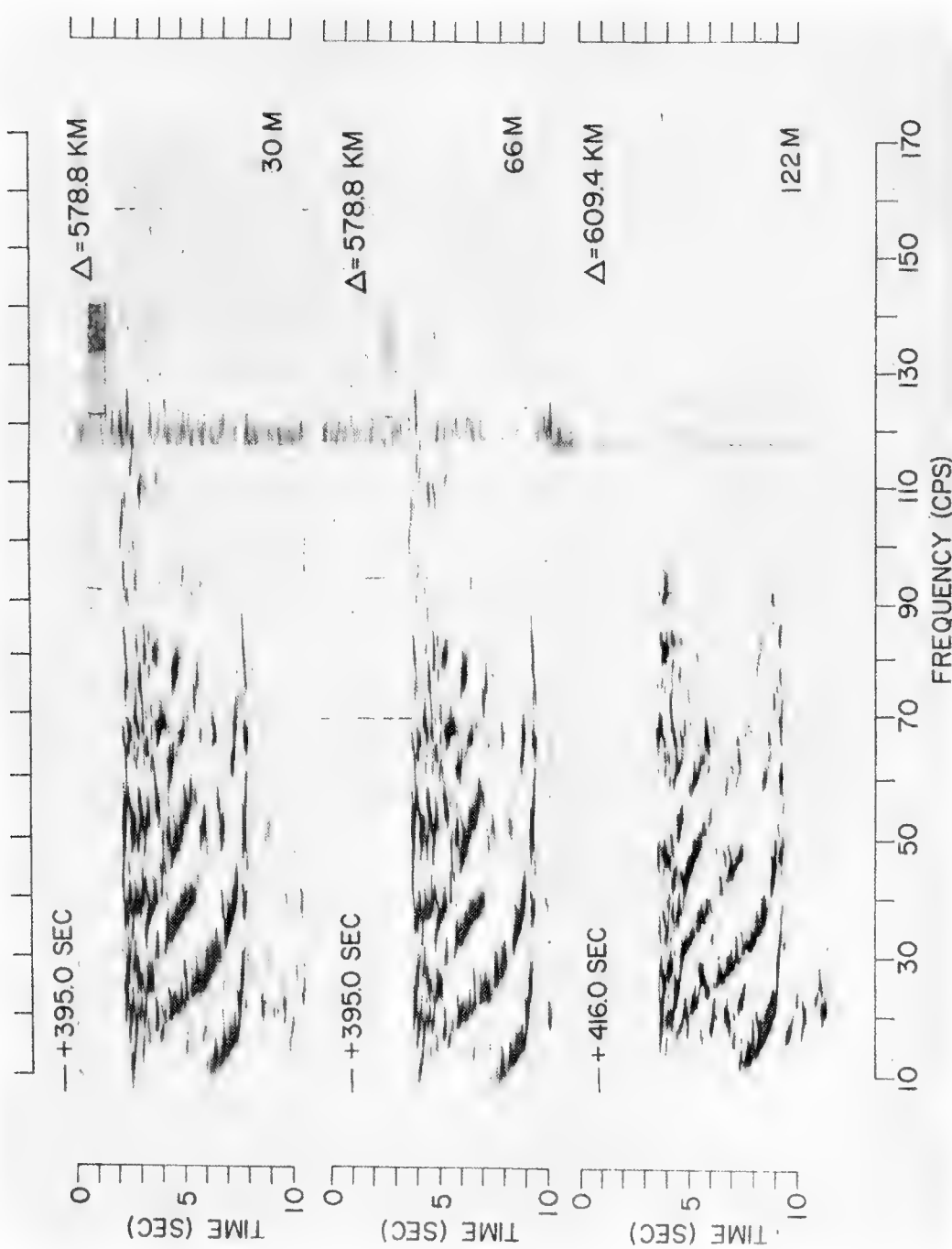


Figure 9. SEQUENCE OF SOUND SPECTROGRAMS OF 5 lb. TNT CHARGES FIRED AT DEPTHS OF 30, 66, AND 122 m. HYDROPHONE AT A DEPTH OF 46 m. SIGNALS TRAVELED ABOUT 600 km. APPROXIMATELY ALONG PATH 3 OF FIGURE 4

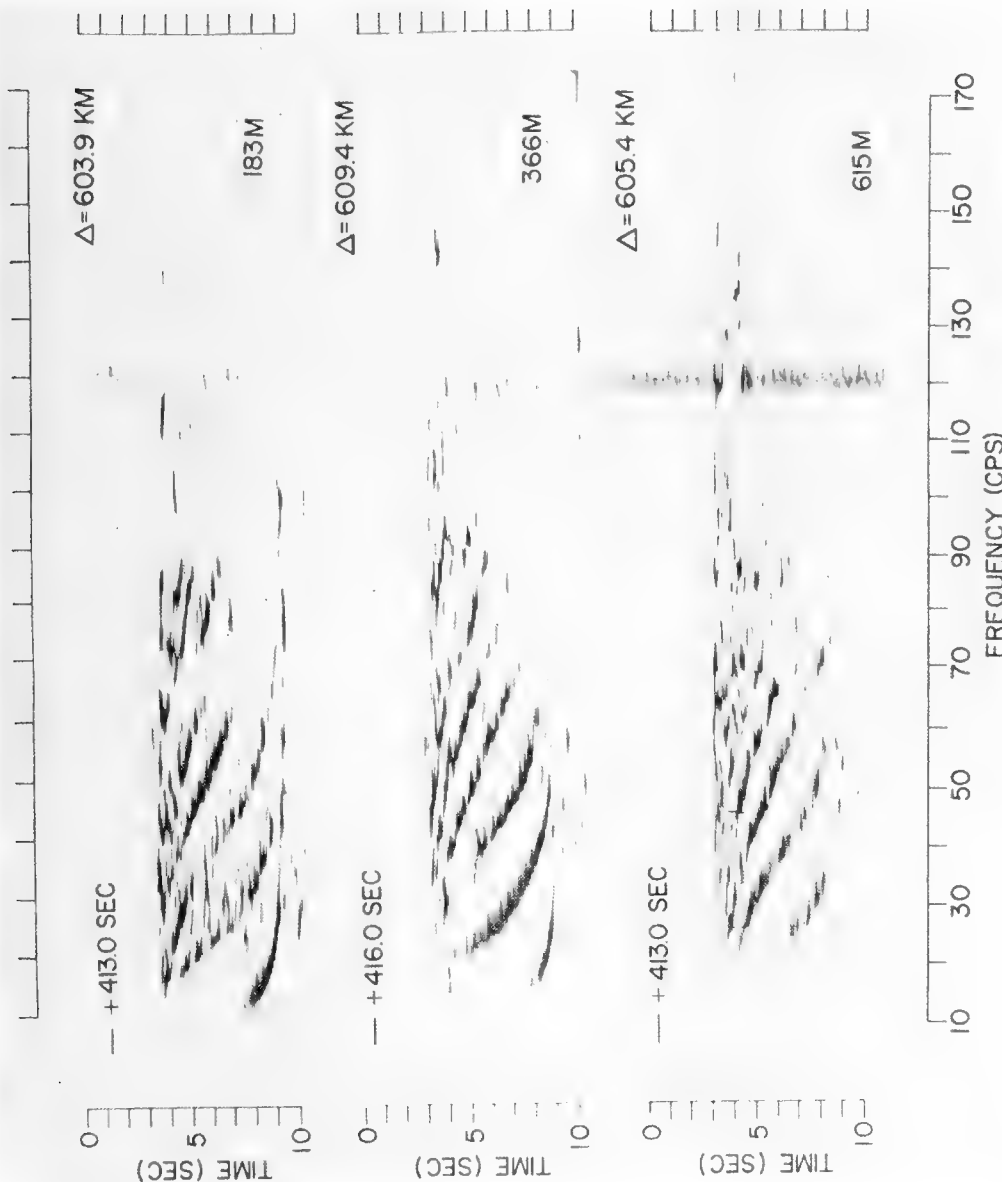


Figure 10. SEQUENCE OF SOUND SPECTROGRAMS OF 5 lb. TNT CHARGES FIRED AT DEPTHS OF 183, 366 AND 615 m. HYDROPHONE AT A DEPTH OF 46 m. SIGNALS TRAVELED ABOUT 600 km APPROXIMATELY ALONG PATH 3 OF FIGURE 4.

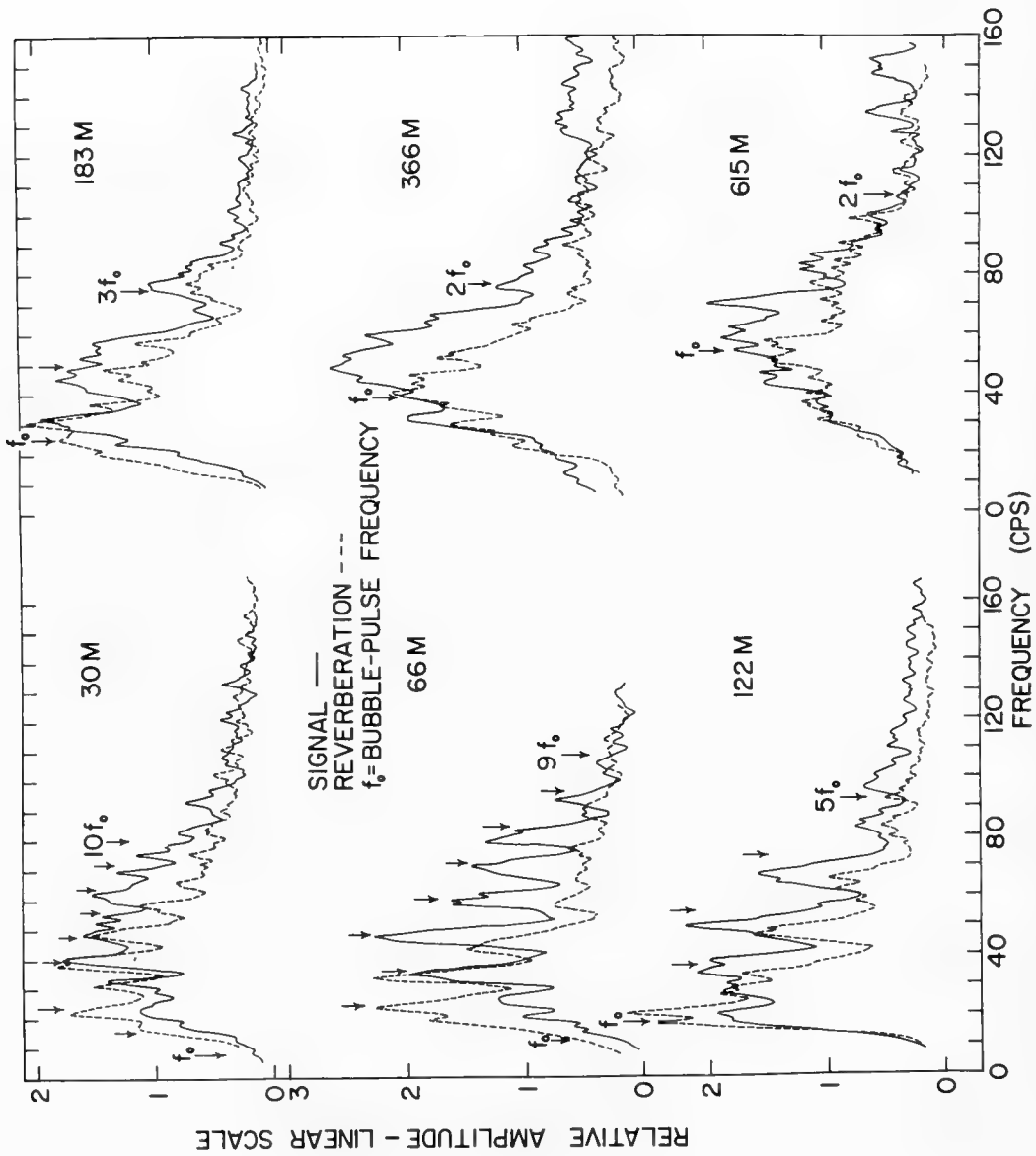


Figure 11. NARROW-BAND SPECTRA OF SHOTS CORRESPONDING TO FIGURES 9 AND 10.
BUBBLE-PULSE FREQUENCY AND HARMONICS INDICATED BY ARROWS.

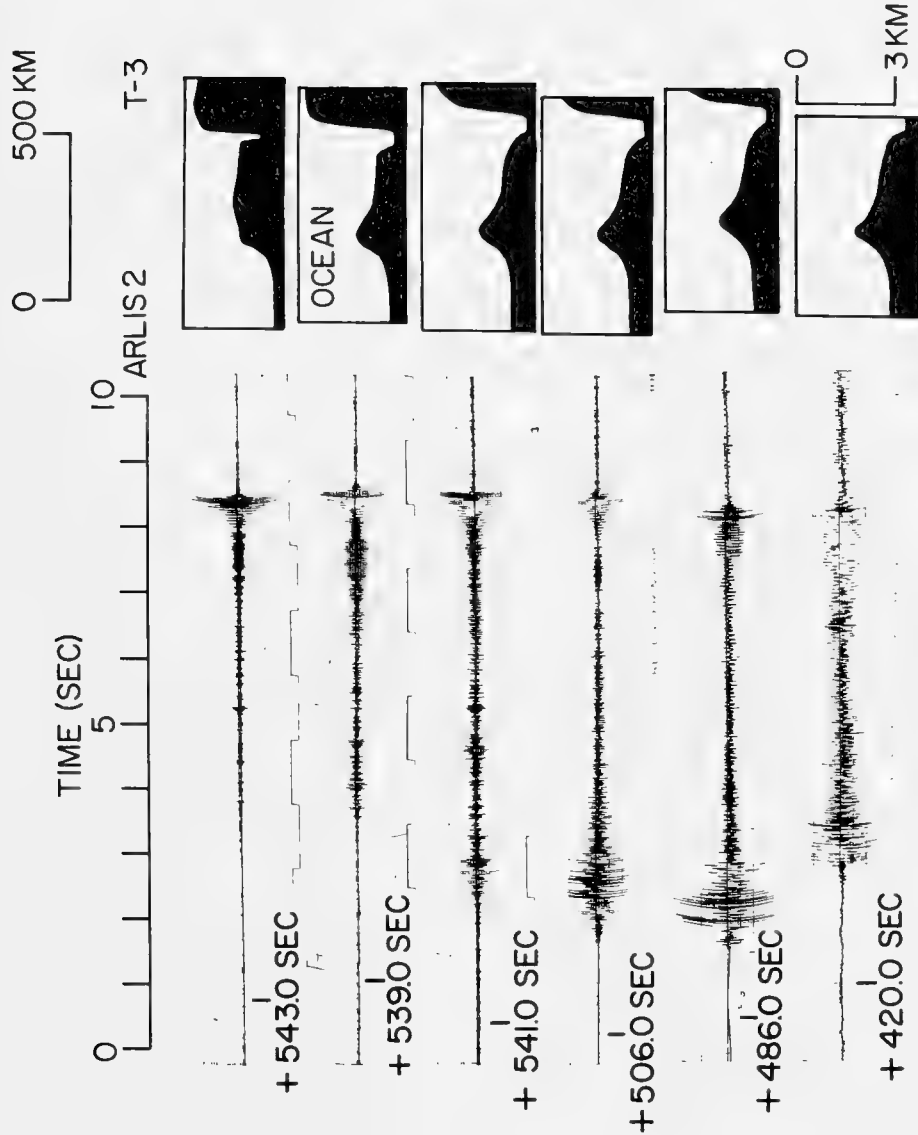


Figure 12. SIGNALS SHOWING THE EFFECT OF BATHYMETRY ON THE AMPLITUDES OF THE WAVES. SHOTS ARE 1 lb. TNT CHARGES FIRED AT A DEPTH OF 71 m. HYDROPHONE AT A DEPTH OF 46 m. PROPAGATION PATHS LIE BETWEEN PATHS 2 AND 3 OF FIGURE 4.

determined by waves which pass over all bottom topography without suffering bottom reflections.

The next four Figures, 13 to 16, will show a comparison of normal-mode theory with the field measurements.

On Figure 13 observed group-velocity dispersion is compared with dispersion computed from a multilayered model which will be described later. The agreement is excellent for the first three modes.

Figure 14 shows the close agreement between theory and experiment of the depth variation of pressure for the first normal mode at two frequencies of 20 and 40 Hz.

Figure 15 shows a computed oscillogram for the first two modes. If we compare peak intensity as a function of range for waves of the first normal mode, we get the type of agreement shown on Figure 16. In these computations the effect of wave scattering from the rough ice boundaries was taken into account using a modified formula of Mellen and Marsh (1965). An RMS ice roughness of 3 m fits the data for Profile 1, while an RMS roughness of 4 m agrees reasonably well with Profile 2. These experiments were performed in 1968 (Kutschale, 1969) and provided solid evidence that indeed there is a close correspondence between surface ice roughness and wave amplitude. We shall return to this matter shortly in connection with propagation loss.

Attention will now be turned to computational aspects of deriving estimates of propagation loss as a function of range. Wave theory will be emphasized because of the close agreement of field data previously shown with computations derived from wave theory. Furthermore, propagation loss of ice vibrations detected by vertical and horizontal component geophones is included in the wave theory and the method is useful at extremely low frequencies or in shallow water.

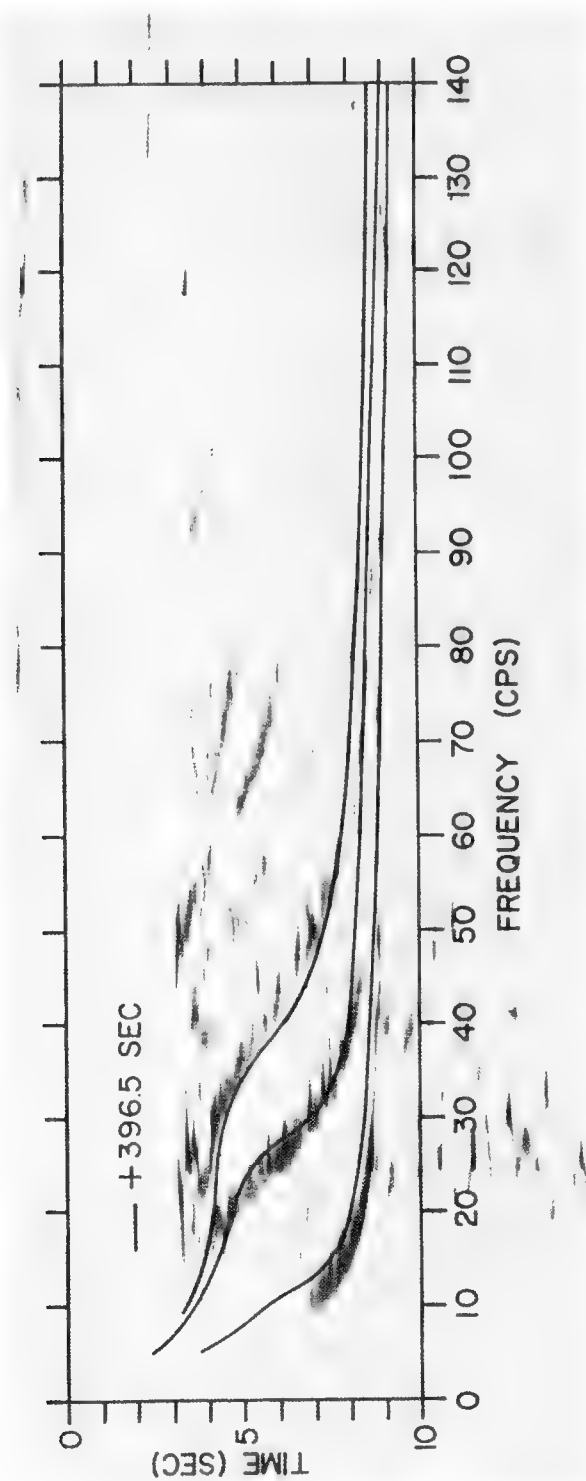


Figure 13. COMPARISON OF MEASURED AND COMPUTED GROUP VELOCITY DISPERSION

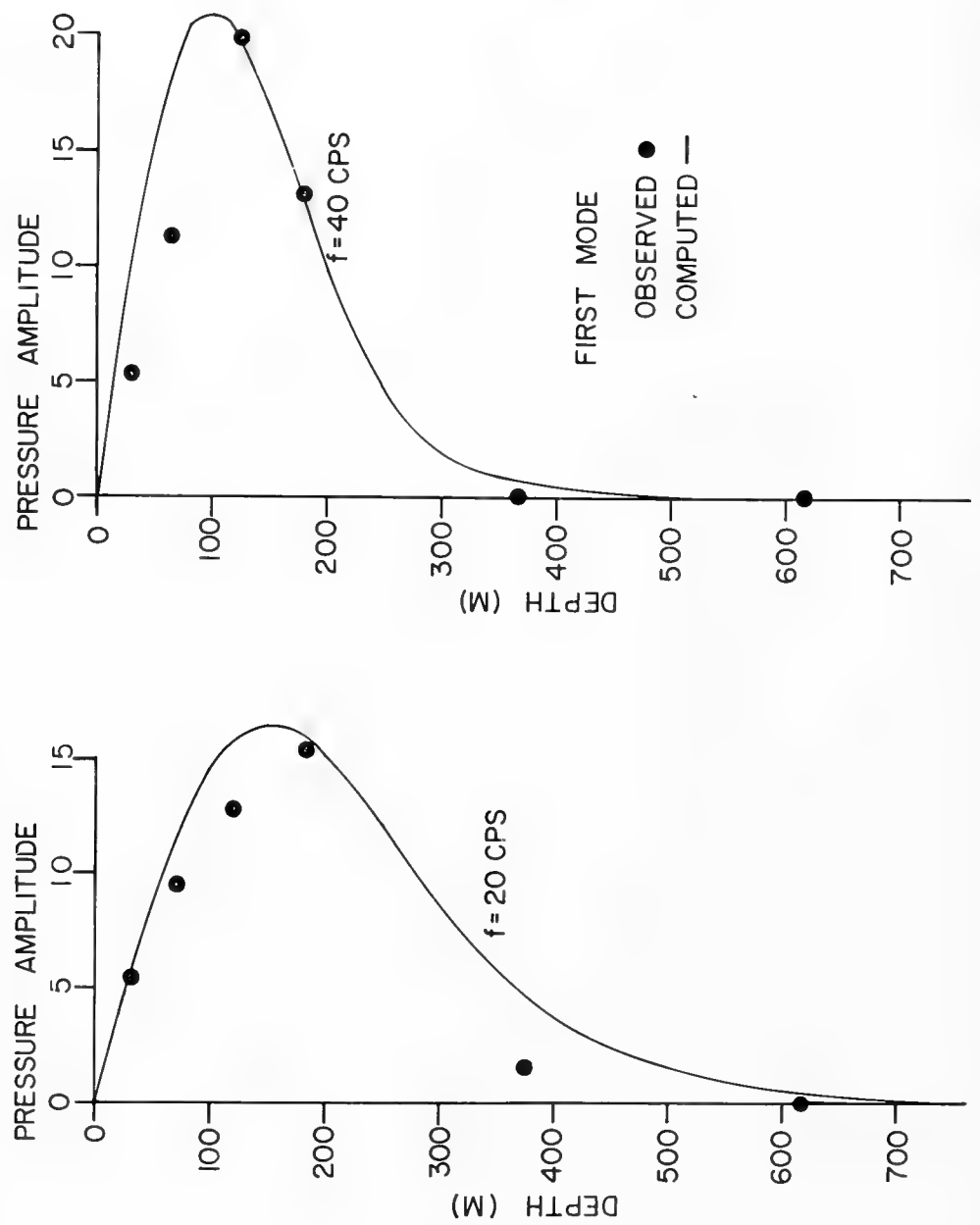


Figure 14. COMPARISON OF MEASURED AND COMPUTED VERTICAL PRESSURE DISTRIBUTIONS FOR WAVES OF THE FIRST NORMAL MODE

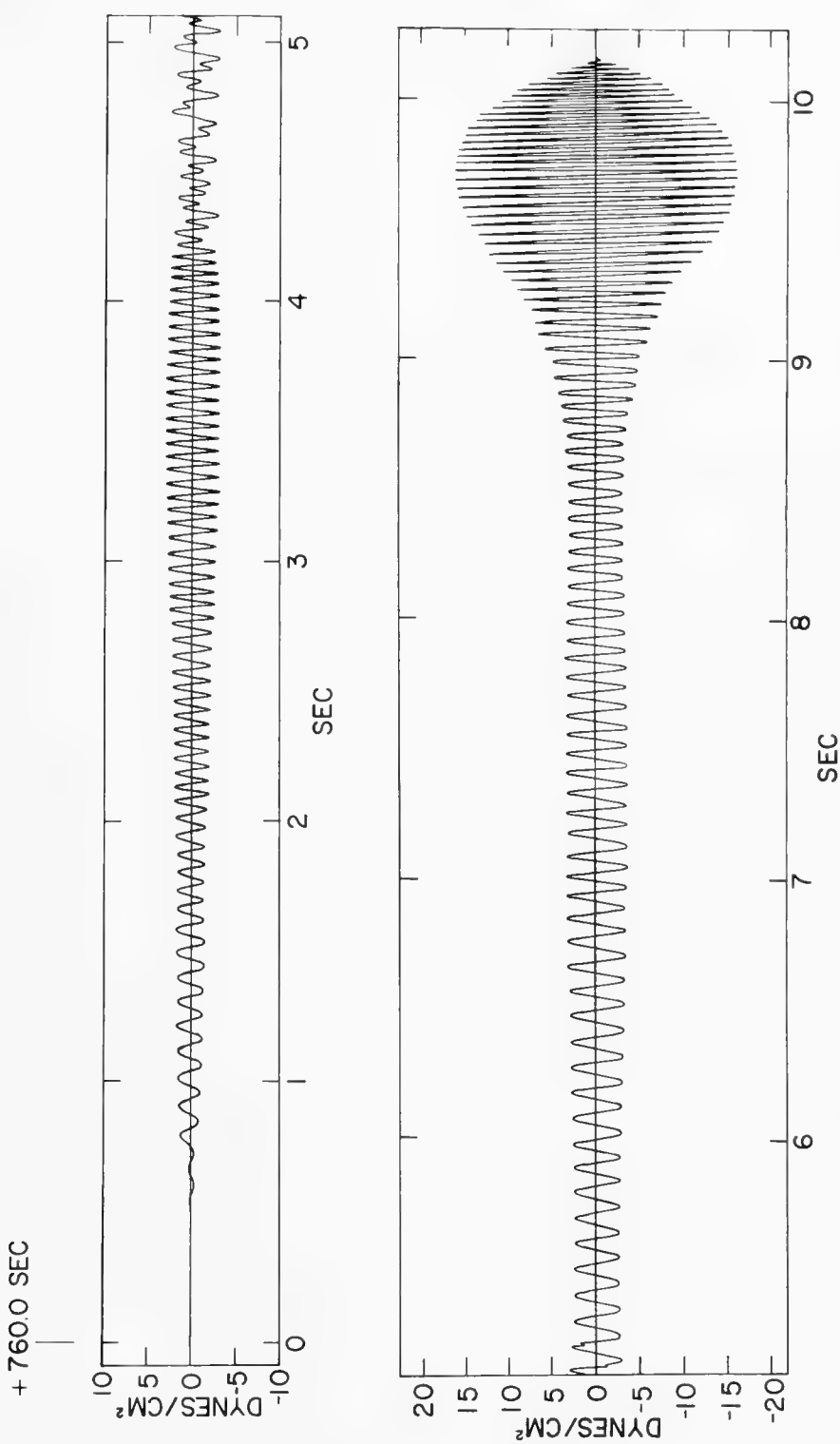


Figure 15. COMPUTED OSCILLOGRAM. FIRST TWO MODES INCLUDED. THE RMS ICE ROUGHNESS 3 m. 5 lb. TNT AT 150 m. HYDROPHONE DEPTH 50 m.
RANGE 1106 Km.

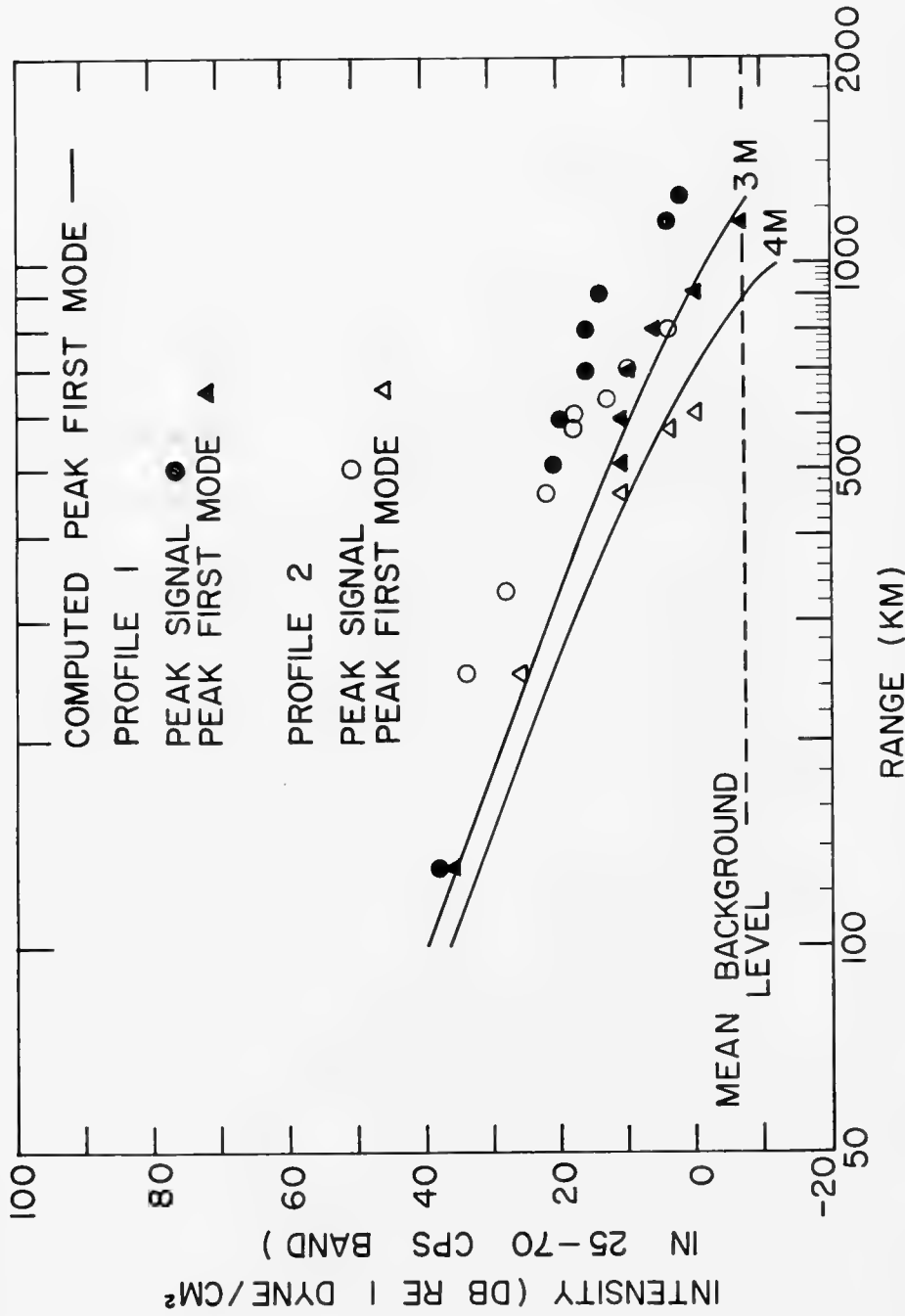


Figure 16.

PEAK SIGNAL INTENSITIES AND PEAK INTENSITIES OF WAVES CORRESPONDING TO THE FIRST NORMAL MODE AS A FUNCTION OF RANGE. RMS ICE ROUGHNESSES OF 3 m AND 4 m. SHOTS 1.8 lb. TNT AT 274 m. HYDROPHONE AT 30 m. PROFILES 1 AND 2 ARE SHOWN IN FIGURE 4.

Figure 17 shows the form of the integral solution of the wave equation derived from a harmonic point source in a multilayered, interbedded liquid-solid half space (Kutschale, 1970). Solid layers represent the ice and they may represent bottom layering. To take account of reflection loss of waves bouncing off the ice, the surface reflection coefficient is modified to yield a specific dB loss per bounce at each ice contact. For simplicity, the loss is taken as independent of the grazing angle, but an angle dependence could be included. The loss per bounce (in dB) appears to increase with frequency in a regular manner. Below about 10 Hz it appears to be essentially zero, except possibly in the areas of roughest ice. Two convenient ways to evaluate the integral solution are:

- Contour integration in the complex k -plane yielding a branch-line integral plus a sum of normal modes. The normal modes predominate at long ranges.
- Direct integration of the integral solution by the Fast Field Program (FFP) technique introduced by Marsh and DiNapoli (see, for example, DiNapoli, 1971).

In the FFP technique the integral solution of the wave equation is evaluated rapidly as a function of range by direct numerical integration employing the Fast Fourier Transform (FFT) algorithm. The prescription is shown on the bottom line of Figure 17. Singularities in the integrand corresponding to the normal-mode poles are removed from the axis of integration by including attenuation coefficients for compressional and shear waves in each layer. In a liquid layer, of course, both the shear velocity and corresponding attenuation coefficient are zero. The effects of this attenuation can be removed at the final stage of the loss computations. A convenient starting point for the FFP is the integral solution of the wave equation derived by the Thomson-Haskell matrix method (Thomson, 1950; Haskell, 1953) for propagation from point harmonic sources in a multilayered, liquid-solid half space (Kutschale, 1973).

$$\rho_h = i \int_0^{\infty} F(s, h, \omega, k) 2 J_0(kr) k dk$$

s = source depth
h = hydrophone depth
 ω = angular frequency
k = wave number

r = range

$$\rho(r_n) = \sqrt{\frac{2}{\pi r_n}} \Delta k e^{-k_0 r_n} \sum_{m=0}^{N-1} (X + iY) e^{-2\pi i m n / N}$$

Figure 17. FORM OF INTEGRAL SOLUTION FOR A MULTILAYERED MEDIUM. BOTTOM LINE SHOWS METHOD OF IMPLEMENTING INTEGRATION BY THE FAST FOURIER TRANSFORM ALGORITHM.

A comparison of the FFP computations with those computations by normal-mode theory from the corresponding integral solution are identical, but the FFP technique is far more convenient and often faster, since the computations are done directly from the integral solution without first computing the roots of the dispersion equation and then summing the normal modes.

Figure 18 shows an example of propagation loss computed by the FFP. Loss at several thousand range points is computed simultaneously giving the fine detail of the fluctuating loss with range from the 10 Hz CW source. When comparing computed loss with loss measured from explosive signals, it is necessary to average intensity with range by taking a running average in range and converting to propagation loss.

Figure 19 shows the absolute value of the integrand for the computations corresponding to Figure 18. The peaks in the integrand correspond to the normal-mode poles at phase velocities less than the speed of sound in the lower half space. For higher phase velocities, peaks correspond to "leaky modes" computed from the branch-line integral contribution (Kutschale, 1970).

Figure 20 shows a comparison between data, the FFP and ray theory. The data curves of Mellen and Marsh (1965) and Buck (1968) are based on measurements made from several hundred shots at various depths over paths in various areas. Nevertheless, the composite curves are in reasonably good agreement with computed curves by FFP and ray theory. The computations by ray theory were made by Chow (personal communication) of Aerophysics Research Corporation, Bellevue, Washington.

Figure 21 is a sample of comparison of experiment and theory for a constant shot and hydrophone depth. These data were measured in

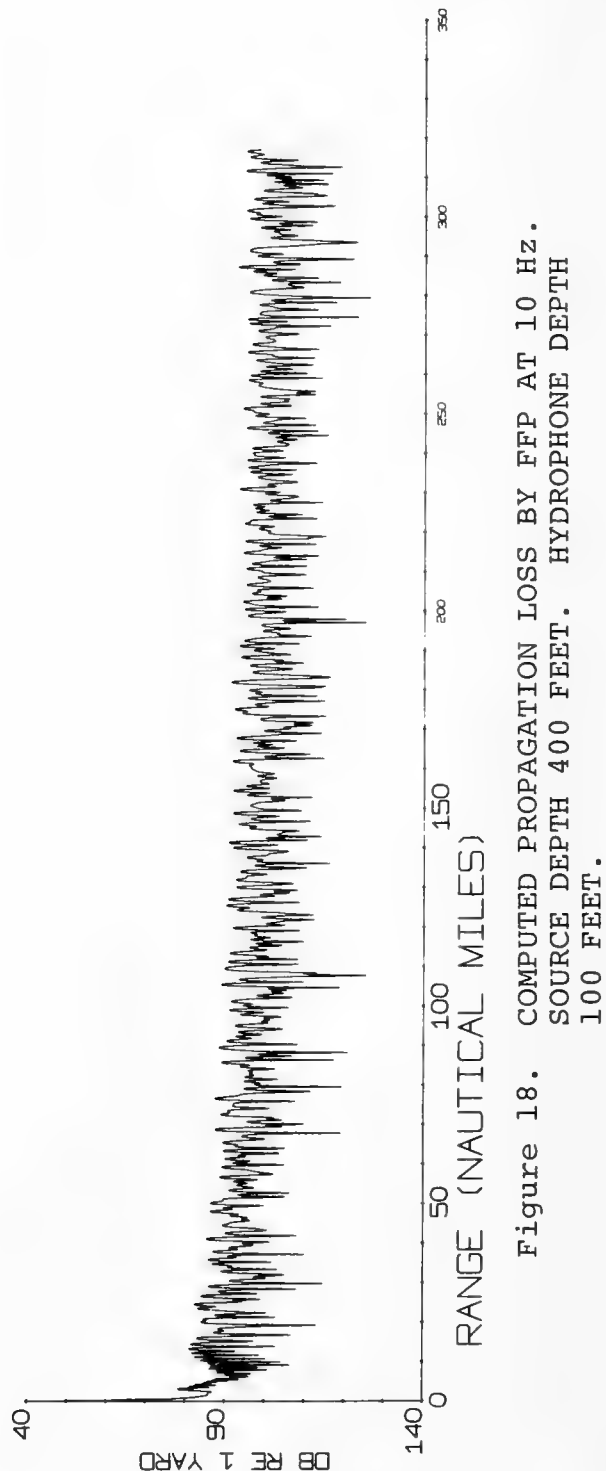


Figure 18. COMPUTED PROPAGATION LOSS BY FFP AT 10 Hz.
SOURCE DEPTH 400 FEET. HYDROPHONE DEPTH
100 FEET.

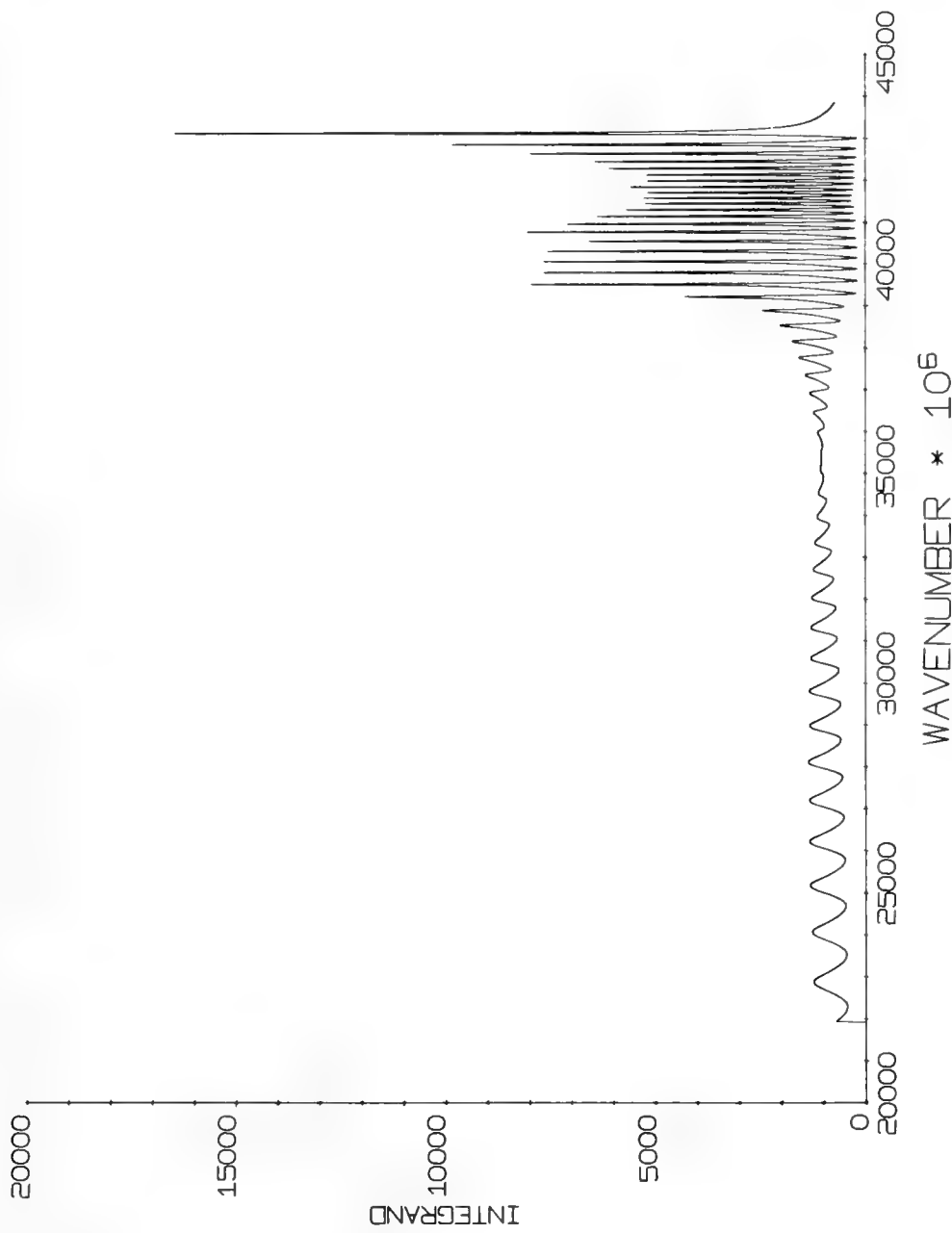


Figure 19. ABSOLUTE VALUE OF INTEGRAND CORRESPONDING TO FIGURE 18.
FIRST MODE CORRESPONDS TO PEAK AT LARGEST WAVE NUMBER.
OTHER MODES CORRESPOND TO PEAKS AT LOWER WAVE NUMBERS.

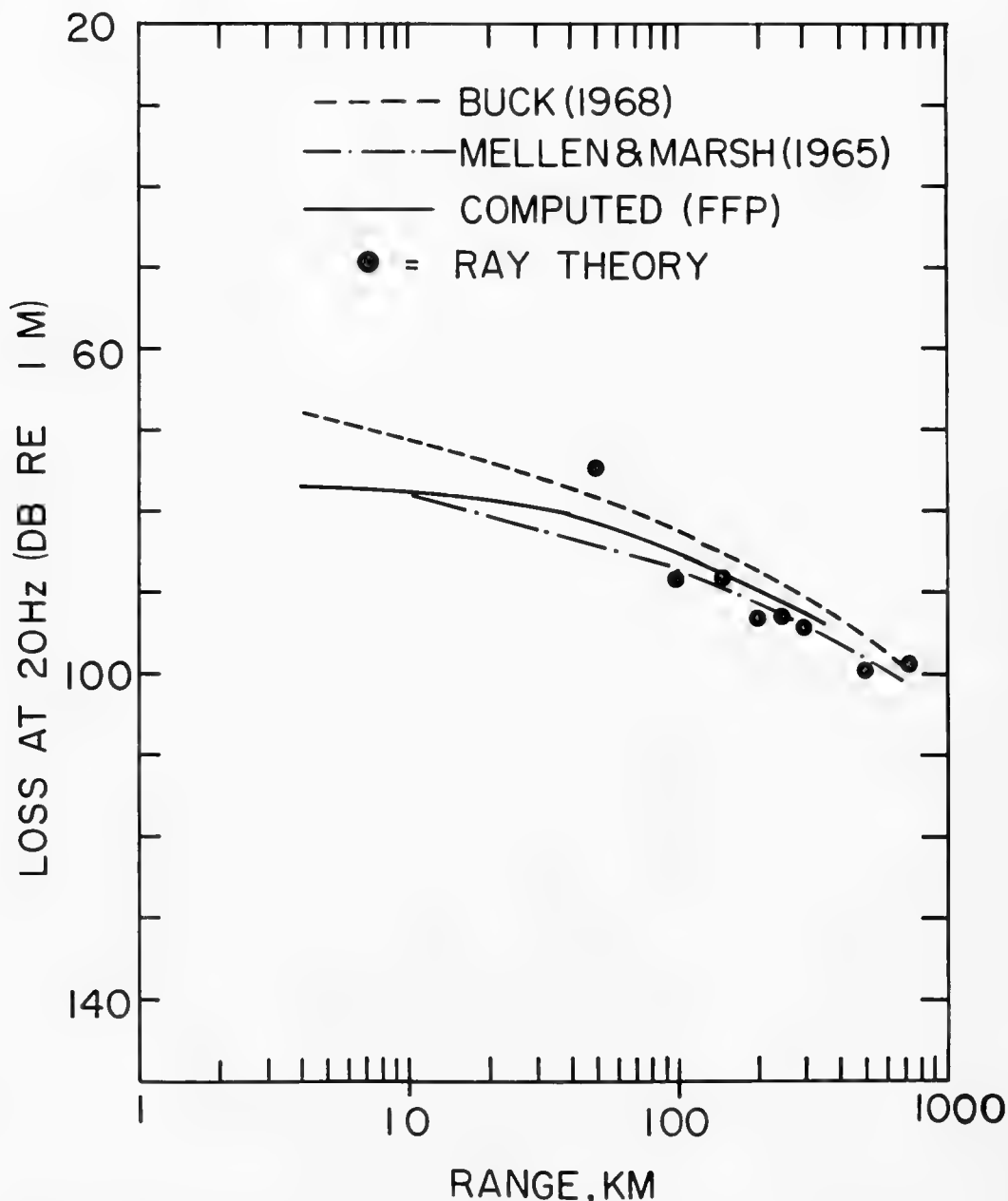


Figure 20. COMPARISON BETWEEN MEASURED AND COMPUTED PROPAGATION LOSS. THE DATA CURVES OF MELLEN AND MARSH AND BUCK ARE FROM MEASUREMENTS MADE FROM SEVERAL HUNDRED SHOTS AT VARIOUS DEPTHS OVER PATHS IN VARIOUS AREAS.

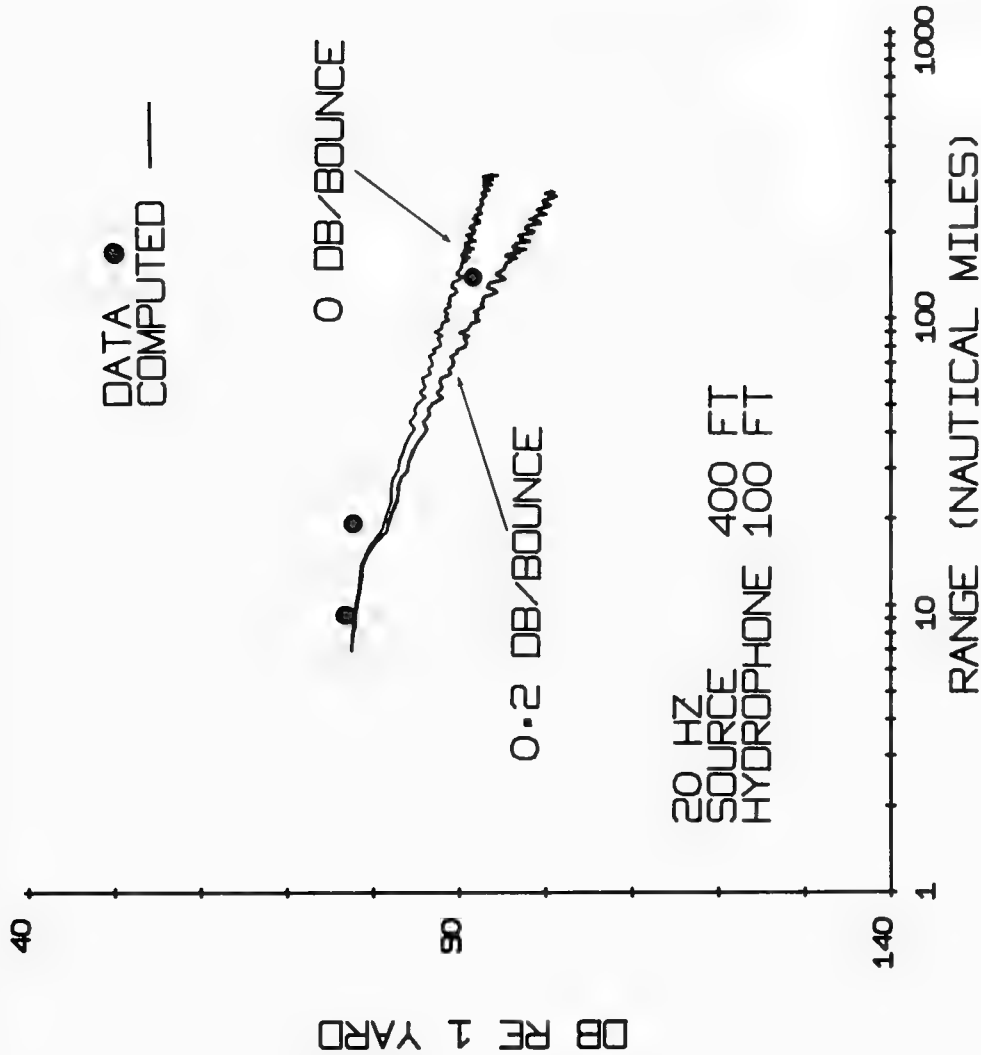


Figure 21.

DETAILED COMPARISON OF EXPERIMENT AND THEORY FOR A CONSTANT SHOT AND HYDROPHONE DEPTH. SOURCE LEVELS WERE MEASURED IN THE FIELD.

1970 with great care by Buck, Magnuson, and Chalfant (1970) between several ice stations. They are the best measurements available under carefully controlled conditions and serve as a good check on the computer modeling.

For the comparison at 20 Hz, 0 and 0.2 dB per bounce were assumed for reflection loss. Data at about 800 nautical miles fall along an extension of the loss curve for 0.2 dB per bounce. The computations will be extended to longer ranges, but 0.15 to 0.2 dB per bounce is consistent with the airborne measurements for the area. The measurements of Buck, Magnuson, and Chalfant show clearly the strong depth dependence of loss for waves below about 70 Hz. Above 100 Hz, the depth dependence is relatively weak. As an illustration, for a shot at 60 feet the loss of Figure 21 is nearly 10 dB higher than that shown for the 400-foot shot.

Attention will now be turned to the important question of predicting reliable estimates of propagation loss as a function of range for given source and detector depths in deep water of the central Arctic Ocean.

The pioneering thrust in this area was made by O. I. Diachok of the Naval Oceanographic Office. We have collaborated on extending the work from the marginal sea ice zone to the central Arctic Ocean. Later, an extensive series of experiments completed during May 1974 will be briefly described.

The basic question is whether reliable estimates of propagation loss as a function of range can be obtained from measurements of surface ice roughness and computer modeling. Experiments strongly suggest that this is the case.

The first question which may be raised is whether topside roughness is related to bottomside roughness. Experience shows that, speaking in broad terms, the ice is compensated at depth. Figure 22 shows a set of coincident topside and bottomside measurements illustrating the above point. However, it should be stated that one is not really concerned with the exact nature of the correspondence if a consistent rule is found relating topside roughness to propagation loss.

That such a rule exists is strongly suggested by data of the type shown in Figure 23 (Diachok, 1973). On this figure, dB loss per bounce appears to vary smoothly as a function of the ridge index, n , defined as the number of pressure ridges per km of path. Similar plots are obtained at other frequencies but, of course, the dB loss per bounce for a given n is strongly frequency dependent, being far smaller at 20 Hz on the figure. Typical values of dB loss per bounce for $n = 3$ are: 5 Hz, 0; 10 Hz, 0; 20 Hz, 0.15; 50 Hz, 0.7; 100 Hz, 1.3; 160 Hz, 2.5.

Another very important fact is that n appears to vary in a regular pattern geographically and seasonally. This is indicated in Figure 24. Note that the greatest ice roughnesses are north of Ellesmere Island.

Figure 24 sets the stage for describing the recent experiments conducted in cooperation with O. I. Diachok of the Naval Oceanographic Office. We were fortunate that Ice Island T-3 was located in some of the roughest ice in the central Arctic Ocean north of Ellesmere Island. By setting flight lines in various directions, we could sample considerable variations of ice roughness along propagation paths. I should mention that this was not the first airborne experiment designed to relate roughness to propagation loss over long ranges but, during the other two experiments in 1968 and 1970, a

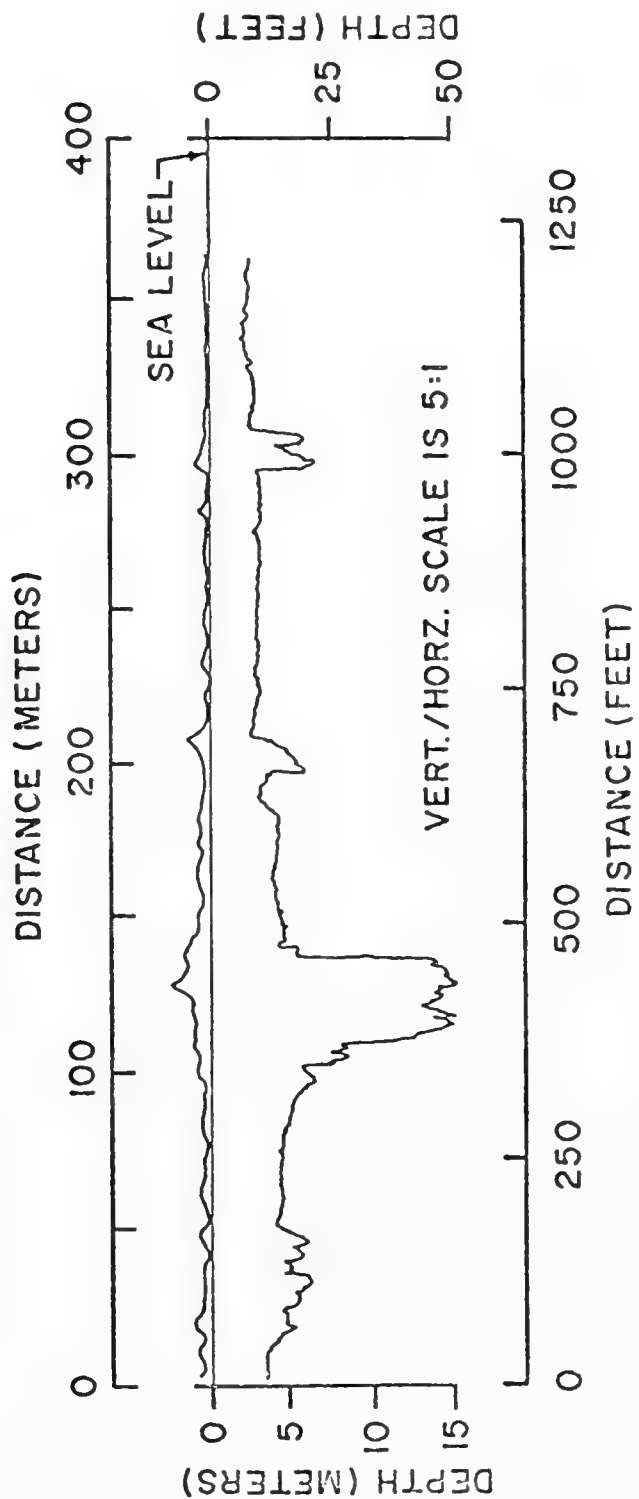


Figure 22. COINCIDENT MEASUREMENTS OF SURFACE AND BOTTOM ICE ROUGHNESS
(AFTER DIACHOK, 1973)

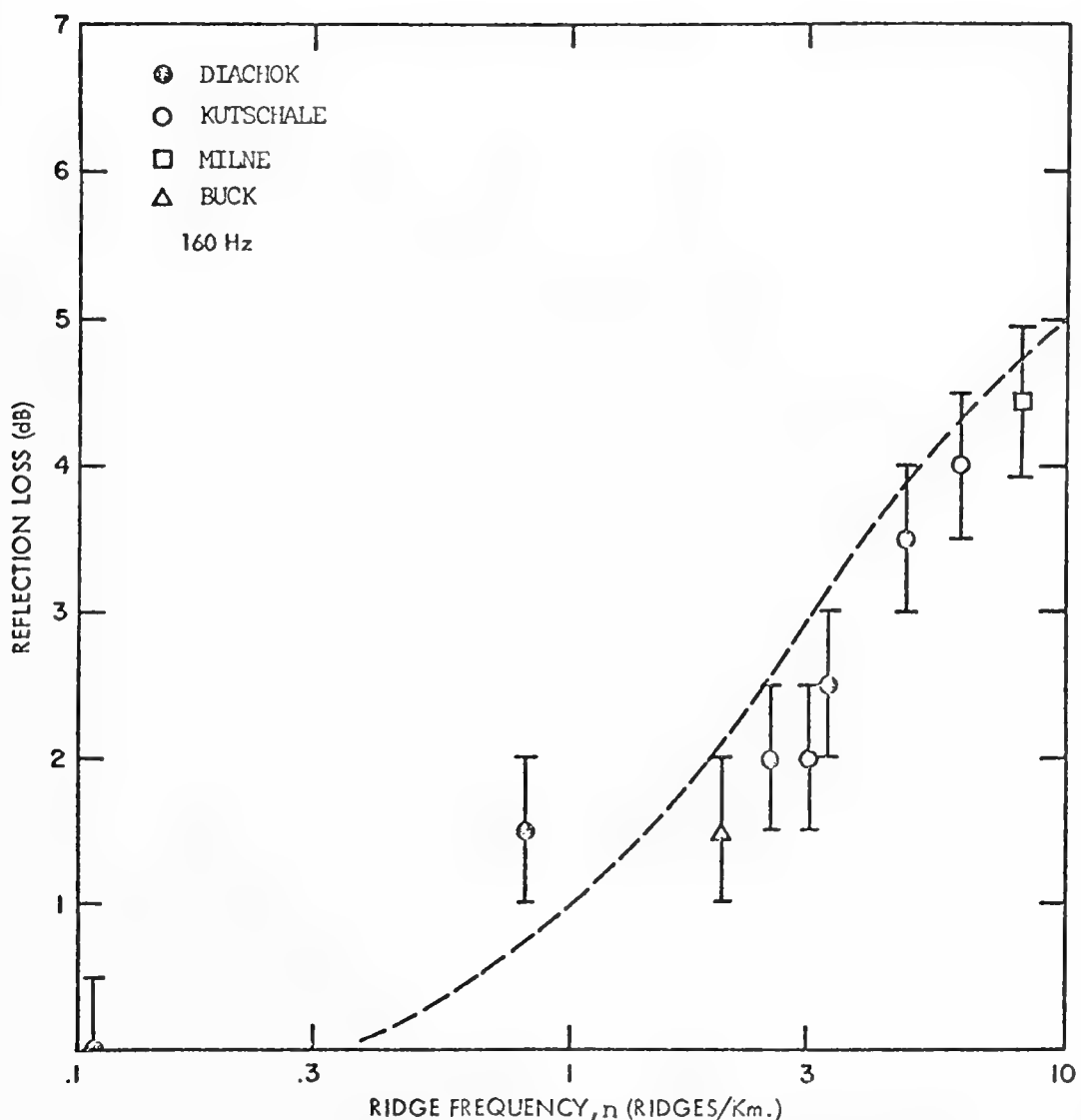


Figure 23. EXPERIMENTAL ESTIMATES AND COMPUTED PREDICTIONS (---) OF REFLECTION LOSS PER BOUNCE AT 160 Hz AS A FUNCTION OF RIDGE FREQUENCY (AFTER DIACHOK, 1973).

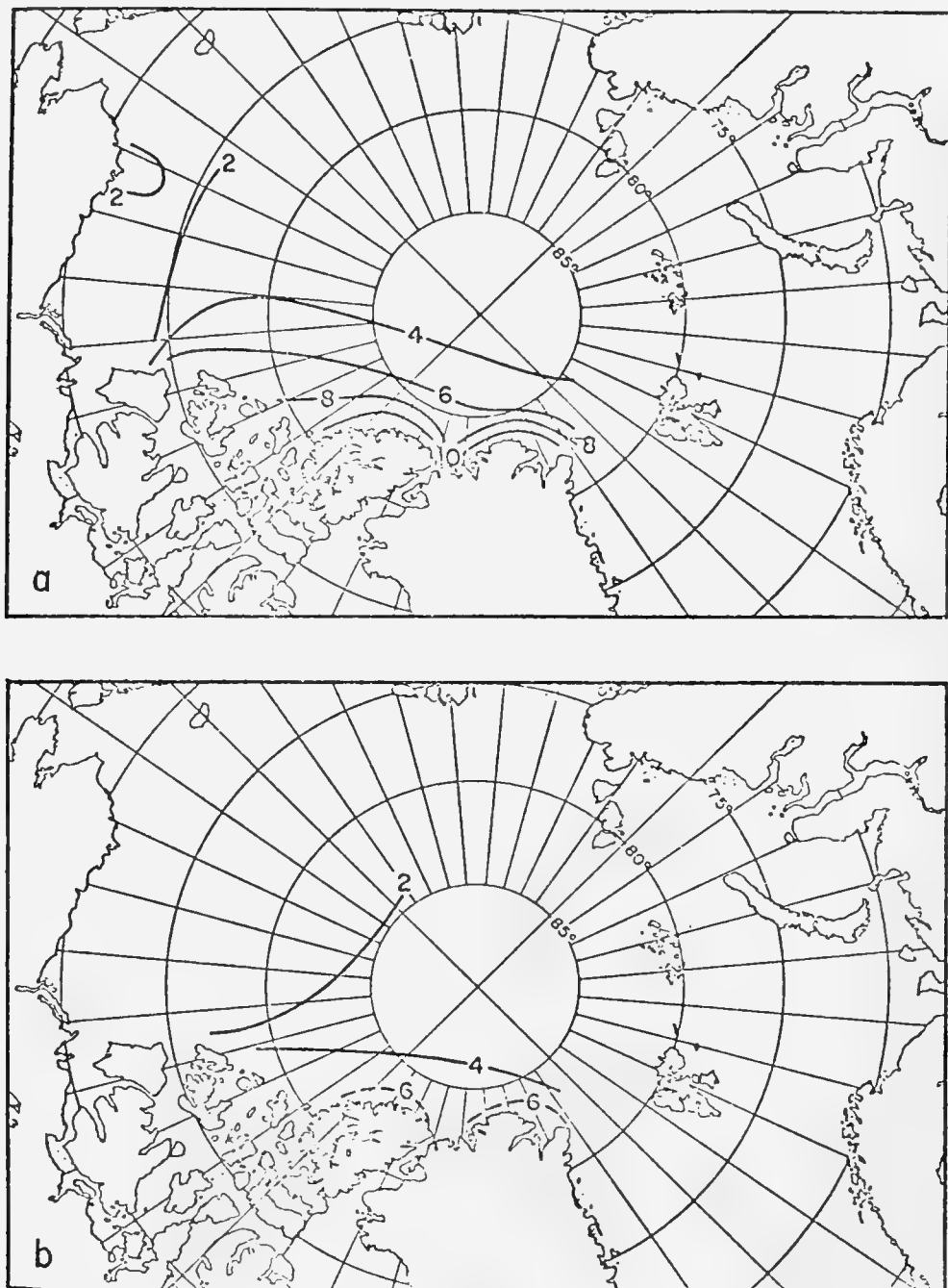


Figure 24. GEOGRAPHICAL VARIATION OF RIDGE INDEX, n , DURING
(a) WINTER AND (b) SUMMER (AFTER DIACHOK, 1973).

laser profiling system was not available aboard the Navy aircraft, and we had to rely on visual observation. In the recent experiments we had the benefit of previous experience and new devices such as inertial navigation, ice-penetrating SUS, a laser profiling system and specially modified sonobuoys. We employed two Navy P-3 aircraft and made four runs radiating from T-3. These two aircraft subsequently worked together north of Banks Island in the smooth ice area and completed three more runs using sonobuoys as listening devices. Coincident measurements were thus obtained of propagation loss and surface roughness in areas showing the greatest known contrast of roughness. I would like to point out that it is not easy to hit a small lead with a SUS charge dropped by air, but the Navy personnel did a supreme job in this respect to give us a generally high density of shots with range.

A few words are in order about how the dB loss per bounce is derived from the field data. This is done by comparing the measured propagation loss with computed curves for various loss per bounce until the measured and computed curves coincide. This, of course, puts a severe requirement on the reliability of the computer model. Experience has shown that the FFP is most useful at frequencies below 100 Hz where wave effects are significant, but both ray theory and the FFP are reliable above 100 Hz up to 315 Hz, the upper limit of measurement. Figure 25 illustrates this for an identical model of surface loss. The curves by ray theory were computed by M. S. Weinstein of Underwater Systems, Inc., Silver spring, Maryland.

For predictive purposes the process is reversed. One obtains an estimate of loss per bounce from airborne measurements of surface roughness to enter in the computer program.

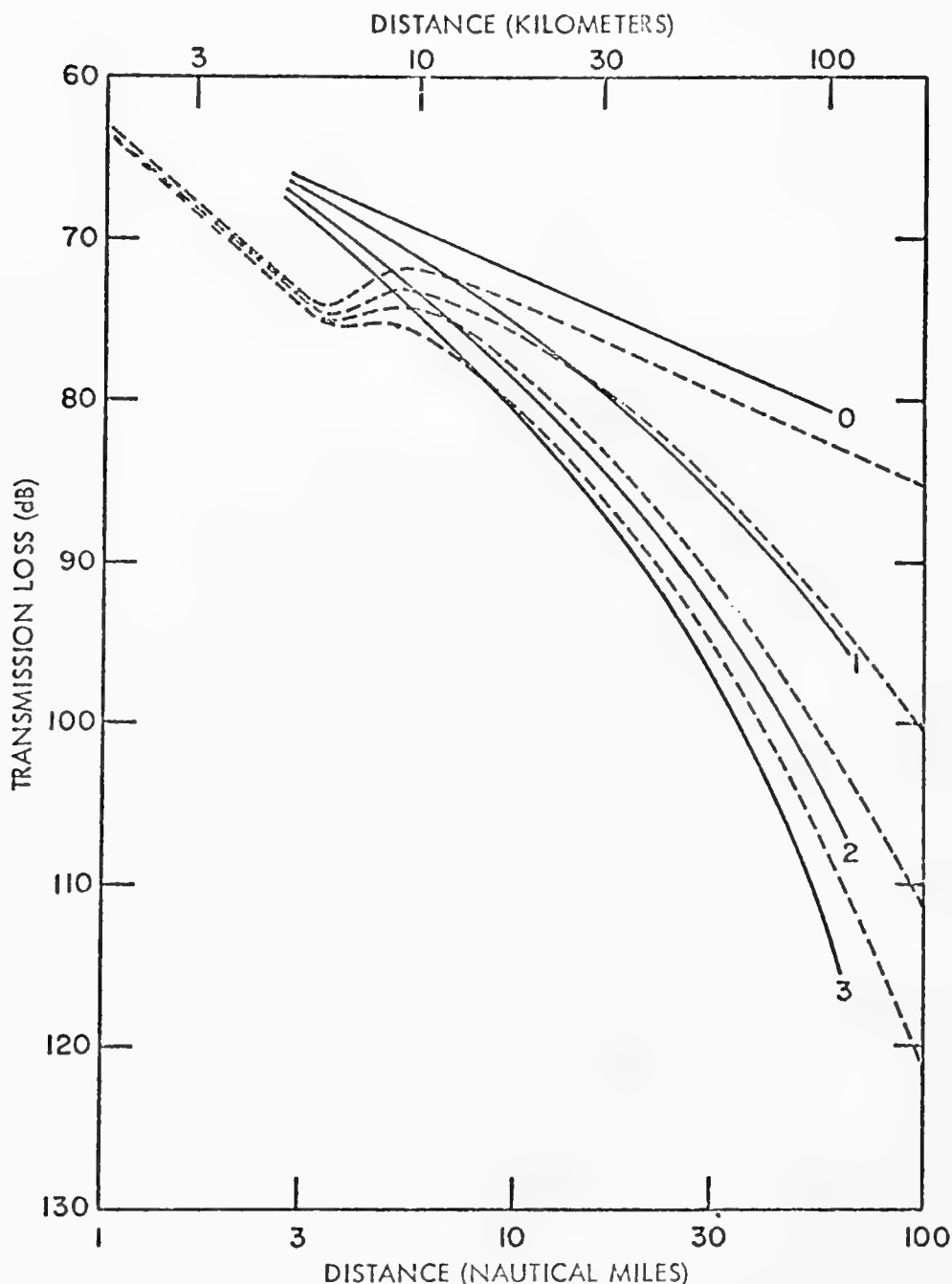


FIGURE 25. COMPARISON OF WAVE-THEORETICAL COMPUTATIONS BY KUTSCHALE (—) AND RAY-THEORETICAL COMPUTATIONS BY WEINSTEIN (---) OF ARCTIC PROPAGATION LOSS AT 160 Hz FOR SURFACE LOSSES OF 0, 1, 2, and 3 dB PER BOUNCE (AFTER DTACHOK, 1973).

I should mention a few additional aspects of the effects of the ice layer on propagation. For an ice layer 3 m thick, the effect on pressure amplitudes at depth and on dispersion is small. But this thin ice sheet causes a large change in particle motions near the surface. Waves are elliptically polarized in the ice in the plane of propagation. Particle motion is retrograde elliptical at the surface and prograde elliptical at the bottom of the ice. This orbital motion is similar to that of flexural waves in the ice. Flexural waves generated by large-scale ice deformation at the boundaries of floes are the principal source of ambient ice vibrations.

Figure 26 shows the ratio of horizontal to vertical particle motion at the surface for flexural waves and hydroacoustic waves. The ice is an antinode for vertical particle velocity and thus geophones are useful devices to detect low-frequency waves.

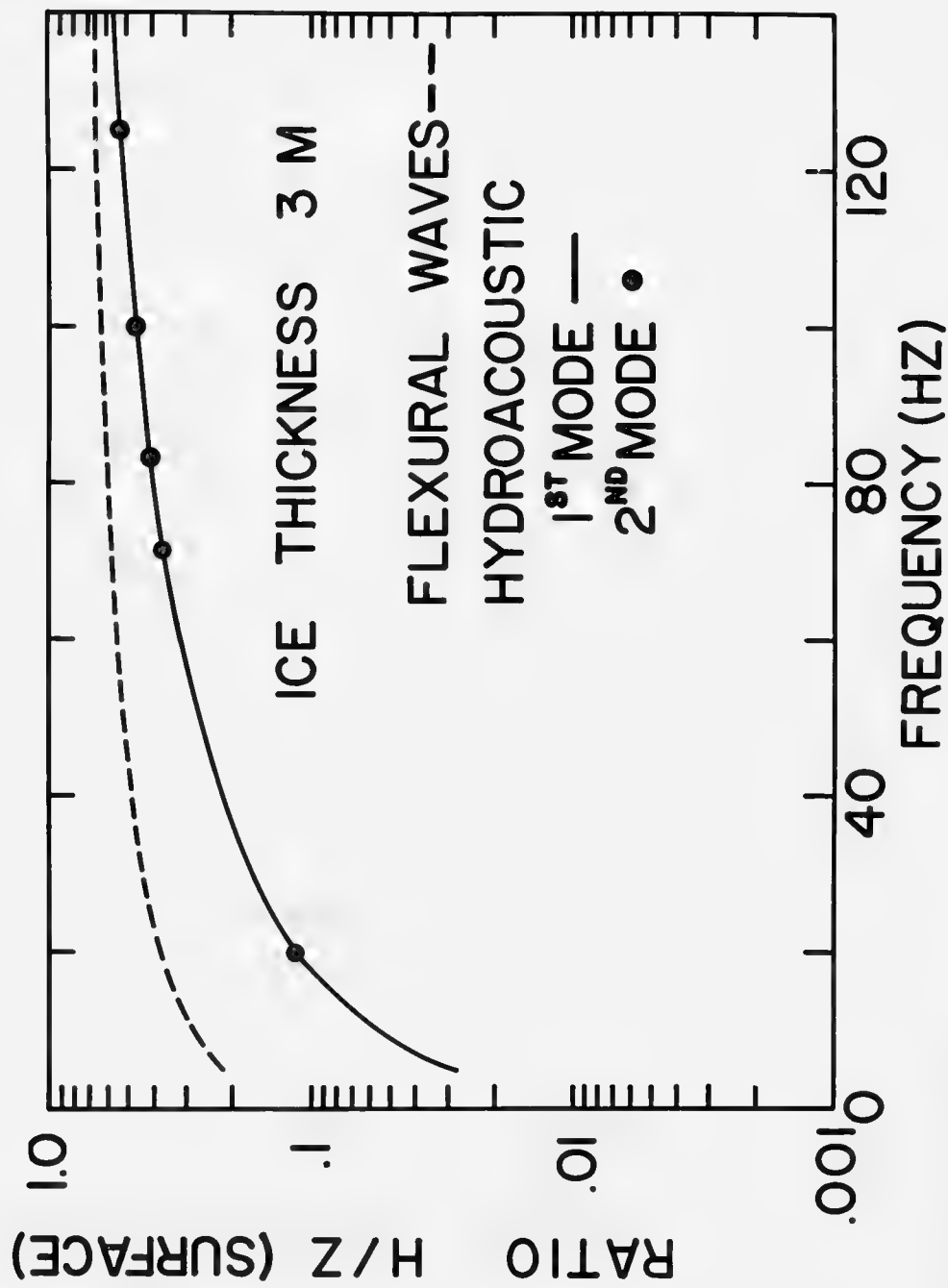


Figure 26. RATIO OF HORIZONTAL (H) TO VERTICAL (Z) PARTICLE MOTION AT ICE SURFACE FOR HYDROACOUSTIC WAVES AND FLEXURAL WAVES

REFERENCES

Alberta Society of Petroleum Geologists, *Geological Map of the Arctic*, Toronto: University of Toronto Press, 1960.

Buck, B. M., Arctic acoustic transmission loss and ambient noise. In: J. E. Sater (ed.), *Arctic Drifting Stations*, Montreal: The Arctic Institute of North America, pp. 427-38, 1968.

Buck, B. M., A. W. Magnuson, D. A. Chalfant, "Underwater Acoustics Experiments at Three Manned Stations in the Central Arctic — Spring 1970 (U)," AC Electronics, Defense Research Lab., G. M. Corp. TR 70-101, December 1970. CONFIDENTIAL

Diachok, O. I., Preliminary empirical model of low frequency under-ice reflection loss, NAVOCEANO Technical Note No. 6130-3-73, 1973.

DiNapoli, F. R., "Fast Field Program for Multilayered Media," Naval Underwater Systems Center Report No. 4103, 1971.

Haskell, N. A., The dispersion of surface waves on multilayered media, *Bulletin of the Seismological Society of America*, 43: 17-34, 1953.

Hecht, R. J., "Sound Propagation Experiments Conducted Under the Polar Ice Pack During the Summer of 1958," USN/USL Report No. 465, February 1960. CONFIDENTIAL

Hecht, R. J., "Arctic Ocean Propagation Measurements," USN/USL Tech. Memo 911-010-61, July 1961. CONFIDENTIAL

Kutschale, H.W., Long-range sound transmission in the Arctic Ocean, *Journal of Geophysical Research*, 66:2189-98, 1961.

Kutschale, H.W., Arctic hydroacoustics, *ARCTIC*, 22:246-264, 1969.

Kutschale, H. W., "The Integral Solution of the Sound Field in a Multilayered Liquid-Solid Half Space with Numerical Computations for Low-Frequency Propagation in the Arctic Ocean," Lamont-Doherty Geol. Obs. of Columbia University, Tech. Rept. No. 1, 1970.

Kutschale, H. W., "Rapid Computation by Wave Theory of Propagation Loss in the Arctic Ocean," Lamont-Doherty Geological Observatory of Columbia University Tech. Rept. No. 8, 1973.

KUTSCHALE: LOW-FREQUENCY PROPAGATION IN THE ICE-COVERED ARCTIC OCEAN

Kutschale, H.W., "The Period Equation by Ray Theory for Propagation in the SOFAR Channel," unpublished report, Office of Naval Research, Code 468, January 1971.

Marsh, H. W., and R. H. Mellen, Underwater sound propagation in the Arctic Ocean, *Journal of the Acoustical Society of America*, 35: 552-63, 1963.

Mellen, R. H., and H. W. Marsh, *Underwater sound in the Arctic Ocean*, New London, Connecticut: U. S. Navy Underwater Sound Laboratory, Report MED-65-1002, 1965.

Pekeris, C. L., Theory of propagation of explosive sound in shallow water. In: *Propagation of sound in the ocean*, Geological Society of America Memoir, 27:1-117, 1948.

Thomson, W. T., Transmission of elastic waves through a stratified solid medium, *Journal of Applied Physics*, 21:89-93, 1950.

Worzel, J. L., and M. Ewing, Explosion sounds in shallow water. In: *Propagation of sound in the Ocean*, Geological Society of America Memoir, 27:1-53, 1948.

ARCTIC ENVIRONMENTAL LF ACOUSTICS
MEASUREMENTS, MODELS AND PLANS

Beaumont M. Buck

Polar Research Laboratory, Inc.

Measurement of low frequency (LF) propagation and noise have been made at two types of manned ice camps in the Arctic over the past decade. Floe ice stations are the best acoustic platforms but are short-lived (2 to 3 months in the spring). Ice islands provide long-term facilities, but man-made noise levels are high and the large, thick "islands" have their own environmental acoustic character that is not necessarily representative of Arctic pack ice. The under-ice acoustic environment varies considerably with both geographic location and time and, since logistics costs of manned experiments are high, only a limited sampling has been possible to date. This paper highlights the current state of deep Arctic LF acoustics empirical data, presents a simple propagation model and describes an extensive ambient noise experiment in preparation for 1975-77 that utilizes the latest in unmanned remote stations.

Arctic "deep" water is conveniently defined by the nature of the propagation under conditions of the stable velocity profile that obtains in the 1.5 million square miles deeper than about 500 meters. Underwater explosives have been used almost exclusively for transmission experiments. However, tame submarine targets have been periodically available in the Arctic to test detection feasibility of the largest circular array installed in any ocean. The ice itself affords a unique opportunity for such installations and, together with the extremely low ambient noise conditions that prevail at times, an excellent testing ground for underwater explosives as acoustic sources.

Deep Arctic ray theory is now well comprehended and, with measurement data, enables an understanding of many practical aspects of propagation important to low-frequency sonar, for example, optimum hydrophone and target depths for maximizing or minimizing signal-to-noise ratios. Almost all sound energy from long ranges arrives in the depression angle sector of 5 to 17 degrees below the horizontal. At ranges of over 100 nautical miles, the propagation is as

BUCK: ARCTIC ENVIRONMENTAL LF ACOUSTICS MEASUREMENTS,
MODELS AND PLANS

good or better than in open ocean areas, but only in the very low frequency spectrum; above about 100 Hz, it is considerably worse. Transmission loss can be closely approximated with a simple low-pass filter model that has been derived empirically.

Deep Arctic ambient noise is dominated by ice dynamics and can vary in level from close to Wenz's "lower limit" to that of the open ocean under near-hurricane conditions. Local wind force correlates highly with ambient levels, as does ice speed. Long-term median levels are highly dependent on geographic location with the quietest location in the ocean being the center of the Pacific Gyre. Under high noise conditions the noise is highly anisotropic. High correlation between noise-level time series at stations separated 150 miles has been observed. There is evidence that low-frequency noise is vertically directional and the predominant energy is close to or slightly below the dominant long-distance signal ray arrivals. Therefore, the usefulness of a vertical array is doubtful. Signal-to-noisewise, a horizontal seismometer frozen into the ice is comparable to a 100-foot deep hydrophone and slightly better at the lowest frequencies.

Preparations are under way for a large-scale central Arctic ambient noise experiment in conjunction with Project AIDJEX. Up to 24 unmanned stations collecting noise level and weather data at the synoptic times every 3 hours for up to 2 years is planned. Satellite and HF telemetry will be used in this experiment which will be the most extensive and complete low-frequency ambient noise experiment ever conducted in any ocean area.

The stable sound velocity profile of the ice-covered Arctic is characterized by a steep positive gradient to around 500 meters followed by a more gentle positive gradient to the bottom. This causes a concentration of shallow RSR rays that travel in the upper 500 meters and suffer a relatively large number of reflections per unit distance and a group of more widely spaced, deep rays that reflect less often (see Figure 1). The bottom of Figure 1 is the signature of a shot from 780 nautical miles showing the distinct

BUCK: ARCTIC ENVIRONMENTAL LF ACOUSTICS MEASUREMENTS,
MODELS AND PLANS

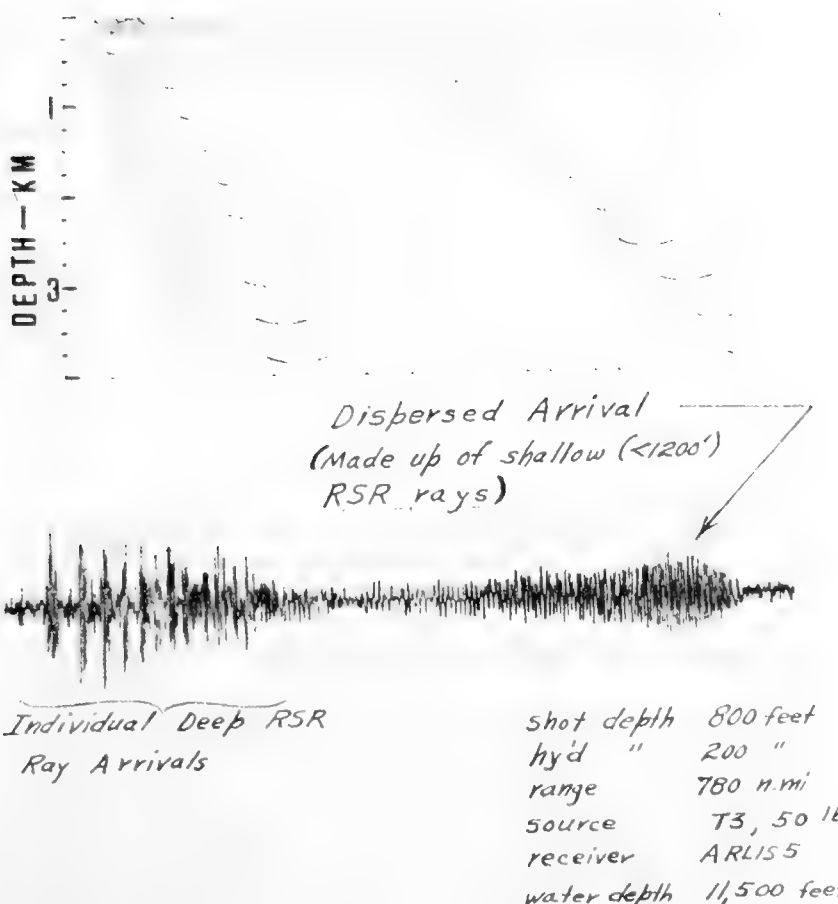


Figure 1. SCHEMATIC RAY TRACE AND SHOT SIGNATURE

deep ray arrivals and, to the right, the later-arriving shallow rays which are geometrically dispersed. This ability to distinguish the two groups of rays for separate energy analyses enables some interesting propagation studies that will be explained later. As a generalization, very low-frequency energy is split about equally between the two groups, which leads to a convenient definition of "Arctic Deep Water."

Figure 2 defines the geographic area to be covered in this paper. The 500-meter basin is almost completely ice-covered all year except for the ice limit shown in the neck of the Greenland Sea. Therefore, "Arctic Deep Water" is deeper than 500 meters and is ice covered.

A few more definitions are useful: "Central Arctic Shallow Water" is that area shown here that is shallower than 500 meters. "Marginal Ice Zones" are those areas where the ice pack edge, which can be quite diffuse, meets open water. This can be deep, as in the Atlantic side, or shallow, as in the rest. The "Canadian Archipelago Arctic" is generally locked-in, shore-fast ice. All of these areas are considerably different acoustically. This paper concerns only "Arctic Deep Water," although by omission it does not imply any less interest or activity in those other areas.

The remainder of this paper consists of some general observations on Arctic deep water acoustics, specific propagation results, ambient noise data, signal-to-noise analyses, and, finally, a brief description of future work.

Some think of the Arctic as a quiet ocean — it is, and it isn't. It is reputed to have low transmission loss — it does and it doesn't. Figure 3 is a sample comparison of Arctic and open

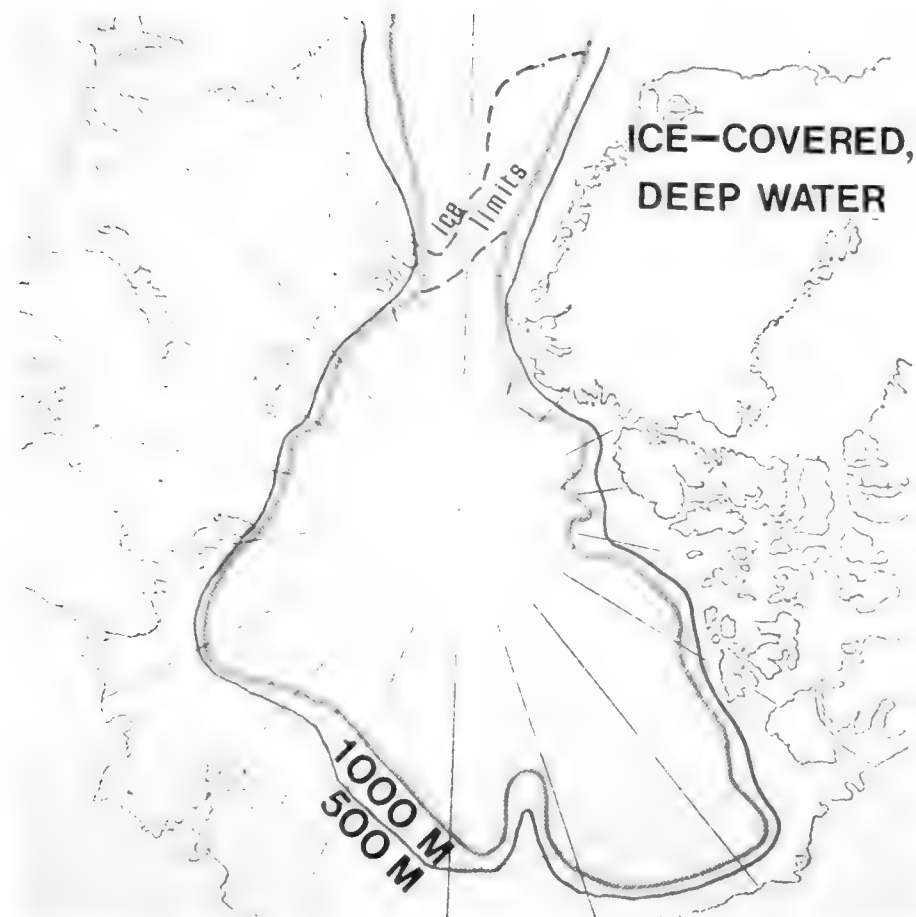


Figure 2. GEOGRAPHICAL AREA OF CONSIDERATION

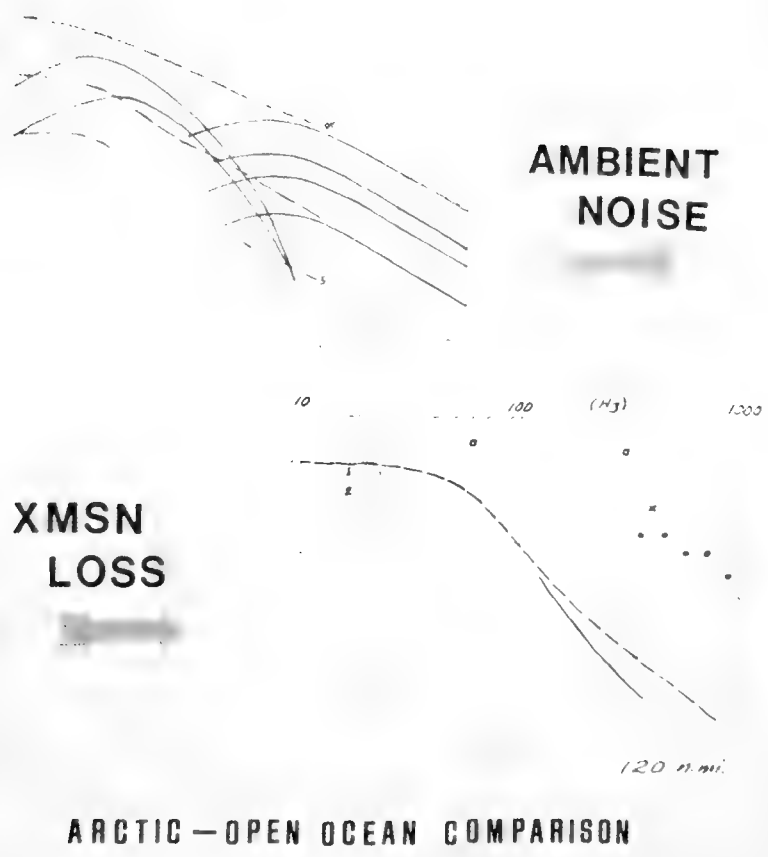


Figure 3. COMPARISON OF ARCTIC AND OPEN OCEAN AMBIENT NOISE AND TRANSMISSION LOSS

BUCK: ARCTIC ENVIRONMENTAL LF ACOUSTICS MEASUREMENTS,
MODELS AND PLANS

ocean noise and propagation. Shown on the top figure are the familiar Wenz curves for deep water. Superimposed are the 5, 50, and 95 percentiles of hourly measurements taken over a 2-month period in the spring from a floe station 150 miles north of Barrow, Alaska, on the southwest edge of the Pacific Gyre. Note that 5 percent of the time the noise is only 10 dB above Wenz's "lower limit," but another 5 percent of the time it is considerably higher than the open ocean "usual deep water traffic" below 200 Hz and higher than a wind-force-5 surface wave noise above 200 Hz.

The bottom figure compares selected samples of open ocean transmission loss data with Arctic deep water at 120 nautical miles. Only below about 60 Hz is the loss in the Arctic comparable at this range. At 400 Hz it is some 40 dB greater than Artemis data and 50 dB greater than for the wintertime Mediterranean.

The comparisons in Figure 3 are representative, only, since the Arctic has been found to be highly variable, not only diurnally and seasonally, but also geographically. For example, measurements have indicated ambient noise levels (see Figure 4) at or near the center of the Pacific Gyre (position "A") are 8 to 10 dB lower than Gyre edge (positions 5 and 6), and long-term measurements show that an ice island, such as T3, is also much quieter.

As one might expect for the RSR conditions of the Arctic, long-range, low-frequency transmission loss is determined by bottomside ice roughness, bottom depth and source and receiver depths. Low frequency ambient noise in the central Arctic is almost totally caused by ice dynamics — pressure ridging, cracking and grinding of the moving ice.



Figure 4. EXPERIMENTAL LOCATIONS

Because of the lack of a good logistics support capability, controlled experimental data have been difficult to come by. The U.S. has lacked a good remote telemetry station capability such as the Russians have in their DARMS (Drifting Automatic Remote Meteorological Stations), and almost all of the acoustic data have been taken from noisy, expensive, manned ice camps. In 1970, however, we had the first opportunity for operating two floe stations exclusively for underwater acoustics measurements, shown in Figure 4 as 5 and 6 (for Arctic Research Lab Ice Station ARLIS-5 and ARLIS-6), simultaneously with an ice island (T3). At these stations we had hydrophones at 30, 100, and 200 feet for sampling the propagation and the ambient noise. We expended over 2 tons of explosives in charges ranging from blasting caps to over 100 pounds each, while the stations drifted with the pack, allowing different path bottom topography. There were no man-made noise sources or 60-cycle generators within 100 miles of the floe stations during the measurements. The experiment lasted for over 2 months during the spring of 1970. While other acoustics measurements had been made at various floe stations before 1970, none had been so extensive or under such controlled conditions. Most of the data shown in the next figures were taken during this experiment. Almost all of the remaining acoustics measurements made in the Central Arctic have been made from ice island stations. Ice islands are very large (T3 is 7 x 4 miles, 100 feet thick, and a 3 billion ton solid chunk of ice) broken-off pieces of glacial ice from Ellesmere and have their own acoustic properties, not necessarily characteristic of pack ice. They are extremely rare but sought out as scientific platforms because of the permanence and, therefore, logistic economy they afford.

Almost all propagation work in the Arctic has been done with underwater explosives and few CW projectors have been employed.

Therefore, we are naturally interested in the character of explosives, and especially in their source energy. The Arctic affords in two ways an excellent testing ground for shot source energy. First, it is a highly stable platform from which shots, projectors, and hydrophones can be easily and precisely positioned and, second, at selected times the noise is extremely low. In 1970 we conducted the following experiment to test Weston's predictions of source energy. A low-frequency projector was suspended below the ice and CW signals received on hydrophones at distances of 1.2 and 2.3 nautical miles away to "calibrate" the path. Then the projector was raised and an explosive lowered to the same depth through an ice hole. The CW transmission loss was added to the shot signal energy flux density to attain energy source levels. Forty shots, ranging from 0.0012 to 126 pounds TNT equivalent (measured from the bubble pulse frequency) were detonated and measured with the results shown in Figure 5. Weston's predictions of source energy were subtracted from the measured values at 11 analysis frequencies. Here all the shots were averaged at each frequency but there was no observed dependence on yield. The variation was due more to CW signal fluctuations than differences between shots.

Somewhat typical in acoustic experiments is another measurement opportunity which comes along to cloud rather than clear the issue. This was an experiment in shallow, ice-covered water in the Bering Sea in 1973. Over a particular propagation path at a range of 15 nautical miles, with a sloping bottom, we noted the repeated signature from a MK61 (1.8 pounds TNT) at 60 feet (see top left of Figure 6). This is the first time we had ever seen such a signature at a reasonably long range, one where the multipaths were so limited that the shock energy almost completely died out before the arrival of the first bubble pulse which, in turn, died out before the second

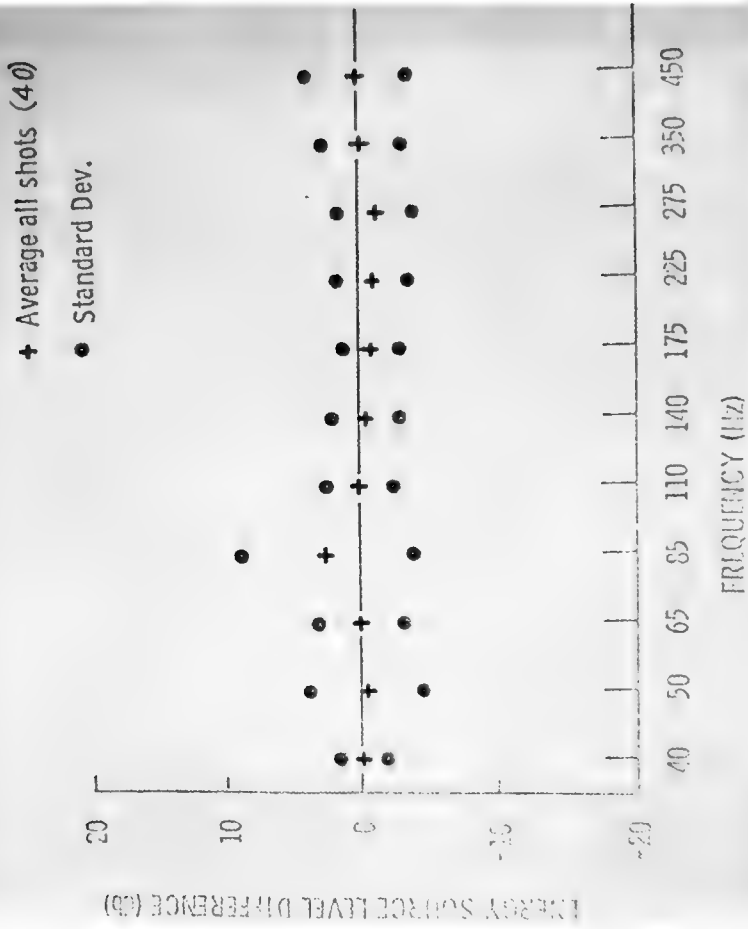


Figure 5. MEASURED MINUS WESTON'S SUM ENERGY SOURCE LEVELS VS FREQUENCY FOR ALL SHOTS

BUCK: ARCTIC ENVIRONMENTAL LF ACOUSTICS MEASUREMENTS,
MODELS AND PLANS

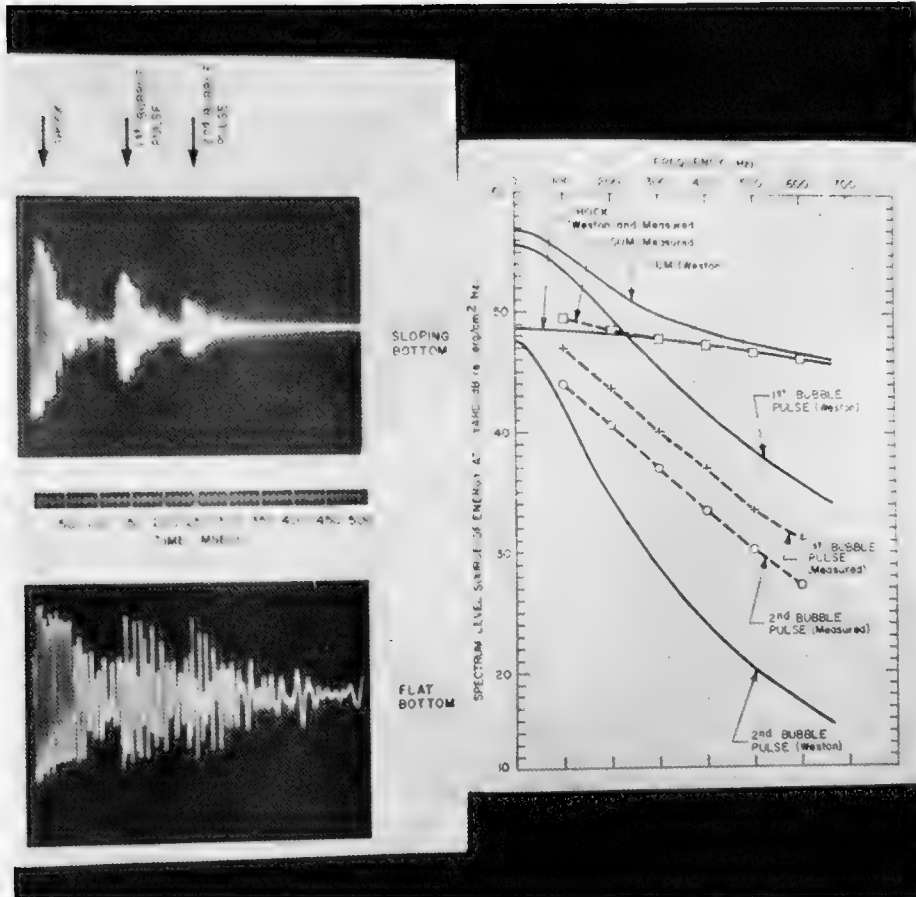


Figure 6. SIGNATURE TRACES AND SPECTRUM LEVEL

BUCK: ARCTIC ENVIRONMENTAL LF ACOUSTICS MEASUREMENTS,
MODELS AND PLANS

bubble pulse arrival. The usual signal is that of the bottom illustration. Anyway, this allowed an energy analysis of each impulse separately.

Sixty feet is considerably above Weston's "critical depth" for a 1.8-pound charge and bubble migration effects can be expected to reduce the energy of the bubble pulses but not of the shock wave. Therefore, the bubble energies were plotted relative to that of the shock wave and then compared with Weston's predictions. The results indicate 3 to 8 dB less total energy below 200 Hz. The previously described Central Arctic test did not indicate this much difference for the 60-foot MK61, thus the issue of the shallow, bubble migration zone is not resolved and additional tests are called for.

During the 1970 three-station experiment, daily shot series were conducted with each ice station being used for both sending and receiving. Also, ski-equipped light aircraft were employed to gain short-range paths. Shot depths were 60, 200, 400, 600, and 800 feet; shot sizes were 1.8-pound modified MK61s and 50-pound MK14s. Source yields of each shot were measured by monitoring the bubble pulse frequency and Weston's equations used for source energies. The floe stations each drifted well over 100 miles during the 2 months and allowed paths of different bottom topography. The detailed transmission loss data from these experiments were reported elsewhere.

In analyzing all of these data, it was quite apparent that the Arctic as a propagating medium was strikingly similar to a low-pass filter with slope and insertion loss increasing and break frequency decreasing all smoothly as range increased.

BUCK: ARCTIC ENVIRONMENTAL LF ACOUSTICS MEASUREMENTS,
MODELS AND PLANS

We took all of the data for the case of a 400-foot source, 100-foot hydrophone and water depths greater than 3,000 meters and fitted them to a cascaded filter model made up of 1-pole (i.e., -6 dB/octave slope) filters. This empirical model is shown in Figure 7, which is best explained by way of an example. At 200 nautical miles, the filter is made up of three 1-pole filters in series (-18 dB/octave slope) each with a 3 dB break frequency of 48 Hz and a total insertion loss of 54 dB. The model can be used at any range to derive loss without using an integral number of filters by determining the insertion loss, 3 dB break frequency and slope and applying a Bodie plot ($-10 n \log [1 + f/f_{3dB}]$).

In Figure 8 are plotted transmission loss measurements as a function of frequency at ranges of 23, 72, 200, and 480 nautical miles, which correspond, respectively, to one, two, three, and four 1-pole stages of the model which are plotted in solid lines. The empirical fit is seen to be quite good.

Figure 9 is taken from one of Hank Kutschale's figures where he compares early measurements by the author and Bob Mellen with his computed FFP and ray theory models. We have added the much more extensive 1970 data and the filter model of the previous two figures. Over 100 km, our controlled measurements and filter model agree almost exactly with Kutschale's computed FFP. The difference at short range is to be expected since RRR rays and, hence, local bottom topography plays an important role.

It was previously mentioned that the Arctic's stable vertical velocity profile was a steep positive gradient from the surface down to about 1,200 feet and a less-steep positive gradient from there to the bottom, and that the concentrated rays traveling in the uppermost

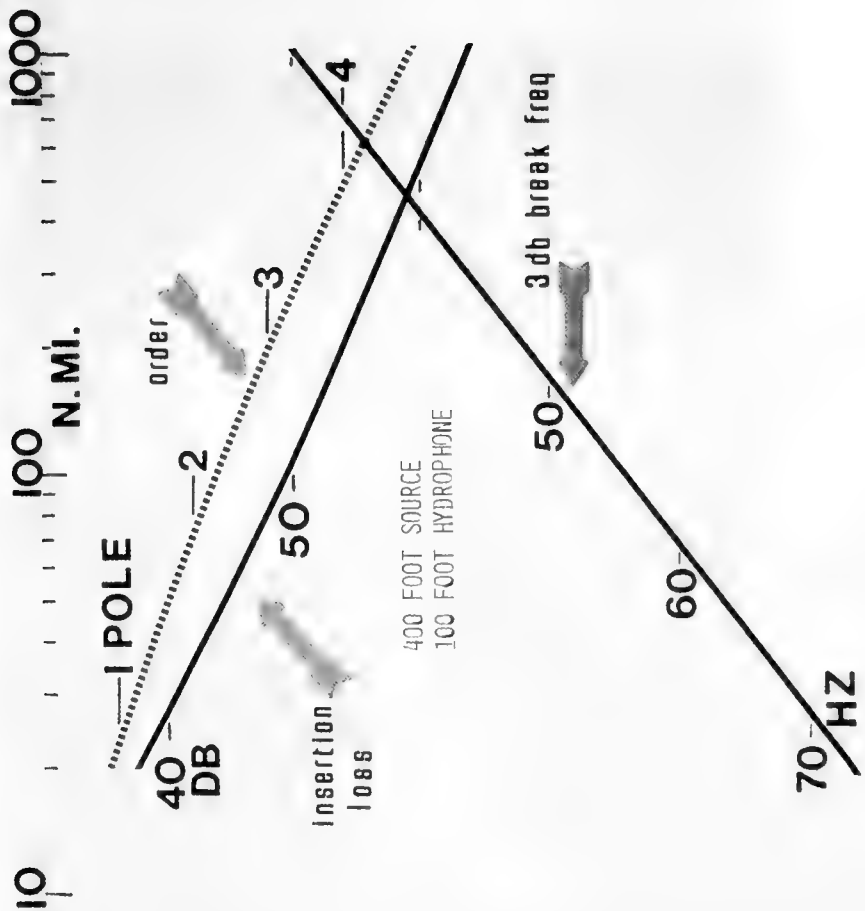


Figure 7. ARCTIC PROPAGATION 'LP FILTER' MODEL

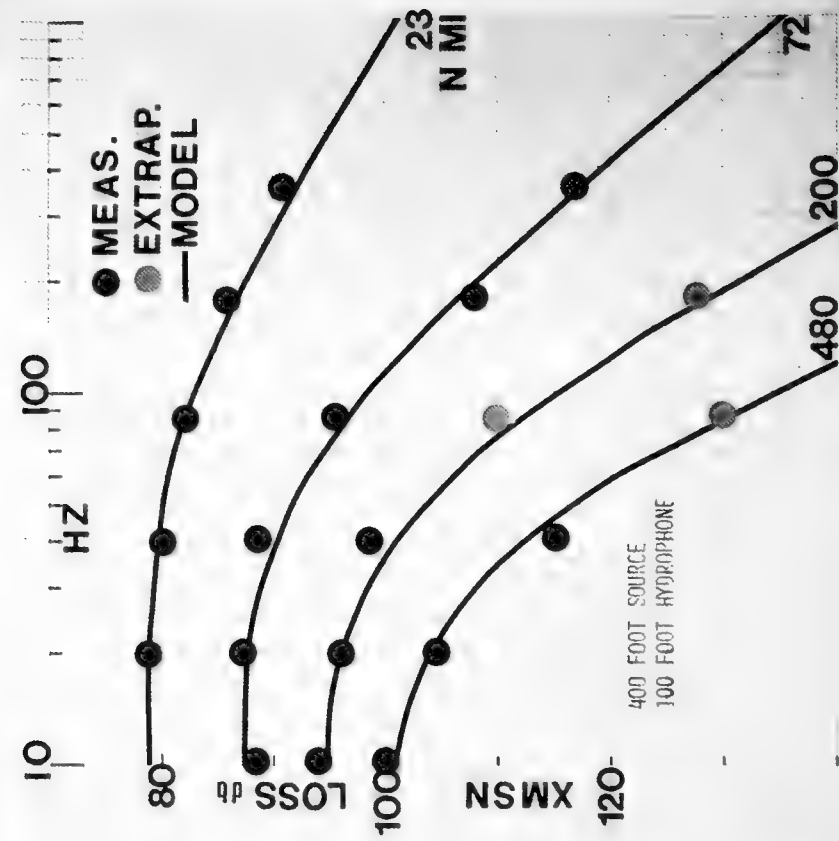


Figure 8. COMPARISON OF MEASURED AND MODELLED TRANSMISSION LOSS

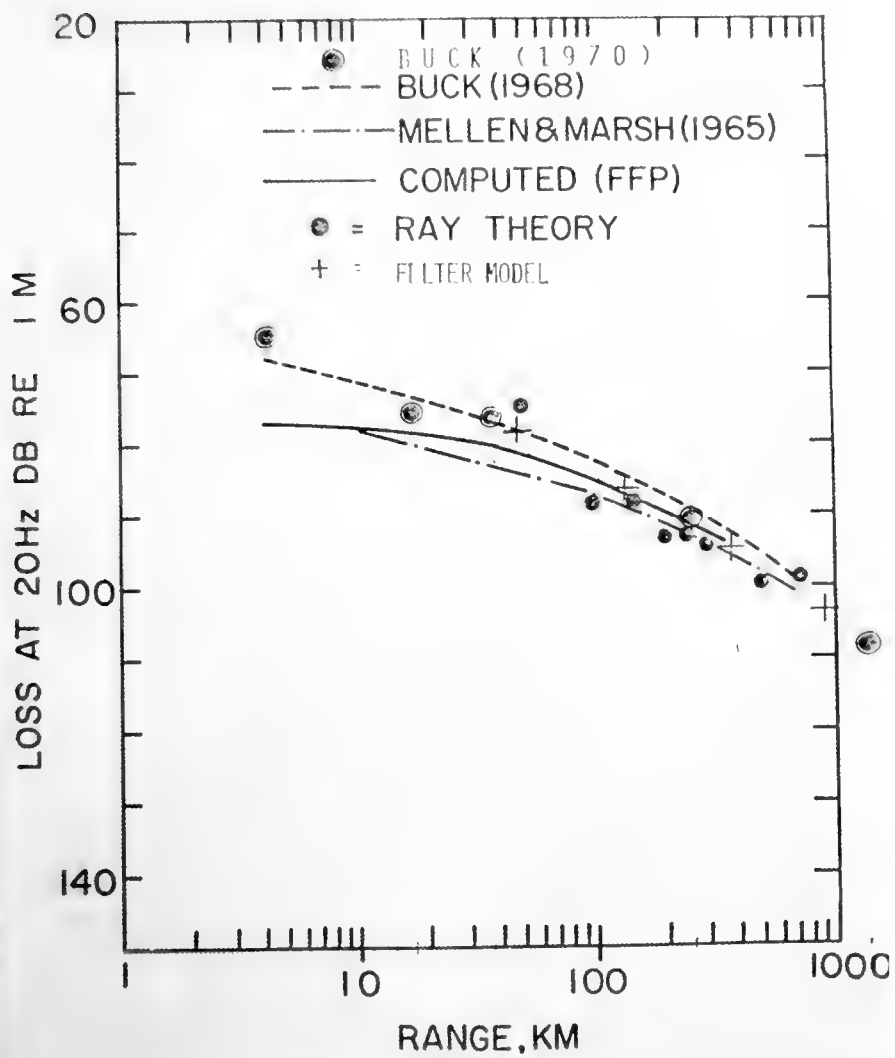


Figure 9. DATA AND THEORY COMPARISONS

1,200 feet were separable from the deep rays in a typical shot signature, allowing separate energy analyses of the two. Figure 10 shows the results of this type analysis at close to 800 nautical miles. Both left and right plots are of percentage energy versus frequency. The left plot averages all shot depths but separately graphs four propagation paths by mean bottom depths. For example, at 20 Hz over the path of mean bottom depth 9,200 feet, 58 percent of the total arriving energy has travelled in the RSR rays shallower than 1,200 feet and 42 percent is in the deep rays.

The right-hand plot averages all of the four paths but separates the percentage energy by source depth. For example, at 20 Hz, for the 200-foot shot depth, 25 percent of the shot signal energy is in the shallow rays and 75 percent is in the deep.

It is concluded that in the frequency bank of 10 to 20 Hz, and for source depths of 200 to 800 feet, only 2 to 6 dB signal is lost for a path of 1,200 feet minimum depth relative to the deepest possible long-range path in the Arctic.

Figure 11 demonstrates that the causes of noise in different parts of the Arctic can be quite different. The three sets of plots are for the shore-fast ice of the Canadian Archipelago (top), an ice island (middle), and a floe (bottom). The top of each set is temperature versus time and the bottom is 150 to 300 Hz band noise. In the Archipelago there is very strong correlation between the two time functions but none at the Central Arctic sites. Thermal ice cracking is the major source of noise in static shore-fast ice but this effect, while present, is far overshadowed by gross ice dynamics in the Central Arctic.

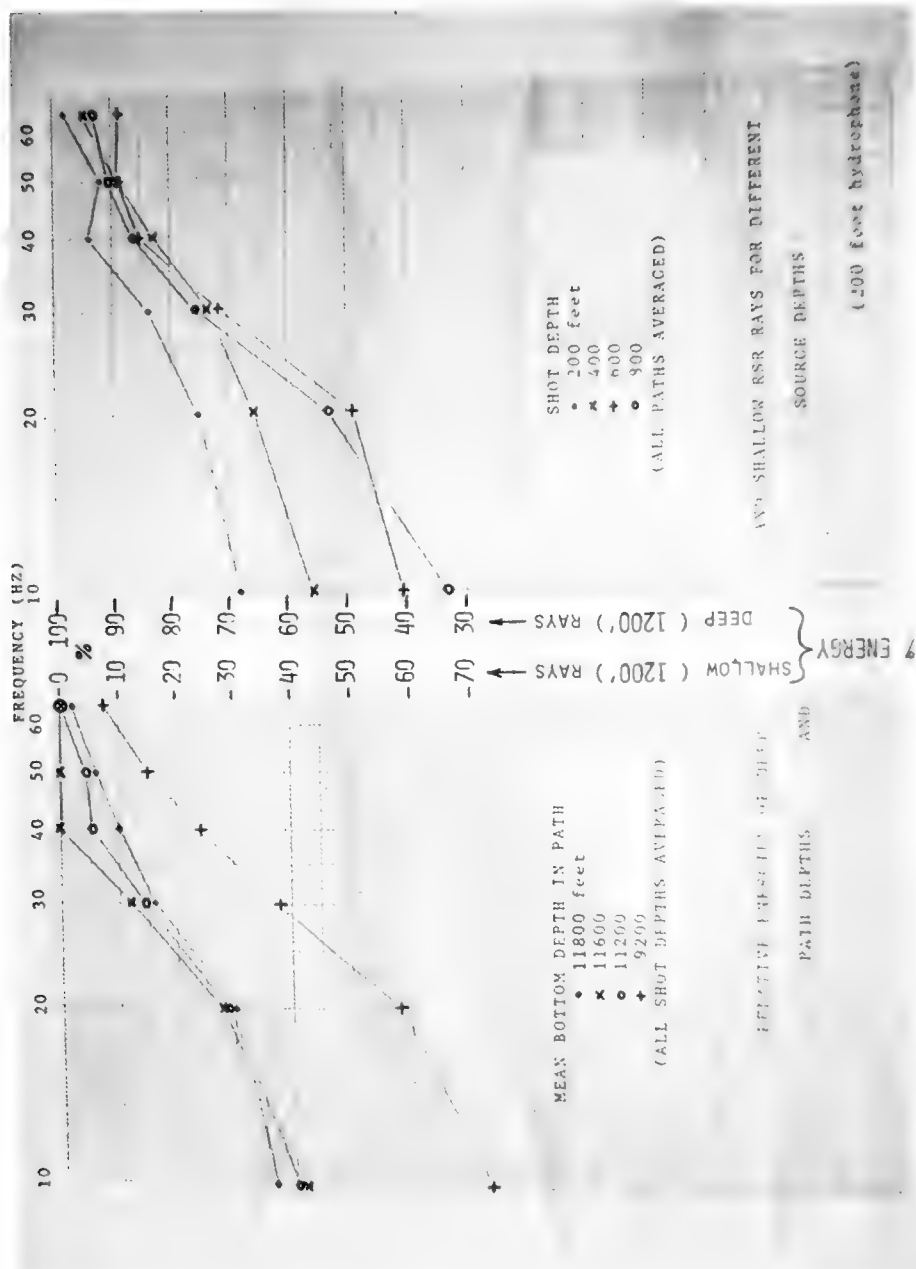


Figure 10. ENERGY PARTITION BY BOTTOM DEPTH AND SOURCE DEPTH

BUCK: ARCTIC ENVIRONMENTAL LF ACOUSTICS MEASUREMENTS,
MODELS AND PLANS



Figure 11. TEMPERATURE EFFECTS ON AMBIENT NOISE (150-300 Hz)

Figure 12 shows cross correlations of the ambient noise-level and wind time-functions at the ice island (left) and the two floe ice stations (center and right) during the 2-month experiment in the spring of 1970. The correlation is seen to be very high at the floe ice stations as might be expected from the premise of ice dynamics being the major source of noise since ice pack movement is caused primarily by wind. The correlation for the ice island location is not as strong. T3 is a very large solid mass of ice (3 billion tons displacement) which has considerable inertia. A hydrophone mounted below its center sees mostly noise generated at the ice island's edges where there is considerable pressure-ridging activity. Naturally, there is some correlation between noise and wind, but the inertial forces cause a smearing which is evident in the periodicity of the T3 correlation functions.

Figure 13 shows the cross correlations of ambient-noise-level time functions between two floe stations (left set of curves) which were about 150 nautical miles apart at the southwest edge of the Gyre and between a floe station and T3 (right) separated by about 750 nautical miles. We believe the inference here is that windstorms are widespread in the Arctic and not that noise sources are common. However, the fall-off of correlation with frequency evident in these curves argues the other way. We just do not have sufficient data at this time to say.

A test was run with a hydrophone below pack ice to determine ambient noise level change with depth. The results are shown in Figure 14 where the levels are plotted as a function of depth in wavelengths. The noise level at each frequency is relative to the noise at 2λ . Deeper than 1λ to 2λ , the noise was almost constant. These curves are the sort you would expect for approaching a pressure

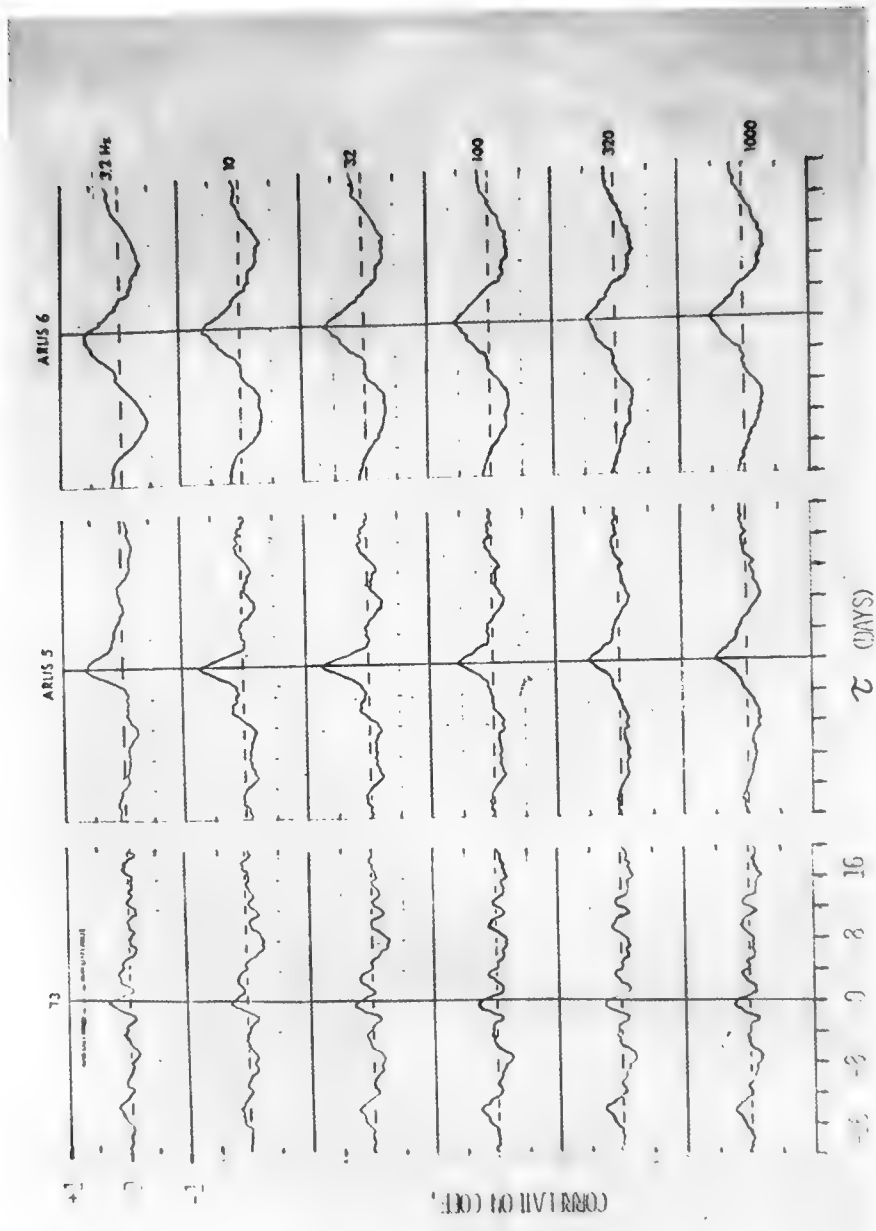


Figure 12. CROSSLINKAGE OF SURFACE WIND AND NOISE LEVELS

BUCK: ENVIRONMENTAL LF ACOUSTICS MEASUREMENTS,
MODELS AND PLANS

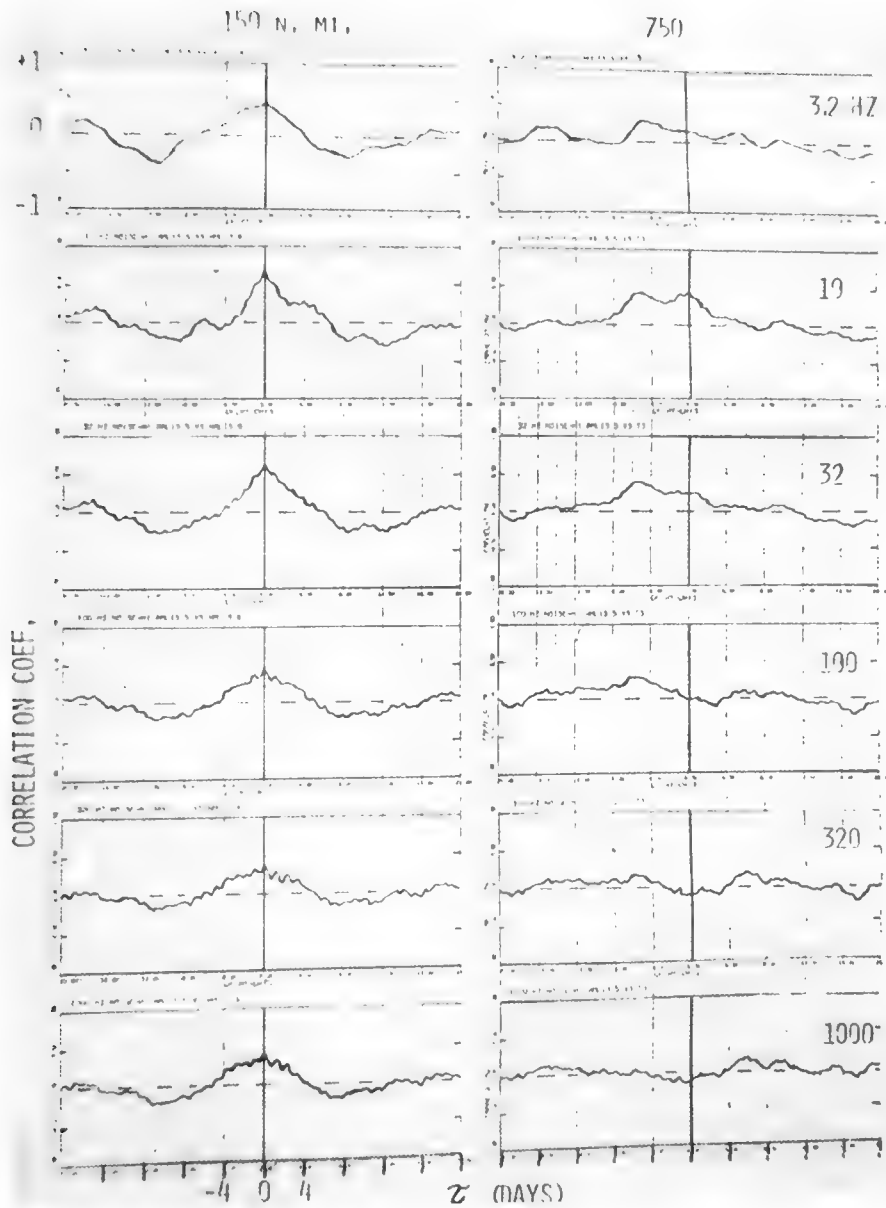


Figure 13. CROSSLCORRELATION OF NOISE LEVELS AT DIFFERENT STATIONS

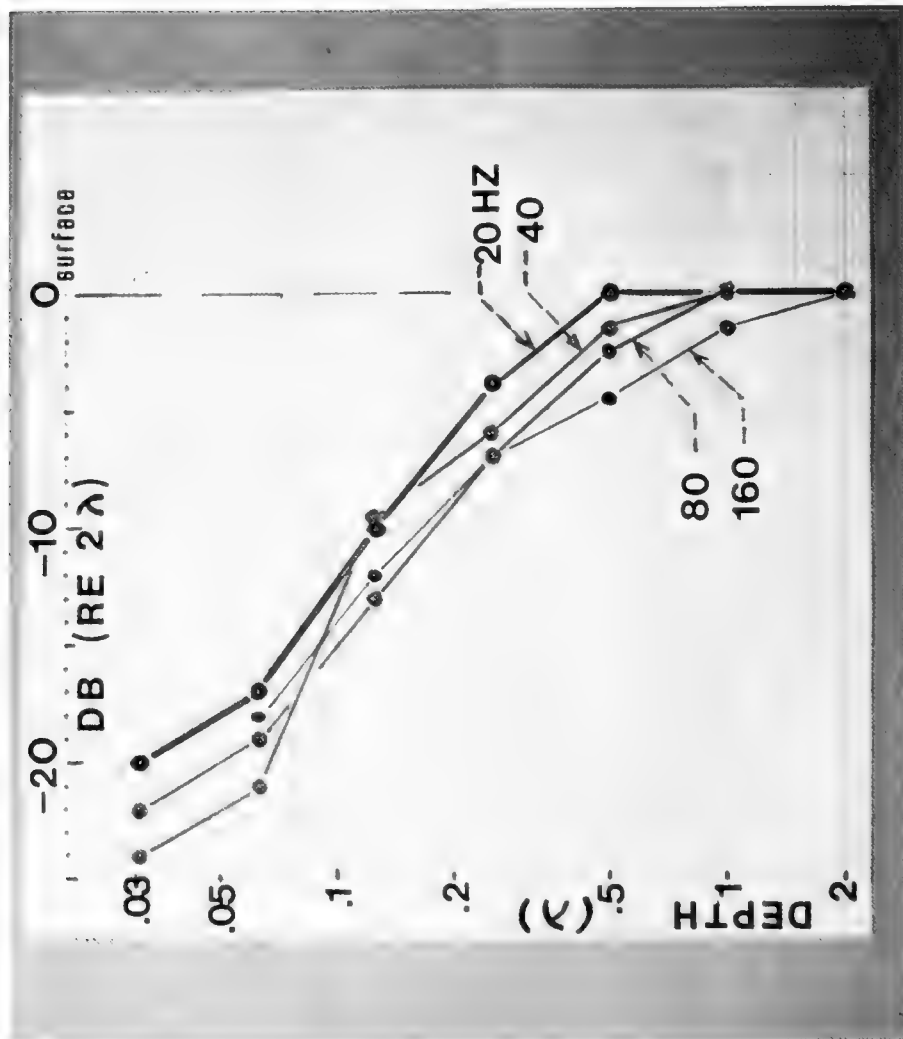


Figure 14. AMBIENT NOISE LEVEL VERSUS DEPTH

BUCK: ARCTIC ENVIRONMENTAL LF ACOUSTICS MEASUREMENTS,
MODELS AND PLANS

release surface where the noise sources are not directly overhead, as is the case of gravity waves in the open ocean, but are arriving from a distance through rays that are fairly close to the horizontal.

Lacking a long vertical hydrophone array to make a proper measurement of vertical directionality of noise, we attempted to do the next best thing by matching the data of Figure 14 to the Lloyd's Mirror function ($\sin [2\pi(D/\lambda) \sin \beta]$). The results (see Figure 15) of this rather crude analysis are best described by an example. At 20 Hz the measured increase of noise level with depth shown in Figure 14 can be closely approximated by a ray bundle arriving 20° to 24° below a horizontal, perfect pressure release surface. Similarly, at 40 Hz the angle is 13° to 25° , etc.

The data of Figures 14 and 15 were taken in one day and are too small a sample to be necessarily representative. However, in consideration of the fact that 100 percent of the energy from long-range targets is arriving in the sector 5° to 17° , the possibility of gain through a vertically directive array is at least interesting. To do any good at the lower frequencies the array would have to have on the order of 10 elements and extend to below 1,000 feet.

Two low-frequency DIMUS sonars have been installed at ice island T3, one for a short experiment in January 1960 and the second in 1965. The arrays for both of these were mounted through sea ice adjacent to the island (Figure 16). In 1967 a 1,200-foot diameter, 32-element array was installed through the 100-foot thick ice of the island itself in the approximate location shown in this figure. These systems were used to investigate feasibility of large-aperture, digitally processed arrays in the Arctic. It is believed that they still hold the record for being the largest circular arrays ever

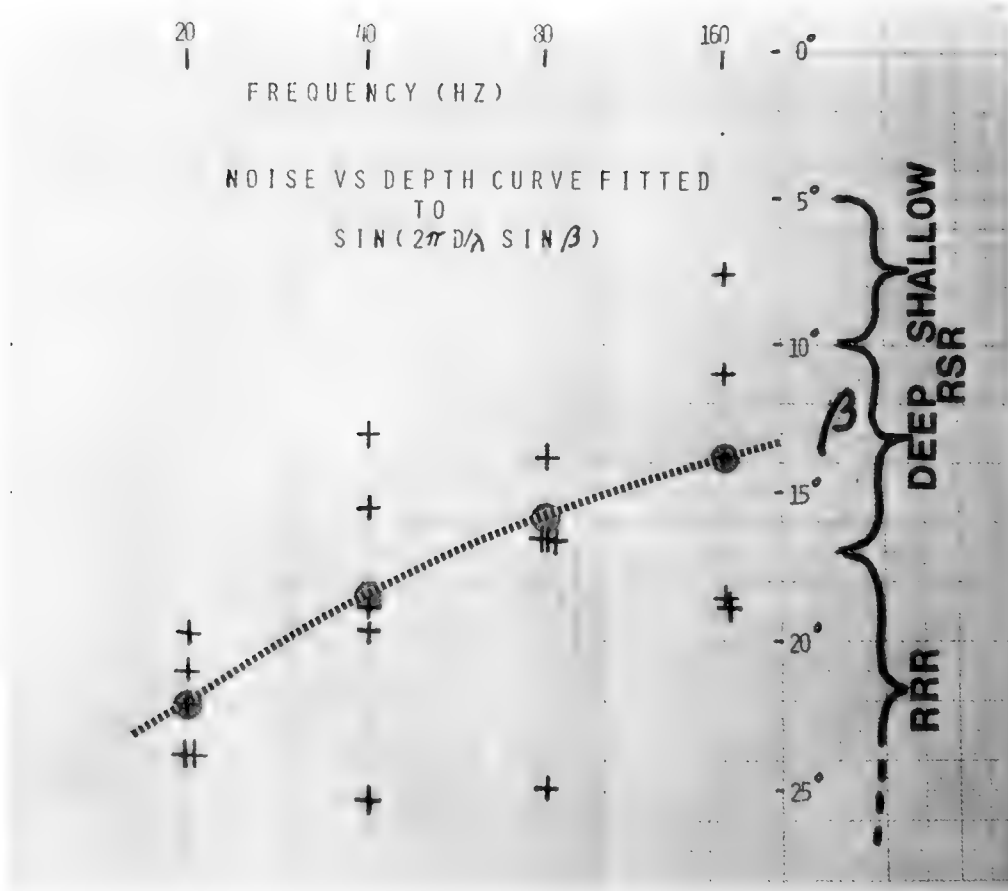


Figure 15. NOISE VS DEPTH CURVE FITTED TO
 $\sin(2\pi(D/\lambda) \sin \beta)$

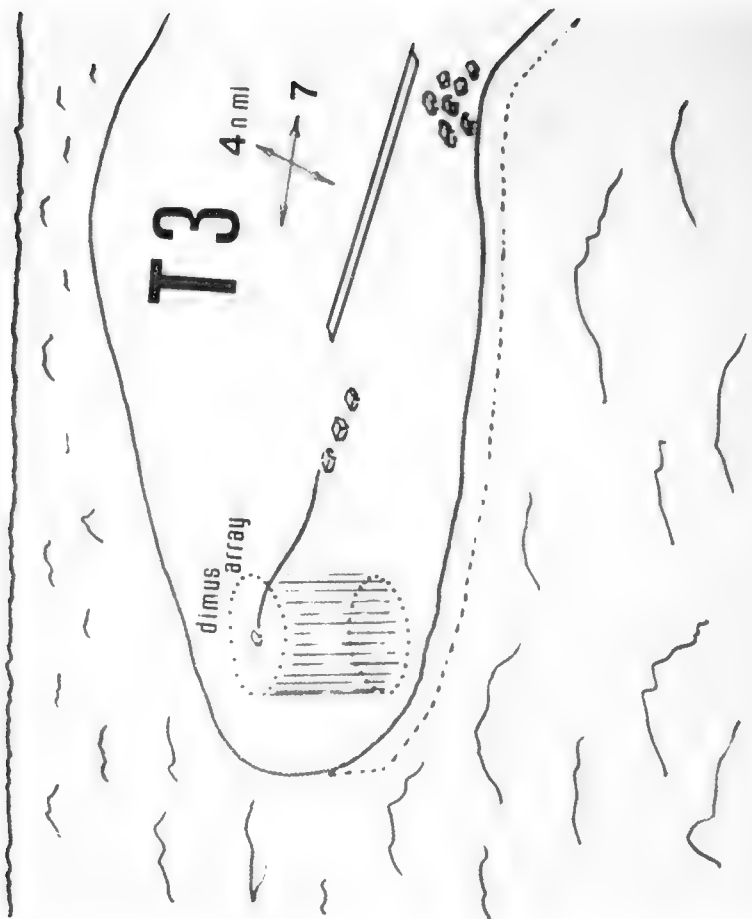


Figure 16. LOCATION OF DIMUS ARRAY ON ICE ISLAND T3

installed and certainly the largest ever installed at or close to the effective sound channel axis. The systems were tested using CW projectors in the far field. Attained array gain was measured over a reasonably long period by monitoring the S/N outputs of a single hydrophone in the array and of the processed beam containing the projector. The background noise was found to be anisotropic and, at certain times, highly so. Occasionally the array gain equalled the directivity index (DI), but on the average it was a few dB below, and at times it dipped to 7 dB below.

Figures 17 and 18 present three dimensional pictures of the broadband output of the T3 DIMUS under a couple of background noise conditions. 360° of relative bearing (128 beams) are shown on the x axis, beam output on the y axis, and time on the z axis.

An informative way to view Arctic low-frequency environmental acoustic data is to present the data in terms of signal-to-noise ratios instead of transmission loss and ambient noise independently. The next few figures make this type of comparison. In all cases one parameter is compared with another so the end result is a ratio of signal-to-noise ratios. In every case we have used shot energy for the "signal" and median ambient noise as "noise."

Figure 19 presents S/N as a function of frequency for three source ranges. Here source depth is 400 feet and hydrophone depth is 100 feet. For all three ranges the S/N is normalized to 0 dB at 10 Hz. The importance of very low frequencies to detection at extreme ranges in the Arctic is apparent from the two bottom curves.

Figure 20 presents relative S/N ratios for three hydrophones at different depths below 12-foot thick pack ice. The 200-foot sensor is the reference and the 100-foot and 30-foot units are plotted relative

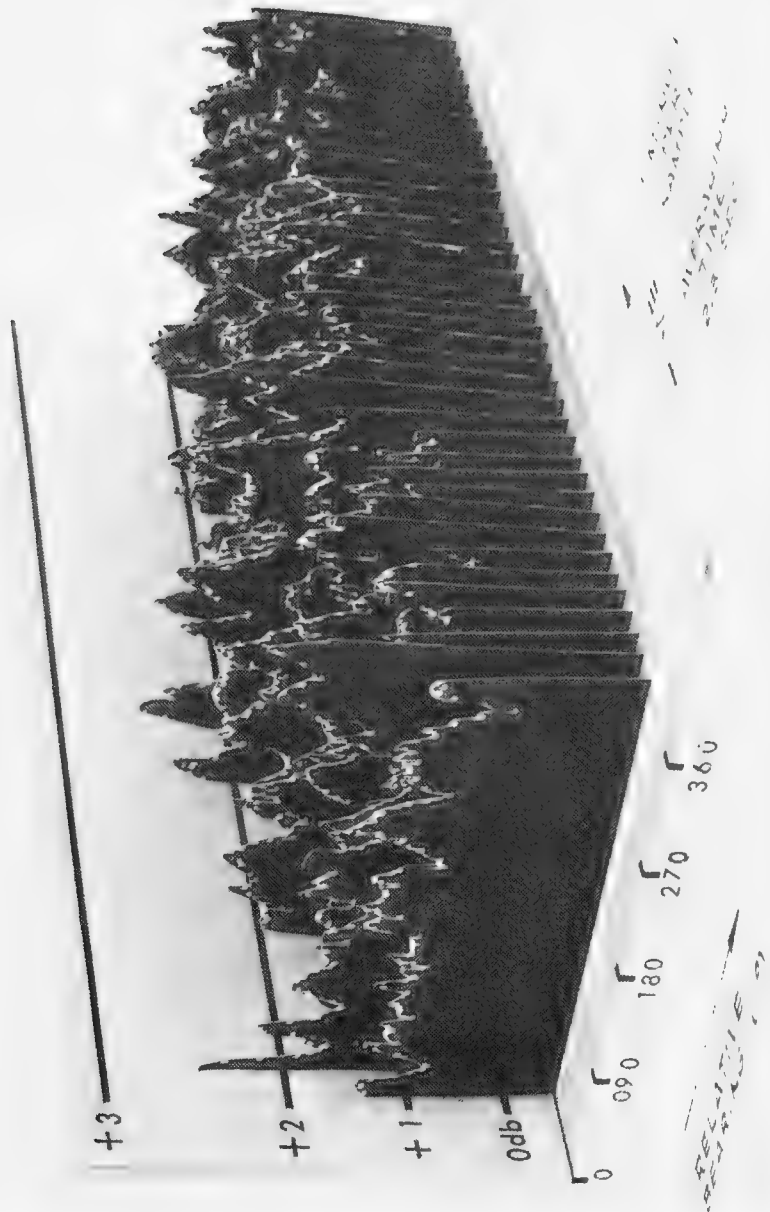
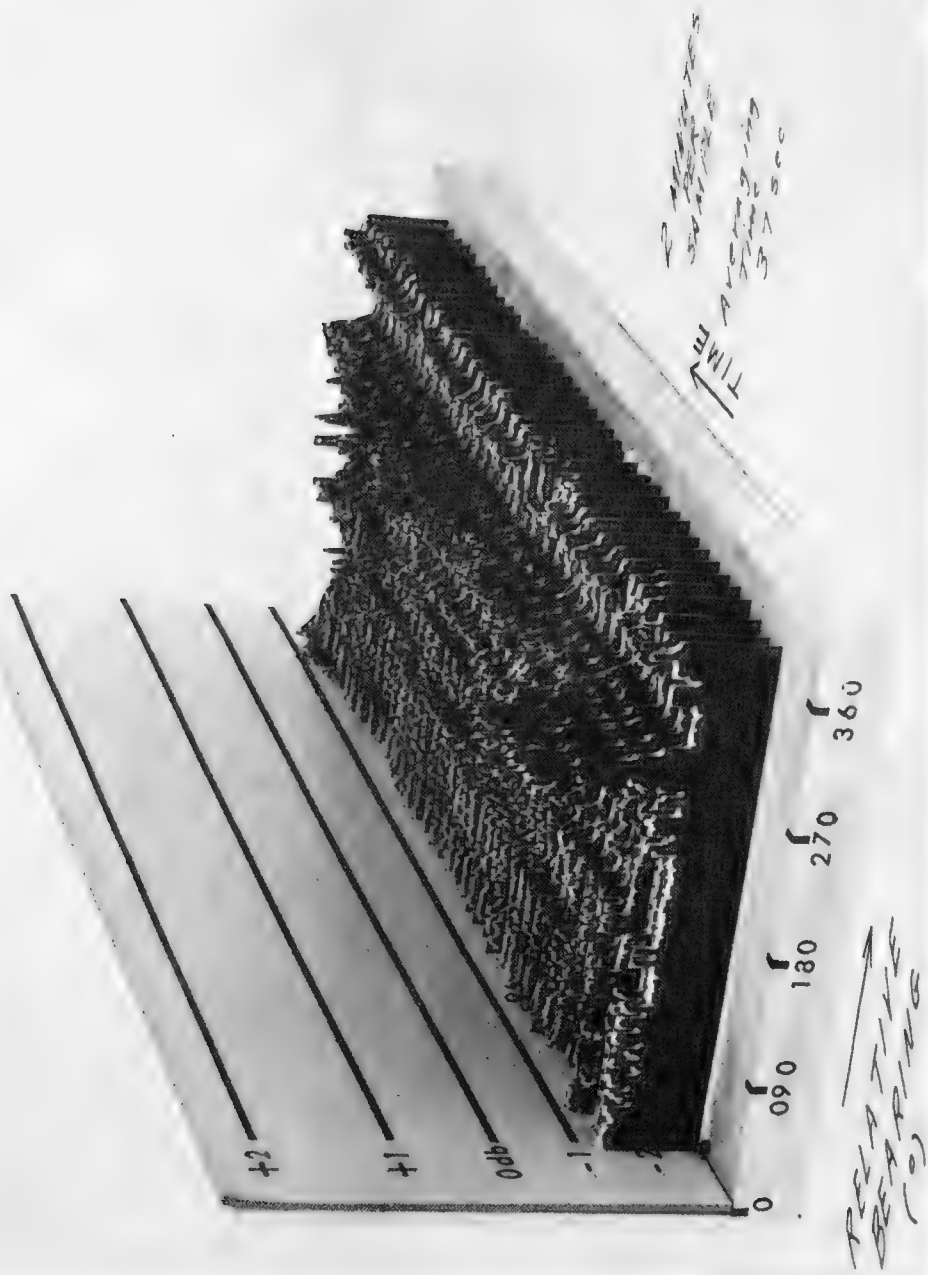


Figure 17. DISPLAY OF BROADBAND NOISE OUTPUT OF DIMUS -
BACKGROUND A

Figure 18. DISPLAY OF BROADBAND NOISE OUTPUT OF DIMUS -
BACKGROUND B



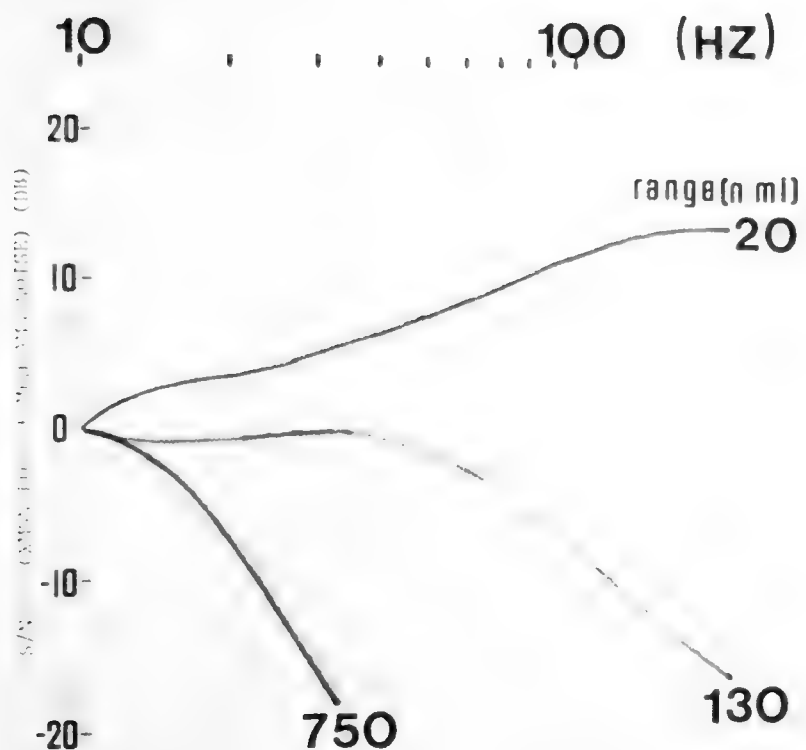


Figure 19. SIGNAL-TO-NOISE CHARACTERISTIC OF DEEP CENTRAL ARCTIC (100 FOOT DEEP HYDROPHONE)

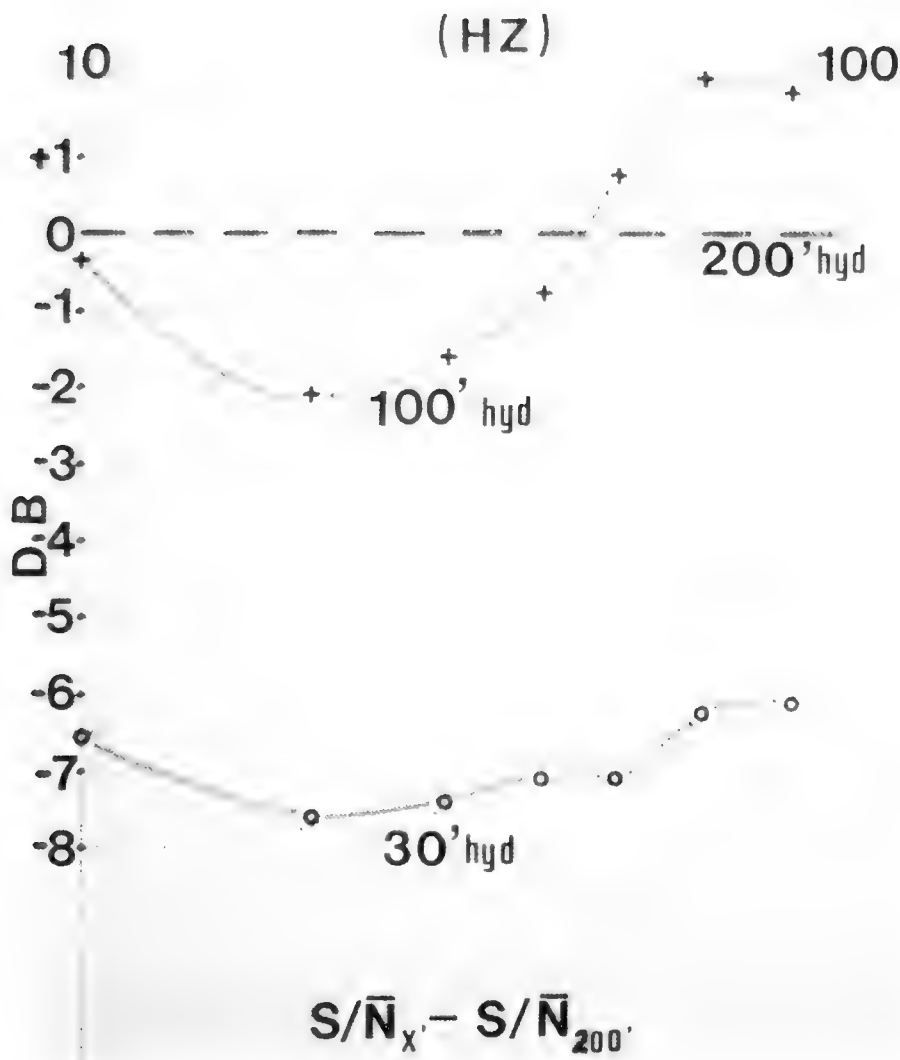


Figure 20. RELATIVE SIGNAL TO NOISE RATIO
VERSUS FREQUENCY

to it. At 20 Hz, the 200-foot hydrophone is 2 dB better than the one at 100 feet and 7.6 dB better than the 30-footer. However, the 100-foot depth almost flattens the noise below 30 Hz where the 200-foot depth does not.

In most Arctic experiments we use vertical or horizontal seismometers, or both, frozen into the ice above the hydrophone. In Figure 21 are plotted relative S/N ratios for a 100-foot hydrophone and a vertical seismometer (Δ) and a horizontal seismometer for various source depths. Below about 30 to 40 Hz, the horizontal seismometer is superior; however, 3 dB of this is due to the directivity of that unit. The vertical seismometer S/N is 6 to 7 dB below that of the 100-foot hydrophone.

Figure 22 compares an ice island with a floe station as an acoustic platform for hydrophones 200 feet below the ice top surface. In all these figures, the floe station (ARLIS 5) 200-foot hydrophone is used as a reference. The top figure shows the median levels for 2 months of hourly readings. The T3 phones were installed through 3-inch holes 100 feet through the island in 1968 and, of course, froze in so there was no way to check-calibrate the crystal units themselves. However, the preamps were topside and regularly checked for gain. We have shown the April-May ambients for 1968, 1969, and 1970 as the next best thing to a direct crystal calibration. There is seen to be no drastic change in the 2 years, nor was it expected. The noise at T3 was 5 to 9 dB quieter than at ARLIS 5. How much of this difference was due to geographic location and how much to the different types of ice immediately over the phones, is unknown.

The second data set of Figure 22 is transmission loss for four different source depths. Reciprocal paths were used for this comparison and

BUCK: ARCTIC ENVIRONMENTAL LF ACOUSTICS MEASUREMENTS,
MODELS AND PLANS

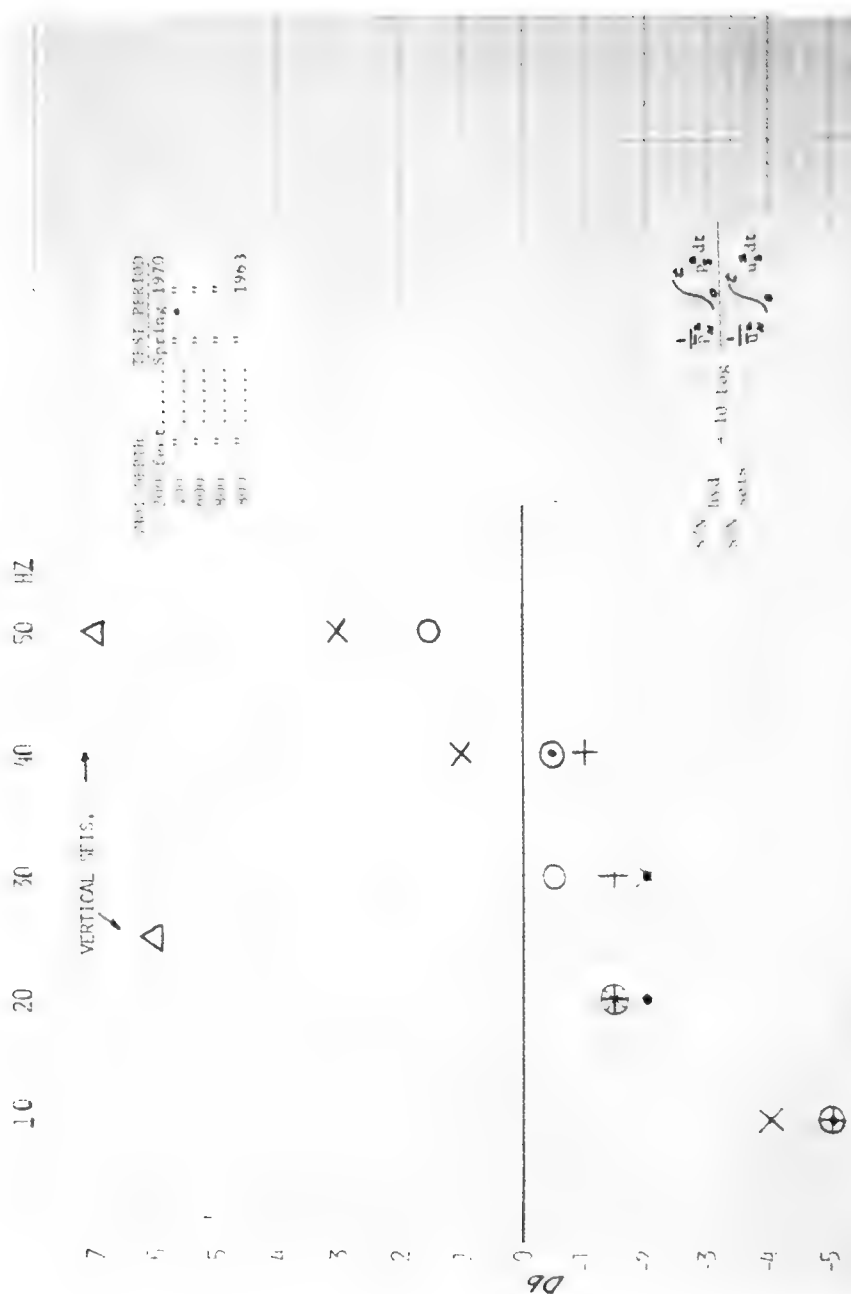


Figure 21. RELATIVE SIGNAL-TO-NOISE RATIOS FOR HYDROPHONE AND SEISMOMETER

BUCK: ARCTIC ENVIRONMENTAL LF ACOUSTICS MEASUREMENTS,
MODELS AND PLANS

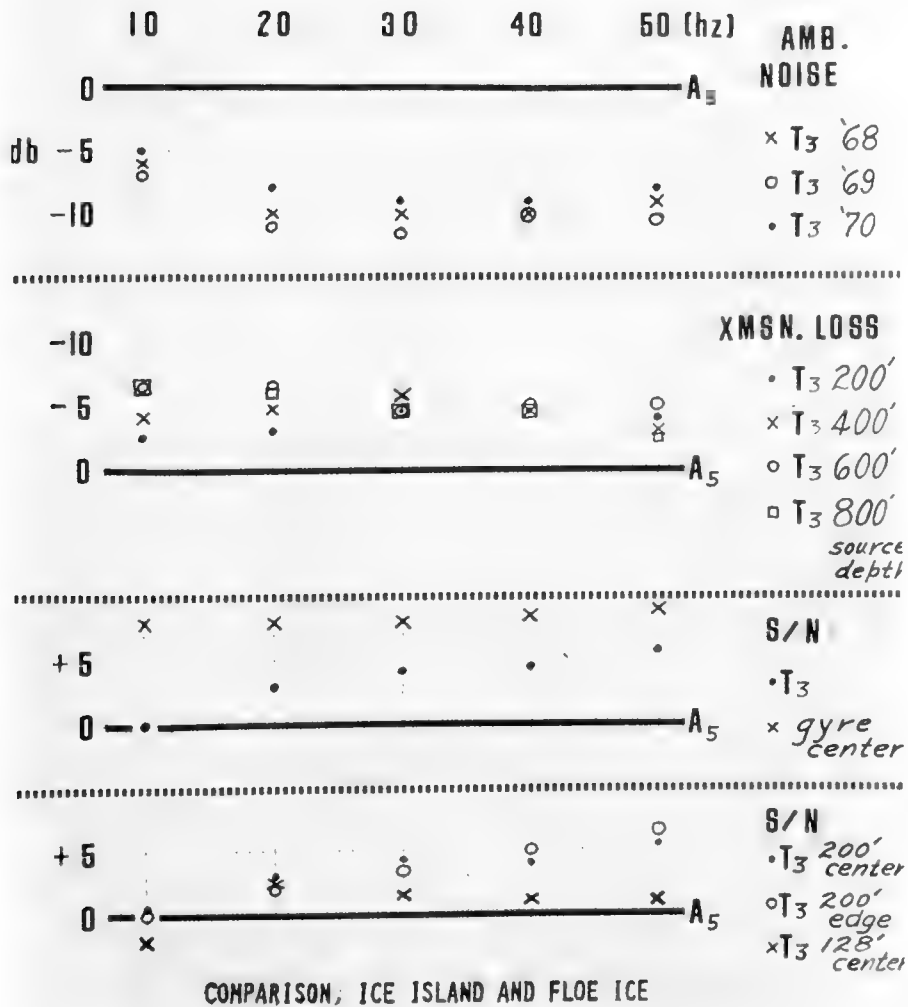


Figure 22. COMPARISON OF ICE ISLAND AND FLOE ICE [REFERENCE IS THE FLOE STATION (A_5) 200-FOOT HYDROPHONE]

BUCK: ARCTIC ENVIRONMENTAL LF ACOUSTICS MEASUREMENTS,
MODELS AND PLANS

it is seen that the loss using T3 as receiver averaged about 5 dB greater than ARLIS 5 as receiver. We have only two possible explanations for this behavior: The T3 hydrophone lost sensitivity in the 2 years after calibration (but the top figures depicting noise indicate it did not); or reflection conditions due to the presence of the 7 × 4 miles, 100-foot thick ice island are different from the 9- to 12-foot thick pack ice and caused the added loss (shots from T3 were set off in the pack ice immediately adjacent to T3 while the phone was in the center of T3).

The data third from the top are S/N relative to ARLIS 5 of the ice island and the 1972 floe station near the center of the Gyre (for the latter, ARLIS 5 transmission loss was used). Gyre-center floe ice is 8 to 9 dB better than Gyre-southwest-edge floe ice and 3 to 8 dB better than the ice island.

The data at the bottom of Figure 22 are S/N ratios for three different hydrophones at T3 relative to the 200-foot phone at ARLIS 5. These three are: a unit 200 feet from the top ice surface installed at the center of T3, an identical one close to an edge of the island, and a third one located 128 feet below the top ice surface at the center of the island. Location has little effect, when averaged as these data are, but depth starts to be important above 30 Hz.

The next set of figures describes an Arctic deep water test planned for 1975-1977. As previously mentioned, Central Arctic ambient noise is caused predominantly by ice dynamics. There is a large-scale experiment called AIDJEX (Arctic Ice Dynamics Joint Experiment) scheduled for the period March 1975 to June 1976 to collect and then analyze and model ice pack motion for the understanding and prediction of ice dynamics. An ambient noise measurement project has recently been included in AIDJEX which, if it all comes off according to plan,

BUCK: ARCTIC ENVIRONMENTAL LF ACOUSTICS MEASUREMENTS,
MODELS AND PLANS

will be the most extensive and thorough ambient noise experiment ever conducted in any ocean.

Figure 23 shows the installation locations of ten "Arctic Environmental Buoys" (AEB) being developed by PRL for NOAA. These are HF telemetry stations for automatically collecting and telemetering to one of four manned camps in the center of the ring. The ring will be 300 or 400 km in radius. These stations will collect temperature and precise barometric pressure readings at the synoptic times every 3 hours for geostrophic wind calculations. Each is equipped with TRANSIT satellite receivers that will automatically measure precise location and enable ice strain measurements of the buoy field. Expected unattended AEB life is 16 months.

At each AEB location, but separated by at least 1 mile, will be a Synoptic Random Access Measurement Station (SYNRAMS) which PRL is also developing. These will be used to collect temperature, barometric pressure, and ambient noise level data in four 1/3-octave bands (3.2, 10, 32, and 1000 Hz) at the synoptic times and transmit them via the NIMBUS F satellite back to the CONUS. SYNRAMS has a built-in navigational capability accurate to about 2 miles.

Figure 24 shows the 1-year drift histories of U.S. and U.S.S.R. manned camps and ships and can be used to estimate the distribution of the 15 SYNRAMS after their life goal of 2 years.

Figure 25 shows the predicted SYNRAMS locations at the end of their battery life in 1977 after having telemetered 6,000 synoptic samplings of 1/3-octave levels, temperature, atmospheric pressure, and location. By taking advantage of the ice drift, we can expect to have buoys in parts of the Arctic where we have never been able to have manned camps, and a well distributed field which, together with



Figure 23. INSTALLATION LOCATIONS FOR AEB AND SYNRAMS



Figure 24. ONE-YEAR DRIFT HISTORIES
OF US AND USSR STATIONS

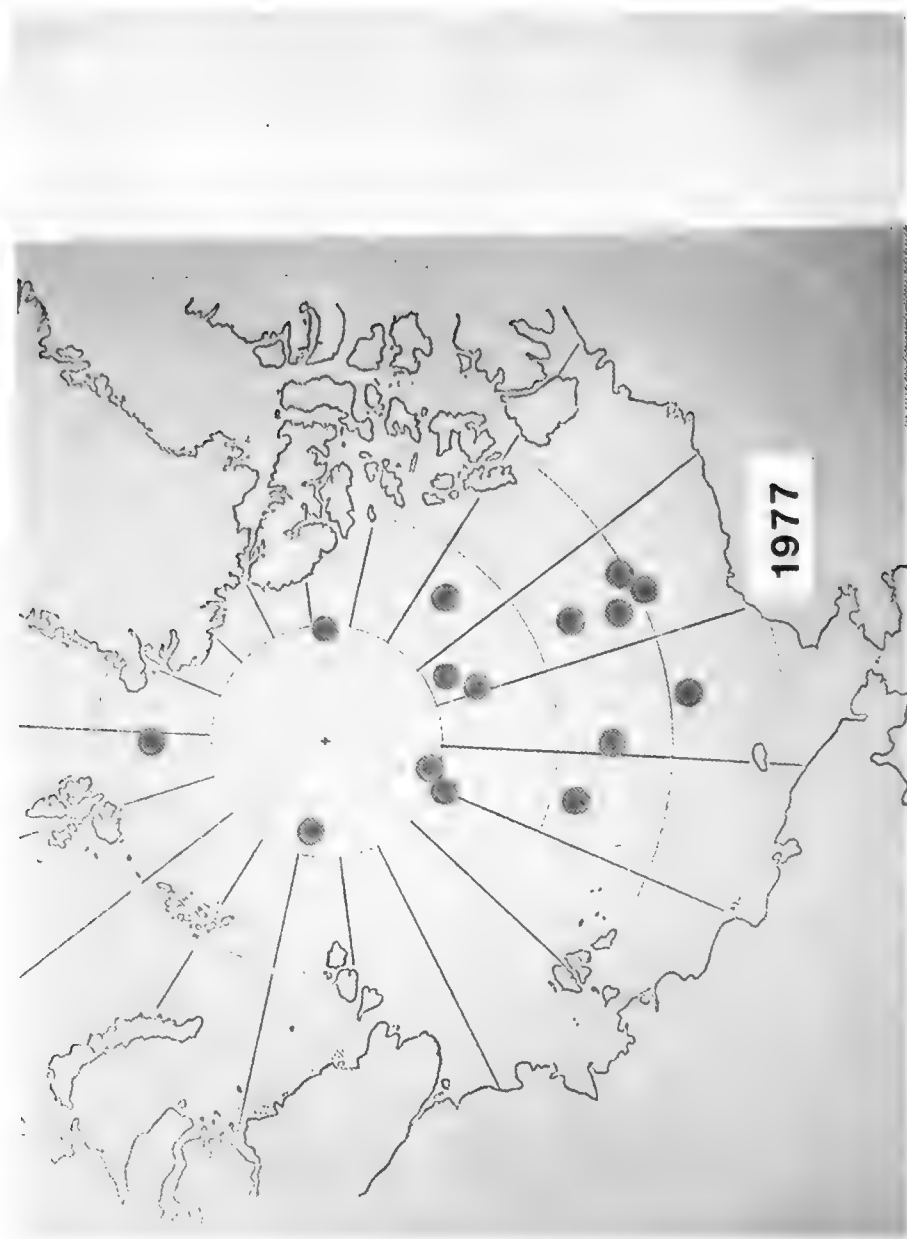


Figure 25. ESTIMATED DISTRIBUTION OF 15 SYNRAMS
LOCATIONS AFTER 2 YEARS

BUCK: ARCTIC ENVIRONMENTAL LF ACOUSTICS MEASUREMENTS
MODELS AND PLANS

shore weather stations and remote sensing satellites, should yield an excellent picture of Arctic meteorological conditions.

Figure 26 is an illustration of an AEB. It is 40 feet high and extremely difficult to make quiet for windy conditions. Figure 27 illustrates why we went to the SYNRAMS, which is inherently a much quieter structure, and why it will be at least 1 mile from the AEBs. Another function of SYNRAMS will be to provide a navigational back-up for the AEB.

BUCK: ARCTIC ENVIRONMENTAL LF ACOUSTICS MEASUREMENTS,
MODELS AND PLANS

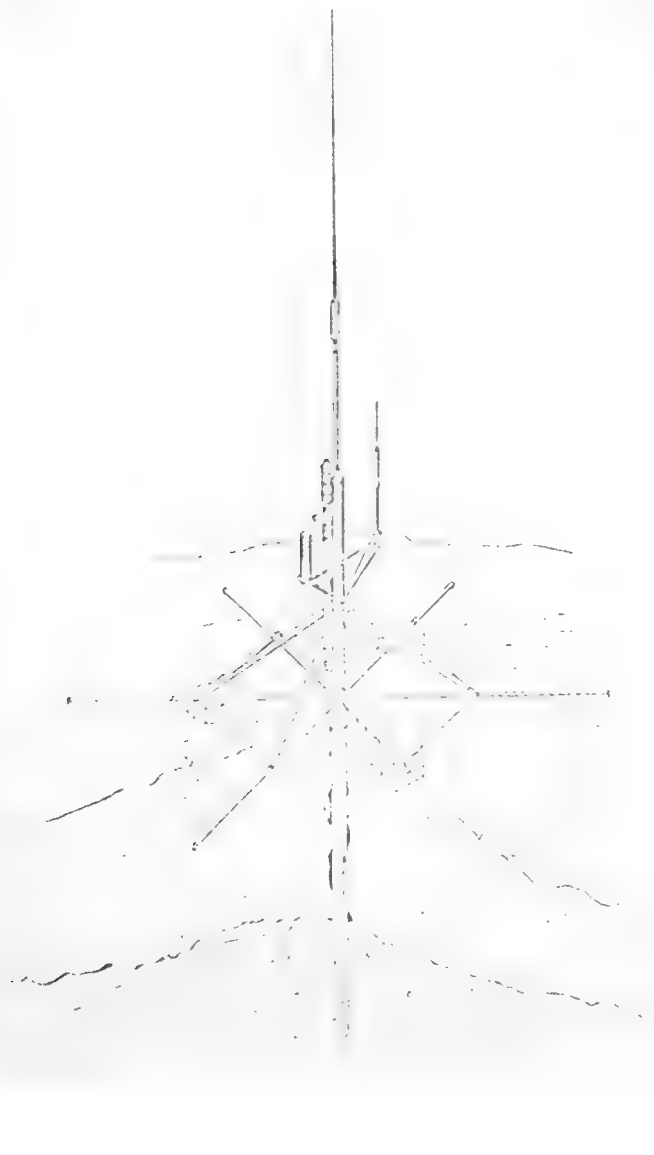


Figure 26. ARCTIC ENVIRONMENTAL BUOY (AEB)

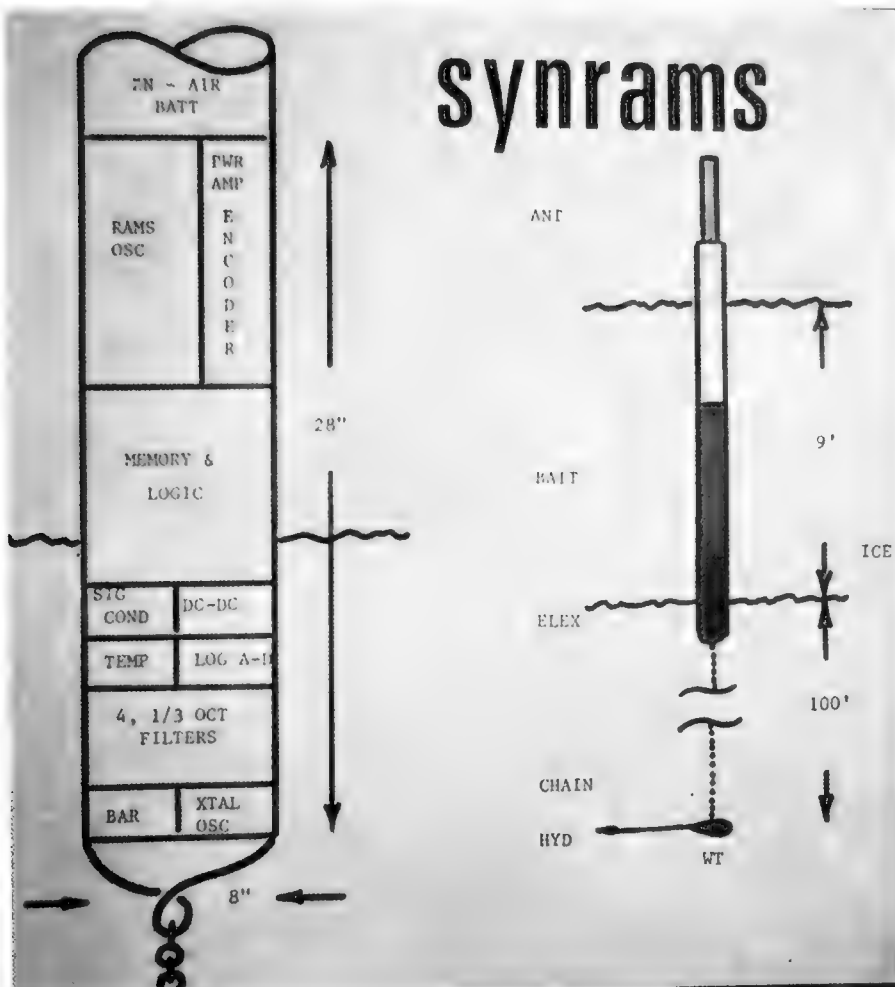


Figure 27. ILLUSTRATION OF SYNRAMS

ENVIRONMENTAL FACTORS AFFECTING LOW FREQUENCY PROPAGATION IN THE OCEAN

David G. Browning

Naval Underwater Systems Center
New London, Connecticut

A summary is made of our understanding of the effect of environmental factors on low frequency sound propagation, based on recent NUSC experiments and analyses. Modeling programs developed by DiNapoli, Kanabis, Weinberg, and others are used to illustrate the influence of bottom composition, bottom slope and bathymetric features and to determine the low frequency transmission characteristics of ocean sound channels. The present status of our program to predict the temporal and spatial variations in sound transmission by an understanding of the basic acoustic-oceanographic interaction mechanisms is discussed. Our priorities for further data collection are given.

Basically, the simplest type of sound channel experiment is illustrated in Figure 1. With both the receiver and source at the sound channel axis, we drop shots as a function of range to get propagation loss as a function of range.

A very simple model, outlined in Figure 2, is used to get the attenuation as a function of range. Spherical spreading is assumed out to a certain range R_o and then cylindrical spreading from then on with attenuation along the range. We plot this to get a linear fit for the attenuation.

Figure 3 illustrates the type of fit that we get from our data. We have used a very simple spreading model, what you might call a crude fit to the data. Naturally, when any more sophisticated methods come along, we are the first to try to see if this will improve upon things.

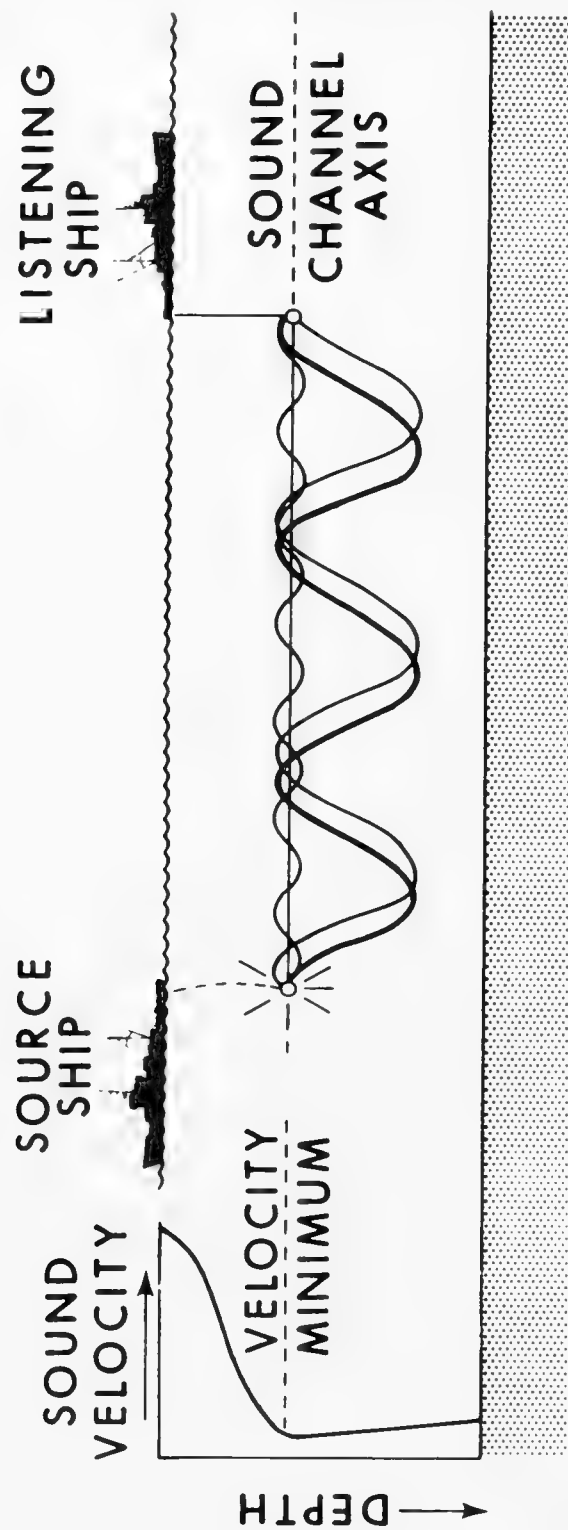


Figure 1. DIAGRAM OF EXPERIMENT

BROWNING: ENVIRONMENTAL FACTORS AFFECTING LOW FREQUENCY
PROPAGATION IN THE OCEAN

ASSUME SPHERICAL SPREADING TO R_o ,

THEN CYLINDRICAL.

$$\begin{aligned} N_w &= 20 \log R_o + 10 \log \frac{R}{R_o} + \alpha R \\ &= 10 \log R_o + 10 \log R + \alpha R \end{aligned}$$

LET $H_o = 10 \log R_o$

$$N_w = H_o + 10 \log R + \alpha R$$

WE PLOT:

$$(N_w - 10 \log R) = \alpha R + H_o$$

Figure 2. SPREADING MODEL

BROWNING: ENVIRONMENTAL FACTORS AFFECTING LOW FREQUENCY
PROPAGATION IN THE OCEAN

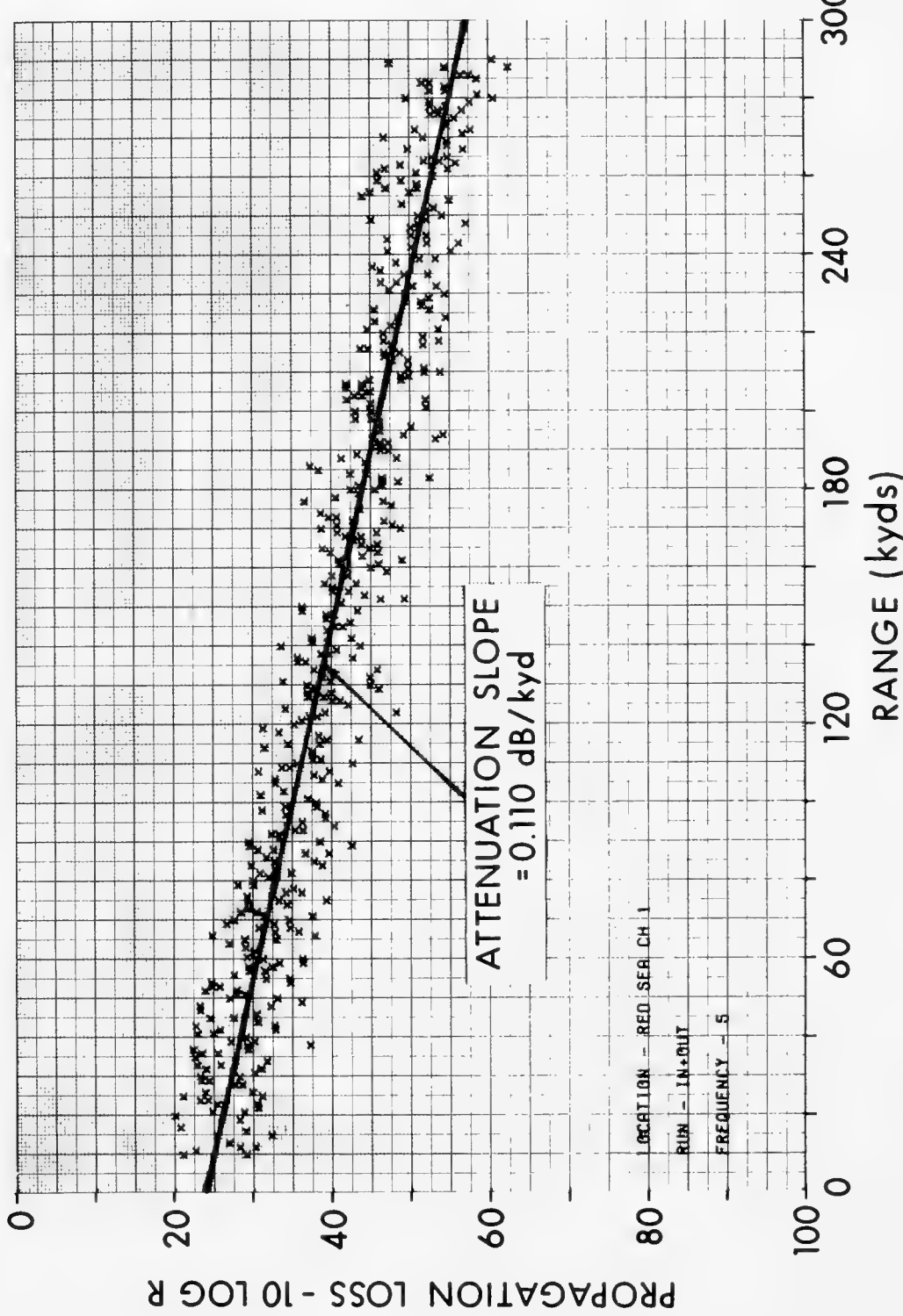


Figure 3. REGRESSION ANALYSIS OF ATTENUATION DATA AT 1410 Hz

BROWNING: ENVIRONMENTAL FACTORS AFFECTING LOW FREQUENCY
PROPAGATION IN THE OCEAN

Figure 4 shows the type of attenuation data Bob Mellen presented. It varies from location to location, but tends to be a relatively consistent picture of what is happening. Also, Figure 4 contains the Thorp formula.

After doing experiments in the deep ocean, we went to Hudson Bay, which was a shallow location, and found that the attenuation coefficients (Figure 5) were even higher than the Thorp formula, which is based on what we had consistently measured in the deep ocean.

Our first thought was: Is this experiment being contaminated by bottom effects? This, of course, not only entered our minds but the modelers were also quick to point this out. At this time, Fred DiNapoli in our laboratory was polishing his FFP program, so we said, "Let's get together and exchange ideas and see what we can come up with." It could be done with any of the many modern techniques such as Chick Weinberg's or others that have been mentioned, but it happened to be at a time that it would provide a good test for the FFP and also a good test for attenuation measurements.

What we were trying to answer in rough terms was this (see Figure 6): Was there an effect besides the basic absorption caused by diffraction out of the sound channel or scattering as Mellen has talked about? In other words, we wanted to see which of these components contributed to the increase in attenuation above the Thorp formula.

Figure 7 shows roughly what the conditions were up North. The Hudson Bay profile has a relatively shallow axis with a very strong gradient on the top. The average bottom depth was roughly about 500 feet. The bottom tends to be hard: bedrock over a thin layer of sandy clay.

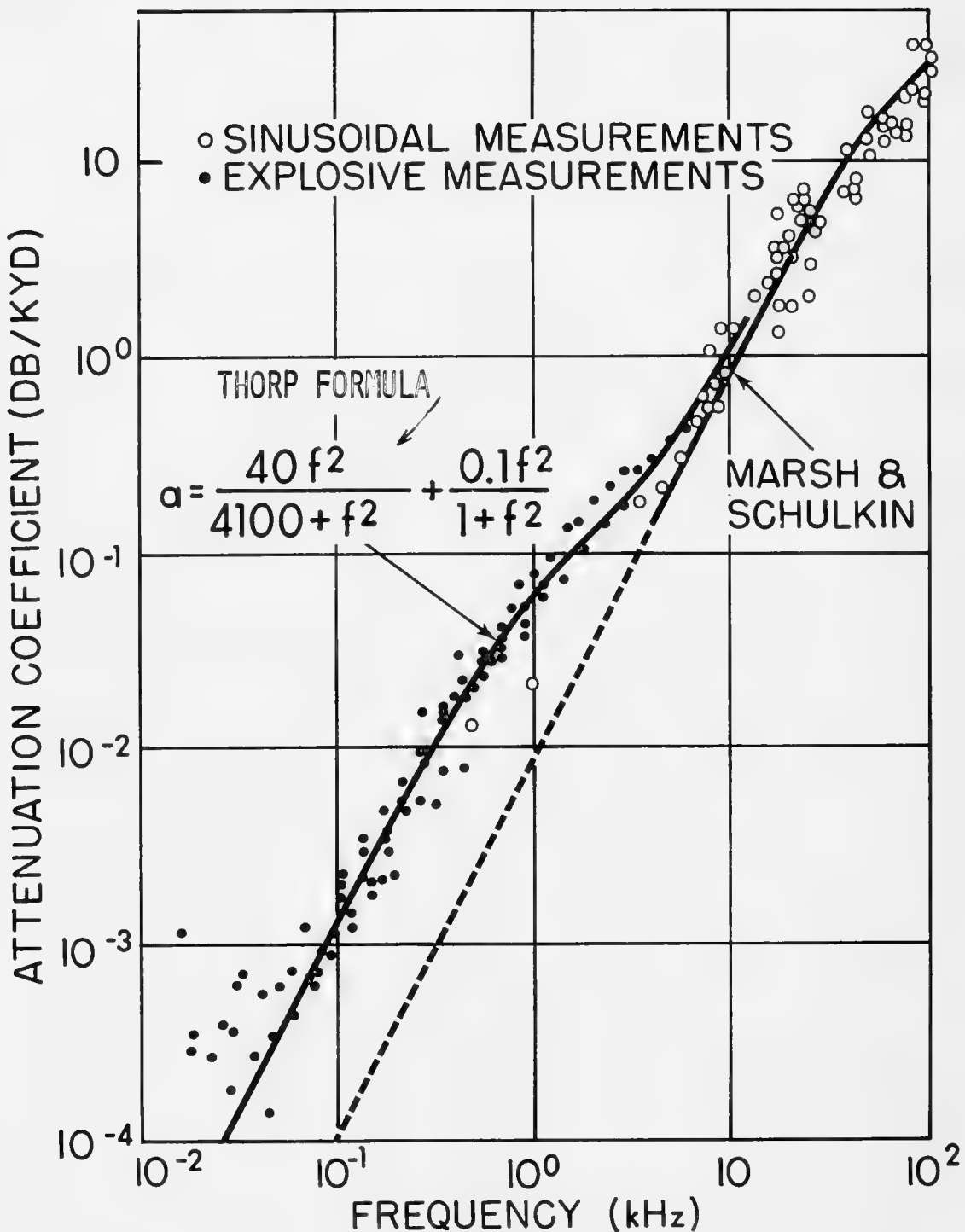


Figure 4. EXPERIMENTAL ATTENUATION COEFFICIENTS

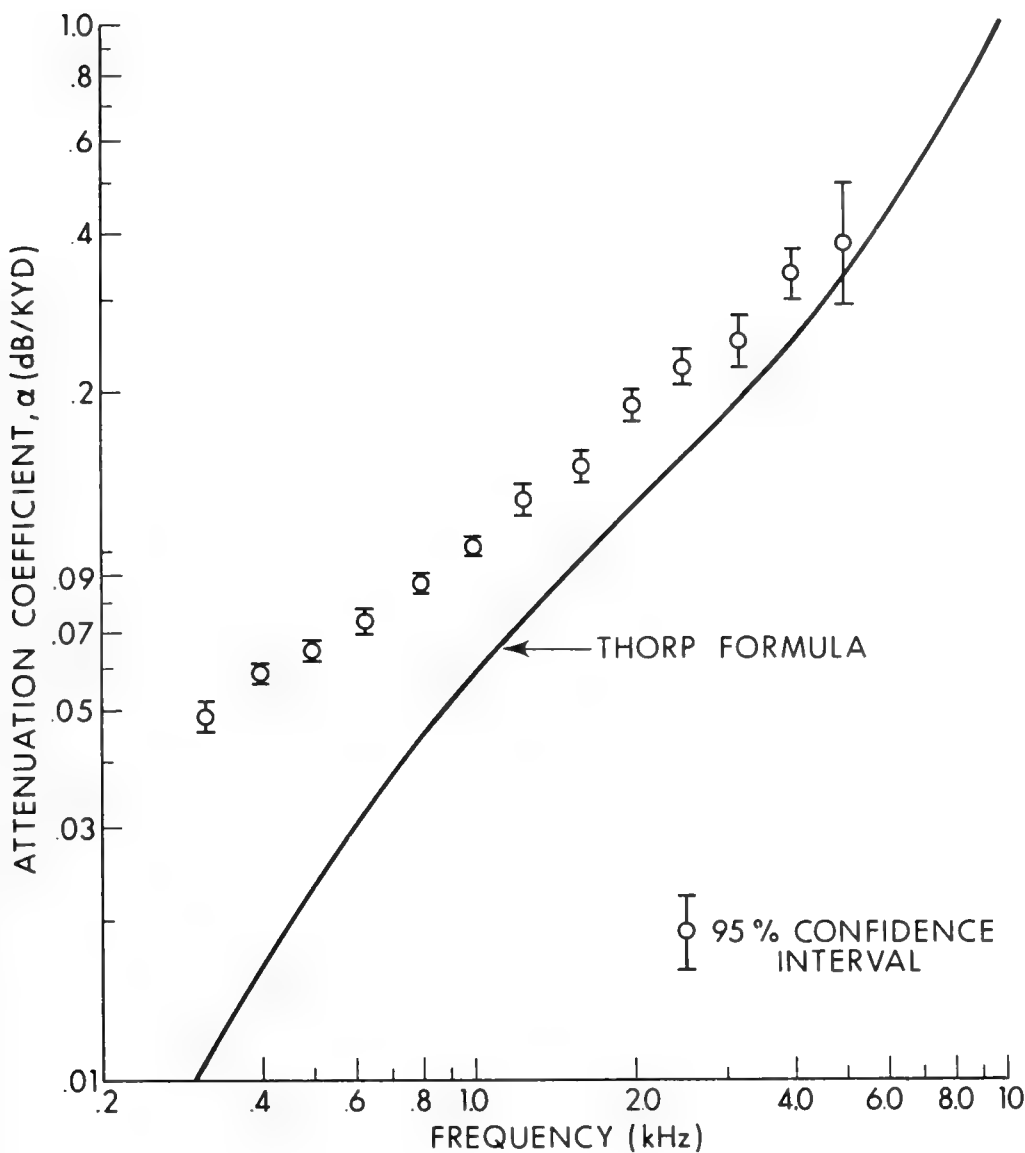


Figure 5. HUDSON BAY-1970 EXPERIMENTAL ATTENUATION RESULTS

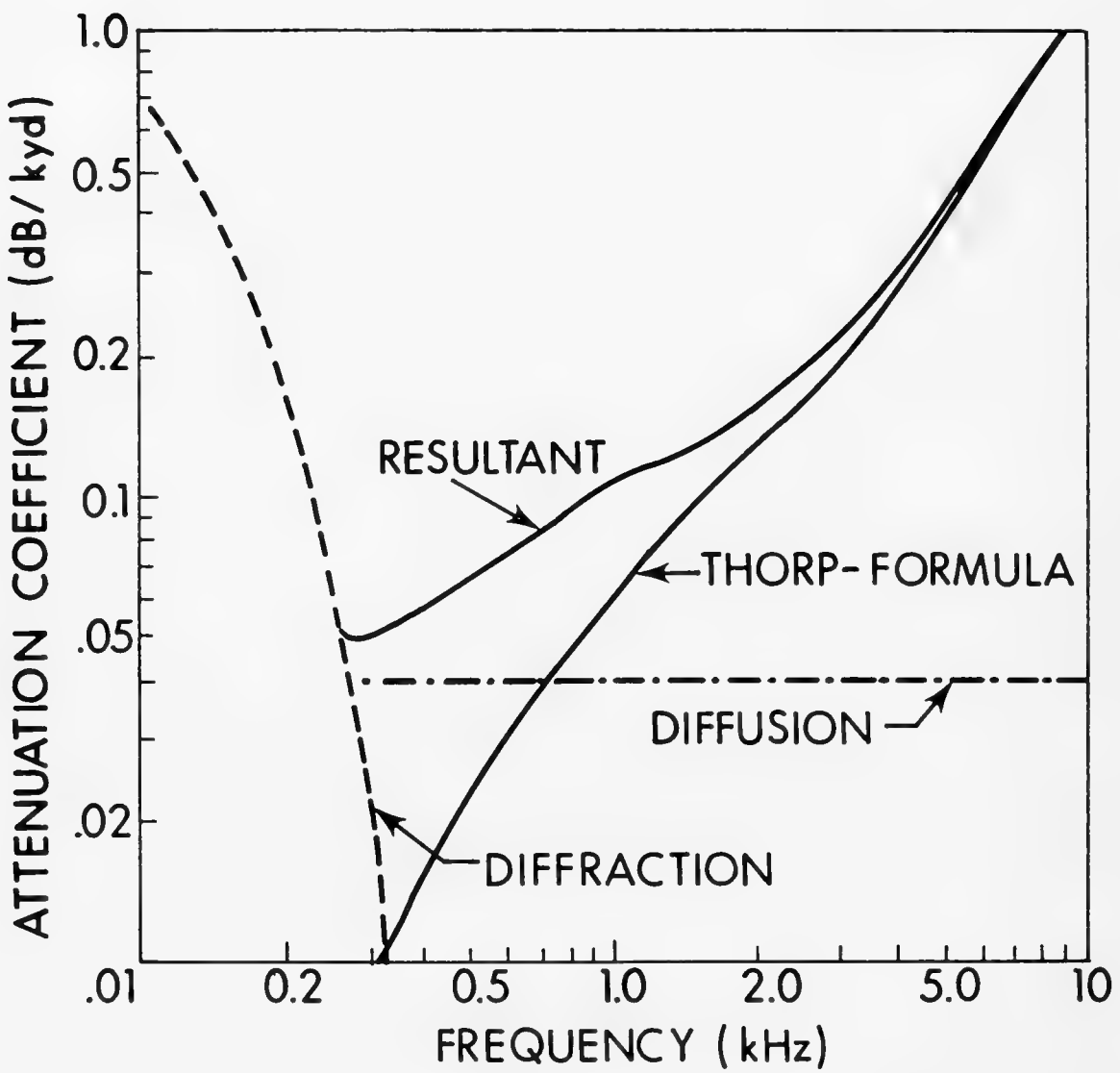


Figure 6. THEORETICAL SOUND CHANNEL ATTENUATION

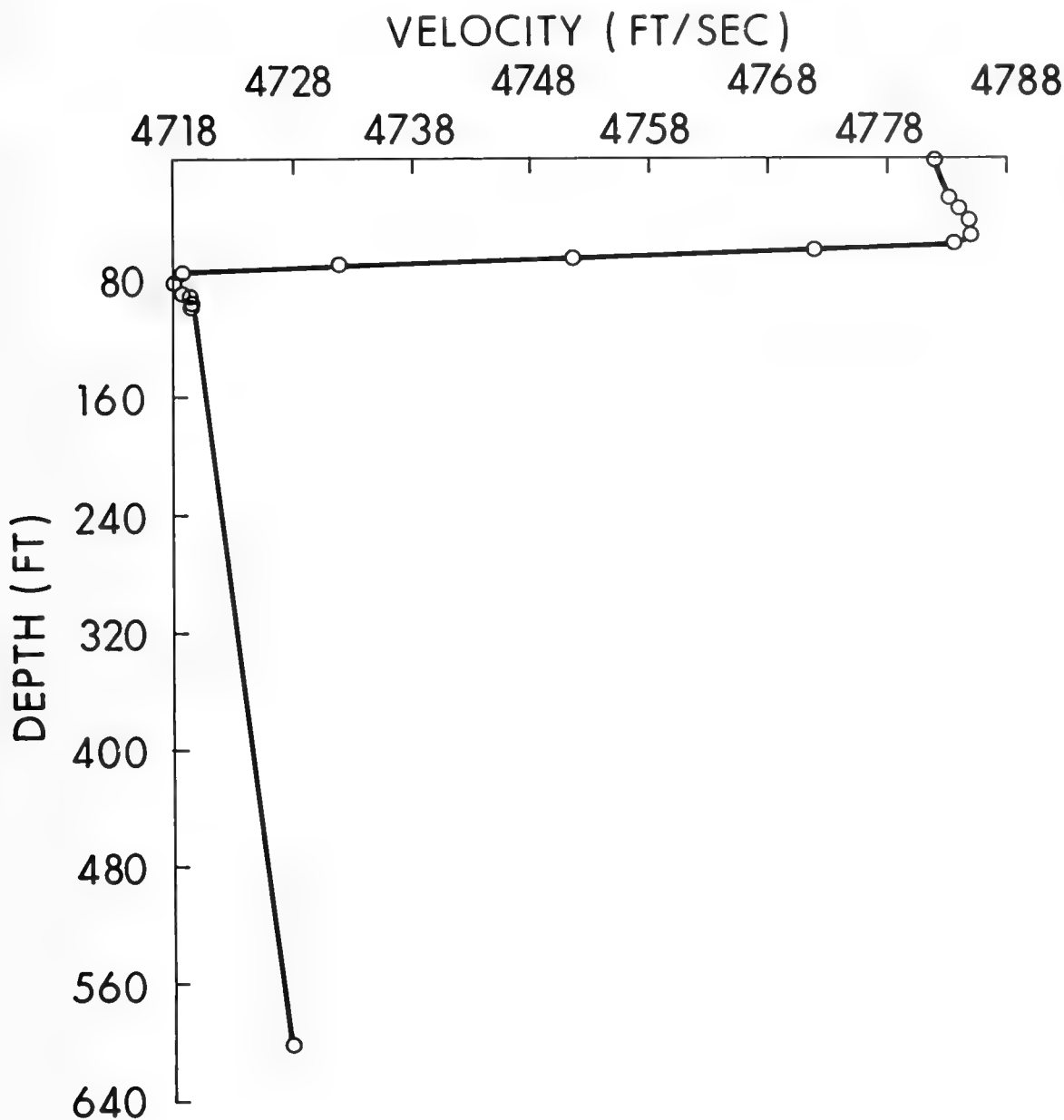


Figure 7. HUDSON BAY VELOCITY PROFILE, 15 AUGUST 1970

BROWNING: ENVIRONMENTAL FACTORS AFFECTING LOW FREQUENCY
PROPAGATION IN THE OCEAN

Figure 8 shows the results of DiNapoli's program for two different types of bottom: (A) a hard, low-loss bottom which essentially has no loss at all except at the very high grazing angles, and (B) a high-loss bottom, where there are large losses per bounce.

To put this in terms that experimentalists really get a feeling for and understand, we would run the program at a particular frequency for the two bottom conditions and various profiles, and compare the results obtained for a high-loss bottom with those obtained for a low-loss bottom.

The idea was that if we were at a high enough frequency so that there was no significant leakage out of the sound channel, then the results obtained by the two methods would be the same. In other words, if the sound energy does not see the bottom, it does not matter what the bottom is made of. Figure 8 is a demonstration of this point. These results correspond to a high frequency, several kilo-Hertz, and it is seen that basically the same answer obtains for either type of bottom, because all the energy is going right down the sound channel.

Figure 9 illustrates a case, at 50 Hz, where the bottom loss is obviously a factor. The minute the sound starts hitting the bottom, the high-loss bottom is just going to suck it right up, and the propagation loss gets much greater with the high-loss bottom than with the low-loss bottom.

We found, amazingly enough, that for frequencies above 300 Hz there was *no significant difference* using the high-loss or the low-loss bottom in DiNapoli's program.

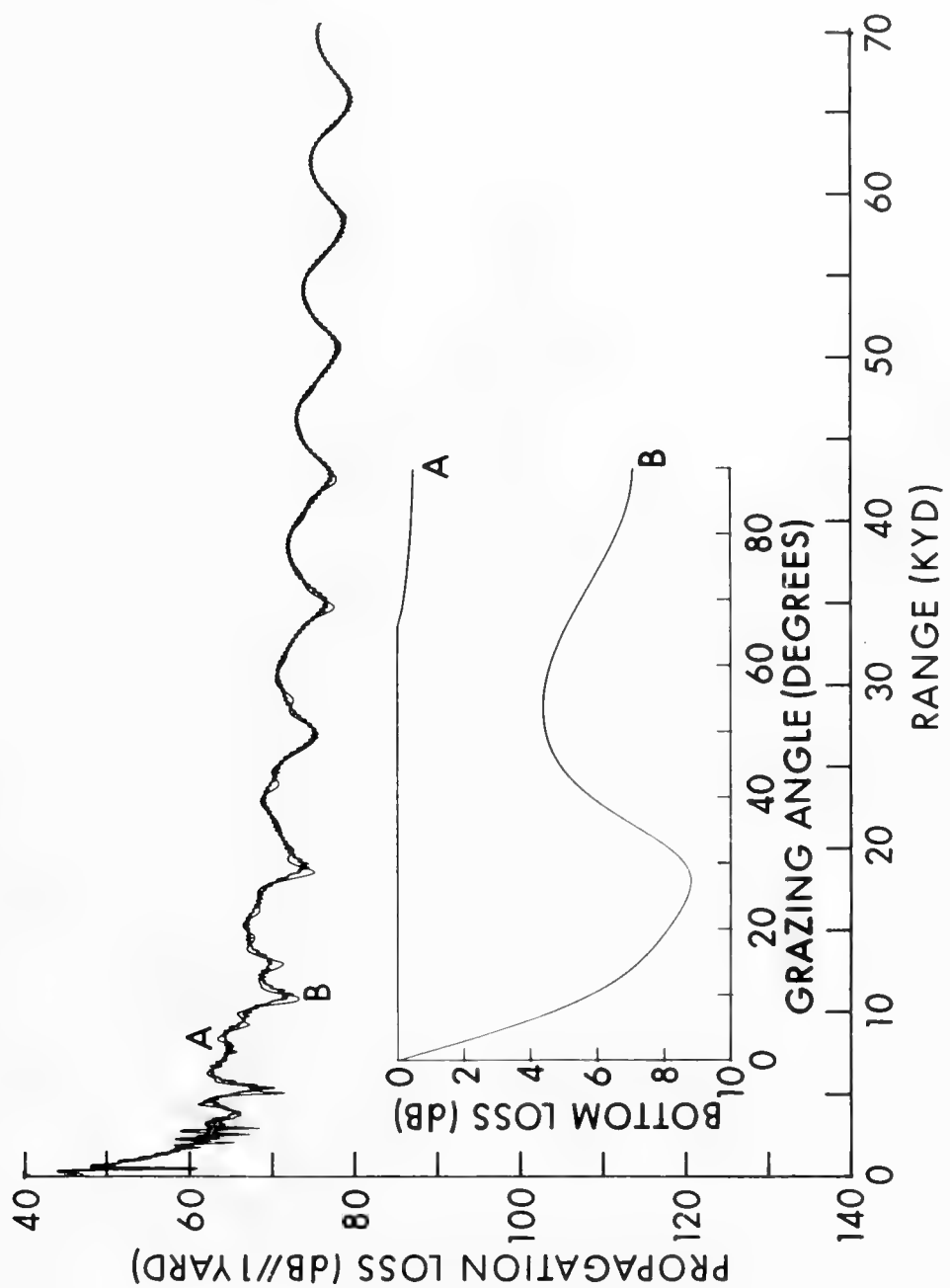


Figure 8. FFP MODEL RESULTS FOR TWO BOTTOM TYPES (HIGH FREQUENCY)

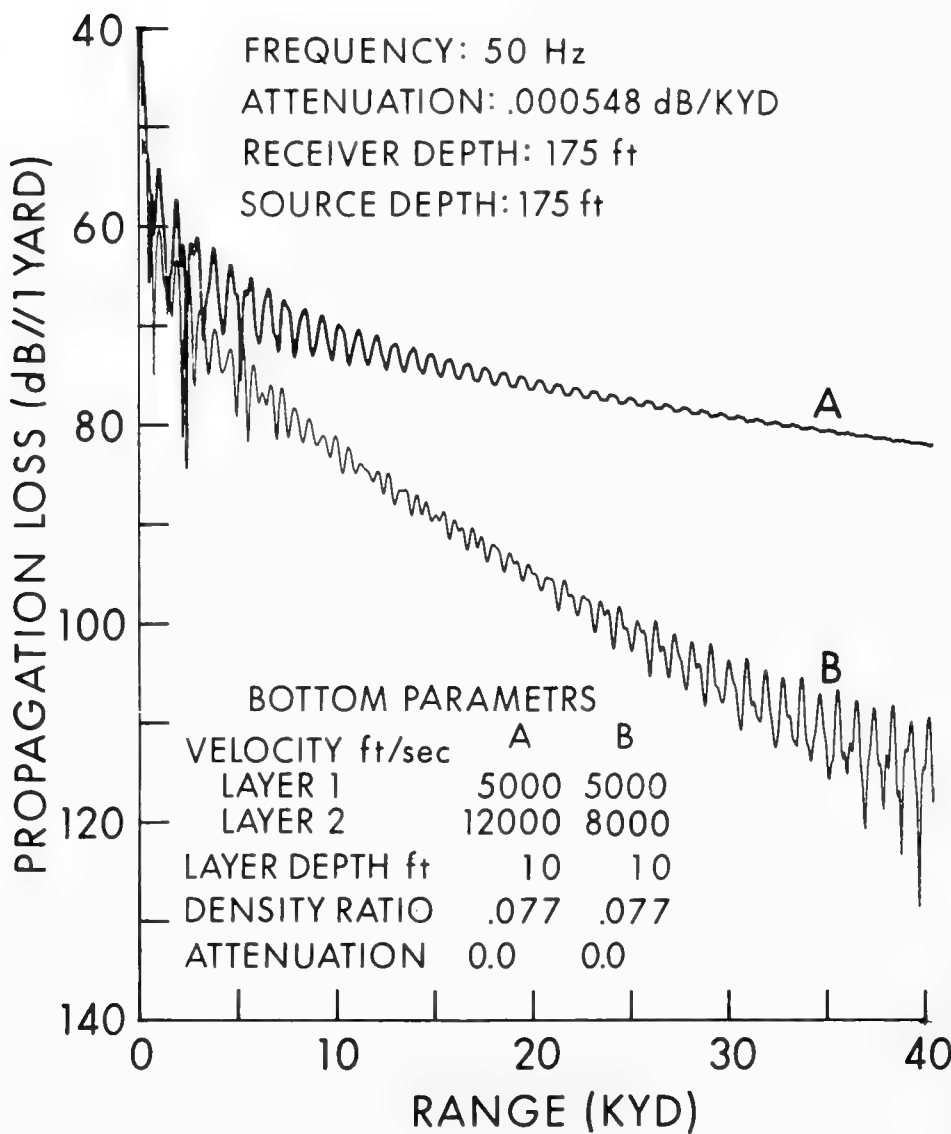


Figure 9. FFP MODEL RESULTS FOR TWO BOTTOM TYPES (LOW FREQUENCY)

BROWNING: ENVIRONMENTAL FACTORS AFFECTING LOW FREQUENCY
PROPAGATION IN THE OCEAN

The amount of attenuation can also be varied in the propagation-loss program. Figure 10 shows examples for various values of attenuation: one, three, and six times Thorp's coefficient. We took our experimental data (and again we are limited because we are using shots at discrete ranges, so we cannot see the fine detail that is predicted with a model) and chose a value of attenuation for the program which yielded the best fit. Figure 11 is the comparison of our experimental data with the FFP prediction program using an attenuation value of 0.054 dB per kiloyard at 400 Hz. A similar fit was obtained at 1000 Hz with attenuation of 0.113.

Now, we asked, if we get this value of attenuation for our best fit by overlaying the curves, what would we obtain if we applied the same linear fit that we used for our experimental data? That is, if we make a least squares fit, what value of attenuation would we come up with? The answer (see Figure 12) was 0.1126 compared with 0.1135. So there was hardly any difference between taking a straight-line fit to the data and overlaying the curves. Much to our surprise, these data points generated using a sophisticated modeling technique were almost identical to plain cylindrical spreading in the sound channel.

Figure 13 shows estimates of error. The squares indicate the amount of variation which gave an equivalent fit to our particular data points. You can see there was nothing here to convince us that cylindrical spreading was not as good as any other model for the case that both the receiver and source are on the sound-channel axis.

We have used the same analysis many times, for example in Lake Superior (a case where we felt there might be a problem), and we have come up with the same answer.

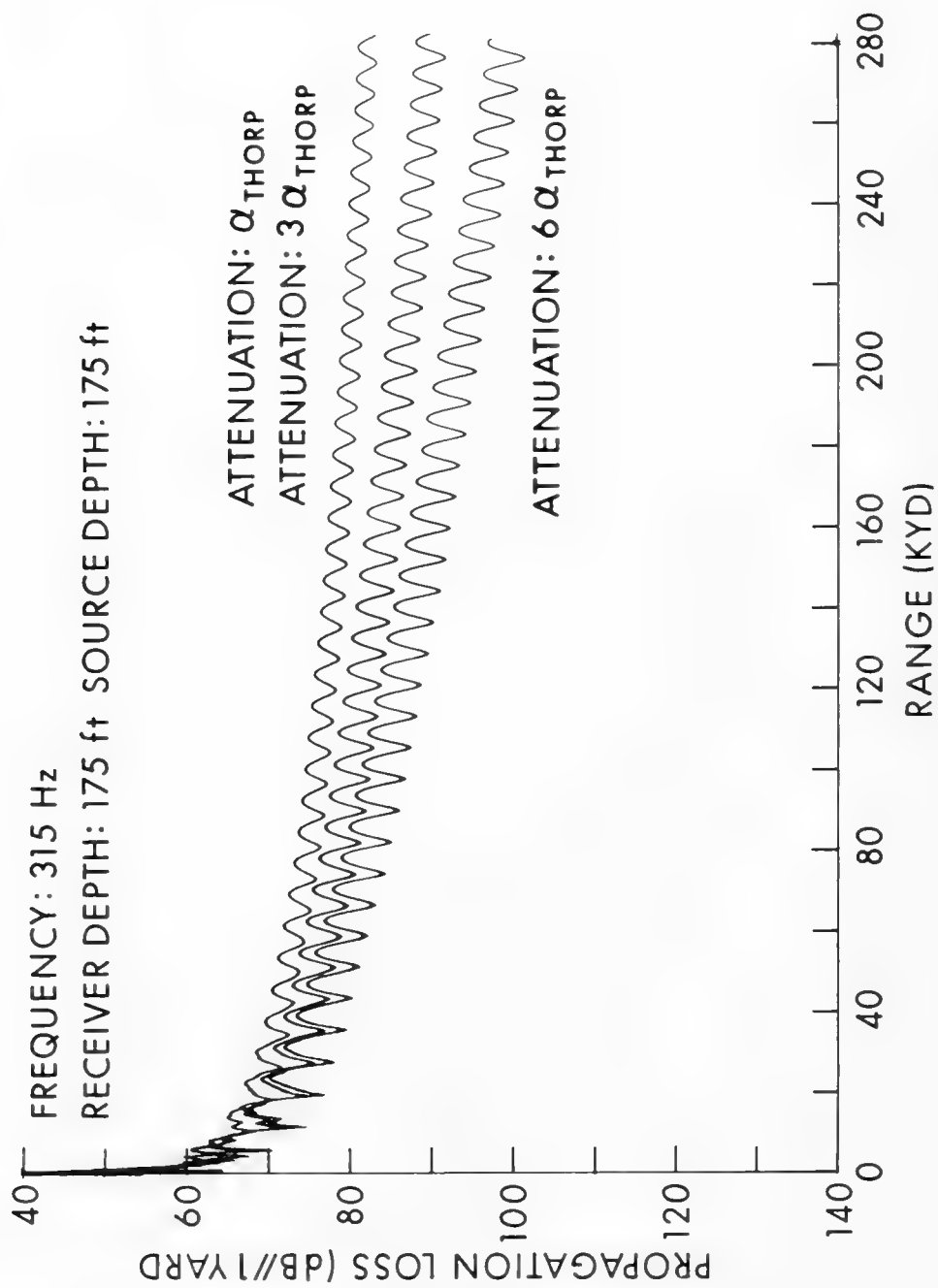


Figure 10. PROPAGATION LOSS VERSUS RANGE FOR THREE ATTENUATION FACTORS

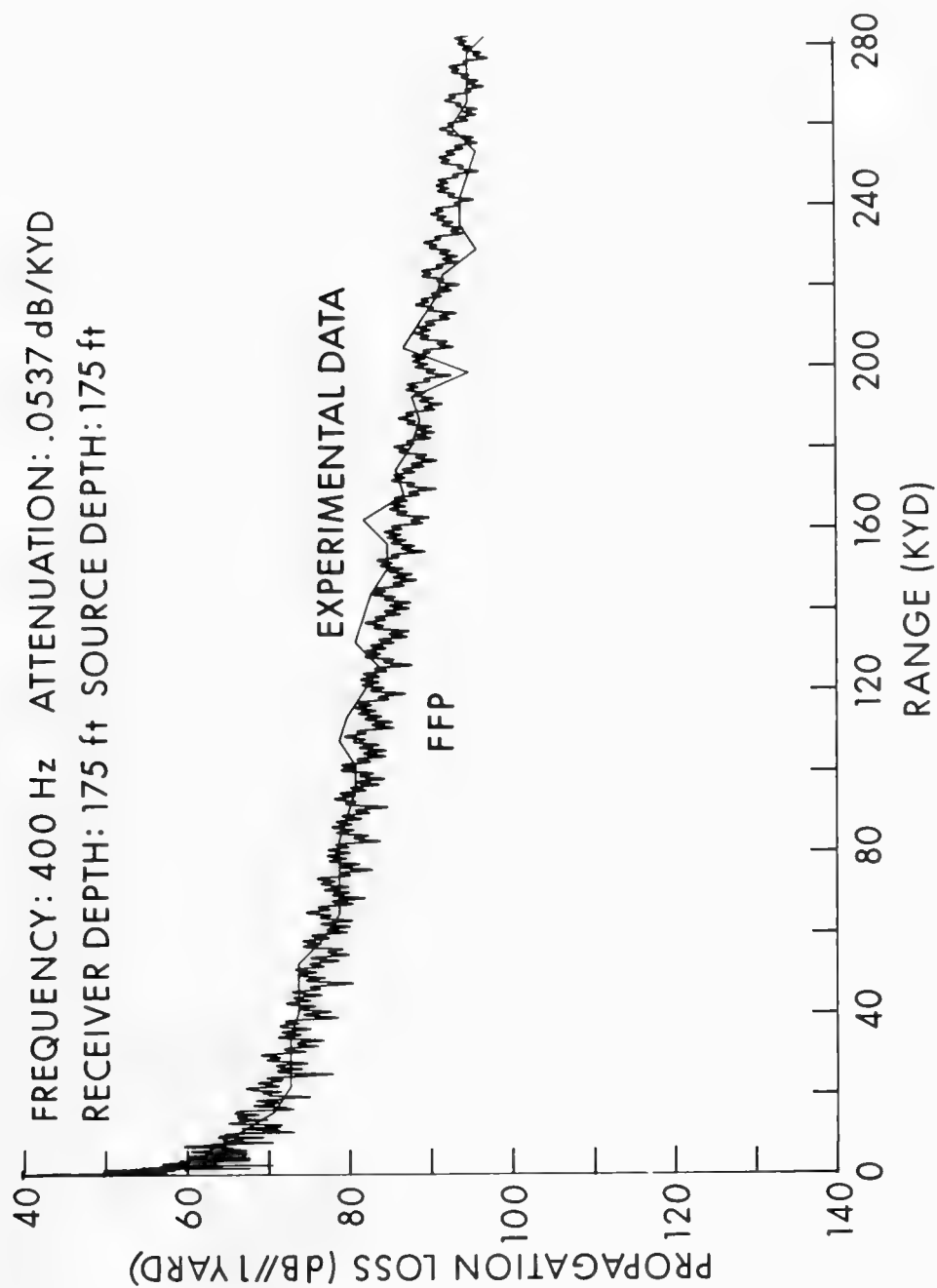


Figure 11. COMPARISON OF EXPERIMENTAL DATA WITH THE RESULTS OF FFP

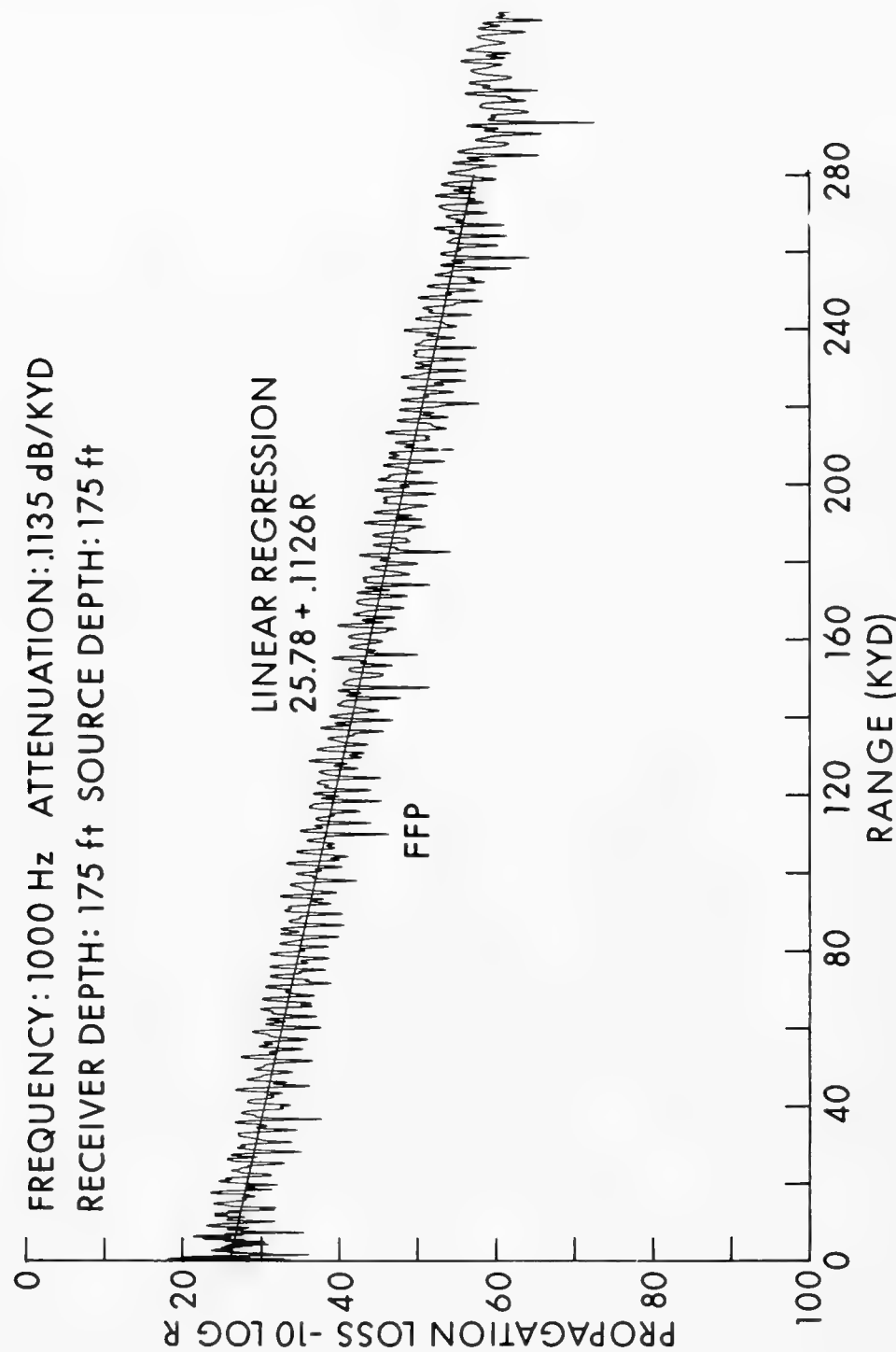


Figure 12. LINEAR REGRESSION OF FFP RESULTS

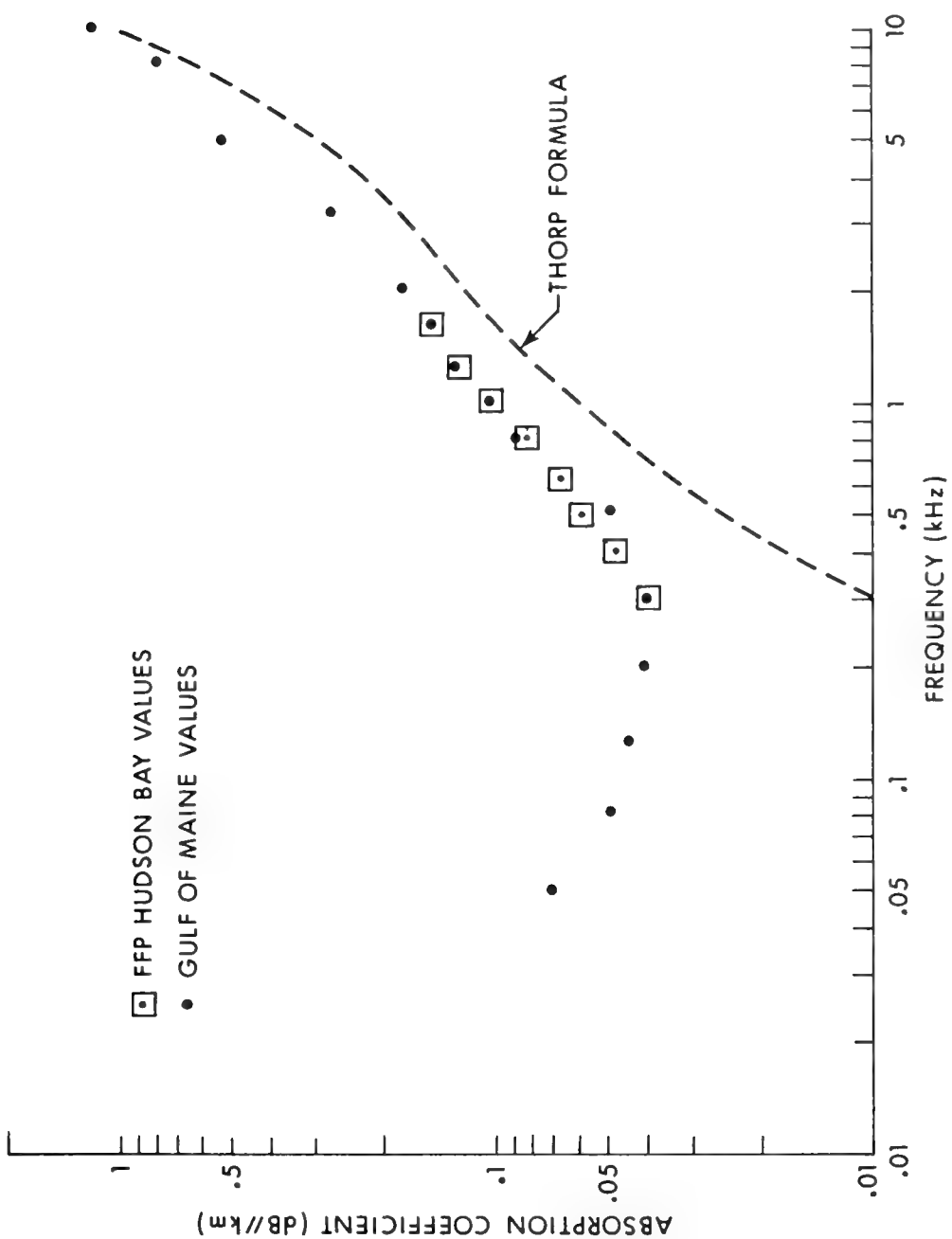


Figure 13. ESTIMATES OF MODEL ERROR

BROWNING: ENVIRONMENTAL FACTORS AFFECTING LOW FREQUENCY
PROPAGATION IN THE OCEAN

Once we had this, we thought we should extend it to typical deep-ocean environments and see what would be predicted about significant leakage out of a sound channel.

Figure 14 shows two profiles used for these predictions. One corresponds to the KIWI 1 experiment which Bannister has described and which was performed in the South Pacific. The other is the ATOE experiment, with a run east from Bermuda, which produced a large amount of good data appropriate to our comparisons.

We wanted to see where channel leakage becomes significant as a function of bottom depth and as a function of frequency. Also, where is there a significant difference between these two profiles in terms of propagation loss?

Figure 15 shows the bottom loss curves that we used. We felt for this case that we need not be as sophisticated as we were before, so we assumed a relatively simple form, since the effect would be the same.

Figure 16 is the comparison of propagation loss for the ATOE and KIWI profiles. We limited the depth for the KIWI profile so that both profiles had the same depth, 10,000 feet. Figure 16 is for 25 Hz, with both source and receiver at the sound channel axis. For KIWI, the axis depth was 3,000 feet, and for ATOE 2,700 feet.

As you can see, in terms of average loss, these curves are practically identical. The conclusions for our purposes was that for average propagation loss, which would, of course, result in attenuation along the sound channel axis, we could treat ATOE and KIWI as the same.

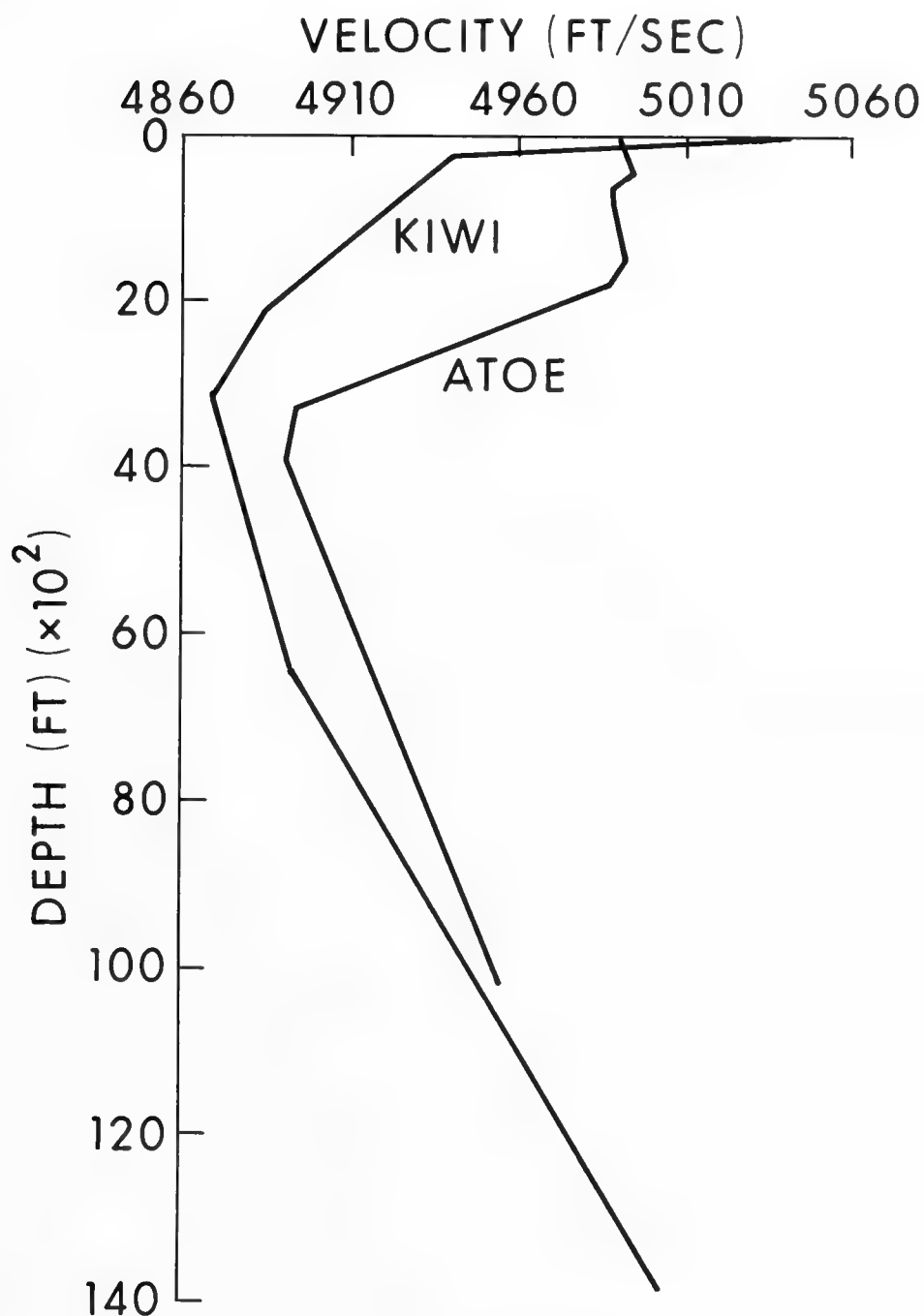


Figure 14. TWO DEEP-OCEAN PROFILES

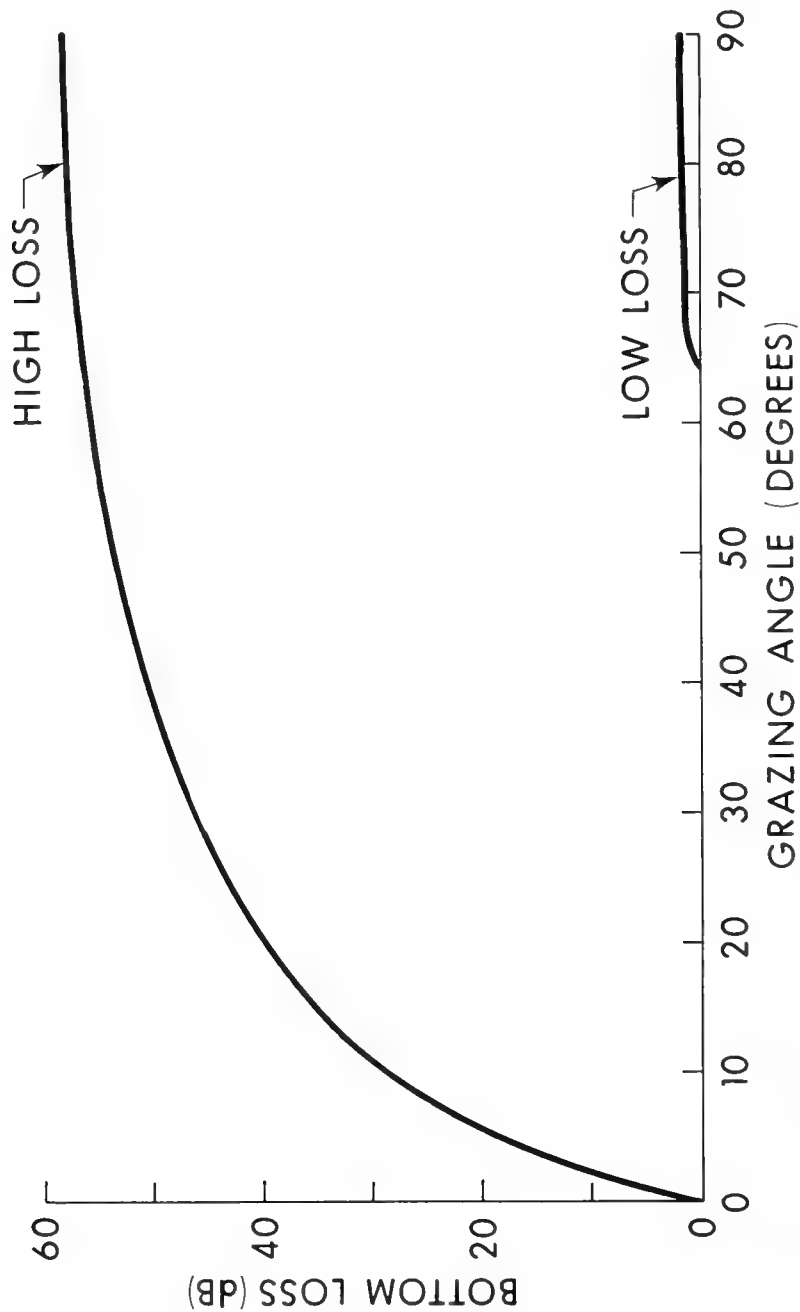


Figure 15. BOTTOM LOSS VERSUS GRAZING ANGLE

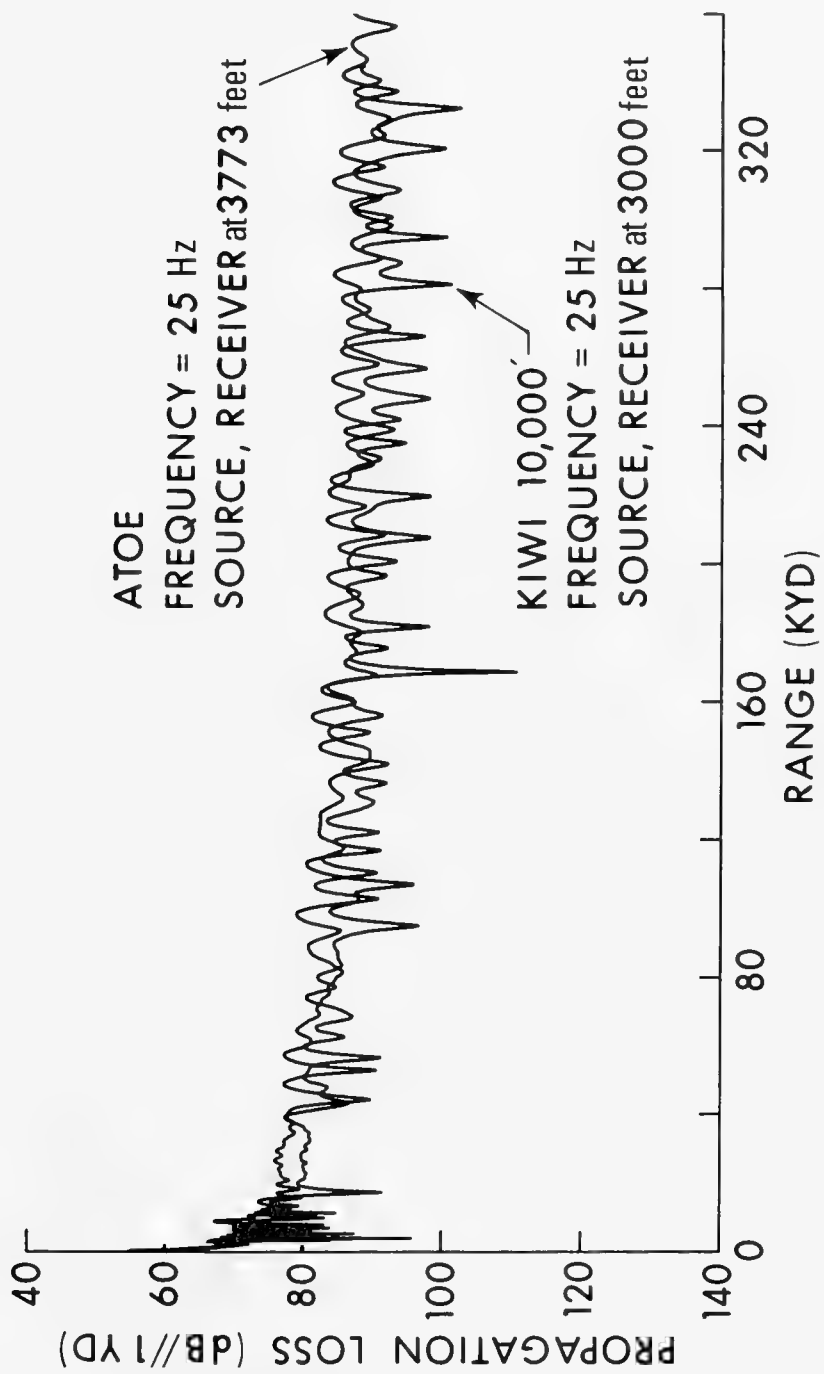


Figure 16. PREDICTED PROPAGATION LOSS VERSUS RANGE FOR KIWI AND ATOE PROFILES

BROWNING: ENVIRONMENTAL FACTORS AFFECTING LOW FREQUENCY
PROPAGATION IN THE OCEAN

Figure 17 shows the KIWI-profile transmission loss at 25 Hz. The axis is at 3,000 feet, along with source and receiver. We are comparing the high-loss and the low-loss bottom. As you can see, they fall right over each other.

First we compared the two profiles at a nominal frequency to see how the details compared. We next vary the frequency. Figure 18 represents the situation at 10 Hz, and you can start to see a difference appear both in the general level and in the detail of the propagation loss. They both go simultaneously because the minute the energy is being absorbed, you are losing in the amount of energy reflected.

Figure 19 shows the results at 1 Hz for the KIWI profile. Here there is really a significant difference between the high- and low-loss bottoms. Again, from an experimental point of view, you come to the question of what is significant. If you are talking attenuation, a small difference in propagation loss is very significant because attenuation is very small. It is a bit subjective where you draw a line about whether there is a significant difference and where there is not.

We made a series of model runs with different bottom depths. For a given frequency, if bottom depth is raised, then there will be certain modes that cannot be contained that could be contained in deeper water. Conversely, for a given bottom depth, that number of trapped modes will vary with frequency (see Figure 20). Figure 21 shows the KIWI-loss prediction at 25 Hz for bottom depths of 4500 and 4000 feet.

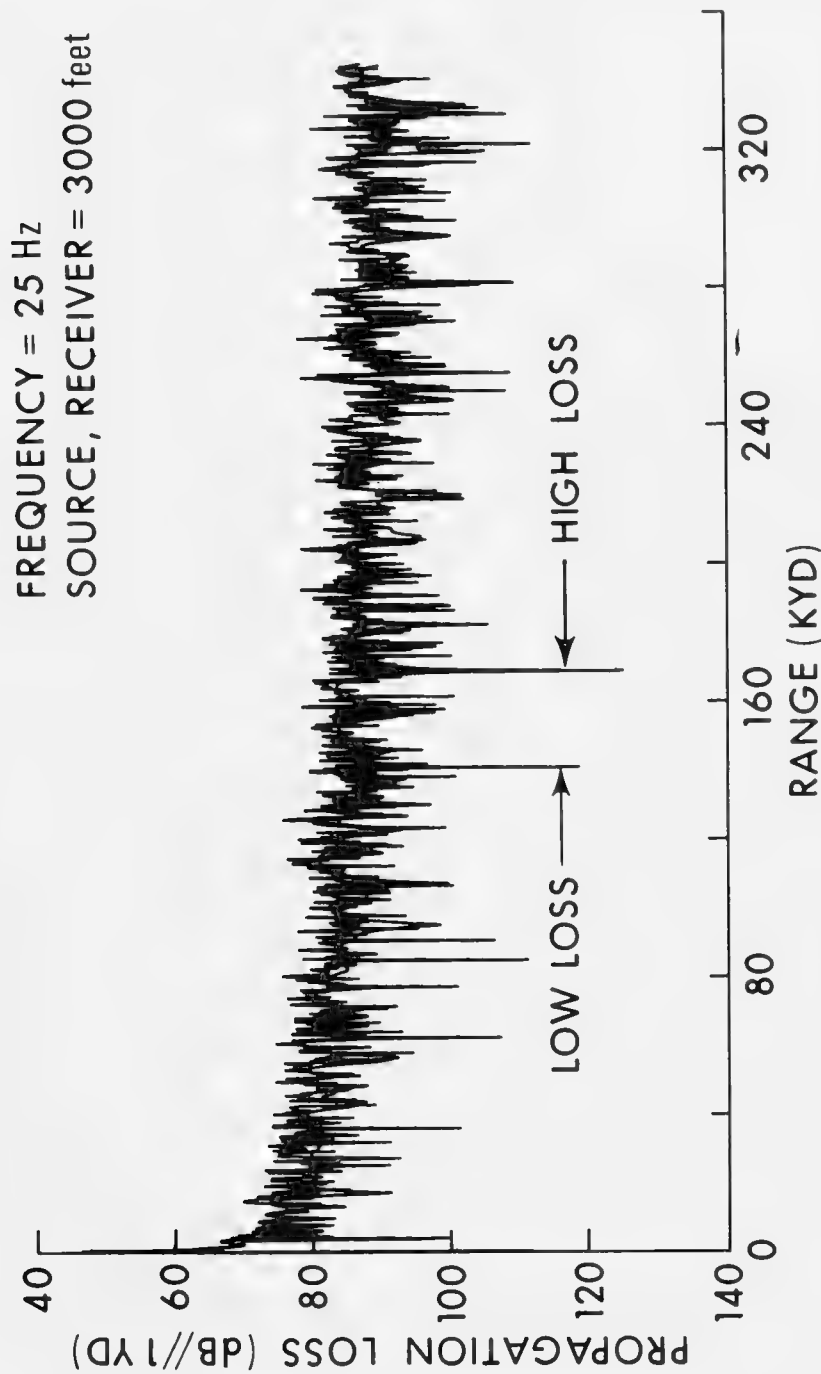


Figure 17. KIWI-PROFILE PREDICTIONS FOR HIGH- AND LOW-LOSS BOTTOM

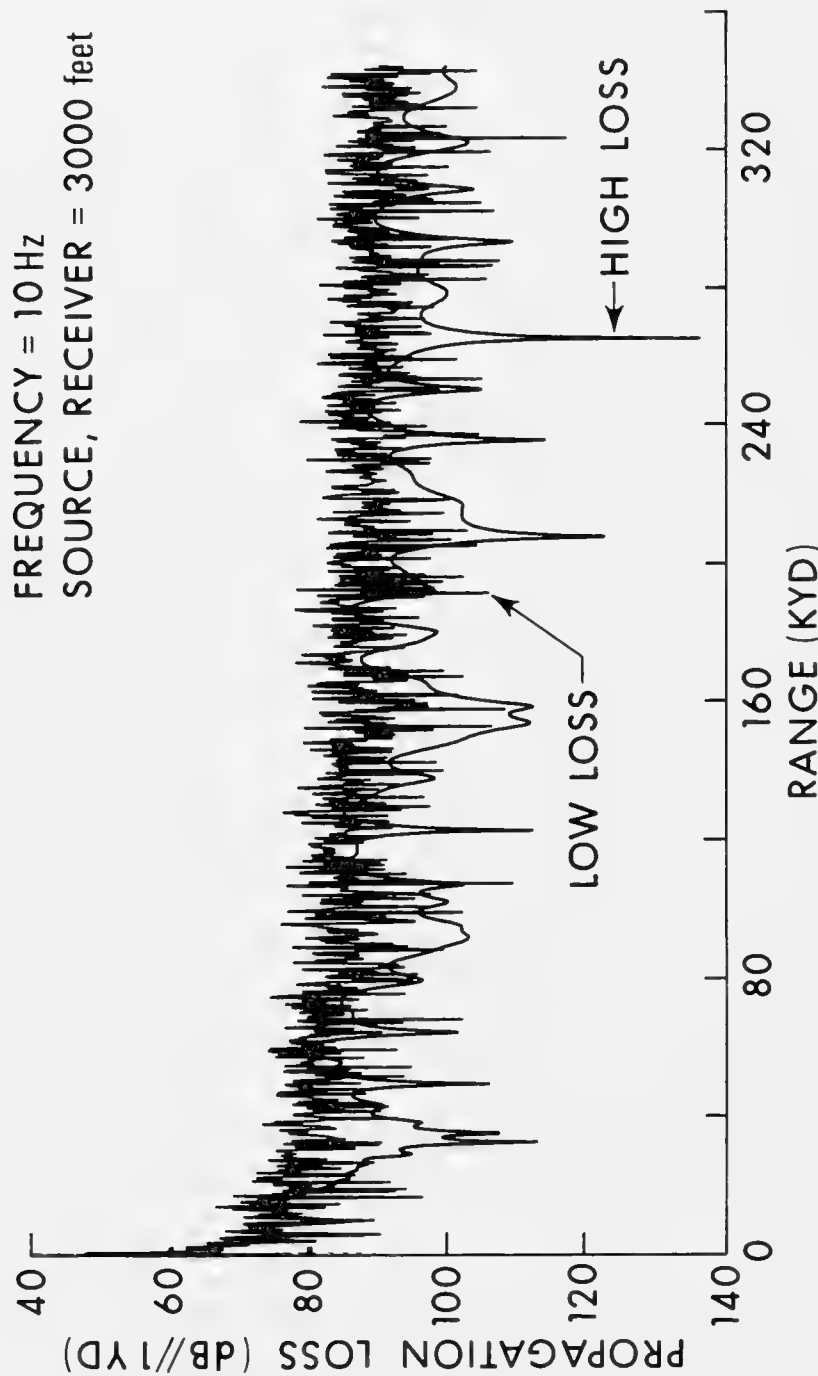


Figure 18. KIWI-PROFILE PREDICTIONS FOR HIGH- AND LOW-LOSS BOTTOMS

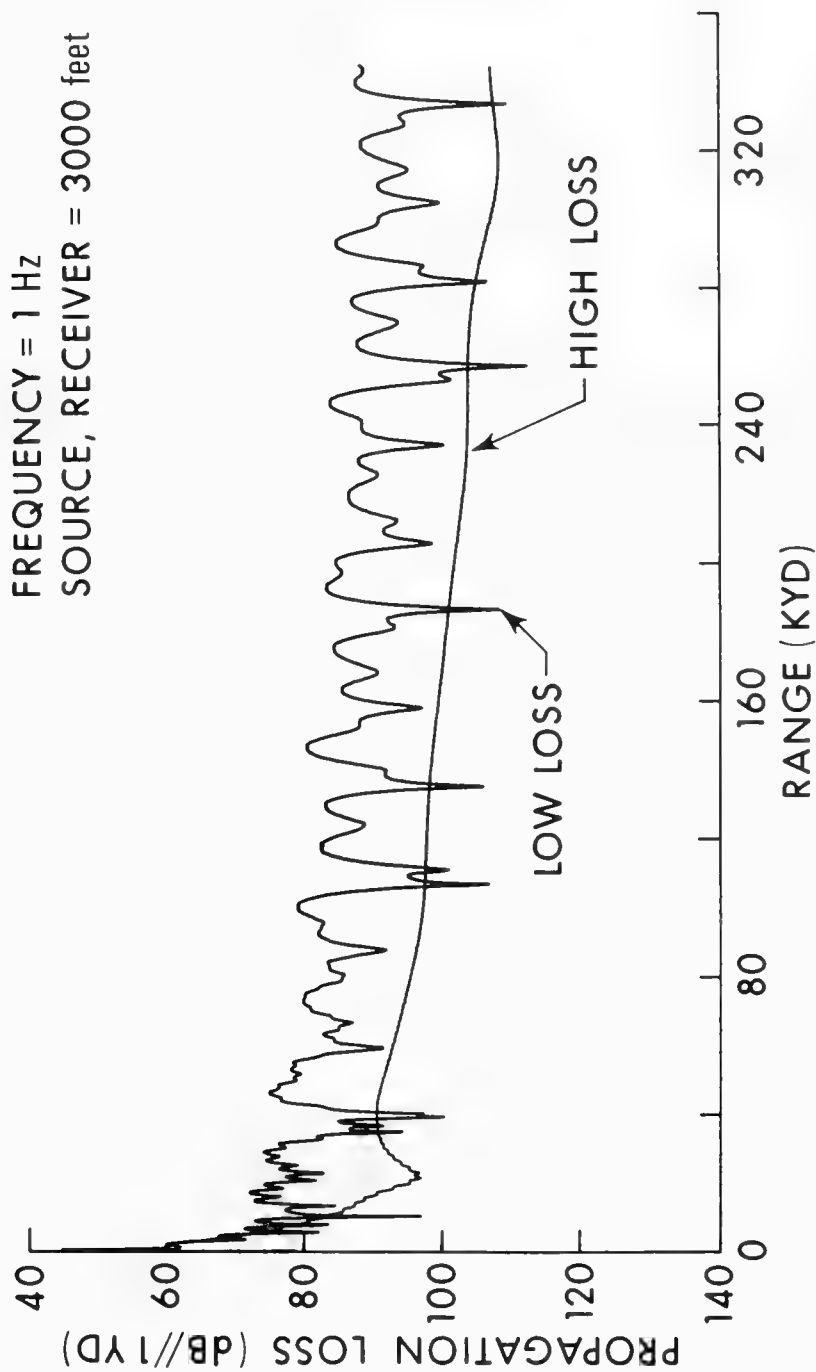


Figure 19. KIWI-PROFILE PREDICTIONS FOR HIGH- AND LOW-LOSS BOTTOM

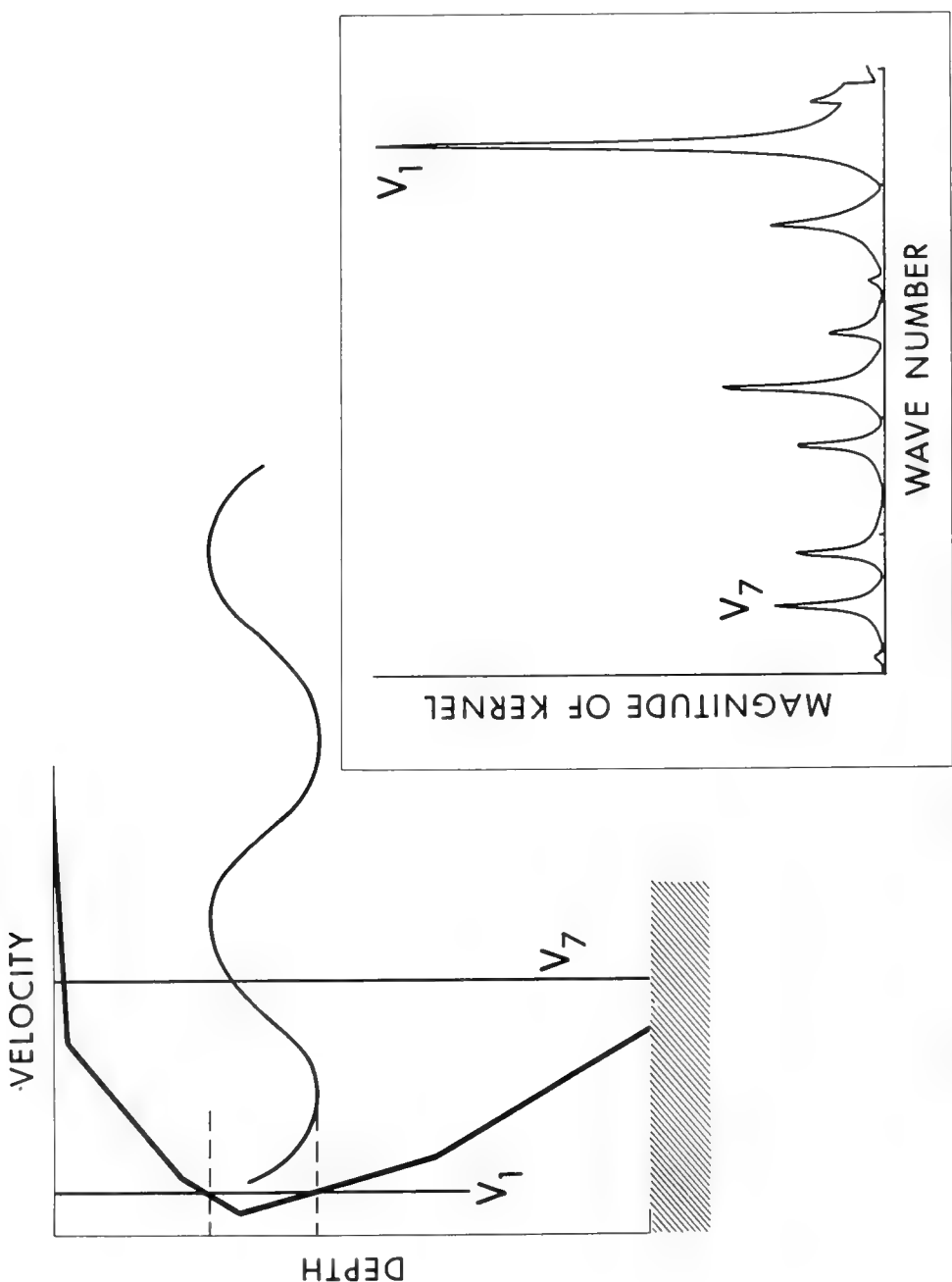


Figure 20. EFFECT OF DEPTH ON MODE STRUCTURE

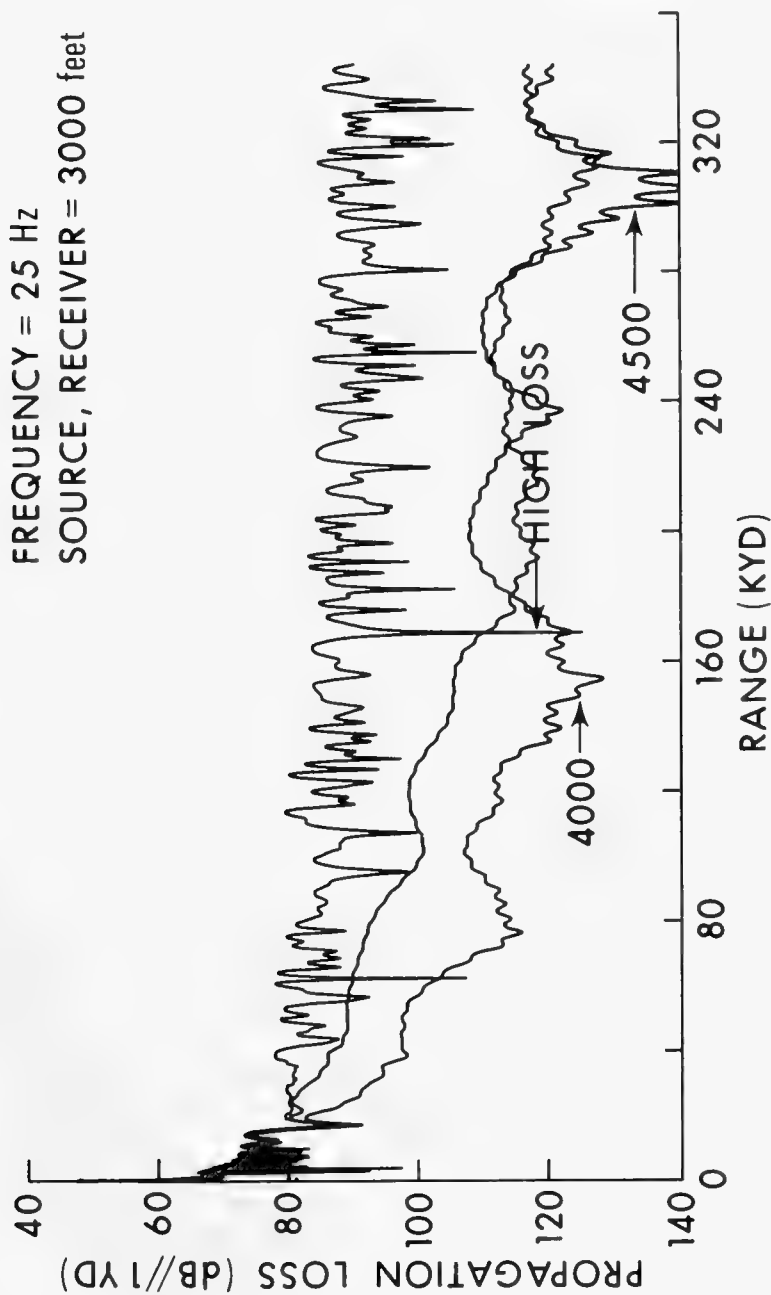


Figure 21. PREDICTED KIWI PROPAGATION LOSS VERSUS RANGE FOR THREE BOTTOM DEPTHS:
4000, 4500 and 10,000 FEET

BROWNING: ENVIRONMENTAL FACTORS AFFECTING LOW FREQUENCY
PROPAGATION IN THE OCEAN

The curve of Figure 22 indicates a region where diffraction from the sound channel would not contaminate the attenuation coefficient calculations. In the region above the curve (for example, at 60 Hz and a bottom depth of 12,000 feet) there is no significant loss from the sound channel. On the other hand, below the curve (for example, at 10 Hz and a depth of 4000 feet), any attempt to make an attenuation measurement would certainly be contaminated.

In summary, this represents our first attempts to compare what the modelers are doing with what we are trying to do experimentally. This relationship can lead to improved determination of attenuation.

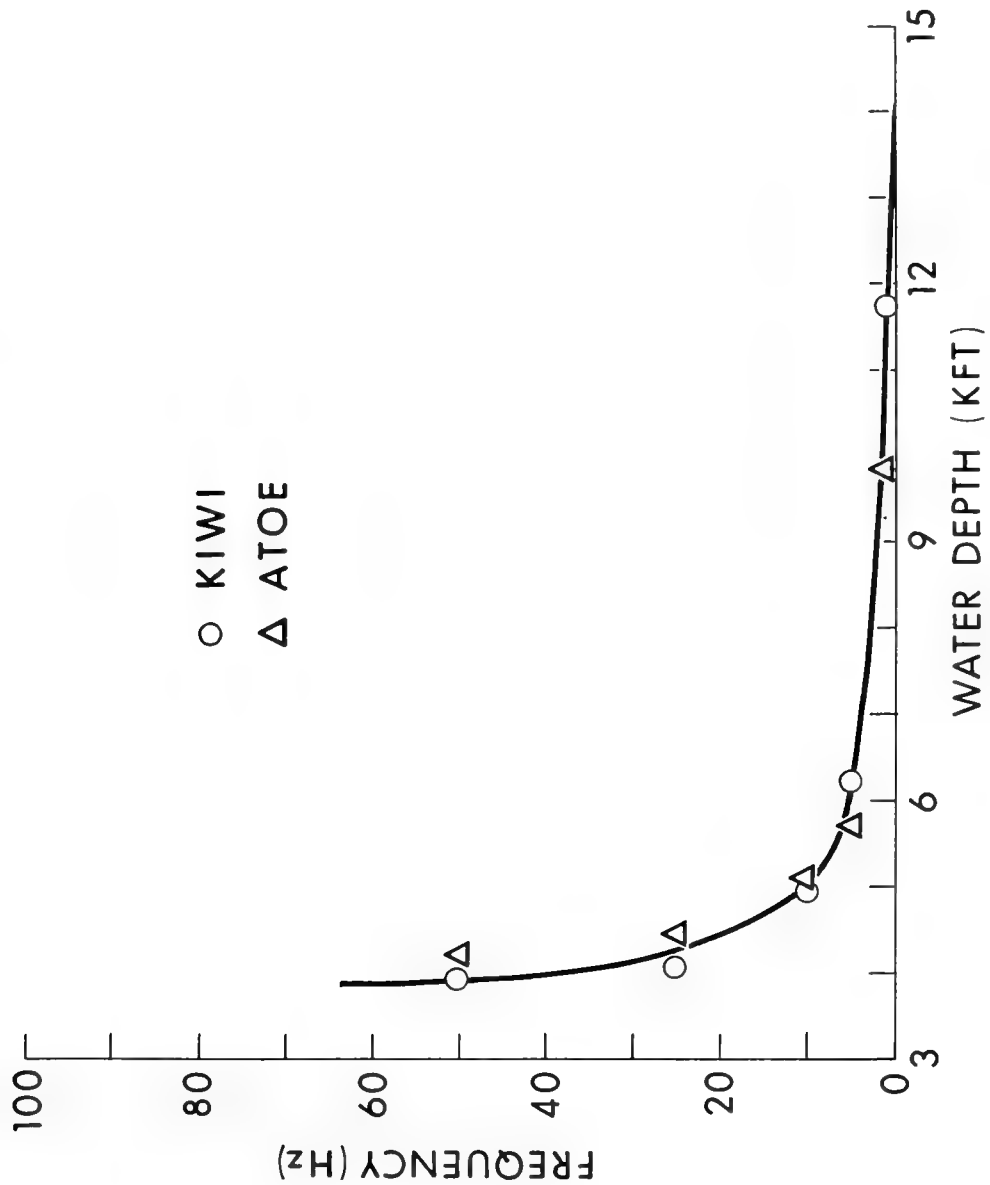


Figure 22. BOUNDARY OF REGION IN WHICH THERE IS SIGNIFICANT CHANNEL LEAKAGE

BROWNING: ENVIRONMENTAL FACTORS AFFECTING LOW FREQUENCY
PROPAGATION IN THE OCEAN

DISCUSSION

DR. S. W. MARSHALL (Naval Research Laboratory): In your discussion of the Hudson Bay data you showed that after you strip out the deep rays the transmission loss goes like $1/R$ plus an attenuation term. Now, if the rays hit the bottom many times over the course of 100 kilometers and even though (as we agree we can't do) you assign so many dB loss per bottom bounce, then that translates to so many dB loss per 100 kilometers, which is a linear function of the range. How can you separate that from what you would attribute to the attenuation?

DR. D. G. BROWNING (Naval Underwater Systems Center New London Laboratory): I think when you look at the arrival structure it would be obvious to you if the paths weren't going along the axis but were bottom reflected. For example, I believe recently there's been an experiment conducted in Baffin Bay where you see this happen. When you get to very low frequencies the energy is going out of the channel and hitting the bottom and it's a very loss-less bottom there, so it comes back and you will see a whole train of arrivals.

DR. MARSHALL: Yes, but in the very shallow water of Hudson Bay can you separate those arrivals?

DR. BROWNING: Yes. That's surprising — Even Lake Superior. We went to Lake Superior which is about the weakest channel you could find, and everybody said, "Oh, you're going to have to record FM because the arrivals are going to be falling over one another, and you're going to have a heck of a mess."

BROWNING: ENVIRONMENTAL FACTORS AFFECTING LOW FREQUENCY
PROPAGATION IN THE OCEAN

And we found it was just like a regular sound channel. It's amazing. It's just a question of experience.

This is what we found out. Shallow channels act like deep ones for most frequencies, except when you get low.

Dr. Marshall: So what you're saying -- and this is in question form -- is that the Hudson Bay data -- which I think was the first slide you put on the screen -- really included only that energy which was in the axial RR mode? Is that right?

Dr. Browning: That's what we believe. We can compare peak arrivals versus taking the energy of the whole envelope. We do this too. The cheap way, of course, with sound channels is to take the peak arrival because the axial ray is largest and it keeps by itself. But when we get in Bannister's area that's another problem because they find situations where the axial arrival doesn't come in last.

And so the question is: What if you move between zones where this arrival starts falling off? That's another problem to think about.

AMBIENT-NOISE MODELS

R. C. Cavanagh
Office of Naval Research (AESD)

Ambient-noise prediction schemes are viewed in terms of three basic components: (a) submodels which characterize source locations, levels, and coupling mechanisms, (b) a propagation submodel which calculates the acoustic field at the receiver generated by each source, and (c) an algorithm for combining the fields at the receiver. The results of a survey of noise models in operation today suggest a division into two classes:

- The POINT MODEL is intended to estimate the noise field at a discrete point in space and time; it thus requires detailed source information and precise transmission loss from each source to the receiver
- The FIELD MODEL predicts the noise field averaged over receiver location and time and, hence, permits averaging both the source positions and transmission loss.

Applications and advantages of each type are discussed.

Serious limitations in present noise-prediction capabilities are shown to be related to the ship-source submodel and to the proper treatment of propagation in the range-dependent ocean environment.

My task is to give an overview of our present-day capabilities in the area of ambient-noise prediction modeling. I will discuss where we are now and where we are headed.

During this conference we have spent time discussing the effects of the medium on signal transmission. When we come to the subject of ambient noise, the problem must be an order of magnitude more difficult since it involves the propagation of signals from many sources.

I have heard several comments over the last few days which should help to put the noise-prediction question into perspective. One person told me that he is amazed if he sees good agreement of a present-day ambient noise prediction with an experimental measurement because of the complexity of the inputs and the uncertainties involved. Another person told me that as many as 10 years ago, when we had little information about shipping densities and distributions, it was relatively easy to predict noise levels to within a decibel or two. So this is the point of departure.

This paper addresses the question of ambient-noise prediction modeling and we point out the obvious: anybody can construct an ambient-noise model instantly. Given the sources and a receiver, all we need are the characteristics of the sources, how they couple with the medium, the transmission to the receiver, and a way to add up all the results. Very simple.

Consider first what we might call the ultimate ambient-noise model, one for which we know: the locations and radiation characteristics of all sources in the ocean basin, the mechanism by which each source couples to the medium, and the properties of the sound transmission from each source to the receiver. The contributions of each source are then summed up in a way that is appropriate to the application: whether it be array response or simply omnidirectional reception.

We could stop right here, since we do not have this detail in the information about sources or sound transmission available to us today, and we cannot expect to have it for years to come. Instead, let us use the ultimate model as a basis from which to view what is being done today and what we expect to be accomplished in the near future.

We have identified three submodels that make up an ambient-noise model: source, transmission, and summation. Focus now on the first of these. Ambient noise sources include such things as biologics, rain, seismic activity, oil drills, oil explorations, distant shipping, and wind action. Here we concentrate on what most of the existing models predict: ambient noise resulting from distant shipping and wind action on the sea surface. These two cover the prevailing sources in the regime from 20 Hz up to several kHz as shown in the Wenz-type curves of Figure 1 (after Wenz, 1962).

Consider first the wind noise sources and wind-dependent ambient noise. Our experience has been that wind-dependent noise can be predicted with good accuracy, provided that the wind speed is known and the acoustic frequency is above 200 Hz. Almost every model that we have reviewed either adds a Wenz level as an isotropic component to the noise or performs a ray calculation of the noise level in the following way:

The source is considered to be a continuous distribution of point sources located on or just below the ocean surface. If transmission ray paths are added incoherently, then each source has dipole directivity. Source spectrum levels (dBs referred to 1 μ Pa per unit area of surface at unit distance) will be constant below about 500 Hz and then fall off at 3 dB per octave. Typical values are 70 dB for a 40-knot wind at 100 to 500 Hz and 40 dB for a 1-knot wind at 5 kHz. In an isospeed ocean, these will yield levels consistent with Wenz (1962) or Knudsen (1948) wind noise.

If the model is to estimate depth dependence and vertical directionality, then propagation from each source to the receiver can be predicted by ray theory. Range-averaged transmission loss will

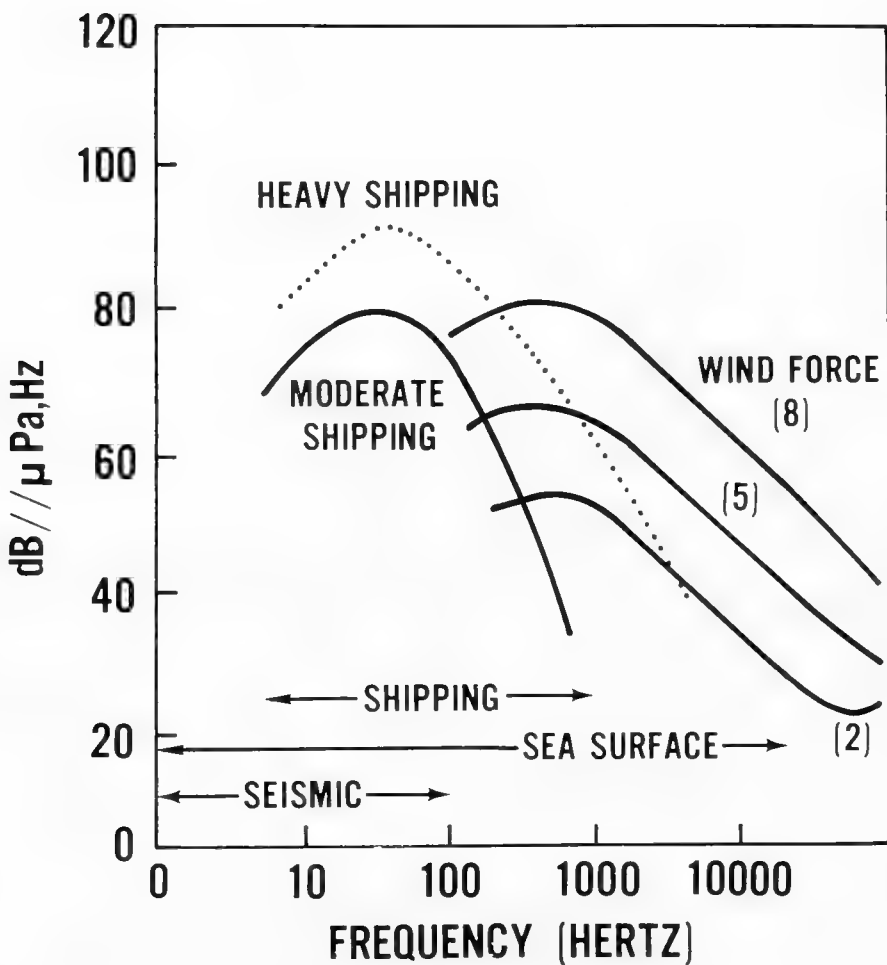


Figure 1. PREVAILING NOISE LEVELS

suffice since the sources are distributed on the ocean surface. The sources' dipole directivity induces the wind-noise directionality in the sense that arrivals will usually be concentrated in steep angles. Note that fluctuations in wind noise are not available from a model like this, except for those long-term variations due to changes in average wind speed.

Let us turn now to ship-generated ambient noise. We would like to know the precise location of each ship in the basin, its speed and course, and its radiated noise level. We want to know how to characterize the source. Is it a point source 20 feet below the surface or is it a distributed source at some other depth?

The model of sound transmission from source to receiver need not have greater resolution than that inherent in the input information for the sources. In other words, if we do not know the location of a ship to within 30 or 40 miles, then there is no point in trying to predict transmission loss any more carefully, unless we are considering the special case of studying the fluctuations of ambient noise resulting from movements of ships. For the usual application in which we are estimating the average ambient noise level, we need an accurate range-averaged transmission loss.

Finally, we will sum the results of each ship's contribution incoherently. If the transmission arrival structure is known, we can extract both azimuthal directionality and vertical directionality.

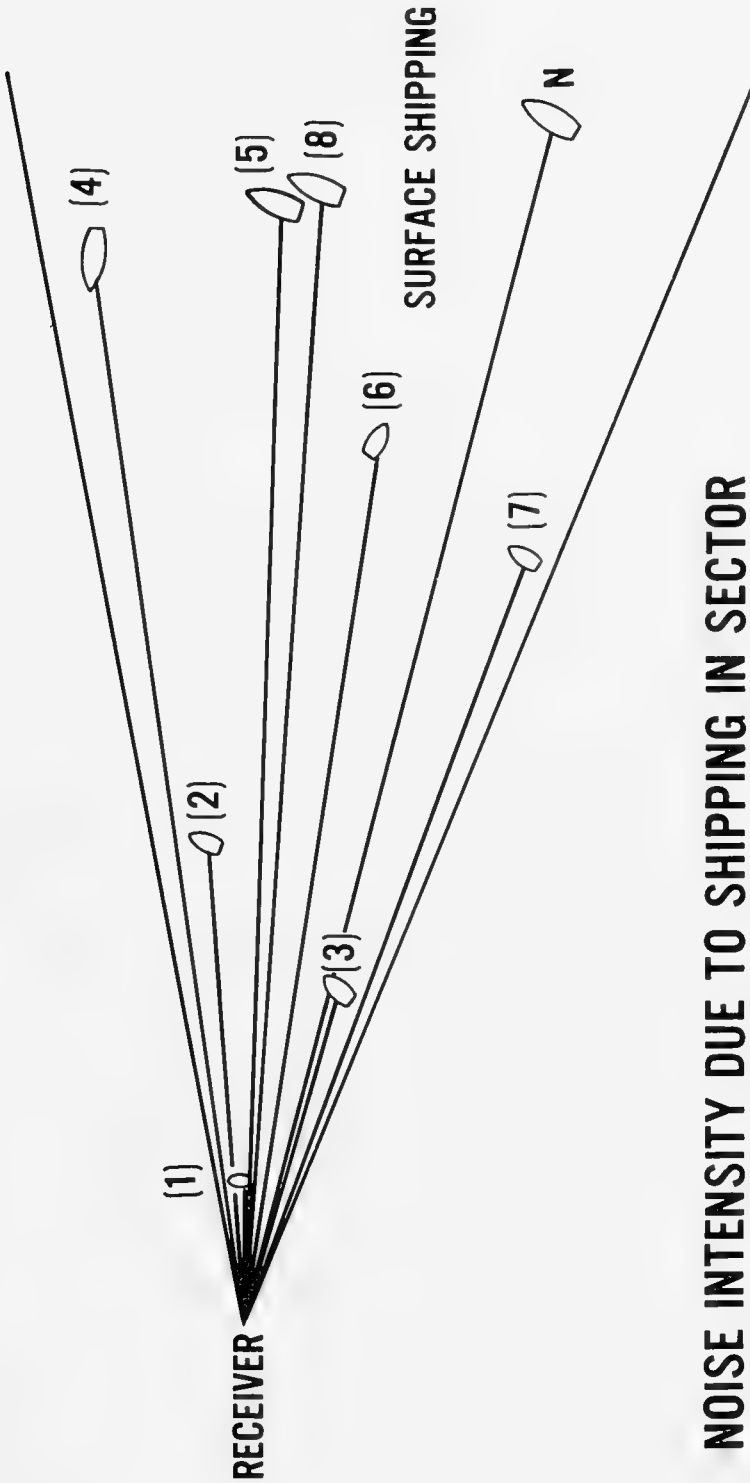
As far as the ship information for model input is concerned, here is what is available today. We have estimates of the average number of ships of each of several types, say merchants and fishing vessels and tankers, in each X-degree cell (or square) in the ocean. Typically, $X = 5$. Some ships make daily reports of their location,

course, and speed. So this information is in addition to the 5-degree cell data, but represents a small percentage of the total number of ships in an ocean basin. In at least one recent experiment in which there was extensive aircraft surveillance of surface shipping, 5-degree resolution was the best that could be accomplished for a large ocean area.

Present information has led us to model the ship source as a point source near the surface that radiates isotropically downward — some modelers put the source at 20 feet below the surface, but do not include the effects of image interference there. The paper given earlier by Mel Pedersen on surface decoupling and the knowledge that we have on image interference suggest that this is a particularly important question: what does the ship source look like and how does it interact with the surface?

Models which we surveyed use an average, broadband, radiated noise spectrum for each type of ship, parameterized on speed and size. In nearly every case, the source levels are derived from the spectrum that was published in the paper by Ross and Alvarez (1964). It shows a maximum at 70 Hz and a falloff of 6 dB per octave above that.

Returning now to the prediction of ship-generated noise, present applications suggest that it is best, since we have only shipping distributions in large latitude-longitude squares, to use what I call a *field model*: one that requires only the average transmission loss as a function of range. In contrast, define a *point model* as one which uses the precise locations of sources and requires a detailed description of the transmission loss. Figure 2 illustrates the point model; every ship is identified, and the resultant noise is simply the sum of the contributions from each source.



NOISE INTENSITY DUE TO SHIPPING IN SECTOR

$$N = \sum_{i=1}^N [\text{SOURCE INTENSITY OF SHIP}(i)] * [\text{TRANSMISSION RATIO FROM POINT}(i)\text{TO RECEIVER}]$$

Figure 2. POINT MODEL

An example of the input to a field model is shown in Figure 3. Entries denote the number of ships per million square miles for ocean regions of 100 nm radial extent.

There appears to be no easy way to predict noise with a point model: the propagation must be estimated in detail. However, in the case of the field model, Talham (1964) developed an approach which exploits the relaxed requirements on transmission loss predictions. Although its direct application is limited to range-independent environments, the method is outlined next, in anticipation of the extension given later.

Let a receiver be located at depth Z_R and range $R = 0$, and assume that a small horizontal region near the ocean surface at range R and on bearing ϕ radians ($\text{re } 0^\circ \text{T}$) radiates sound with an equivalent point source intensity $P(R, \phi; \theta)$, in a one Hertz band, per unit area, at unit distance, in vertical direction θ (radians measured from the horizontal) and horizontal direction ϕ (equal to the bearing in radians). For the geometry of Figure 4(a), the shaded horizontal region has area:

$$\left(\frac{\Delta\phi}{2\pi}\right) \pi \left\{ \left(R + \frac{\Delta R}{2}\right)^2 - \left(R - \frac{\Delta R}{2}\right)^2 \right\} = R\Delta R\Delta\phi, \quad (1)$$

so that the directive, point source intensity for the region is

$$P(R, \phi; \theta) R\Delta R\Delta\phi.$$

The intensity at the receiver due to the source radiation is the source intensity reduced by an appropriate attenuation from transmission. From a geometrical acoustic point of view, sound propagates along many paths from the point source to the receiver. For any one of these, say the path of Figure 4(b), which has initial angle θ_S and

SHIPPING DENSITY INPUTS FOR AMBIENT NOISE MODEL

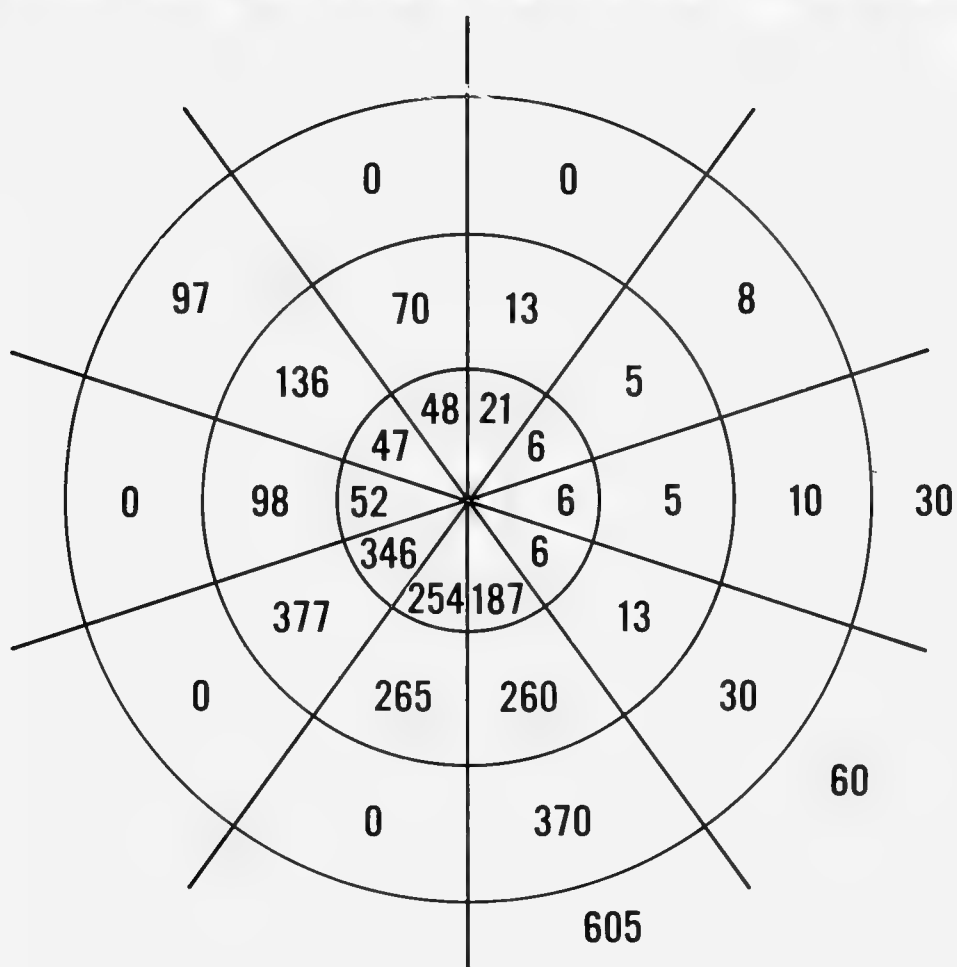


Figure 3. FIELD MODEL

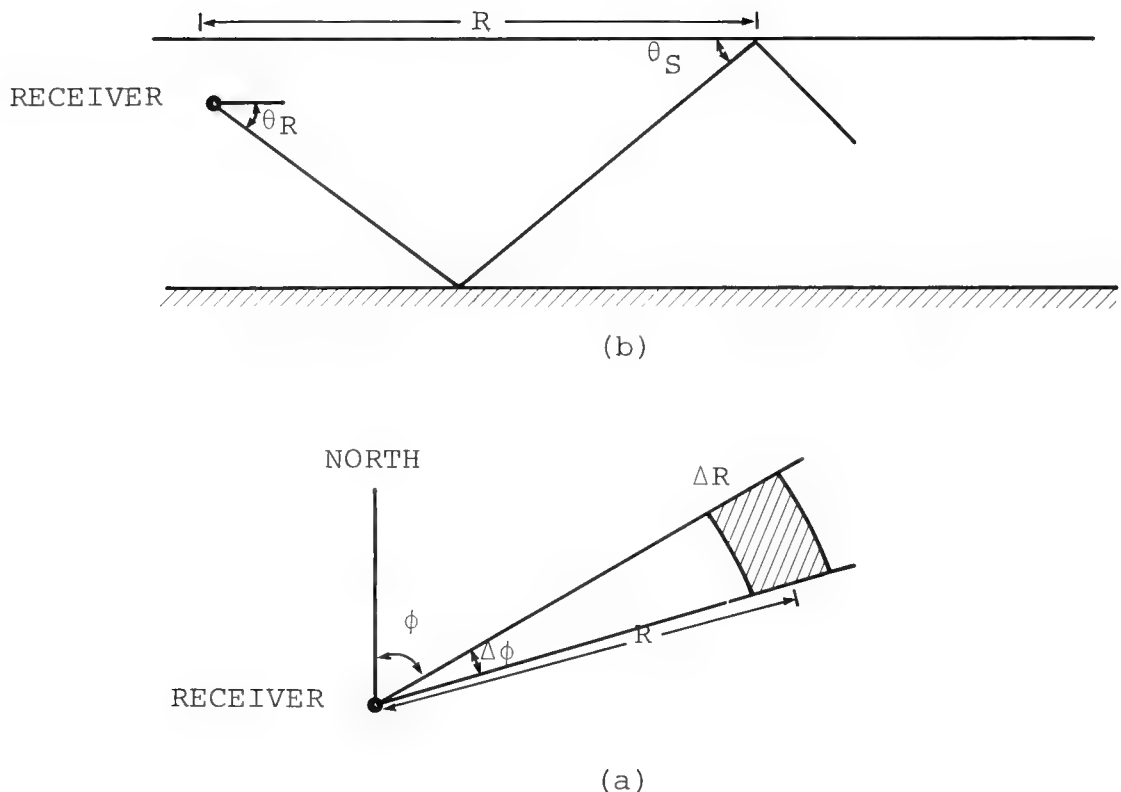


Figure 4. POINT MODEL GEOMETRIES

arrival angle θ_R , the transmission ratio (ratio of intensity at range R to intensity at unit distance) is

$$\tau(R, \phi; \theta_R) = S(R, \theta_S) \beta(R, \phi; \theta_S). \quad (2)$$

Here $\beta(R, \phi; \theta_S)$ accounts for boundary losses and volume attenuation while $S(R, \theta_S)$ is the geometrical divergence factor. From the reciprocity principle,* the transmission ratio is independent of source/receiver identity to within a factor of sound speeds squared. Hence, the spreading loss can be written as

$$S(R, \theta_S) = \frac{\cos \theta_R}{R \left(\frac{dR}{d\theta_R} \right) \sin \theta_S} \left(\frac{C_S}{C_R} \right)^2 \quad (3)$$

where C_S , C_R denote the speeds of sound at source and receiver.

From (1) - (3) it follows that the differential intensity dI contributed by area $dA = RdRd\phi$ at range R and bearing ϕ via this transmission path (θ_R) is

$$\begin{aligned} & dI(\theta_R, \phi; dA(R, \phi)) \\ &= P(R, \phi; \theta_S) \tau dA \\ &= P(R, \phi; \theta_S) \frac{RdRd\phi \beta(R, \phi; \theta_S) \cos \theta_R}{R \left(\frac{dR}{d\theta_R} \right) \sin \theta_S} \left(\frac{C_S}{C_R} \right)^2 \end{aligned} \quad (4)$$

* In sound transmission from source to receiver as modeled with the wave equation, the ratio of squared pressure to intensity at the receiver (in this case, the product of intensity and sound speed) remains the same when source and receiver locations are interchanged.

The corresponding intensity per unit solid angle

$$(d\Omega = \cos\theta_R d\theta_R d\phi)$$

at the receiver is then

$$n(\theta_R, \phi; dA, d\Omega) \equiv \frac{dI}{d\Omega}(\theta_R, \phi; dA(R, \phi)) \quad (5)$$

$$= \frac{P(R, \phi; \theta_S) R dR d\phi \cos\theta_R \beta(R, \phi; \theta_S)}{R \left(\frac{dR}{d\theta_R} \right) \sin\theta_S \cos\theta_R d\theta_R d\phi} \left(\frac{C_S}{C_R} \right)^2 \quad (5)$$

$$= \frac{P(R, \phi; \theta_S)}{\sin\theta_S} \beta(R, \phi; \theta_S) \left(\frac{C_S}{C_R} \right)^2 \quad (6)$$

$$\equiv n(\theta_R, \phi, R).$$

Note that n is independent of spreading losses. The total contribution to the noise field at angles θ_R, ϕ is then found as the incoherent sum of $n(\theta_R, \phi, R)$ over all ranges R .

Until this point there have been no restrictions on the form of the sound speed field $C(z, R, \phi)$. However, to facilitate calculations, the ocean is assumed to be stratified and azimuthally symmetric within an appropriate bearing aperture: $C(z, R, \phi) = C(z)$ for $\phi_1 \leq \phi \leq \phi_2$ and $0 \leq z \leq D$. This allows the use of recursive ray-tracing schemes. It further guarantees that although $n(\theta_R, \phi, R)$ becomes infinite for the ray ($\theta_R = \theta_G$) which grazes the surface, the energy in any interval $(\theta_G, \theta_G + \epsilon)$ is finite, provided that $\theta_G \neq 0$ (i.e., $C_S \neq C_R$).

This approach has been implemented by Bartberger (1969) at NADC and also at AESD.* It can be extended for more realistic descriptions of the ocean environment, namely those in which sound speed and bathymetry vary with range.

The extension uses the *invariance of action* discussed by Weston (1959) and Milder (1969), and more recently applied by Preston Smith (1974). Define the action for a geometric ray as

$$J = \oint \frac{\sin\theta(z)}{c(z)} dz \quad (7)$$

where the line integral is over a complete ray cycle, c is local sound speed, θ is ray angle. For an ocean which is slowly varying in range (i.e., nearly constant over a ray's range period), J is an invariant on a ray. Hence, by tracking the evolution of each ray via J , we can efficiently estimate range-averaged transmission loss or, more directly, calculate n with formula (6).

In summary, given the present resolution of inputs to noise models, a sensible alternative to the expensive point model is the field model equipped with an efficient method of dealing with the range-varying environment.

* AESD Memo, "Fast Ambient Noise Model I (FANM I)," 1974.

REFERENCES

- Bartberger, C. L., "A Model for Ambient Noise Due to Distant Shipping," NADC Tech. Memo 69-008-1, Dec. 31, 1969.
- Knudsen, V. O., R. S. Alford, and J. W. Emling, *J. Marine Research*, 7:410, 1948.
- Milder, D. M., "Ray and Wave Invariants for SOFAR Channel Propagation," *JASA*, 46:1259-1263, 1969.
- Ross, D. and Alvarez, F. F., "Radiated Underwater Noise of Surface Ships (U)," *USN J. Underwater Acoustics*, 14, 1964.
- Smith, P. W., Jr., "Averaged Sound Transmission in Range-Dependent Channels," *JASA*, 55:1197-1204, 1974.
- Talham, R. J., "Ambient-Sea-Noise Model," *JASA*, 36:1541-1544, 1964.
- Wenz, G. M., "Acoustic Ambient Noise in the Ocean: Spectra and Sources," *JASA* 34:1936-1956, 1962.
- Weston, D. E., "Guided Propagation in a Slowly Varying Medium," *Proc. Phys. Soc. (London)*, 73:365-384, 1959.

DISCUSSION

DR. S. W. MARSHALL (Naval Research Laboratory): Ray, I'd like to take issue with you on the question of ambient noise modeling and what is really required. You said that you felt that it was adequate to range-average the transmission loss, and certainly we would all like to have the shipping data in smaller geographical bins than we now have available, whether the numbers are real or perhaps imaginary.

I think what is really required — and I derive this not from my own opinion but from the people I talk to who use the results we have gotten — is the statistics of the noise. And if you really want the statistics of the noise, then you have to retain not only the structure of the transmission loss but also — and this is my opinion — I think that you need to do some type of statistical calculation to establish what a reasonable distribution would be and that a single calculation is not sufficient to do this.

DR. R. C. CAVANAGH: I didn't want to give the impression that we are not interested in the other characteristics of ambient noise aside from an average over days or months.

From a practical point of view in doing production modeling, it is very expensive, as you know, to execute detailed transmission models on 72 or 180 bearings. So, since we typically do have average shipping density inputs, it is practical to use an average transmission.

Good treatments for doing statistics are available. And, of course, we can take realizations of shipping locations and do some statistics on that in selected cases. But for the general practical, production predictions, I think we have to stick to some average transmission for the moment.

DR. DONALD ROSS (Tetra Tech, Inc.): Adding to that, I think we have to recognize that there is a dominant tonal structure in ship noise below about 60 Hz, and this means that even if I know exactly where the ship is and what its name is, it doesn't tell me the spectrum within 5, 10, 15 dB. So what is the use in knowing what the ship is?

DR. MARSHALL: I was not suggesting that knowing where the ship was all that important, really. But it would be nice to have more confidence in the numbers than we now do.

DR. ROSS: There is no way of getting this. Because the ships do not follow the same tracks from one voyage to another. The weather, for example, plays a major role in ship traffic across the ocean.

GEOGRAPHICAL VARIATION OF AMBIENT NOISE
IN THE OCEAN FOR THE FREQUENCY RANGE
FROM 1 HERTZ TO 5 KILOHERTZ

Robert L. Martin and Anthony J. Perrone

New London Laboratory
Naval Underwater Systems Center

Many statistical descriptions of ambient noise have been published, among which are average spectrum level, fluctuation versus frequency, average level versus depth, cross correlation with wind speed versus frequency, decorrelation time versus frequency, directionality, etc. Each description provides information for various requirements such as system design, predictions, model evaluation or to advance our knowledge of the causal phenomena associated with the measurement. These statistical descriptions vary widely with geographic area and it is generally assumed that these variations result primarily from differences in shipping densities, propagation conditions and bottom topography. This paper describes results obtained in many areas of the world and analyzed using several of the statistical descriptors mentioned above. The utility of the results to the various requirements is discussed and the need for measurements to form the basis for broader interpretation of results from areas of interest is highlighted.

GEOGRAPHIC DEPENDENCE OF AMBIENT NOISE

Observations of ambient noise level versus frequency have been made in many areas of the world. These measurements provide valuable descriptions of the areas when they are accompanied by information on the parameters giving rise to the noise (e.g., wind speed, shipping, etc.), the peculiarities of the equipment used to make the measurement (e.g., analysis techniques, hydrophone depth), time extent of the measurement, and the hydrographic peculiarities of the area. In addition to ambient noise level, there are other descriptors useful

in establishing the uniqueness of a given area which may be more important to modelers and system designers than level by itself. These descriptors include correlation of ambient noise time series with concurrent wind speed time series and the autocorrelation of the time series, both as functions of frequency. Recent measurements have shown that these other descriptors as well as level versus frequency differ in different areas and a rationale has been developed on how these descriptors might help system designers and modelers. In addition, measurements in shipping free areas and at low frequencies indicate that the wind speed generated ambient spectrum may be significantly different at low frequency than previously conjectured.

Figure 1 illustrates 1-year time series of ambient noise level in the Bermuda area as observed at the output of several 1/3-octave filters in the range from 10 to 3,000 Hz; the bottom curve is the wind speed time series.

Figure 2 illustrates the noise spectra for the month of January 1966 as reported by Perrone (1969) for one of the deep hydrophones in the Bermuda area for several conditions of wind speed. Each curve represents an ensemble average of several measurements. A special effort was made to eliminate transient noise (biologics, nearby shipping, etc.) from these data prior to processing. The wind speed effect is distinctly pronounced above 100 Hz and below 20 Hz. The measurements were somewhat affected by system noise above 1,500 Hz for the low wind speed conditions and are displayed here as measured and as extrapolated; system noise for higher wind speed conditions at these high frequencies is not a factor in the measurements. A study of these curves indicates that wind speed does not become a dominant factor at this hydrophone until wind exceeds 12 knots and that when it does become dominant the spectra tend to flatten out

MARTIN/PERRONE: GEOGRAPHICAL VARIATION OF AMBIENT NOISE IN THE OCEAN
FOR THE FREQUENCY RANGE FROM 1 HERTZ TO 5 KILOHERTZ

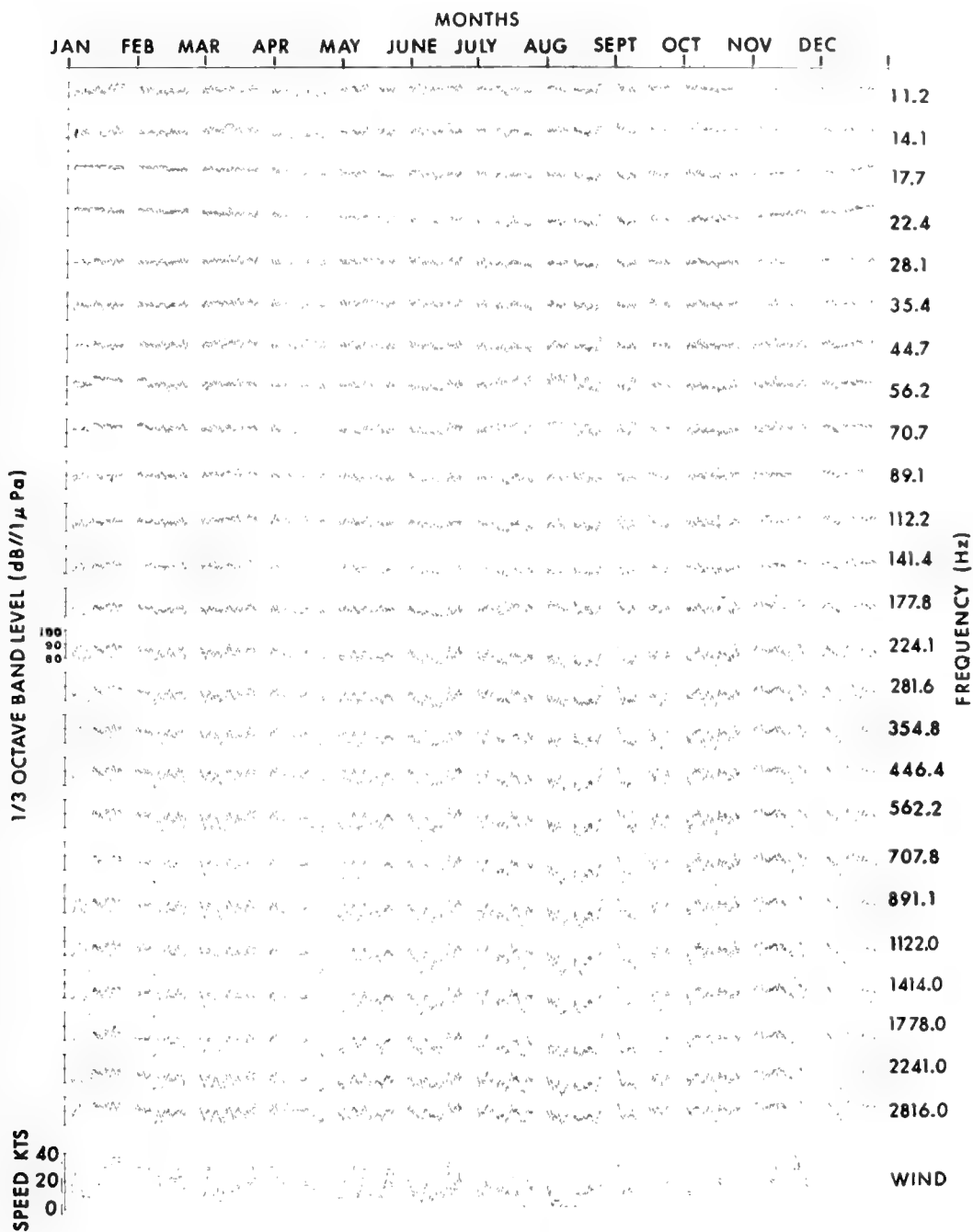


Figure 1. AMBIENT NOISE TIME SERIES - BERMUDA 1966
HYDROPHONE DEPTH 14,000 ft

or have a "humped" shape in the region 100 to 600 Hz. Assuming that the only significant contributors to these spectra are wind speed and shipping, it is possible to propose a synthesis of the two.

In Figure 3, a possible breakdown of the two contributors is shown. Results from the Ionian Sea, as well as Bermuda, are shown here; the Ionian Sea results will be discussed later. The shape of the curves is consistent with that suggested by Wenz (1962). Wind speed curves are purposely terminated at about 100 Hz on the low frequency end because nothing in the data suggests a shape or trend of these curves between 20 and 100 Hz; however, the measured data at and near 10 Hz indicate that wind speed must contribute over this range. Shipping noise in Figure 3 is shown to be significant to 1,000 Hz and possibly beyond for low wind speed conditions. These shipping noise spectra and standard deviations result from consideration of the spectra for the lowest wind speed condition.

The statements made concerning wind and shipping with respect to these data are quantified in Figure 4. These curves represent the cross correlation of the ambient noise level time series at the output of each analysis filter with the wind speed and wave height time series as observed on instruments located at Argus Island some distance away. Incidentally, while the shapes of the two correlation curves (viz., wind speed and wave height) are approximately the same, the fact that the wave height curve levels off at a correlation of 0.6 versus 0.8 for wind speed may be due to the lag in the time it takes for seas to build up and in part to the fact that the wave spectrum at Argus Island may be somewhat different due to it being obtained in shallow water rather than in the deeper water of this measurement site. These curves provide a quantitative average

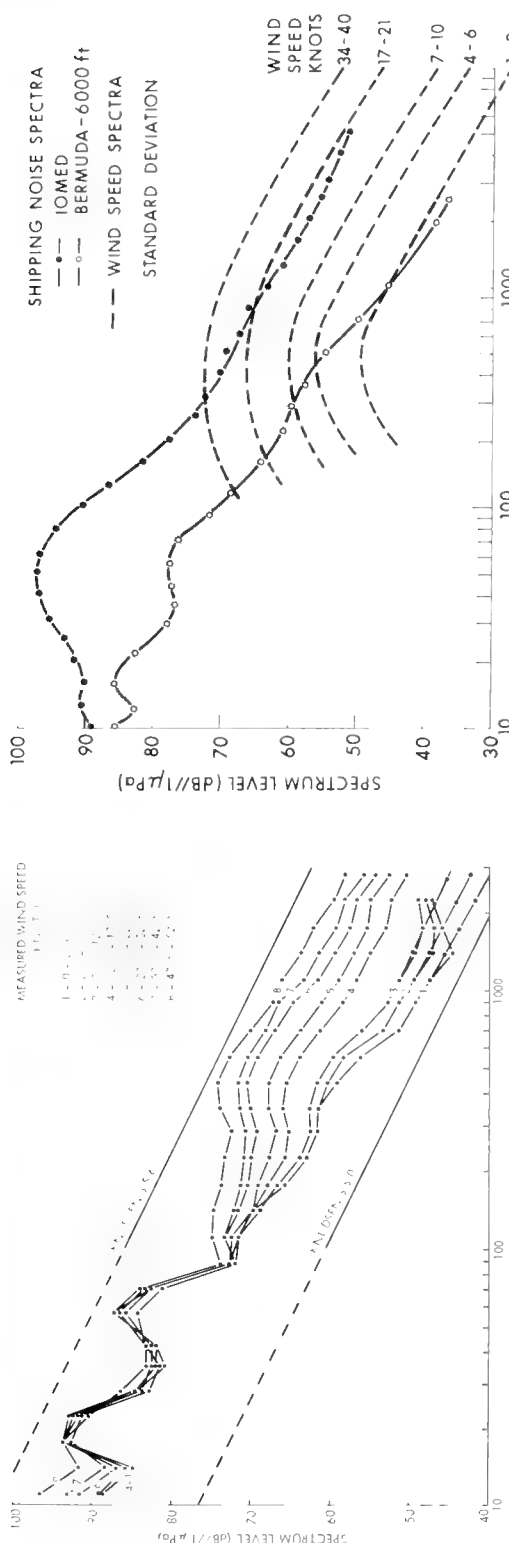


FIGURE 2 . AMBIENT NOISE SPECTRA GROUPED BY
WIND SPEED BERMUDA - 14,000 ft

FIGURE 3 . WIND & SHIPPING NOISE SPECTRA

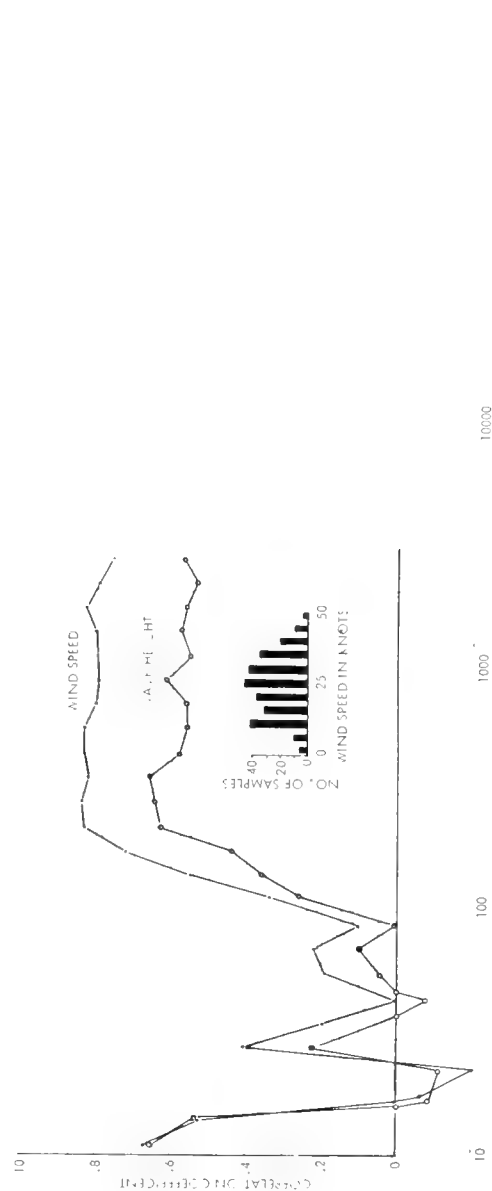


FIGURE 4 .

CROSS CORRELATION OF AMBIENT NOISE LEVELS
FOR "O" TIME LAG

measure of the wind speed and non-wind speed (presumably shipping) contributions to the noise field and permit rapid assessment of the overall importance of the two contributors with frequency. Note the high correlation below 20 Hz and at 30 Hz. It is felt that a correlation descriptor of this type would be useful for model development purposes, especially when attempting to evaluate the model in the transition regions which are noted here to be between 100 and 200 Hz for the Bermuda area.

Figure 5 shows the time series of observed ambient noise level at three frequencies, together with concurrently measured wind speed. This particular data set was obtained in the Ionian Sea, over a period of 9 days. The influence of wind speed on these levels is shown by the cross-correlation curves of Figure 6. While it is evident from a consideration of Figure 5 that 9 days of data represents a small data set for this type of analysis, the resulting correlation curves are remarkably well behaved. These curves represent results from hydrophones at different depths and have essentially the same shape. This shape is quite different from that observed for the Bermuda area, displaying a more gradual and higher frequency transition region (200 to 1,000 Hz vice 100 to 200 Hz) and a lower correlation coefficient above 1,000 Hz. This longer transition region and lower correlation for high frequencies results from a much stronger shipping influence over the entire frequency range of measurement.

This strong lack of dependence on wind speed for the Ionian data is further observed in the spectra of Figure 7. Here, no wind speed dependence is found at 10 Hz but this may be due to the small amount of data at the higher wind speed condition occurring in the measurement period. The levels between 10 and 20 Hz are comparable to those observed in Bermuda but, at 50 Hz, levels in the Ionian Sea are at least

MARTIN/PERRONE: GEOGRAPHICAL VARIATION OF AMBIENT NOISE IN THE OCEAN FOR THE FREQUENCY RANGE FROM 1 HERTZ TO 5 KILOHERTZ

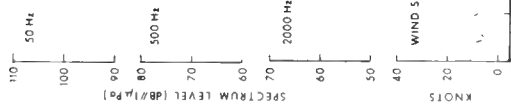


FIGURE 5 . TIME SERIES
NOV 1972

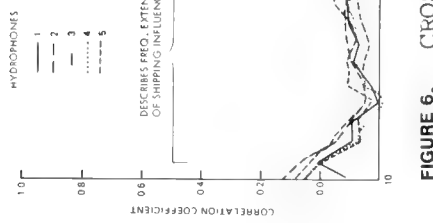


FIGURE 5 . AMBIENT NOISE & WIND SPEED

FIGURE 6 . CROSS CORRELATION OF WIND SPEED & AMBIENT NOISE FOR 0 TIME LAG IONIAN SEA NOV 1972

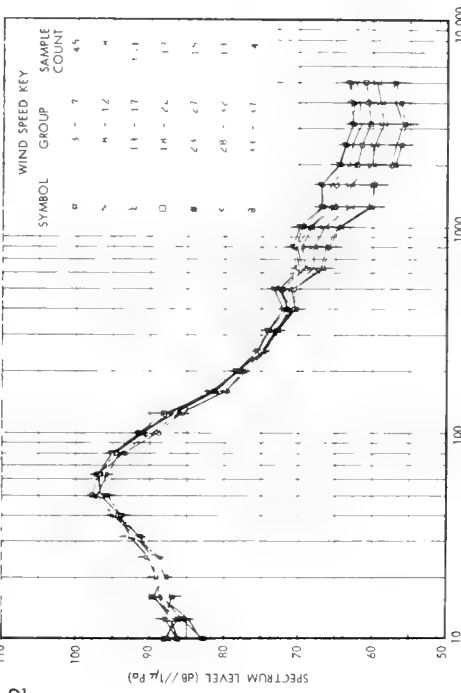


FIGURE 6 . AMBIENT NOISE SPECTRA
IONIAN SEA NOV 1974

10 dB higher than Bermuda, again indicating that the shipping influence is stronger and perhaps of a different character. This difference in character suggests that radiated noise from ships operating in the Bermuda area may differ significantly from those in the Mediterranean Sea; however, in the absence of a quantitative measure of the wind speed effect on noise in the band 10 to 1,000 Hz, it is not possible to assess the validity of that characterization.

While the curves shown in Figures 2 and 7 indicate very little temporal variation of the data below 100 Hz, data taken in the Labrador Basin over a similarly short time period indicate that variabilities on the order of 10 dB are possible. Figure 8 shows results from several different measurements all taken in a general area of a 100 nm square in the central deep water portion of the Labrador Basin 400 nm south of Greenland (see MABS site in Figure 15). The water depth and sound velocity profile shape in this area are similar to those of the Ionian Basin, yielding a large depth excess and a low propagation loss. The area of surface generated noise influence, however, is much more extensive due to the relative sizes of the basins, but the shipping density in the Labrador Basin is at least an order of magnitude less than that in the Ionian Sea. Being that much less and given similar transmission loss properties, the observed levels are also much lower. Also, it is perhaps this very low shipping density which gives rise to the high variability in the data. If only a small number of ships contributes to the noise field at a particular instant of time, then the presence of a few ships more or less can make a large difference in the results. In Figure 8 it should be noted that most of the measurements were obtained over time periods as short as 15 minutes (SONOBUOYS and AUTOBUOYS). These short periods may contain significant effects due to industrial noise sources (sparkers and air guns) which were prevalent during this time and to different

methods used in editing the data. However, even the longer term measurements provided by the Ambient Noise Buoy (ANB) and Moored Acoustic Buoy (MABS) show large differences.

Measurements made on the Grand Banks (Figure 9) show that spectrum levels between 10 and 200 Hz are near the upper range of values observed in the center of the basin. Measurements at this site, however, were made down to 1 Hz. Between 1 and 2 Hz there appears to be a strong wind dependence in the results. The strong trend in the spectrum between 2 and 6 Hz does not have an apparent wind dependence and neither can it be reasonably associated with shipping. More investigations into this very low frequency region are obviously warranted.

Another way of measuring shipping and wind influence on ambient noise is to use the autocorrelation of the ambient noise level time series for each frequency to estimate a time constant or decorrelation time of the noise as a function of frequency. This is shown for the Moored Acoustic Buoy (MABS) data in Figure 10. This time-constant is the value of τ , in hours, that one obtains simply by extrapolating the main lobe of the time series autocorrelation function to zero. While this analysis provides some of the same qualitative information as the wind speed cross correlation analysis, it also provides additional information which could be of value to system designers for both concept formulation and design and ultimately to system analysts for evaluating system performance. In this figure, the time-constant coordinate is divided into three regions designated shipping, wind, and a mixture of the two. The rationale for the wind speed region is shown by the curve of Figure 11 which is a plot by month of the wind speed time-constant in Bermuda. Unfortunately, there is no such simple function which represents a direct measurement of shipping in

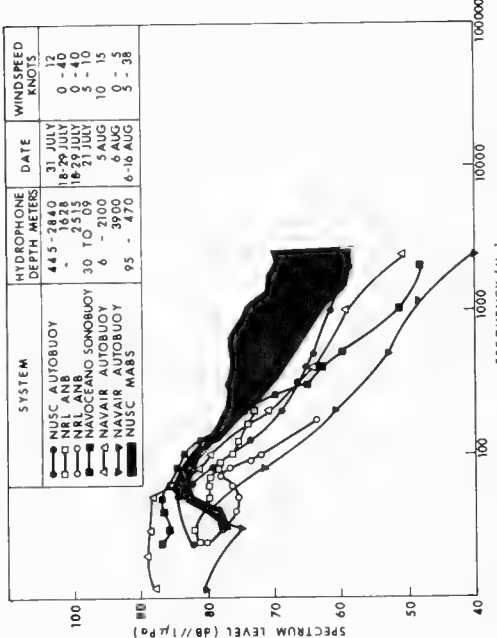


FIGURE 8. AMBIENT NOISE SPECTRA
LABRADOR BASIN

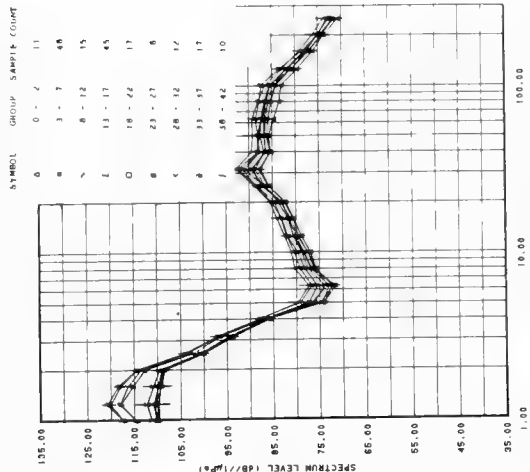


FIGURE 9. AMBIENT NOISE SPECTRUM
VERSUS WIND SPEED GROUPS

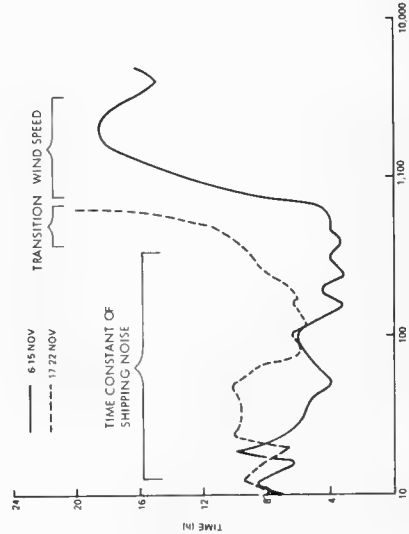


FIGURE 10. AMBIENT NOISE DECORRELATION
TIMES - IONIAN SEA

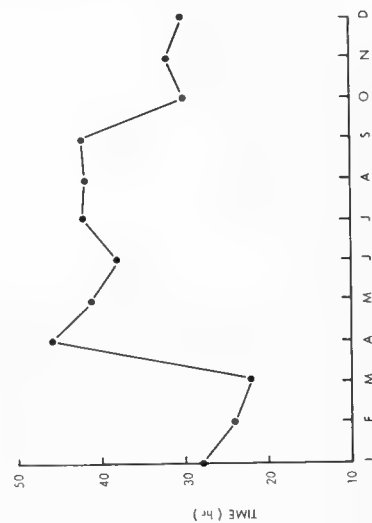


FIGURE 11. ZERO-AXIS CROSSING OF THE
AUTOCORRELATION FUNCTION OF
WIND SPEED FOR TWELVE MONTHS

this respect, so area delineation has to be subjectively chosen. Figure 12 shows several of these curves for the areas discussed in this paper. The frequency region which shows decorrelation times of 4 to 12 hours is associated with shipping dominated noise, and frequencies with long decorrelation times (greater than 25 hours) are identified with wind generated noise. In between, both influences act on the noise and a transition region is obtained. The identification with wind speed, as stated earlier, can be made rather directly by consideration of the cross-correlation curves and by measuring the wind speed autocorrelation function. The very low frequency data obtained on the Grand Banks have time constants peculiar to wind generated noise.

Strong variations of ambient noise versus depth within the same general area are also possible. Figures 13 and 14 show curves of the depth dependence of ambient noise for, respectively, the center of the Labrador Basin and for a site toward the Denmark Straits. The strongest difference between these data sets is below 200 Hz and has already been identified with shipping dependent noise. The levels at the shallow depths agree quite well at these lower frequencies; the differences are at the deeper depths. As shown in Figure 15, the site near the Denmark Straits is more topographically confined than the one in the center of the basin. It is hemmed in by nearby Greenland from the northwest to Iceland in the northeast and by the less confining Reykjanes Ridge from Iceland to the south-southwest. The major shipping lanes are on the side of the ridge opposite this site. It is suspected that the shallow critical depth and the similarly shallow depth of the ridge permit excellent coupling of the shipping lane noise to the shallow hydrophones, as well as an effective proportional blocking considered to result from the increasing depth of the ridge summit toward the southwest and the gaps in the

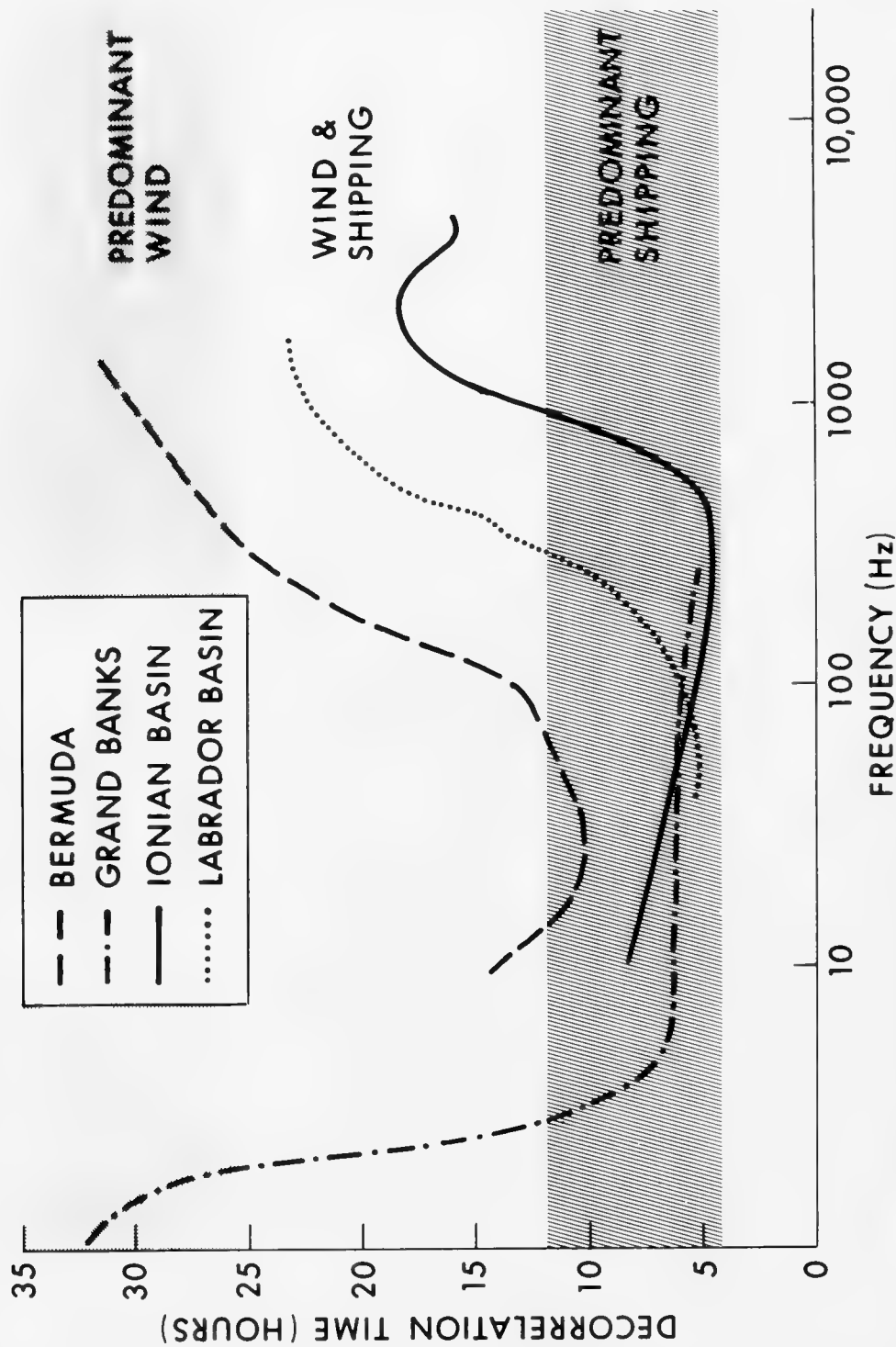


FIGURE 12. DECORRELATION TIMES FOR SHIPPING AND WIND GENERATED NOISE FOR FOUR GEOGRAPHICAL AREAS

MARTIN/PERRONE: GEOGRAPHICAL VARIATION OF AMBIENT NOISE IN THE OCEAN FOR THE FREQUENCY RANGE FROM 1 HERTZ TO 5 KILOHERTZ

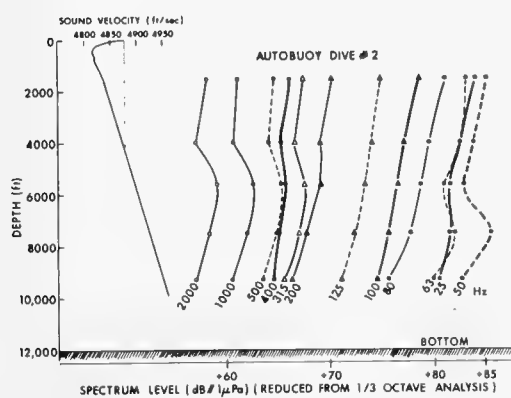


FIGURE 13 • NORLANT '72
AMBIENT NOISE DEPTH
DEPENDENCE

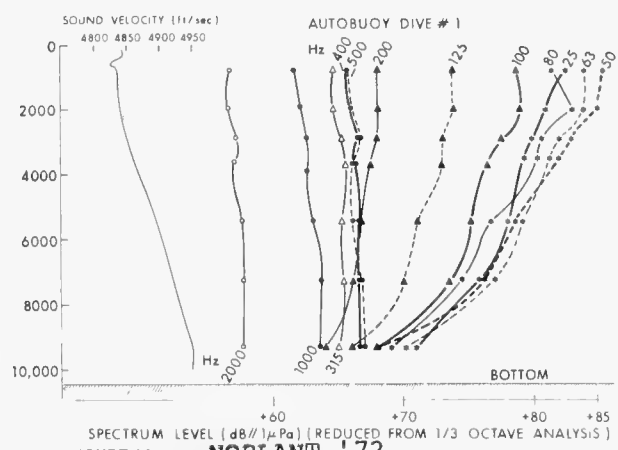


FIGURE 14 • NORLANT '72
AMBIENT NOISE DEPTH
DEPENDENCE

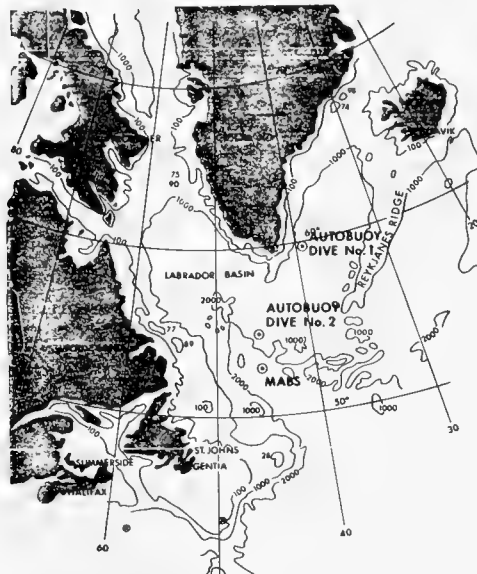


FIGURE 15 • NORLANT '72
AMBIENT NOISE SITES

ridge. While this represents a small data set, the pronounced differences at the two sites suggest that longer term observations would yield the same general conclusions.

Figure 16 shows a composite of results discussed so far. But now consider data from New Zealand (Figure 16) obtained in an area known to have almost no shipping and blocked from the broad open ocean areas by oceanic ridges. Note that the spread of data for the range of wind speeds obtained is independent of frequency from 10 to 1,000 Hz and that the high wind speed curve is similar to that observed in Bermuda. Also, the shape of the curves below 100 Hz is inconsistent with those appearing in the literature for wind generated noise. Measurements in these quiet areas to frequencies of 1 Hz or lower are important in determining the wind generated mechanism(s) giving rise to the ambient noise in the various frequency regions. Long time series are important so that results and conclusions will not be criticized on the basis of sample size. The Bermuda measurements, discussed in part earlier, were obtained over a 1-year period.

Figure 18 presents a phenomenological occurrence of the surface image effect on 1/3-octave noise in the presence of a directional noise field. For AUTOBUOY Dive 1 (Figure 15), the system slowly ascended to the near surface and hovered at that shallow depth for about 30 minutes. The abscissa in Figure 18 is scaled both for time and for depth as determined by a depth gauge in the AUTOBUOY. The ambient noise level is shown to vary slowly with decreasing depth up to approximately 150 feet and then to fall off rapidly for the lower frequencies in particular. If one assumes a surface interference effect in each 1/3-octave band, the results agree quite well with the assumption that the noise is uniformly directional from approximately 0 to 10 degrees. While this is a first order assumption, the

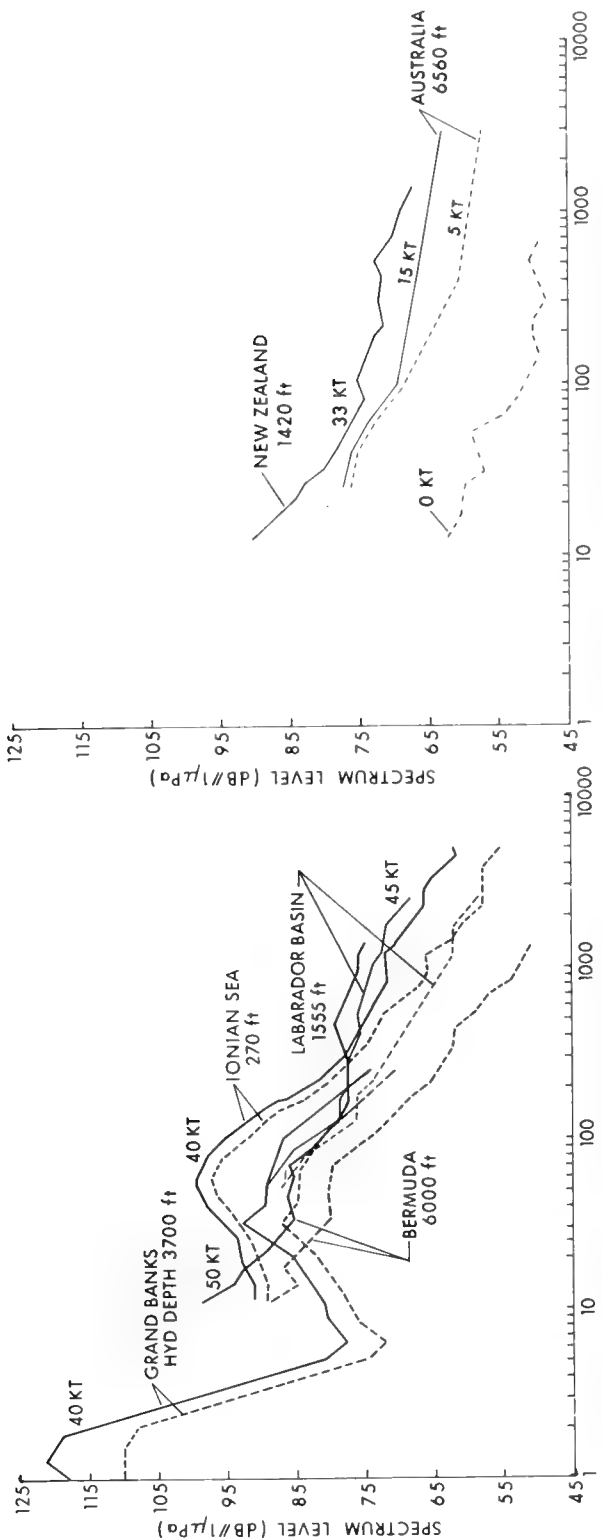


FIGURE 16 . RANGE OF SPECTRUM LEVELS FOR
DIFFERENT LOCATIONS

FIGURE 17 . RANGE OF SPECTRUM LEVELS FOR
DIFFERENT LOCATIONS



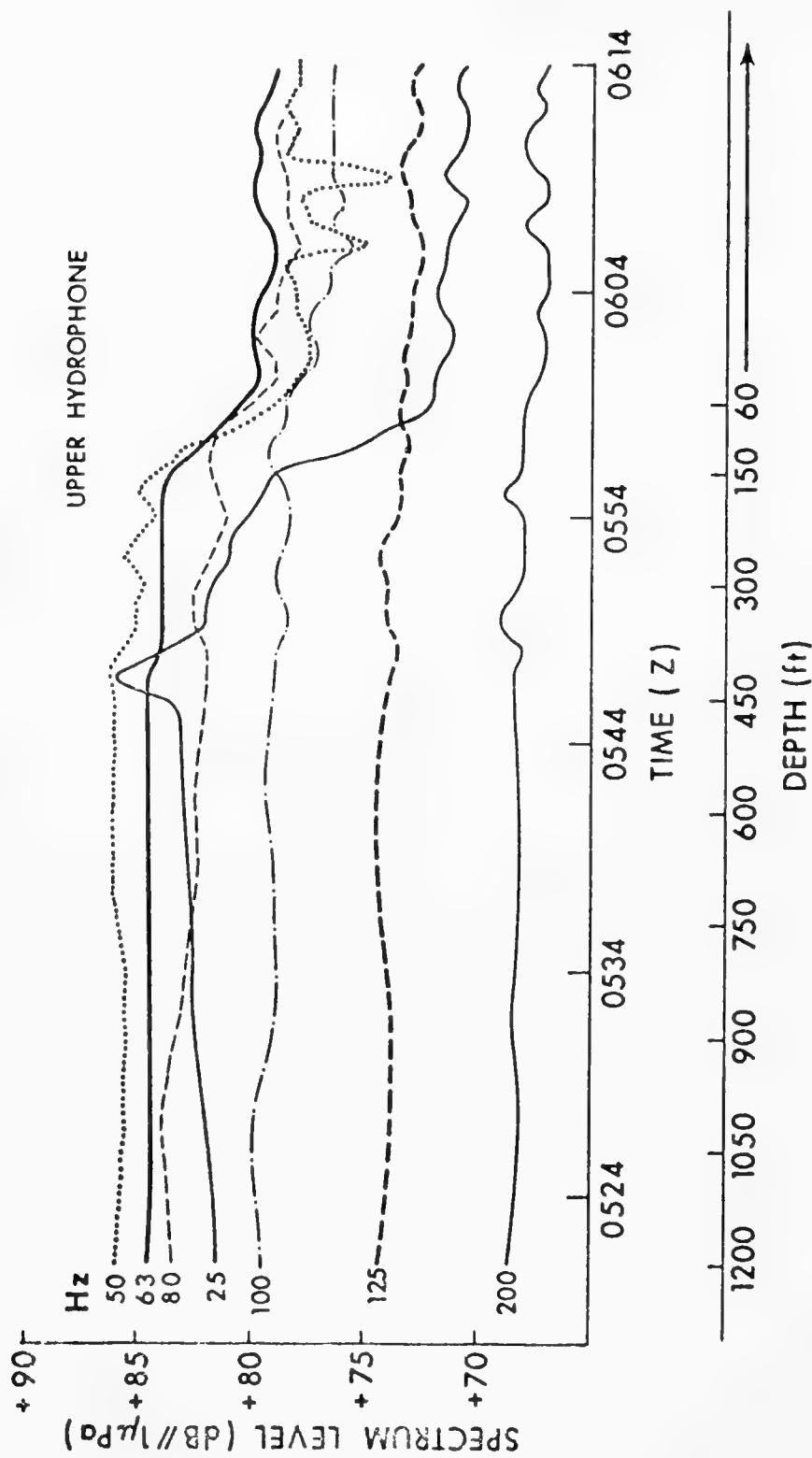


Figure 18. AMBIENT NOISE BOUNDARY EFFECTS AUTOBUOY DIVE NO. 1

physical situation as discussed with respect to Figure 14 indicates that it is realistic.

In summary, this paper describes and compares results of statistical analyses of long time series of ambient noise obtained in widely different geographic areas. These analyses include average level versus frequency, average level versus depth for several frequencies, cross correlation of level with wind speed versus frequency and decorrelation time versus frequency. In addition, the deterministic effect of surface interference on directional noise received at shallow hydrophones is discussed with respect to a measured data set. The possibility is raised that noise in the deep ocean in the vicinity of Bermuda displays significant wind effects in the frequency range 10 to 100 Hz with spectral shape different from that previously supposed.

ACKNOWLEDGEMENTS

This paper was prepared under Ocean Science Department overhead. Analysis techniques described were previously developed under Project A65005, Subproject SF52 552 702, Task 11286, "Ambient Noise Characteristics Affecting Sonar and Physical Oceanography." The principal investigator is R. L. Martin. The sponsoring activity is NAVSEA 06H1, Mr. A. Franceschetti. Much of the data reported were acquired under Project A65015, "Long Range Acoustic Transmission Experiments for Surveillance Systems Development." The principal investigator is R. W. Hasse. Subproject and Task No. R2408 sponsored by ONR102-OS, Dr. R. D. Gaul.

REFERENCES

Perrone, A. J., "Deep-Ocean Ambient-Noise Spectra in the Northwest Atlantic," *J. Acoust. Soc. Am.* 46:762-770, 1969.

Wenz, G. M., "Acoustic Ambient Noise in the Ocean," *J. Acoust. Soc. Am.* 34:1936-1956, 1962.

DISCUSSION

Dr. G. Raisbeck (Arthur D. Little, Inc.): In Figure 4 you showed what appeared to be a negative correlation between wind velocity and noise level, and I wondered if it isn't a typographical error in the displacement of the zero.

Dr. P. W. Smith (Bolt, Beranek, and Newman, Inc.): No. You've never been to sea.

Mr. R. L. Martin (New London Laboratory, Naval Underwater Systems Center): All I can say, Toby, is that it was not a long time series, and we could very well have had this type of offset where we got a slight negative correlation. But I think the figure is correct. I have noticed this before, but I have not ever recalculated it.

Dr. D. Ross (Tetra Tech, Inc.): This effect was observed by Woods Hole people in 1948 during a gale off Nantucket. We called it the "Coast Guard effect." It has to do with the fact that when the sea gets very rough, ships slow down. You would expect less noise from shipping when you have a very high sea state giving you a slight negative correlation of the low frequency noise with sea state. Plus the fact that the surface itself gets very rough which gives you some scattering, so it may be that your propagation actually changes also.

Mr. Martin: I'm glad to hear that, because during this particular set of measurements I think we were heading back to port and only doing about 4 knots and just trying to hang onto the bunk. There was quite a gale.

That may be the reason. I don't know. One of the problems is, though, it is a short data set and you have to be careful what kind of limits you put on the result.

Dr. R. W. Bannister (Defence Scientific Establishment): Is there any set-down procedure for selecting data that is generally accepted within the community?

The concern I have is that I see some New Zealand data superimposed here. In that particular case, I know we excluded ships which we were aware of. And I guess it depends what means you use to be aware of ships.

In other words, this is a very bad way of selecting things because it depends upon the eyes you have or the ears you have.

Is there a criterion for selecting data so that we can superimpose them in some rational way?

Mr. Martin: We did exactly the same thing with the Bermuda data. We just extrapolated through any nearby shipping. We eliminated that portion that was easily identified as nearby shipping. So we are only dealing with the longer range noise.

Dr. Bannister: So this is an eyeball look at the record, is it?

Mr. Martin: Eyeball and earball. We processed the data in real time, so people were listening to it.

I think the answer is that anything that is published in the literature that the investigator was able to get by a bunch of editors is assumed to be valid. (Laughter)

Dr. Ross: I hope the proceedings will indicate laughter.
(Laughter)

Ms. E. A. Christian (Naval Surface Weapons Center): Appreciative laughter.

Mr. Martin: I meant it to.

Dr. S. W. Marshall (Naval Research Laboratory): I'd like to respond to your query. I think any time you adopt rules of thumb for fiddling with data, you are treading on thin ice, and I submit that the proper way to represent a long time series of data if you're interested in a number is to present the entire cumulative probability distribution function and let someone select whatever percentile he wants.

Mr. B. M. Buck (Polar Research Laboratory, Inc.): I'm up to the north again. (Laughter) I don't want to belabor the obvious, but it's on the same question that was just posed. I always felt pretty comfortable in the Arctic making 1/3-octave noise measurements because there are no ships. But it seems to me that to measure 1/3-octaves as a function of depth is more an exercise in propagation than it is in noise.

It seems to me that rather than trying to view with aircraft or whatever means the presence of nearby ships, it seems that better technique would be to make your measurements with narrowband, do a narrowband spectrum analysis and rule out the obvious lines and report the general noise.

Dr. I. Dyer (Department of Ocean Engineering, Massachusetts Institute of Technology): Let's ask Dr. Hersey if there is any chance of doing that.

Dr. J. B. Hersey (Office of Naval Research): I think it's sort of unfortunate that we are not well prepared to illustrate to you the dimensions of the data bank that is accumulating with these buoys that contain several hydrophones distributed through the water column. I'm going to try to get with Earl Hays before this evening and see whether we don't have a few of the feeble little things we have done in just the direction that you are talking about.

The data bank is immense, just overwhelming, with recordings from which we can make measurements of the sort you are describing, and I expect if Roy Gaul (of LRAPP) were here, he would say he already had three contracts let to do that.

But, you know, we are in this field. We're constantly in sort of a state of rolling with the punch. This is a punch that many people in this room, say like a third of us, must have been aware of for a long time. But the opportunity is here right now. We can do this.

I think it is part of the responsibility of this workshop to do just the sort of thing that Beau Buck has just called on us to do, and it is not just in this field. We should be thinking hard about other questions. What do you do about the significance of time series? How do you want to take time series? And a whole series of questions that can be prioritized in the transmission field.

Mr. Martin: As Dr. Hersey said, we have got a data bank that is probably immense and overwhelming and probably very inadequate

at the same time. I think what you would like to do in the world is not only measure very narrowband statistics, as narrow as the signal will permit you to, but also very narrowbeam, looking in different directions, and very narrow time slots, short-term statistics.

You want to do all these things. But the cost of doing them is overwhelming, I think.

Dr. Dyer: Maybe the cost of not doing it is overwhelming.

Mr. Martin: You have to be very careful what kind of experiments you run, because the cost is so large. But you may be able to design experiments that will give you enough information to use in connection with other measurements, like 1/3-octave, so that you might get a picture that will be useful to the Navy. That is my personal opinion.

Mr. E. P. Garabed (Naval Air Development Center): It would be very nice if some distinguished group would make a recommendation on how ambient noise should be reported. Because various groups have various ways of eliminating bad data or ship interference data, and no one reports what that method is. And it is hard to interpret various people's data. So it would be nice if there were a standard format for reporting data.

Dr. Hersey: I do hope that we will be able to display some of the suspended hydrophone data this evening, and I would suggest that, if we do, nobody say anything about what they think they see in this data but go quietly away to your own laboratories. If you can stand it not to work on this problem and have the results of your work influence the assessment of our understanding of the field, I am sorry for you.

MARTIN/PERRONE: GEOGRAPHICAL VARIATION OF AMBIENT NOISE IN THE OCEAN
FOR THE FREQUENCY RANGE FROM 1 HERTZ TO 5 KILOHERTZ

You know, there are just so many exciting things in 10 continuous days worth of ambient noise recordings when you look at it with a sufficiently narrow filter that there is just no way that a scientist can keep his hands off it.

Dr. Raisbeck: Following up a remark of Martin's and also several others that have come by here, I don't think the answer is to standardize the methods by which we sift the data but simply to state what they are in each individual case. I, for one, can see some conceptual validity at say 500 Hertz where we think we are measuring weather-induced noise and sea noise to sort out interfering shipping, but at 50 Hertz where the ambient noise that we think we are measuring is due to shipping noise, I can't even see any philosophical justification for saying that because a ship is close enough, then it is no longer part of the ambient noise that we are trying to measure.

I would follow Sam's statement. Let's give the statistics. And let the user do with it what he will.

Dr. Dyer: I would counter that by saying if you gave the component statistics of two separate populations, you can always mix them later, but if you give the statistics of the complete set, you can't decompose. And so I would encourage whatever decomposition makes sense.

Dr. A. O. Sykes (Office of Naval Research): In all of the measurements, we have not seen any simultaneous propagation loss measurements. There are a couple of reasons for studying ambient noise. Maybe we want to study the mechanisms. But if we are interested in building systems and locating them at some place in

the water column, it seems to me that with the ambient noise measurement, we should have a simultaneous measurement of propagation so that we can determine the signal-to-noise ratio as a function of the depth.

We should do that for frequencies and for sources that are located over ranges that we are concerned with and frequencies that we are concerned with.

Dr. Marshall: In all cases that I know of this morning wherein data were reported, there were transmission loss runs made for their own sake alone as well as for the purpose of understanding the ambient noise. And, indeed, it is in general the signal-to-noise ratio statistic that one really wants to use in system design and interpretation of performance.

Dr. Sykes: Can we ask, where did you find the best place to put it?

Dr. Marshall: That wasn't my assigned topic. (Laughter)

Dr. Ross: I just want to make a comment about your Labrador Sea. I think you were in an area where our statistics show about 400 to 600 fishing vessels and that you are not merchant ship dominated in that sea as much as you are fishing boat dominated, and that would explain some of this rather short-term, up-and-down noise since fishing vessels have a much more sporadic movement to them.

Mr. Martin: I think I made that comment. Most of the fishing vessels, of course, are up in the Grand Banks or that area, and you can hear them all the time. The center of the basin was about 300 or 400 miles away. Any time you have a small number of ships, like

merchants, one less ship influences the data quite a bit, as Ira will probably point out again today.

Mr. C. W. Spofford (Office of Naval Research): I have one rather parochial comment again from the modeler's point of view on the question of gathering more ambient noise data.

In the talks this morning, and a lot of other ambient noise data, I have rarely seen trends in ambient noise or depth dependencies or frequency dependencies which have not fit very well within the context of the kinds of models which we are using.

I would like to see the measurers take into account everything we think the models can interpret and explain for ambient noise and then look for the things which are left which we don't have models for. I think we are in very good shape in terms of ambient noise modeling.

The key questions which I think are still hanging are the ones of ship characteristics: the spectra of the ships, where the ships are, and how the ship couples in the medium.

STATISTICAL ANALYSIS OF SHIP GENERATED NOISE

S. C. Daubin

Rosenstiel School of Marine and Atmospheric Sciences
University of Miami

Factors involved in understanding the features of ship-generated noise are discussed. Data are presented and some of the salient features are identified.

A calculational model for ship-generated noise is presented. The model involves area distributions of ships, source level distributions, deterministic transmission loss versus range curves, and a method for combining this information. Model results are compared with data.

Historically, acousticians have been conditioned to think in a deterministic fashion: they attempt to establish the physics of a situation and derive deterministically the results of some experiment. One of the interesting aspects of the Munk and Zachariasen (1976), Dyson, et al. (1976), and Flatté and Tappert (1975) studies is that the random component in the sound velocity structure will force us to think in the future of transmission loss in terms of a probability density function. In the case of ambient noise, the random nature of the variables involved is so obvious that we have little excuse to think about it other than as a random process. This paper presents some data, statistical results derived from these data, and then a suggested method of interpreting the observations with respect to one component of the various potential sources of ambient noise — namely, the ship-generated component.

Figure 1 shows a time series of ambient noise taken in the Pacific by Gerry Morris aboard the FLIP. Basically, four sets of single hydrophone data in 1/3-octave bands were taken over a period of several hours' duration. Average 1/3-octave spectrum levels are plotted. The

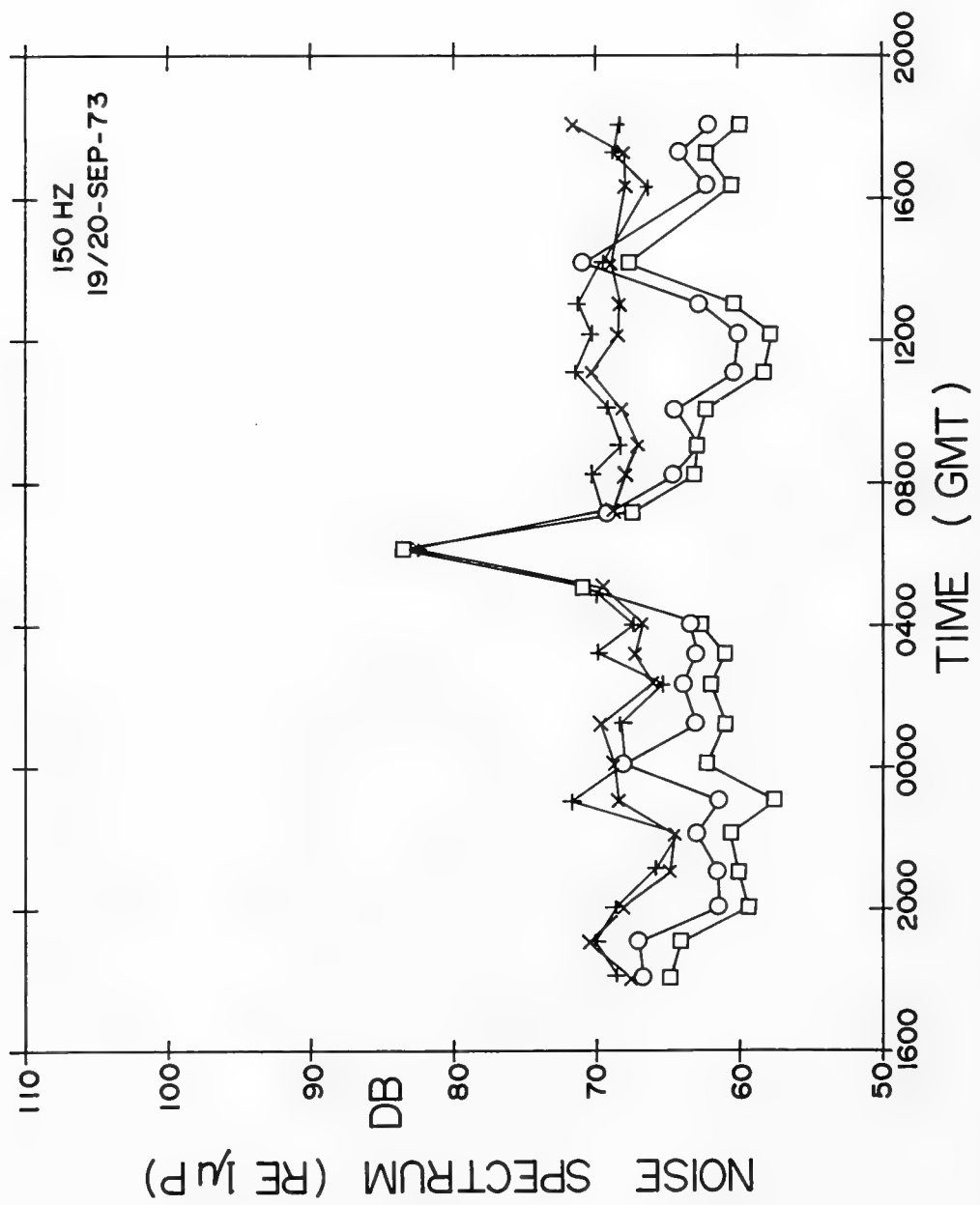


Figure 1. PACIFIC NOISE DATA

high noise period or "hump" in the middle of these data, which exists for the order of 3 hours, is the effect of the passage of a ship.

Figure 2 is a time series of data from the Caribbean. Note that these data cover a period of 10 days, while the previous data covered a few hours. There are four separate 1/3-octave bands, each displayed as a time series of 1-minute energy averages of these data. Within each time series there are several high-noise humps similar to that in Figure 1. To the left of each series is the distribution of these data from the time series.

If we expand a section of a time series from Figure 2, we find a series of these humps on the order of 2 to 4 hours in duration, typically 2-1/2 hours, riding on a background consisting of two parts: very rapid fluctuations and long-term trends. To consider the analysis of such a time series, we must partition it into sets, called statistical sets: Background statistics and foreground statistics, classified according to the integration used to obtain the individual data samples and to the time duration of the set of samples.

The background statistics are those of the type that Ira Dyer has covered extensively for narrow bands, but in our 1/3-octave representation, we see a summation of many such bands. These narrow-band statistics should represent an integration that is long compared with the period of the acoustic signal, yet short compared with the period of the fade of the narrow-band signal, or, alternatively, short compared with the decorrelation time of the narrow-band signal. The duration of such a set should be short compared with a number that I call the set stability time, which in a sense is the decorrelation time of that main time series. For the time series of Figure 2, the stability time is on the order of 2-1/2 hours, which is probably indicative of the fact that the area was heavily trafficked.

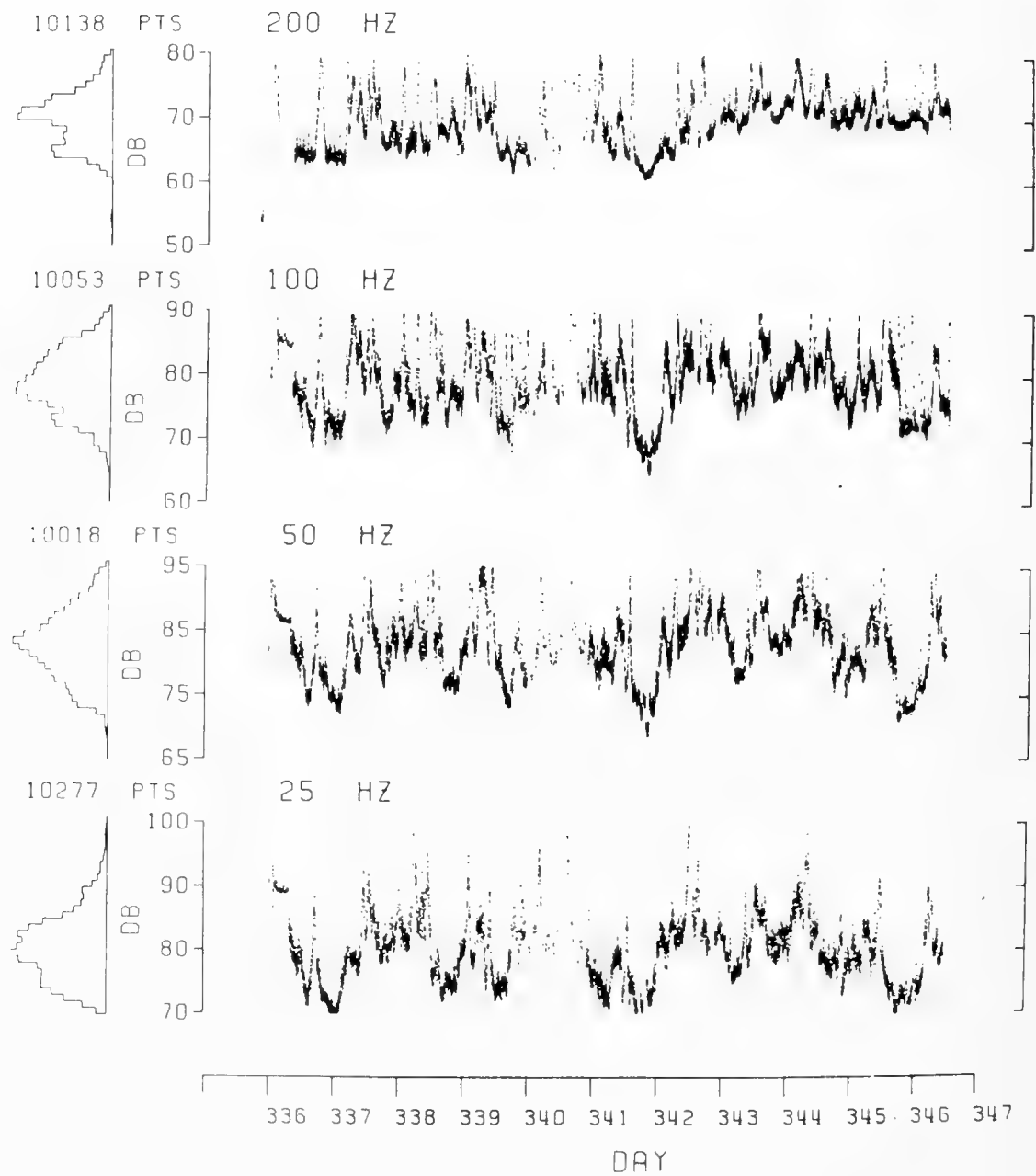


Figure 2. CARIBBEAN NOISE DATA

The foreground statistics require an integration time that is long compared with that used for background statistics and short compared with the set stability time. The total time series duration should be long compared with the integration time.

Figure 3 is taken from Dyer (1970) and shows that the background statistics (calculated in dBs) associated with a single narrow-band source should in theory have a standard deviation of 5.6 dB. When " l " of these sources are at the same strength and are subject to the same average transmission loss, the fluctuation level is predicted to decrease (for 10 sources, it is predicted at about a 1.4 dB standard deviation). In a later paper Dyer extends this to include noise from sources of different strengths and different frequencies but the sources remain a stable set in the sense that the transmission from source to receiver is not intended to change.

Figure 4 shows the power spectrum derived from the time series of Figure 2. The abscissa is in cycles per day. Note the energy peak at about 0.6 of a cycle per day, which happens to be the inertial period where these data were taken. The task of understanding what is going on involves the prediction of many things, such as the means, the variances, the distributions, and the power spectra. We also want to know the mechanisms that are producing such a distribution of energy.

Let us focus on the section of the power spectra above one cycle per day. As mentioned before, the decorrelation time of the time series is on the order of 2-1/2 hours or 0.1 days. Its reciprocal is a measure of the maximum frequency for which significant energy appears within this power spectrum.

Now, the area under the power spectra curves is the variance, as plotted in Figure 5. The time series of Figure 2 corresponds to

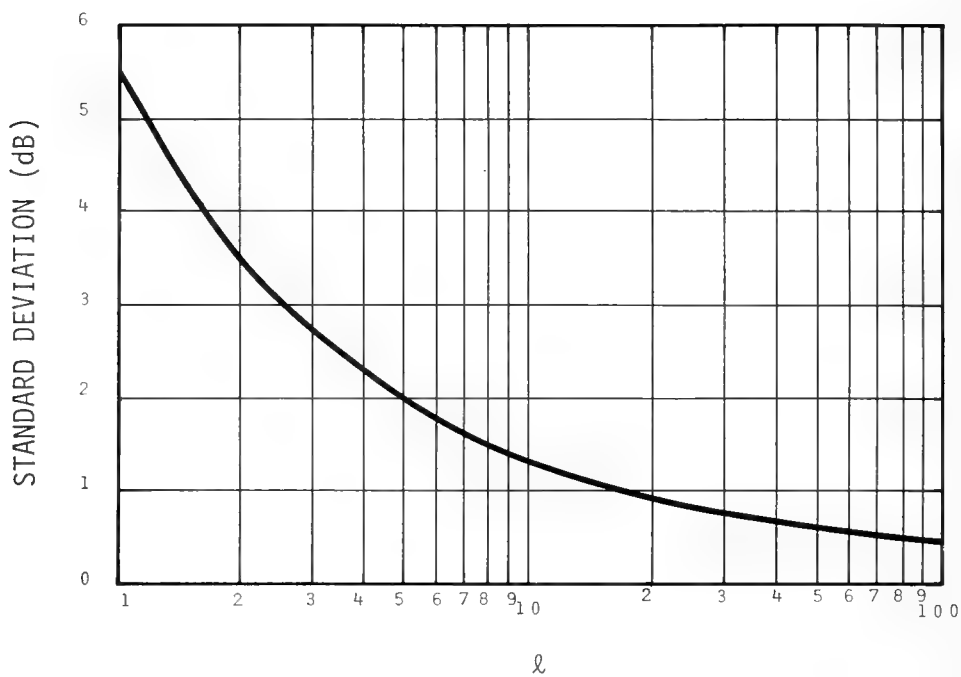


Figure 3. STANDARD DEVIATION OF A SUM OF ℓ RANDOM PHASES OF EQUAL AMPLITUDE

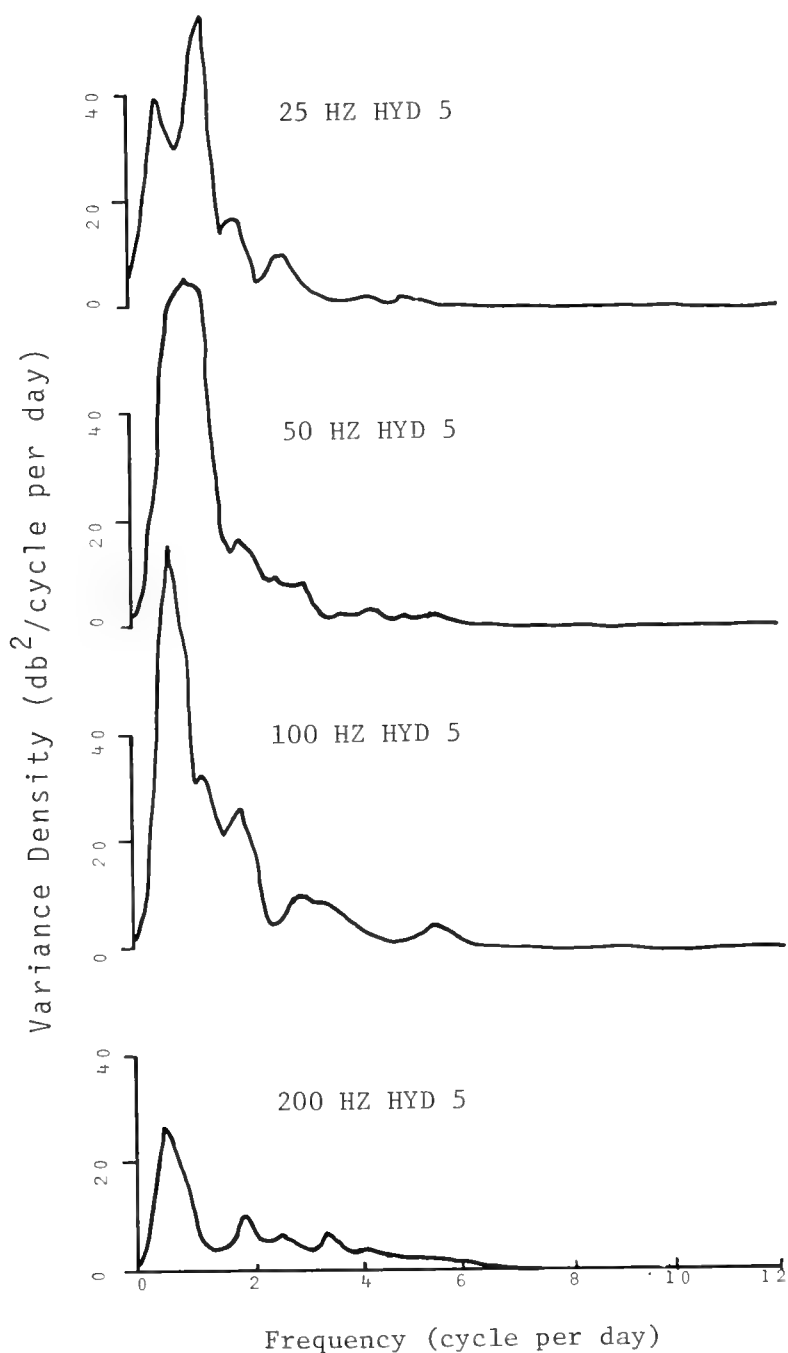


Figure 4. SPECTRUM OF CARIBBEAN NOISE DATA

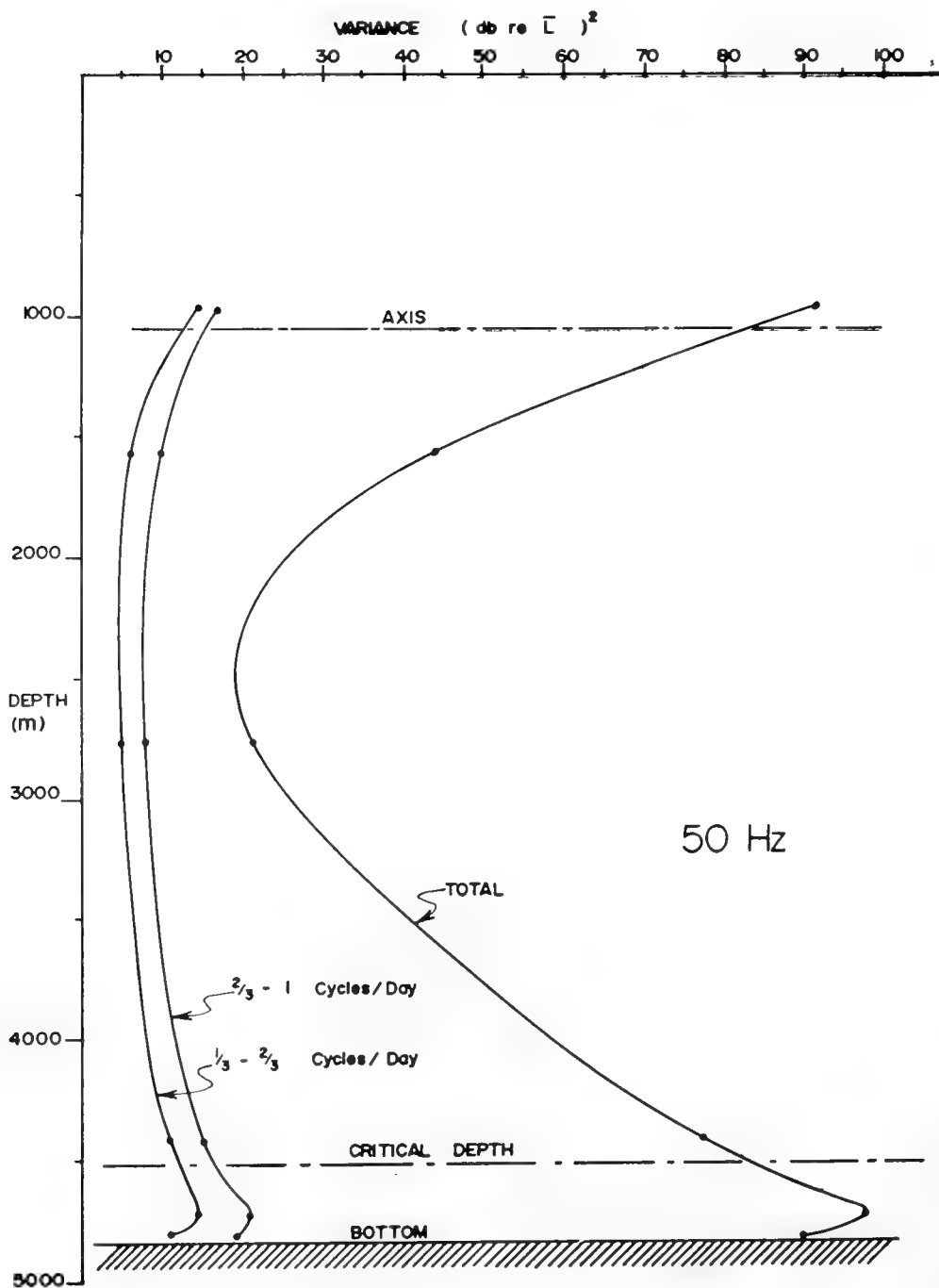


Figure 5. VARIANCE VERSUS DEPTH

data taken near critical depth, about 4400 meters. Axis depth is about 1100 meters, and the bottom is at about 4900 meters. The depth effect is rather strong where the variance is highest, near critical depth and the axis. These observations seem to be consistent with the observations of Marshall and others.

How do we interpret such data and explain the observed means, variances, and other statistics? One of the assumptions we make — perhaps erroneously — is that a major factor in the generation of noise is surface shipping.

Figure 6 shows two examples of ship distributions which might be encountered in an ocean area radius of 450 miles. In one, the overall ship density is about 0.1 of a ship per degree square, while in the other it is about 0.5 of a ship per degree square.

To investigate the relation between shipping and ambient noise, we perform aircraft surveys of surface traffic as part of the field experiment. We use radar or visual methods to obtain position, course, speed of ships; if we are lucky, we get their size and even their identification. We then attempt to relate these observations to the ambient noise data. We have no good measure of the source level of each ship, however. Even if we did know the source levels and the coupling mechanisms to the ocean, and were able to relate them to the noise level at one time, we would have only one point on a curve which is varying with time. We need the statistics of the noise for a long period of time. Hence, this represents an attempt to solve deterministically a problem that is essentially statistical. Therefore, we will treat the problem in its parts, namely, in the statistics of source level and the statistics of ship distributions. From this we should be able to remove from the observed data those components which result from the ship distribution.

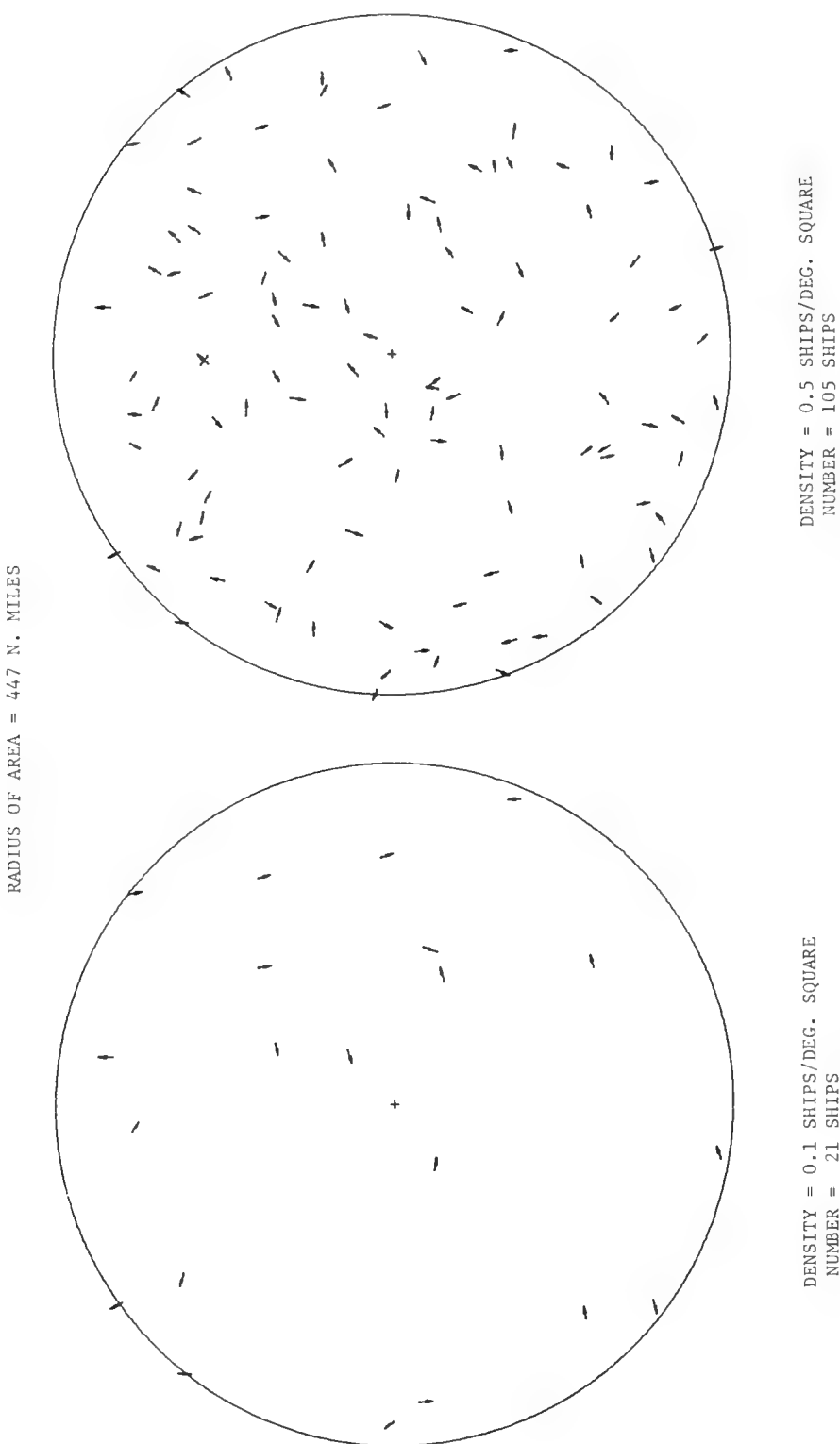


Figure 6. EXAMPLES OF SHIPPING DISTRIBUTIONS

Now, consider Equation (1), the most simple-minded ambient noise model shown during this conference:

$$I = \sum_{j=1}^N T_j S_j \quad (1)$$

where

$$T_j = T(R_j) = \int T(R) \delta(R_j - R) dR.$$

The intensity, I , at the receiving point is an incoherent sum of independent signals from a set of N ships. T_j is the energy transmission from source to receiver, and S_j is the source intensity of the j^{th} ship. Assume further that the transmission loss is a function of range only, and not a function of azimuth. Although we know this to be unrealistic, nevertheless, it is not a bad approximation. Hence, T_j is the value of the transmission curve T at the radial position of the j^{th} ship, R_j .

The problem then is to predict the statistics of the received intensity: its expectation, distribution and, ultimately, its power spectrum. These will be derived from the statistics of the two variables, T_j and S_j , which are to be treated as random variables.

We know from statistics that the expectation value of the product of random variables is given by the product of the expectation values plus the statistical cross-correlation function between these variables times their individual standard deviations:

$$E(I) = N \left(E(T) E(S) + \rho_{TS} \sigma_T \sigma_S \right). \quad (2)$$

An additional assumption for this part of the derivation is that the correlation between the position relative to the receiving site and

the source level is assumed to be zero. This may not be the case in all observations. Equation (2) then becomes:

$$E(I) = N E(T) E(S). \quad (3)$$

Now the average value in any situation of the transmission from source to receiver is given by

$$\begin{aligned} \bar{T} &= \frac{1}{N} \sum T_j = \frac{1}{N} \sum \int T(R) \delta(R_j - R) dR \\ &= \int T(R) \frac{1}{N} \sum \delta(R_j - R) dR. \end{aligned} \quad (4)$$

Allowing the number of ships to get very large, we obtain the expectation value of the transmission curve, that is, the integral over all ranges of the product of the transmission and the probability density in range, $p(r)$ of the ships:

$$\lim_{n \rightarrow \infty} \bar{T} = E(T), \quad (5)$$

with

$$E(T) = \int T(R) p(R) dR. \quad (6)$$

Therefore, the expectation value of the local received intensity is given by

$$E(I) = N E(S) E(T) = N E(S) \int T(R) p(R) dR. \quad (7)$$

Similarly, the variance of the intensity can be calculated as:

$$\text{Var}(I) = N \left[\sigma_s^2 + \mu_s^2 \right] \text{Var}(T) \quad (8)$$

where

$$\text{Var}(T) = \int T^2(R) p(R) dR - \left[\int T(R) p(R) dR \right]^2. \quad (9)$$

To apply these equations, we can construct models of transmission and of surface ship density which correspond to an experimental situation, and obtain an estimate of the variance of the transmission (Equation 9). This is then combined with data for the variance and mean value of source levels to yield the variance of the intensity (Equation 8). Notice that we require only the statistics of source level over the ensemble of ships, rather than the specific value for any given ship.

To illustrate the approach, we have run such a model on a Monte Carlo basis — using ship densities of 0.1 ships per degree square (as in Figure 6) and the simple empirical transmission curve shown in Figure 7. The result is a modeled time series of ambient noise and a distribution of levels given in Figure 8.

Such examples do not relate too closely at this time to the observed data, indicating perhaps that our distribution of ships is wrong, but also perhaps that by removing these components from these observed data we can then have a means of investigating the non-ship-generated statistics in the foreground data.

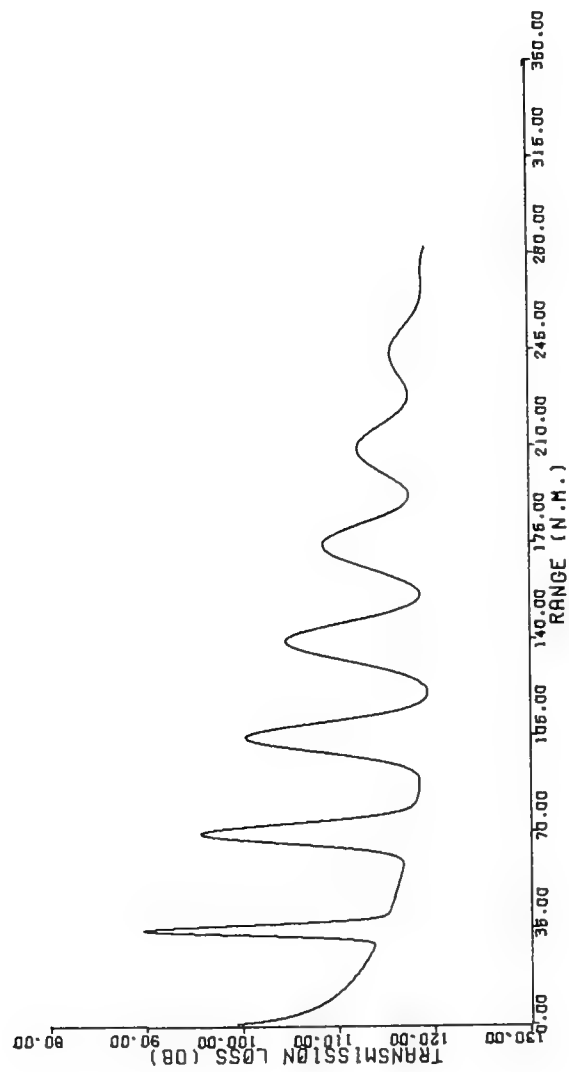


Figure 7. TRANSMISSION LOSS VERSUS RANGE

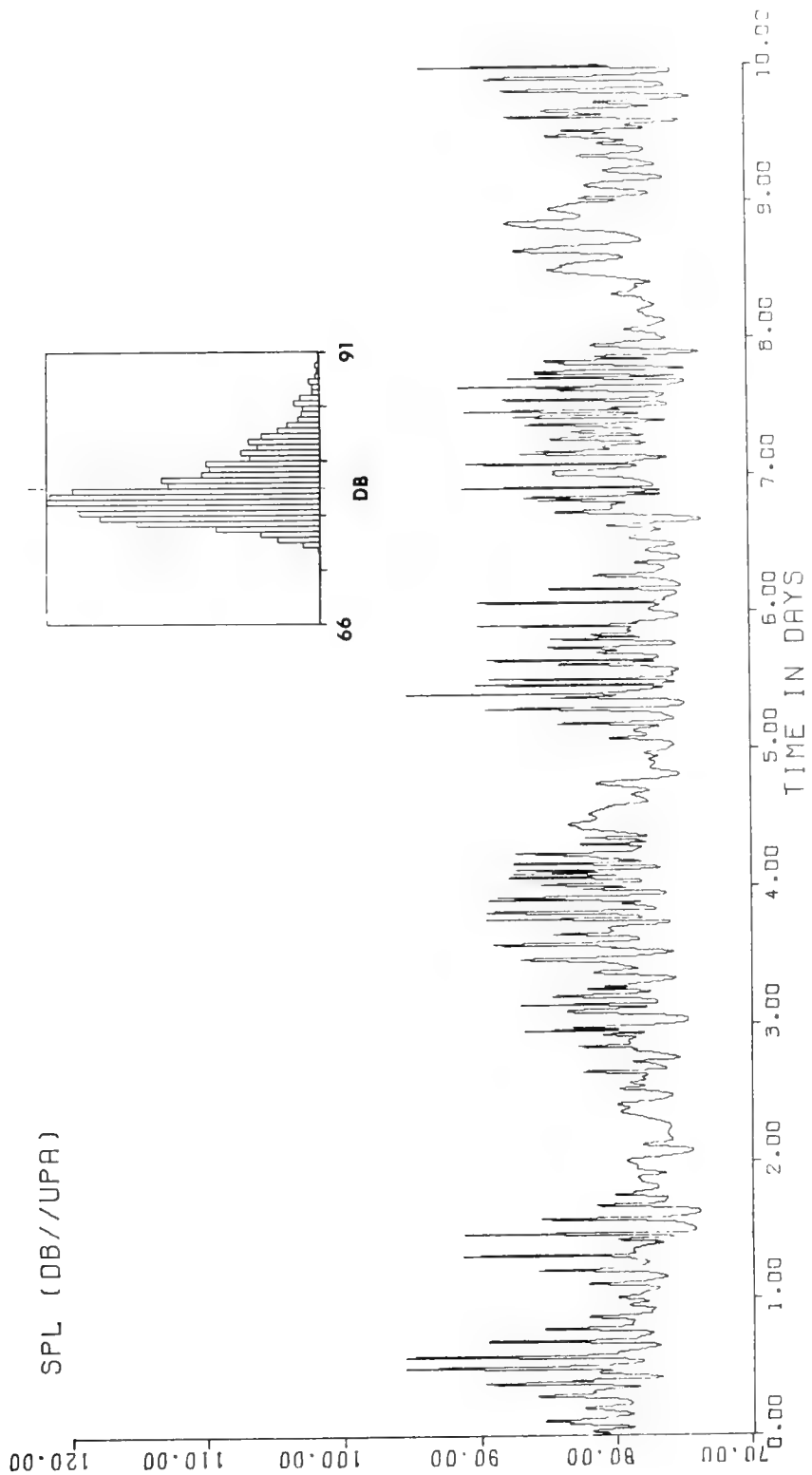


Figure 8. MODEL OF AMBIENT NOISE

REFERENCES

Dyer, I., *J. Acoust. Soc. Am.* 48:342, 1970.

Dyson, F., W. Munk, and B. Zetler, "Interpretation of Multipath Scintillations Eleuthera to Bermuda in Terms of Internal Waves and Tides," *J. Acoust. Soc. Am.* 59:1121, 1976.

Flatté, S. M., and F. D. Tappert, "Calculations of the Effect of Internal Waves on Oceanic Sound Transmission," *J. Acoust. Soc. Am.* 58:1151, 1975.

Munk, W. H., and F. Zachariasen, "Sound Propagation Through a Fluctuating Stratified Ocean: Theory and Observation," *J. Acoust. Soc. Am.* 59:818, 1976.

VERTICAL NOISE DISTRIBUTION

V. C. Anderson

Scripps Institute of Oceanography
University of California
La Jolla, California

A recent experience in attempting to measure the vertical directionality of noise is recounted with the emphasis on several instrumentation pitfalls. Specific problem areas included angular sampling, frequency filtering, data quantization, and common-mode noise. The last problem was the most severe, making data interpretation quite difficult. The filtering problems limited the estimate of noise level to only the high noise directions. Nevertheless, an estimate of the noise directionality at low frequencies was obtained as a function of receiver depth for a deep-water site in the Northeastern Pacific. The results are consistent with energy arriving via sound-channel paths from distant shipping.

INTRODUCTION

This paper addresses primarily the problems associated with a recent attempt to measure vertical noise directionality, and secondarily the results of that measurement attempt. The measurements were made using FLIP in the Northeastern Pacific. Figure 1 illustrates the sound-speed profile at FLIP's location, and the positions of the 500-meter, 20-element measurement array. These positions were occupied twice, in the time sequences indicated in Figures 2 and 3. Additional noise "events" such as nearby ships and biologics are indicated as well. Note that the array positions span depths from the sound-channel axis to 500 meters below the critical depth of 4380 meters. The C and E designators identify actual data sets analyzed.

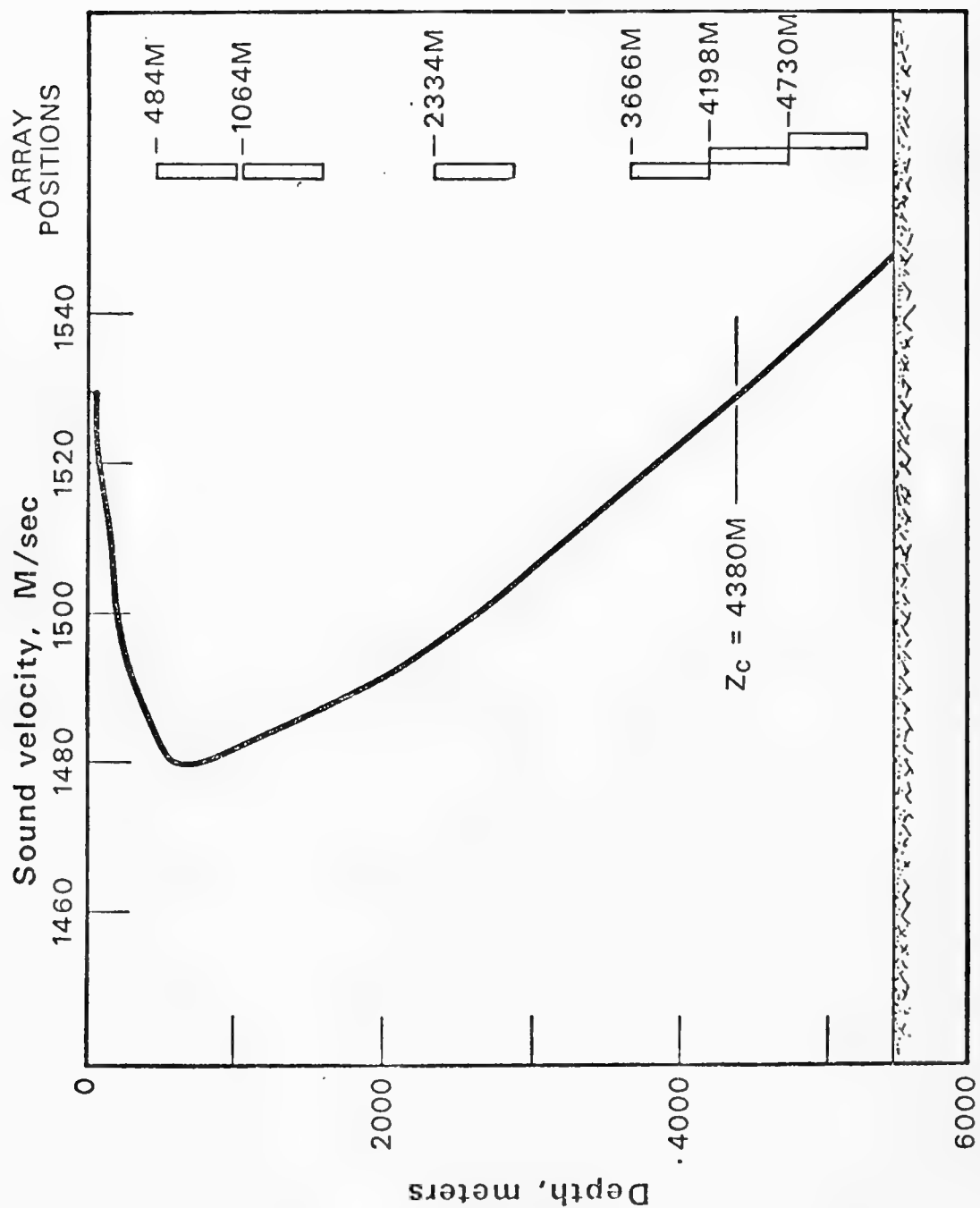


Figure 1. VELOCITY PROFILE AND RELATIVE ARRAY POSITIONS

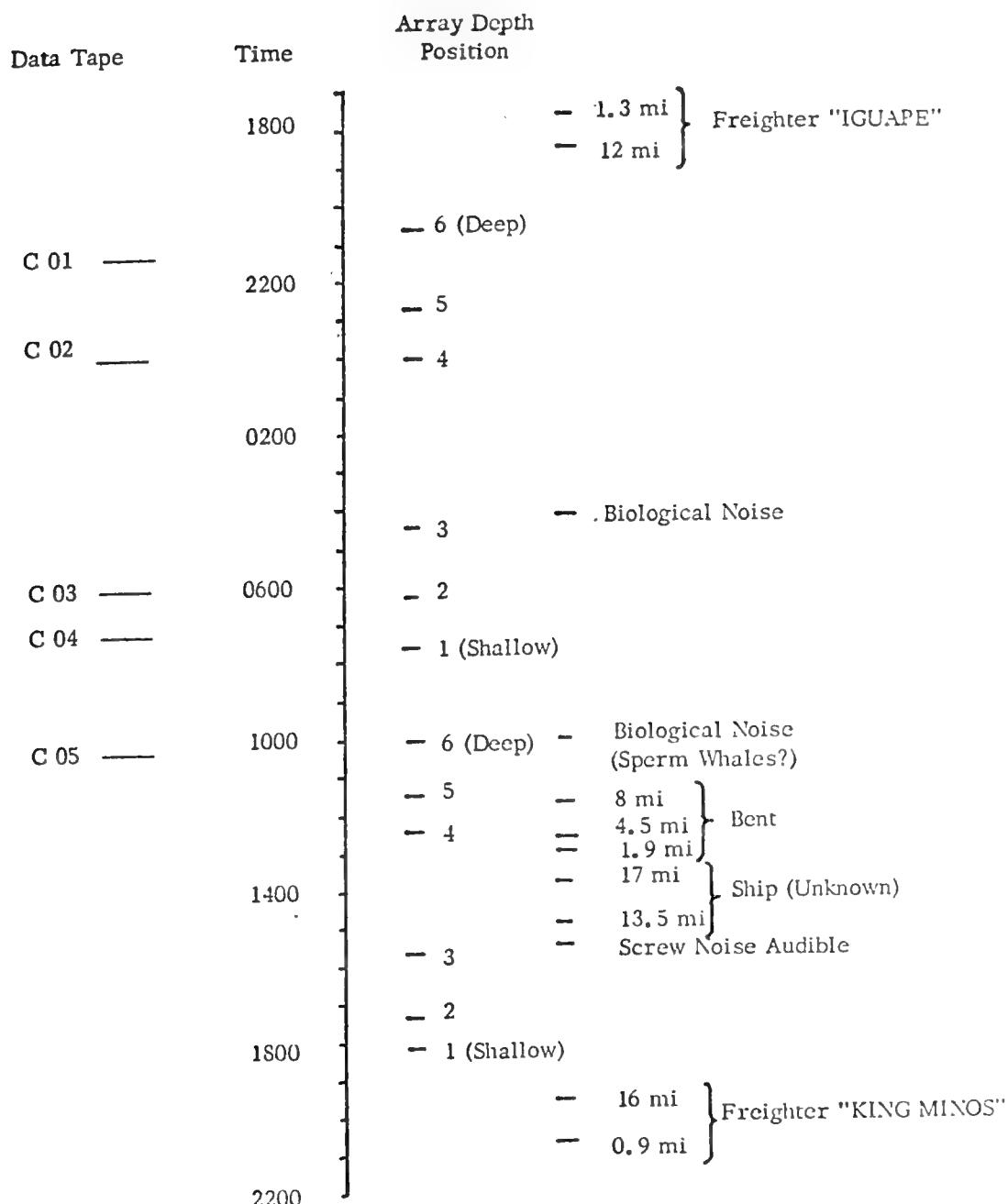


Figure 2. LOCAL SHIP TRAFFIC NEAR FLIP DURING
5-6 SEPTEMBER 1973 NOISE PERIOD

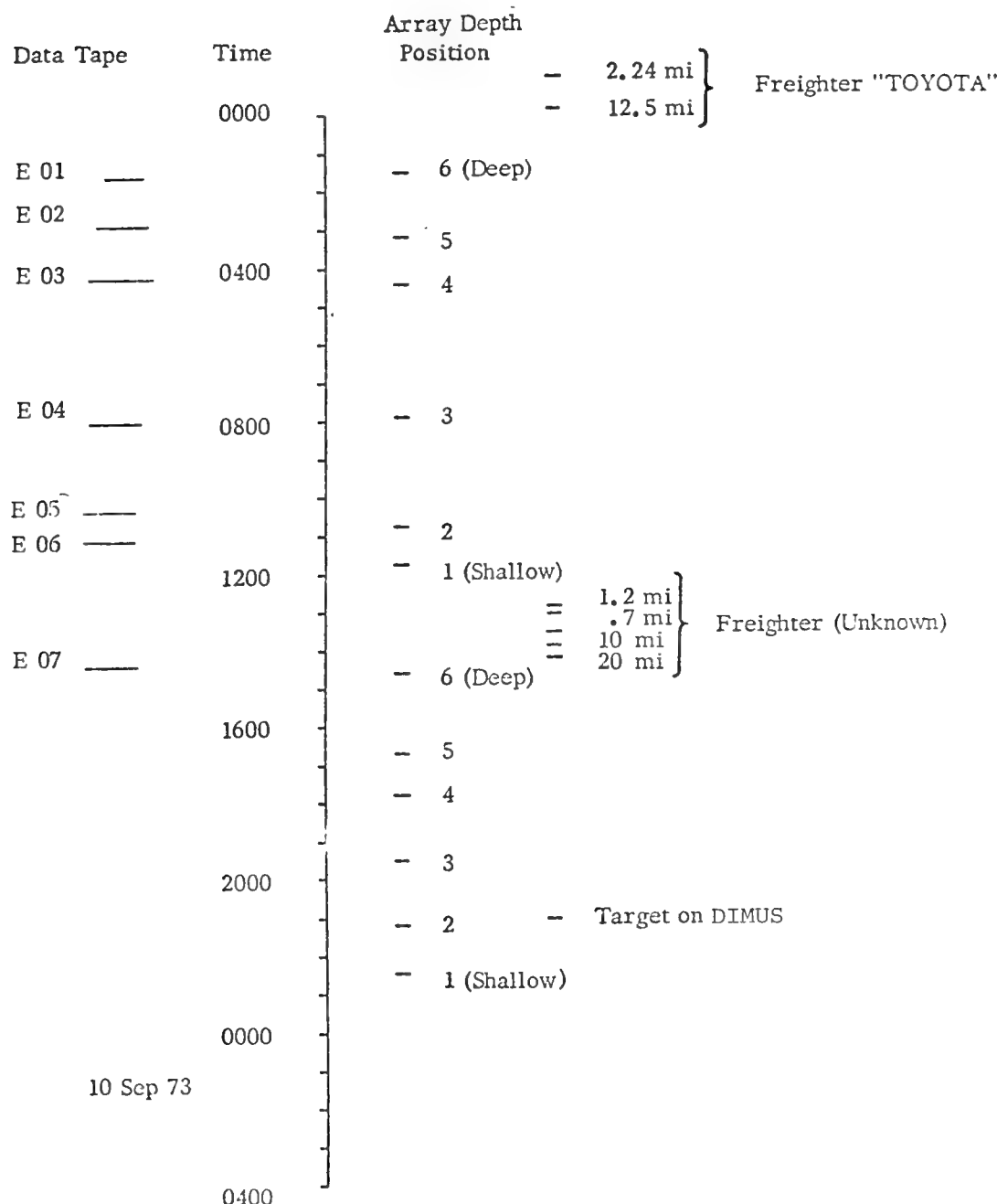


Figure 3. LOCAL SHIP TRAFFIC NEAR FLIP DURING
8-9 SEPTEMBER 1973 NOISE PERIOD.

INSTRUMENTATION

The ability to interpret the measurements was severely limited by the characteristics of the instrumentation system. Specific problems encountered were associated with:

- Angular sampling
- Frequency filtering
- Data quantization
- Common-mode noise.

Figures 4, 5 and 6 illustrate the response of the 128, 1.5-degree spaced, preformed beams to a horizontally arriving signal at frequencies of 23, 36, and 100 Hz, respectively. The beams were formed without shading, and since the array elements were equispaced, the $\sin x/x$ pattern is obtained. At 23 Hz (Figure 4), this pattern is fairly adequately sampled by the selected beams. At 36 Hz (Figure 5), they are somewhat undersampled, and by 100 Hz (Figure 6), they are undersampled to the extent that the near-horizontal beams are steered to the nulls in the $\sin x/x$ pattern. At 100 Hz, the array is underpopulated, resulting in grating lobes at ± 30 degrees from the horizontal direction (90 degrees in the figures). These beam responses play an important role in interpreting the measured data, especially at 100 Hz, as described subsequently.

To obtain data at prescribed frequencies, the basic time series of broadband (digitized at 1 kHz) time-multiplexed beamformer output was multiplied by sine and cosine functions of the center passband

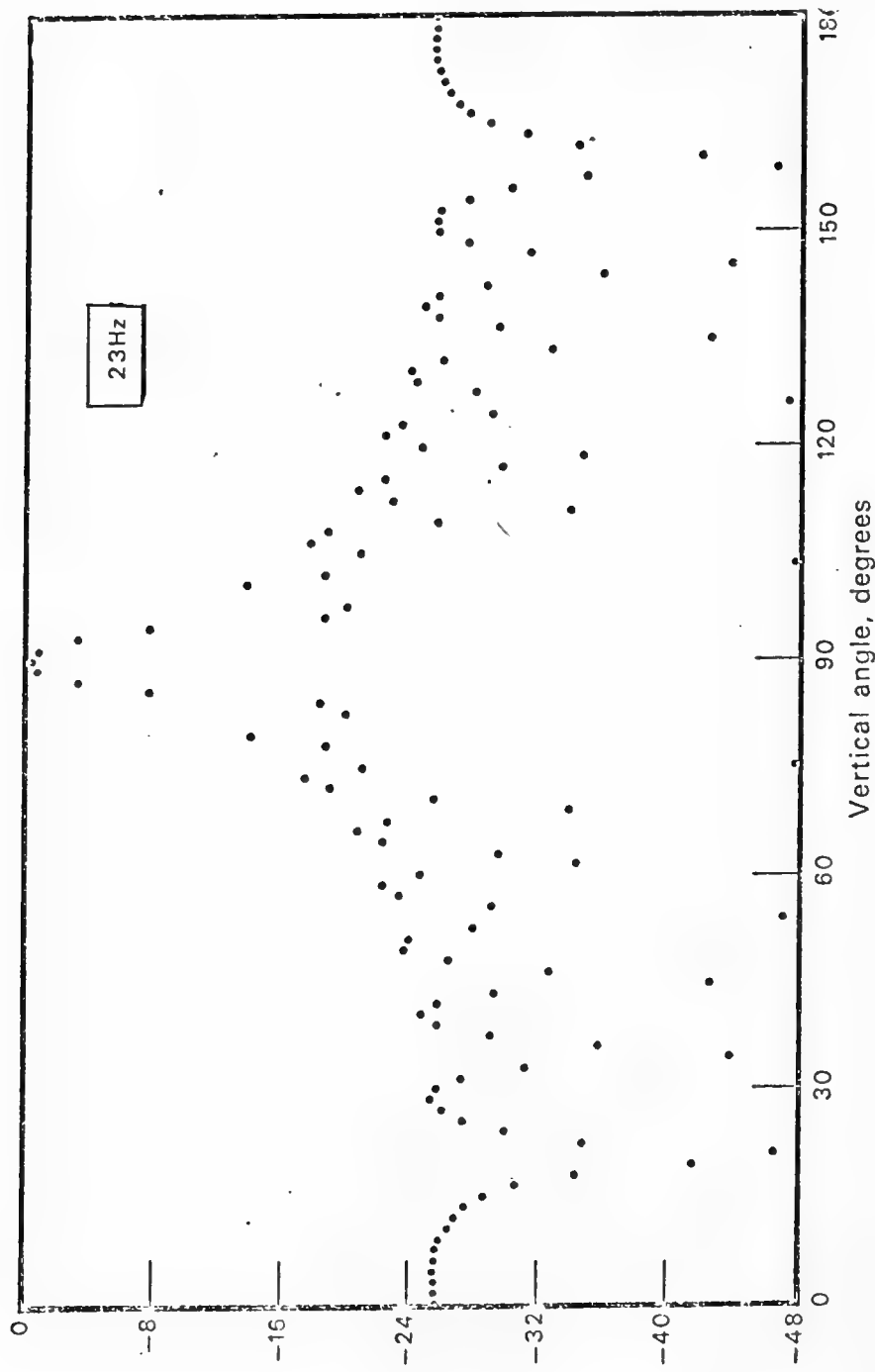


Figure 4. RESPONSE OF BEAMS STEERED TO INDICATED DIRECTIONS TO ENERGY ARRIVING IN THE HORIZONTAL (90-DEGREES) AT 23 Hz

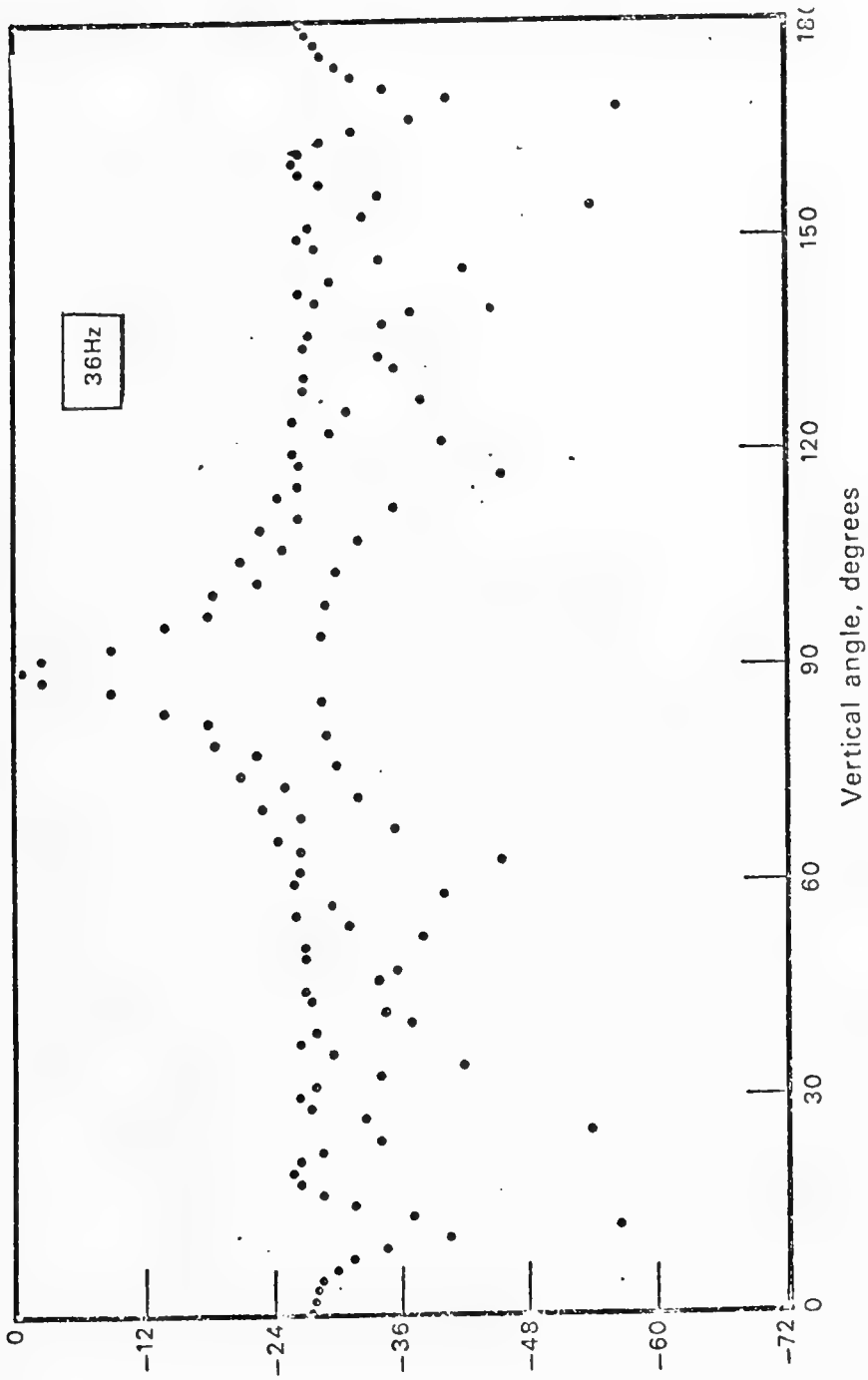


Figure 5. RESPONSE OF BEAMS STEERED TO INDICATED DIRECTIONS TO ENERGY ARRIVING IN THE HORIZONTAL (90-DEGREES) AT 36 Hz

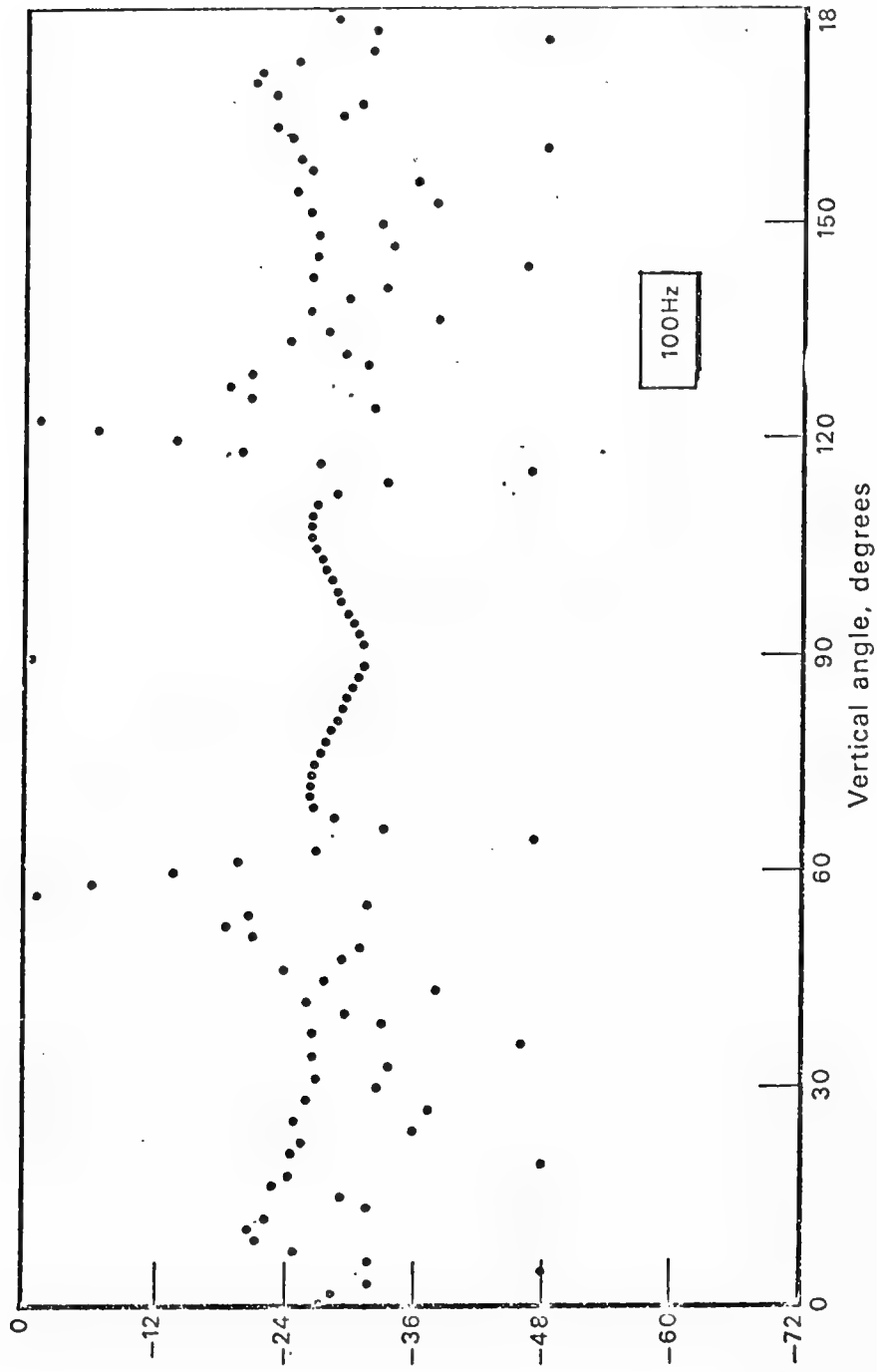


Figure 6. RESPONSE OF BEAMS STEERED TO INDICATED DIRECTIONS TO ENERGY ARRIVING IN THE HORIZONTAL (90-DEGREES) AT 100 Hz

and the resulting spectra averaged with a three-point weight, simulating Hamming shading on the basic time series. The resulting sidelobes in frequency are down 25 dB, as shown for the 23 Hz passband spectrum in Figure 7. This still leaves the possibility for out-of-band noise contaminating the filter output since the total noise band is 500 Hz and the passband is 0.8 Hz. This factor must be considered in the subsequent data interpretation.

The next data problem was encountered during an attempt to construct noise-power histograms. Figure 8a illustrates the type of histogram obtained initially. Because the original 1000-point data set was reduced to a single data point at each frequency of interest, there was a total of only 300 such points for each histogram (corresponding to 10 minutes of data). The combination of quantization errors and the logarithmic tabulation base resulted in some level-bins having no possibility of being occupied. Basically, the level quantization was taxing the available level accuracy, resulting in "noisy" histograms like Figure 8a. This problem was corrected (Figure 8b) by weighting the points and interpolating over the empty bins. These corrected histograms were used to compute the mean power shown in subsequent figures.

Figure 9 displays noise power as a function of steered angle for the three frequency bands of 23, 36 and 100 Hz. While at first these data appear to show highly directional noise, peaked toward the horizontal, closer inspection showed that they were contaminated by common-mode noise: a broadband noise with the same phase at each element so that it appears as a horizontally arriving signal. In fact, these noise patterns, especially at the two lower frequencies, are quite similar to the beam-response patterns shown in Figures 4, 5, and 6 for a horizontal signal.

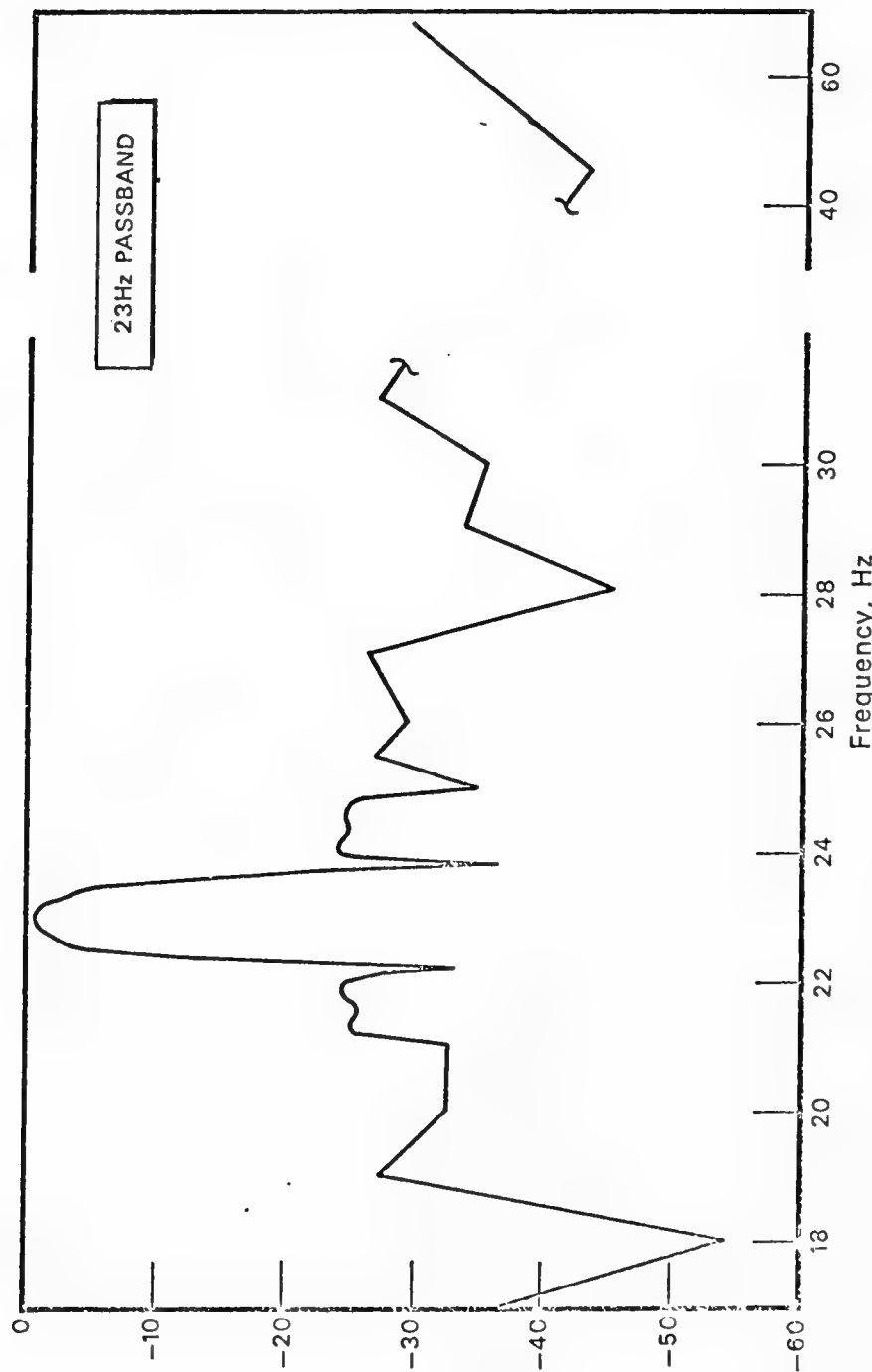


Figure 7. FREQUENCY RESPONSE OF THE 23 Hz PASSBAND

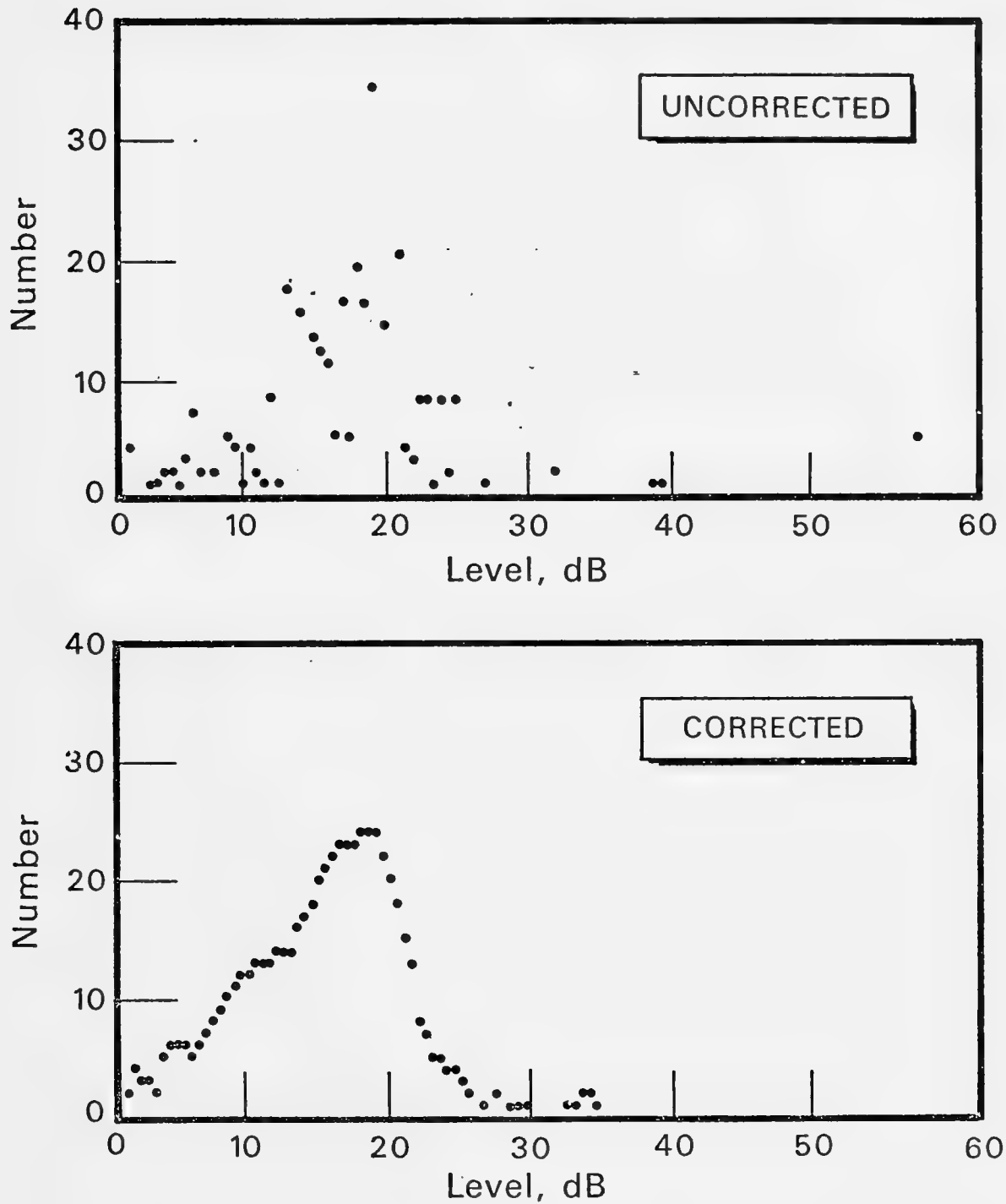


Figure 8. HISTOGRAMS OF NOISE LEVEL ILLUSTRATING QUANTIZATION AND SAMPLING PROBLEMS (6a) AND RESULTS OF WEIGHTING AND INTERPOLATION (6b)

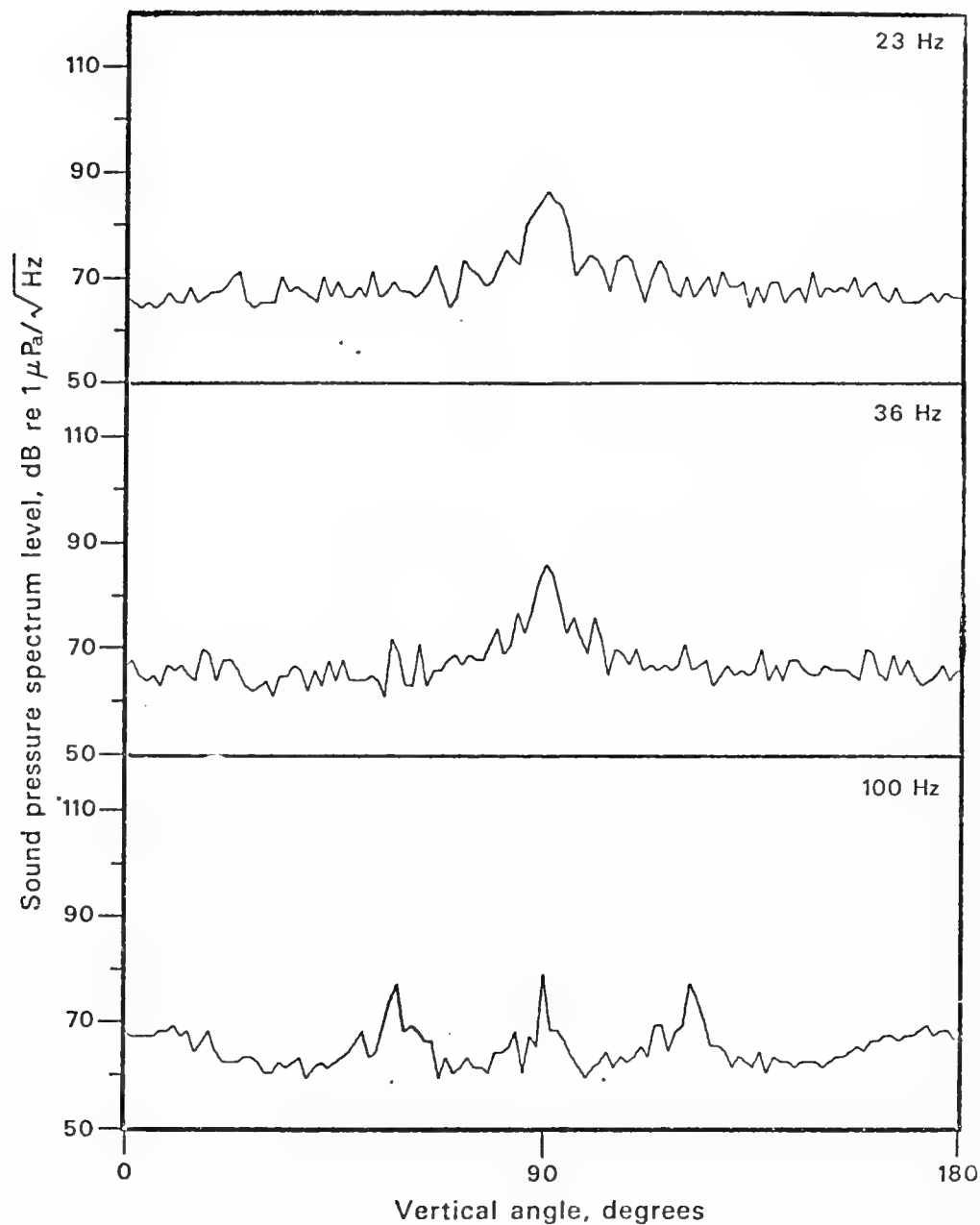


Figure 9. MEASURED BEAM NOISE-DAY 1 (C01) 4300 METERS

Fortunately, all of the 100-Hz beams steered just off the horizontal had nulls in the horizontal (see Figure 6) so that only the horizontal beam (90 degrees) should be contaminated. This is more apparent at the shallower receiver depth of 3781 meters (Figure 10). The high noise plateaus are essentially independent of frequency. Still shallower, the plateau at the lower frequencies continues to grow and is quite discernible (Figures 11 and 12). At 100 Hz, however, the wider plateau overlaps with its images from the grating lobes. Returning to the deep receiver on the first day (Figure 13), the splitting is apparent. It should be remembered that the out-of-band noise associated with the bandpass filter characteristics makes it impossible to infer the attributes of the low-noise directions near the vertical.

Figures 14 through 19 represent the second day's measurements for a denser set of depths. Again, broadening of the noise is apparent in shifting from 100 Hz for deep receivers (Figures 14, 15, and 16) to the lower frequencies for the shallow receivers (Figures 17, 18, and 19). There are some differences between the results on these two days. Notice the more rounded peak at 23 Hz on the second day versus the squarer peak on the first (Figure 12). On the second day, a freighter nearby may have influenced the noise.

Figure 20 illustrates the response of the system to narrowband signals rather than broadband noise. There is sufficient signal-to-noise in this case that out-of-band noise is not a problem. When the filter sidelobes are not important, the beamformer has a much greater dynamic range.

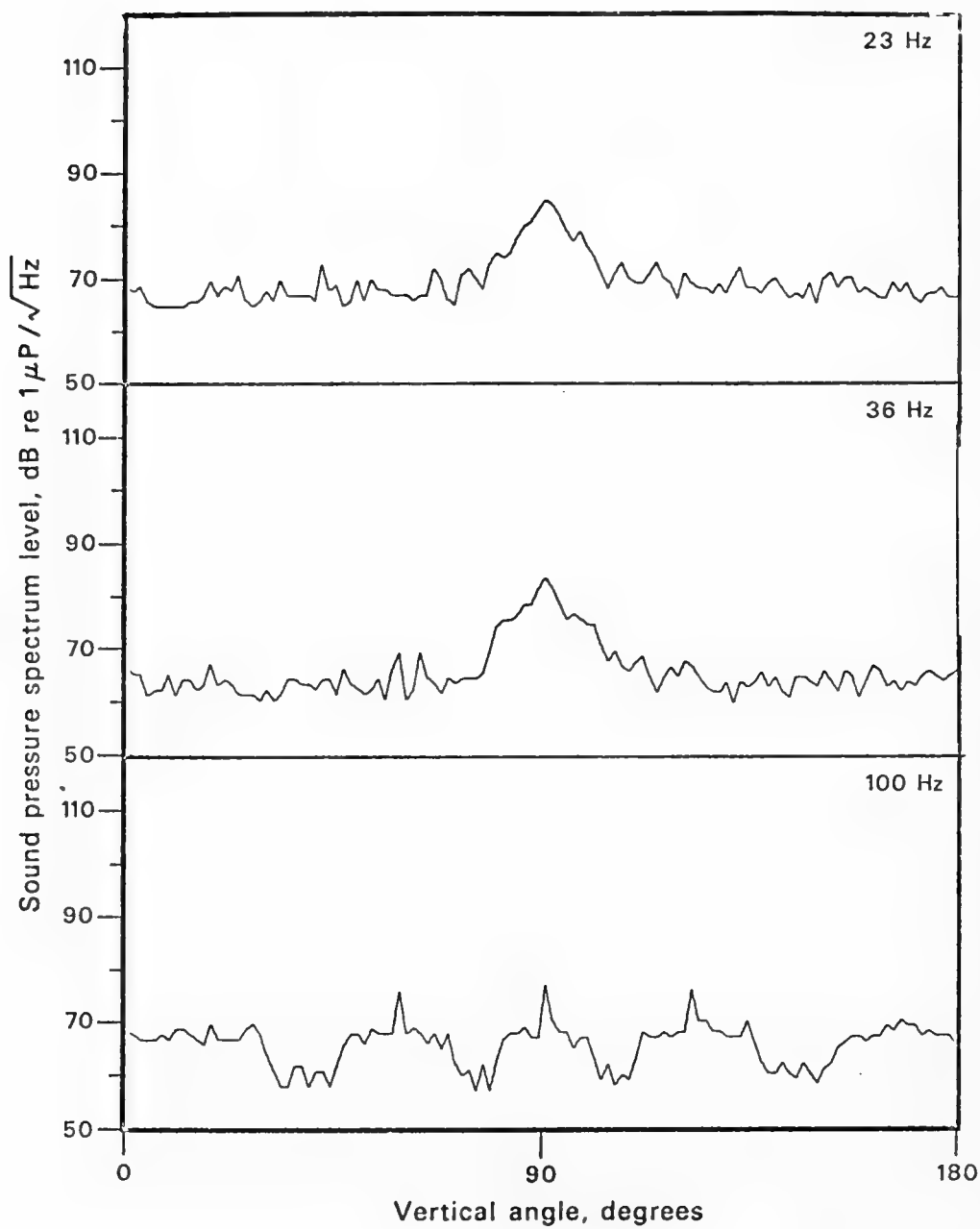


Figure 10. DAY 1 (C02) 3800 METERS

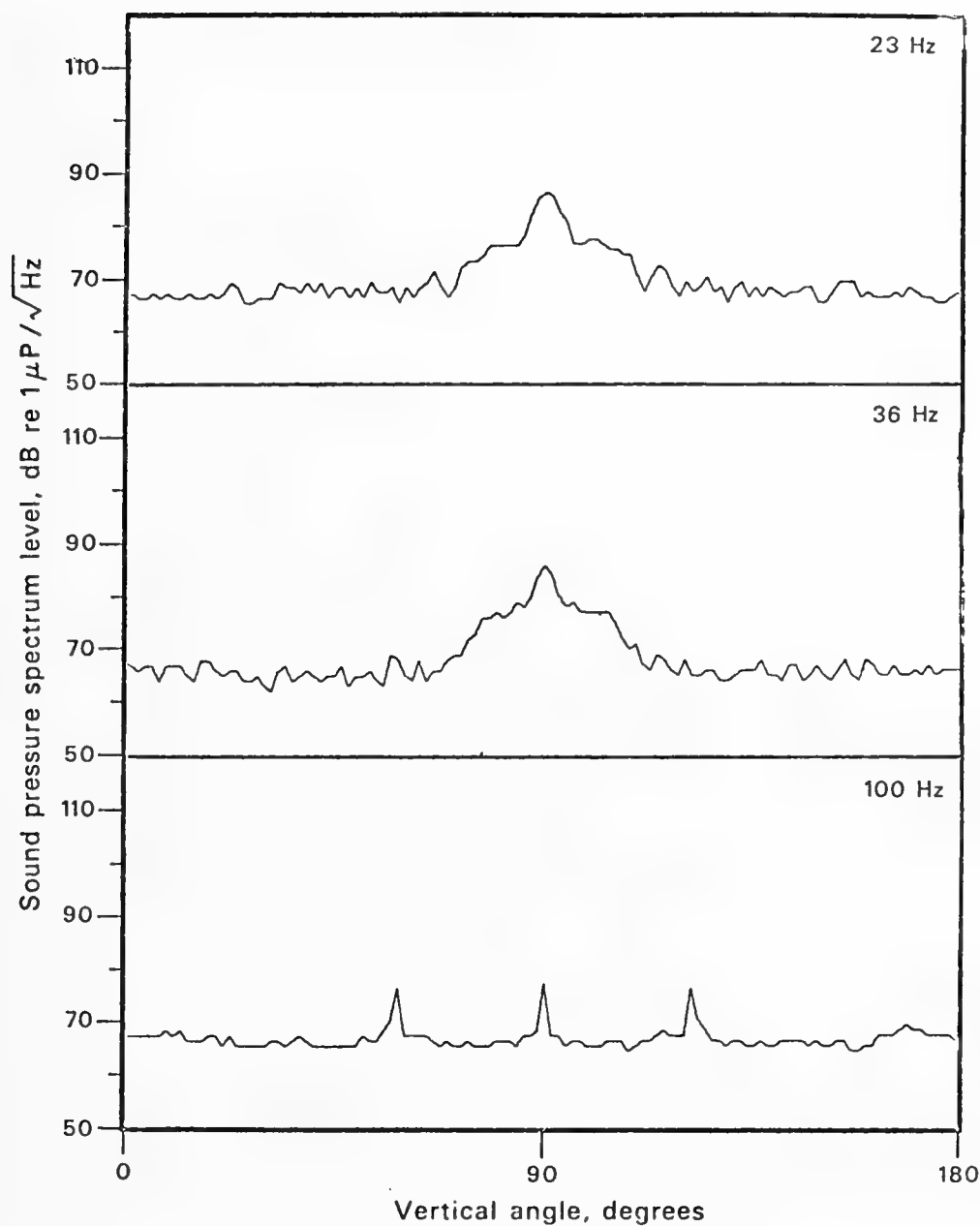


Figure 11. DAY 1 (C03) 1200 METERS

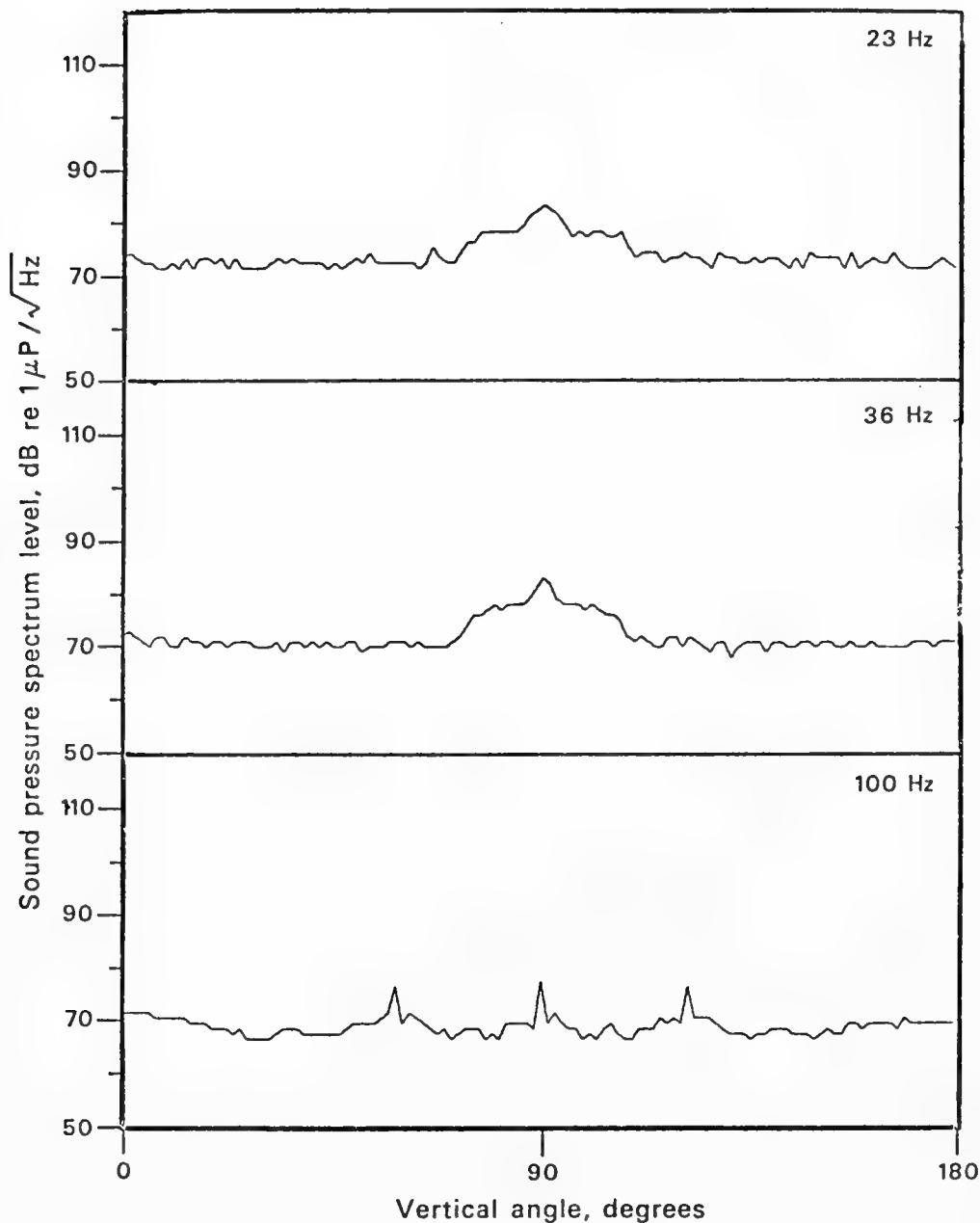


Figure 12. DAY 1 (C04) 700 METERS

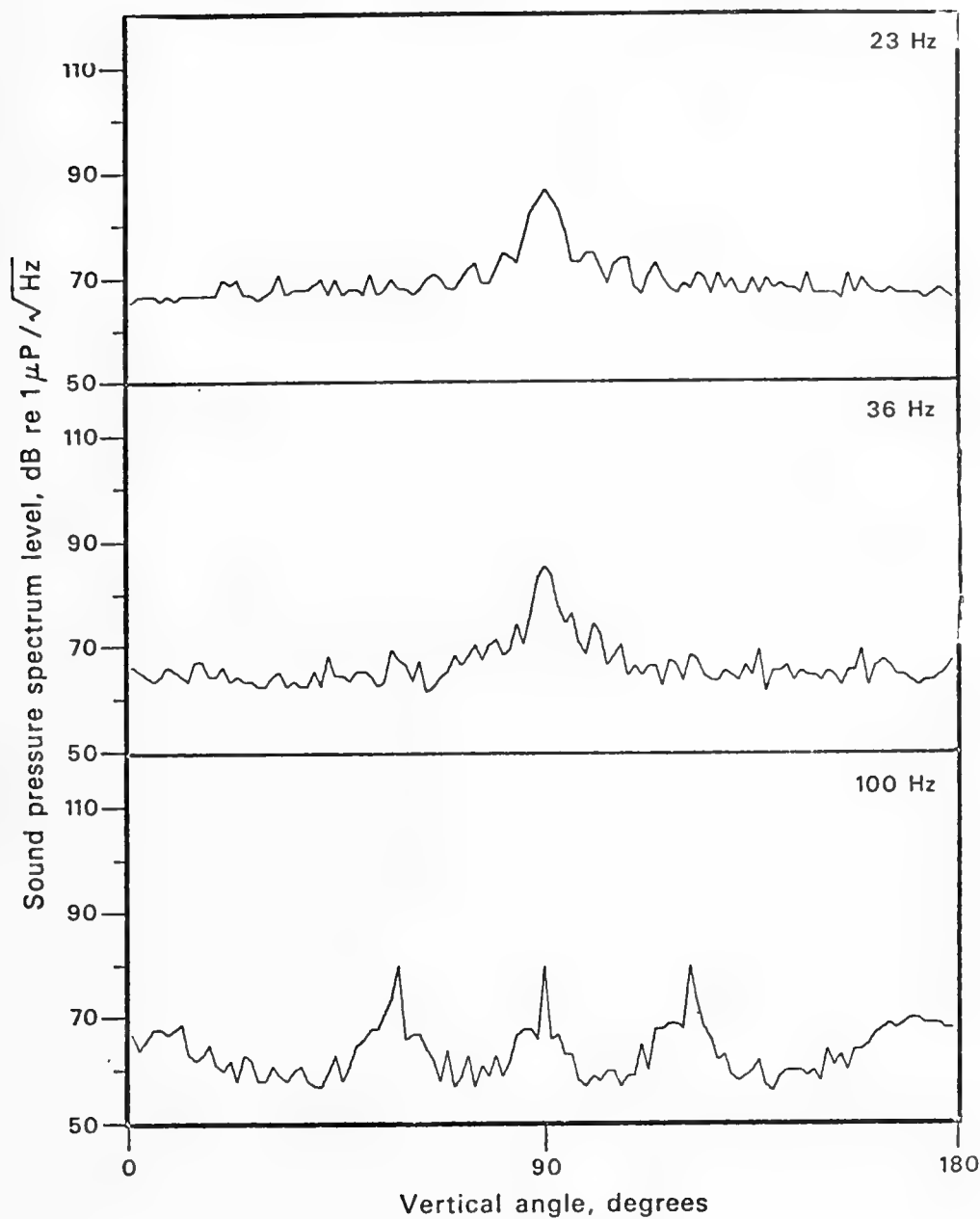


Figure 13. DAY 1 (C05) 4800 METERS

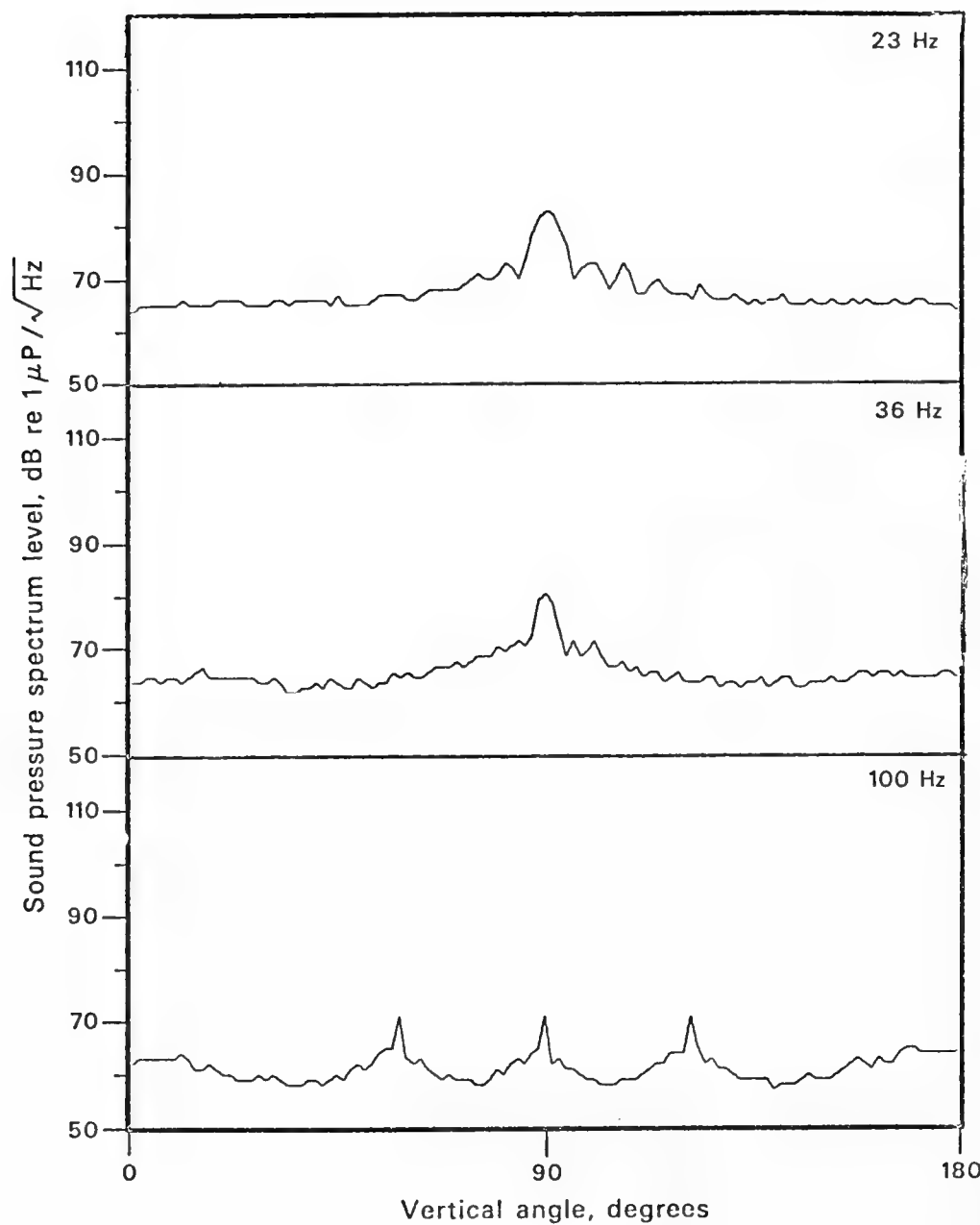


Figure 14. DAY 2 (E01) 4800 METERS

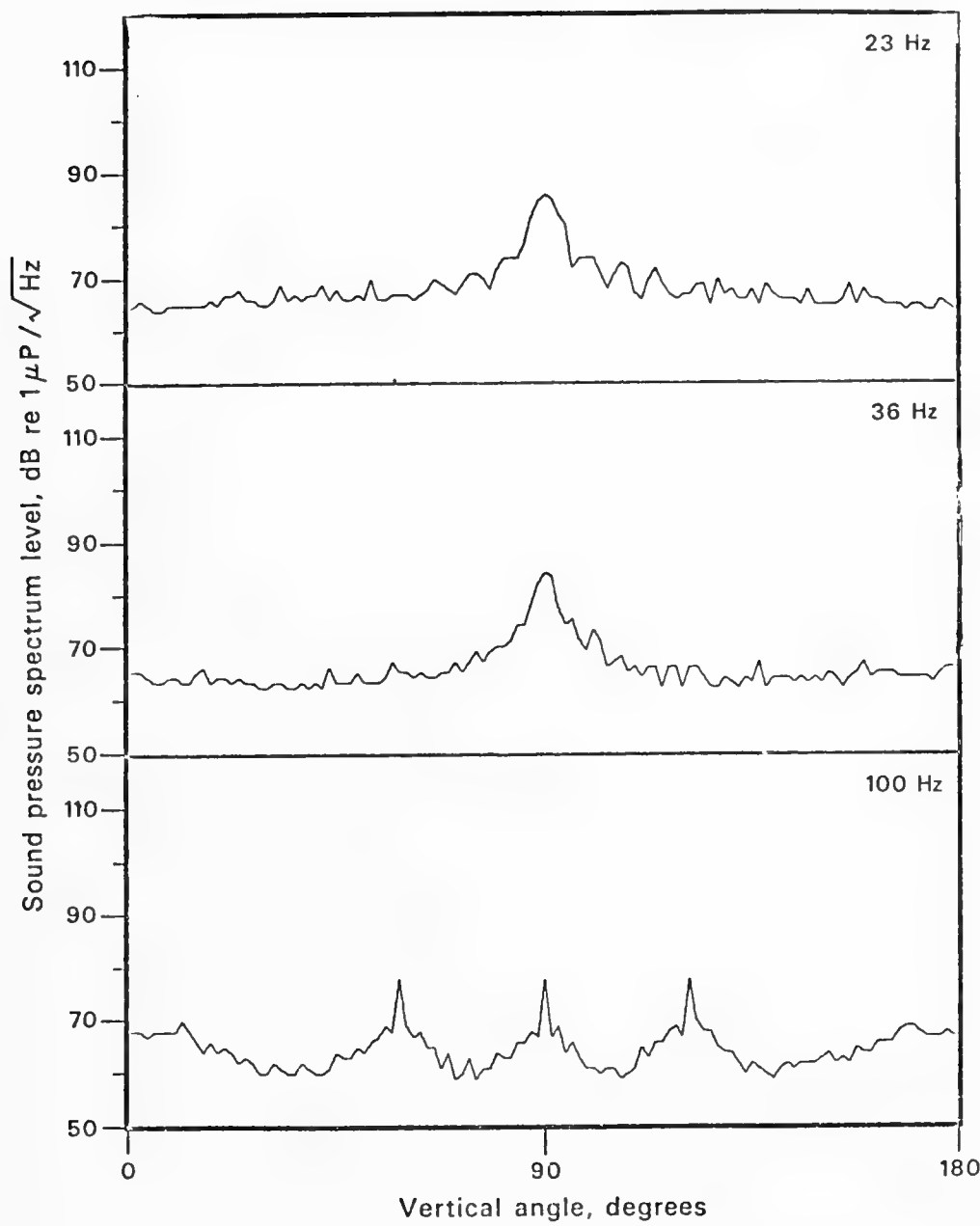


Figure 15. DAY 2 (E02) 4300 METERS

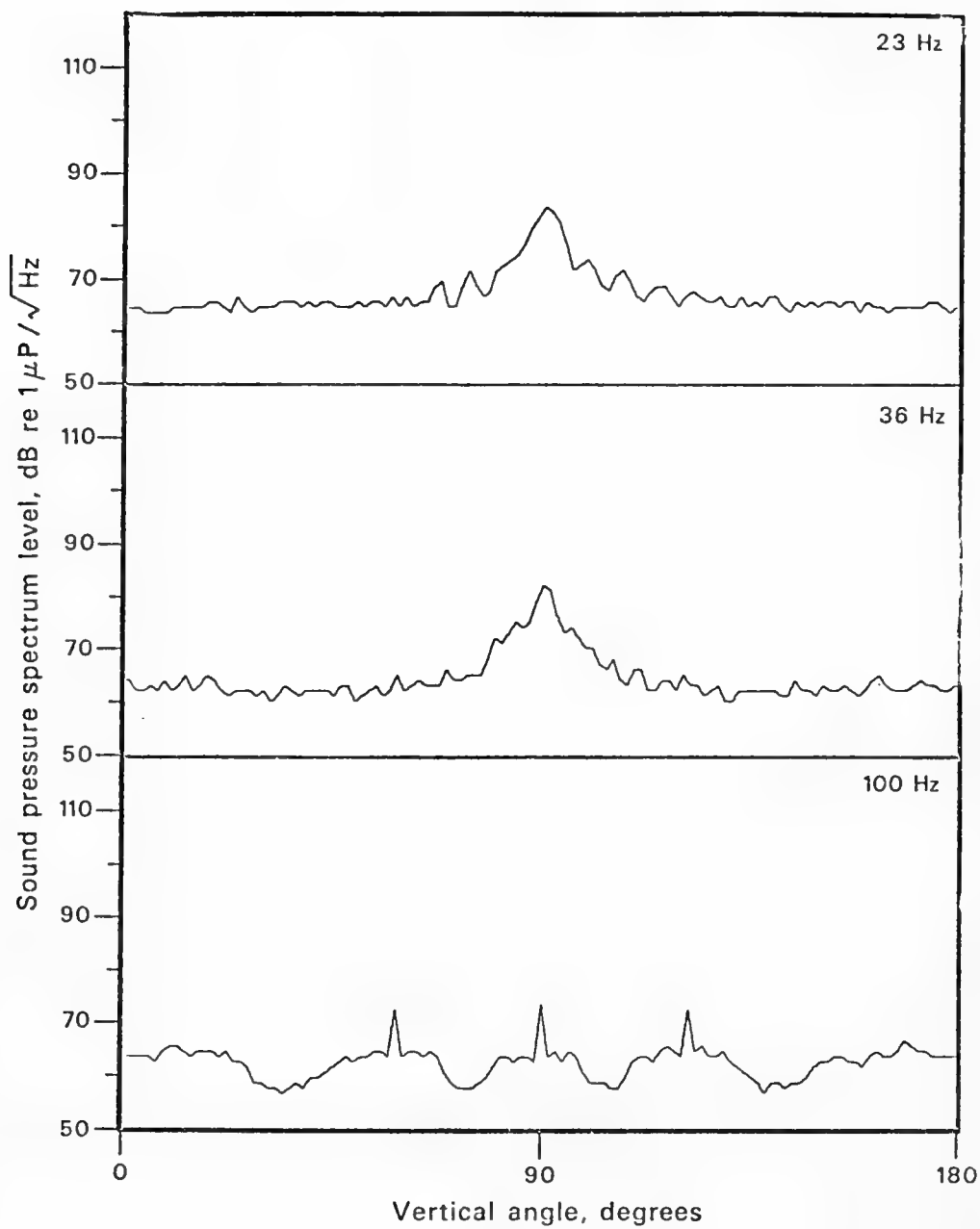


Figure 16. DAY 2 (E03) 3800 METERS

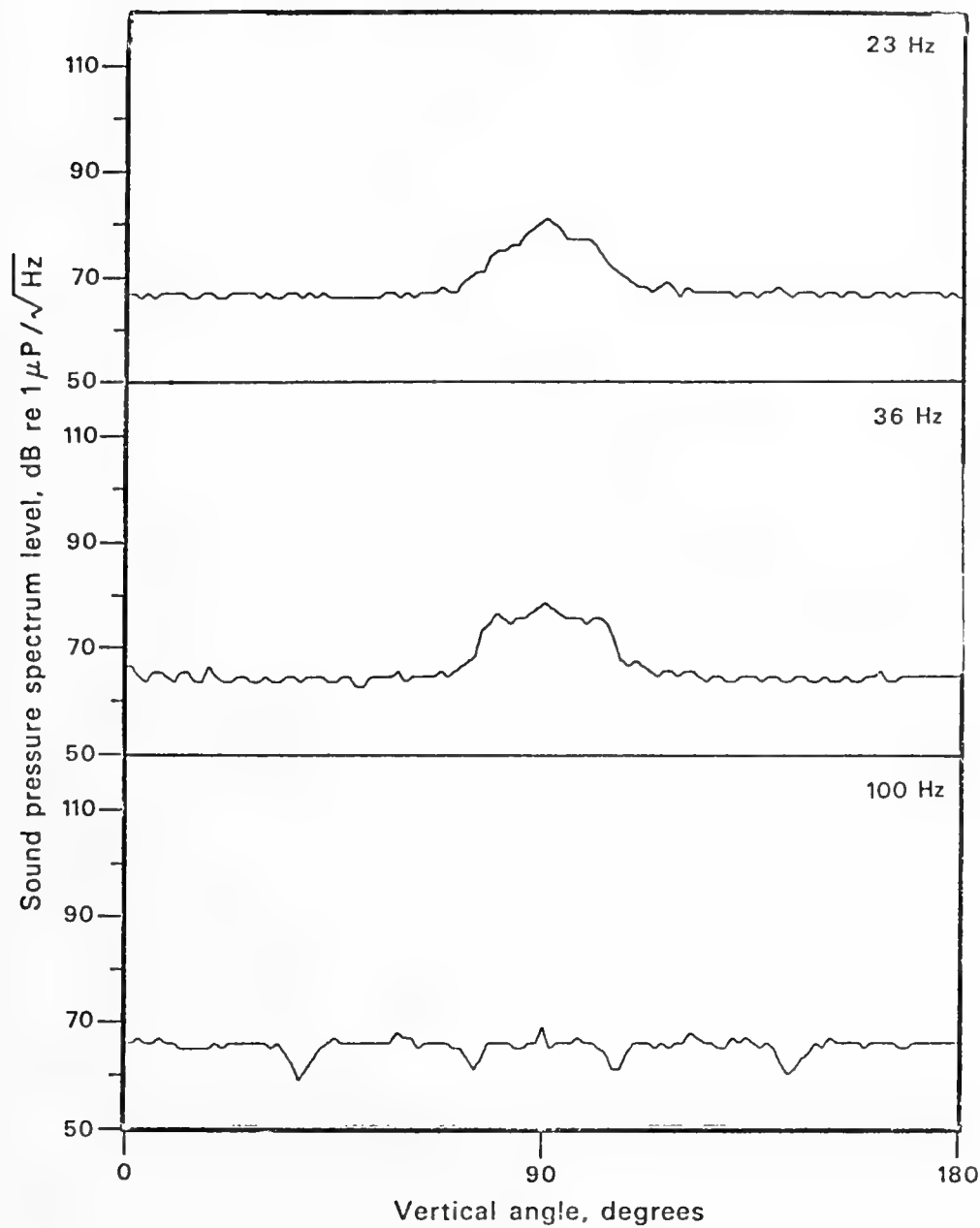


Figure 17. DAY 2 (E04) 2500 METERS

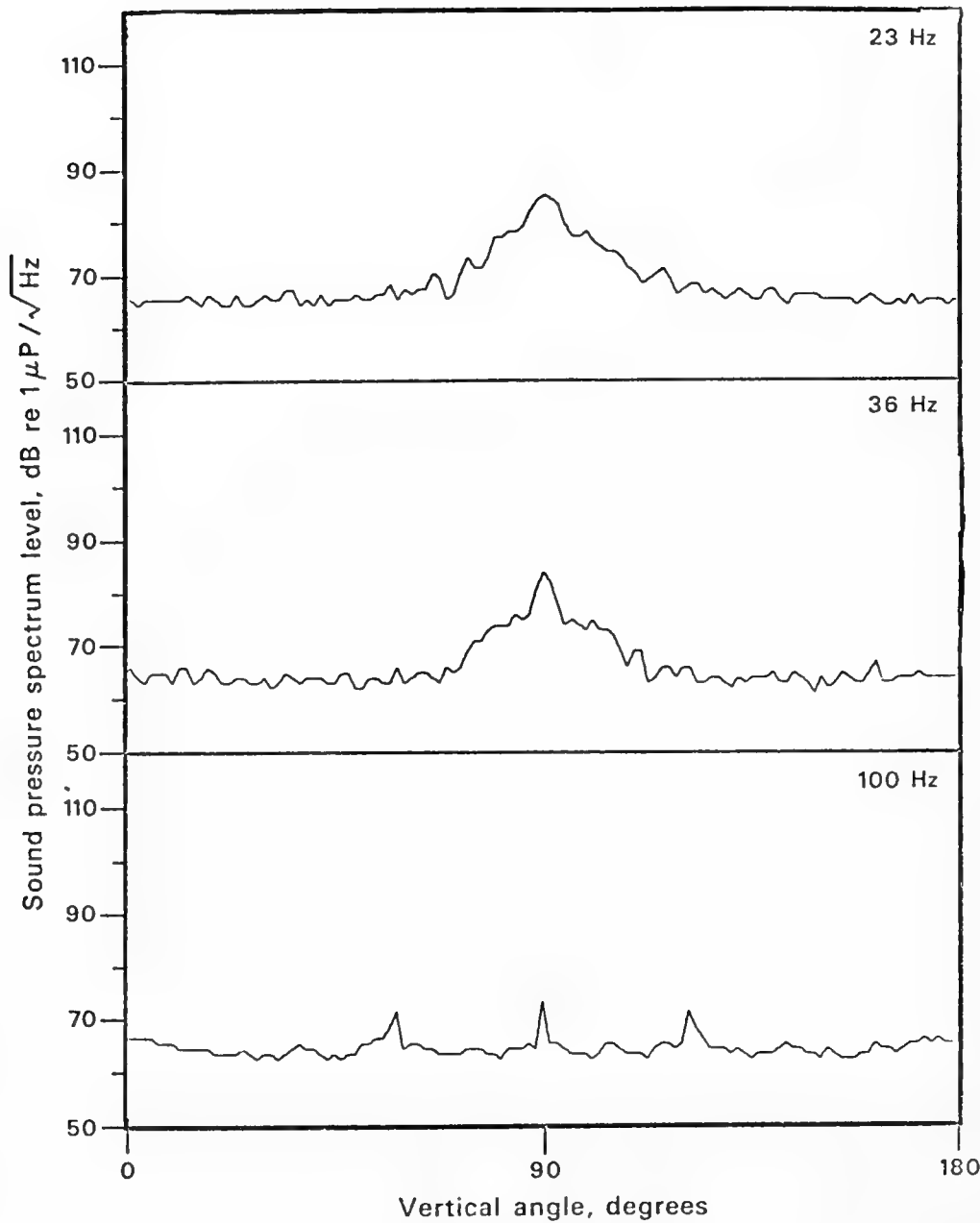


Figure 18. DAY 2 (E05) 1200 METERS

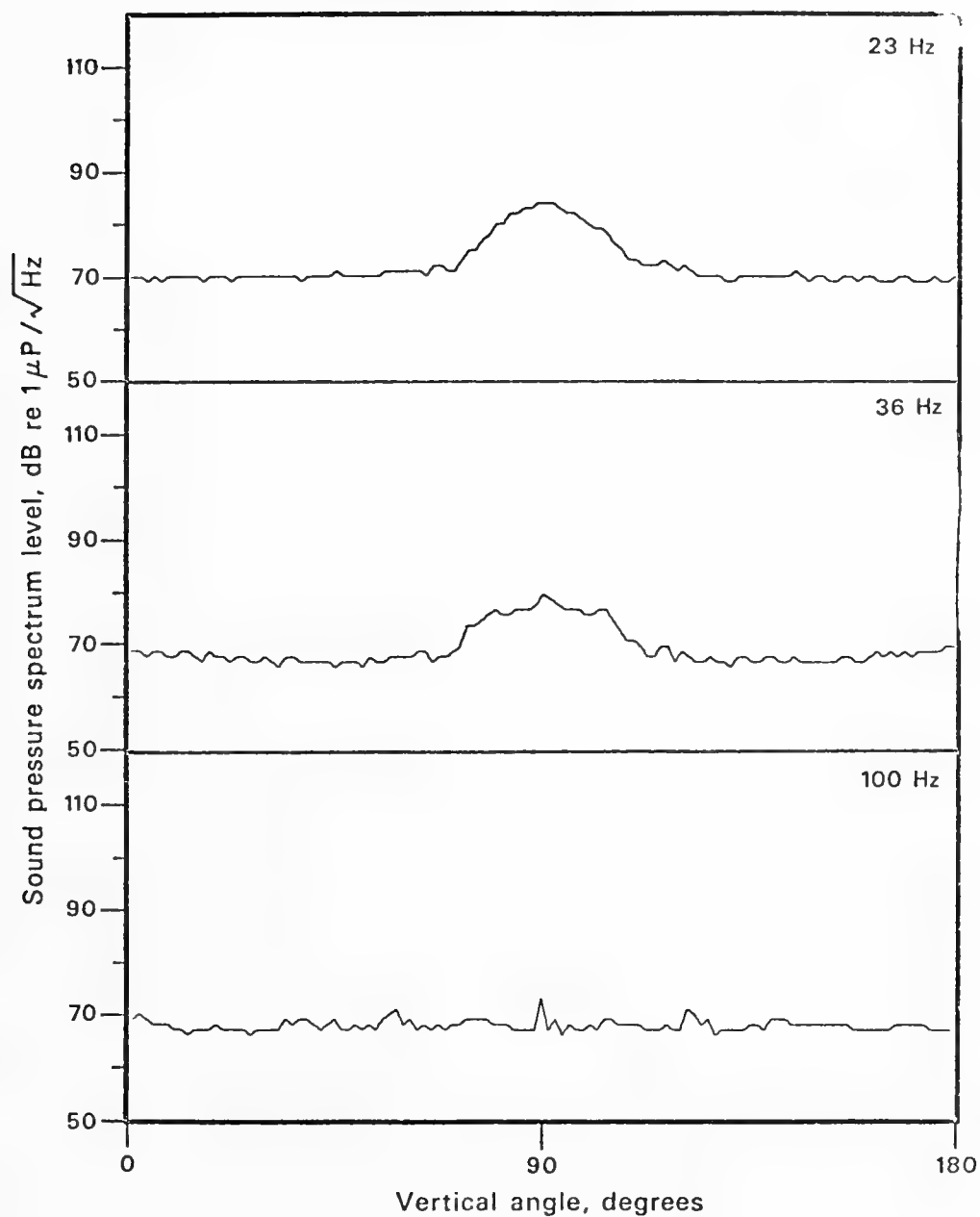


Figure 19. DAY 2 (E06) 700 METERS

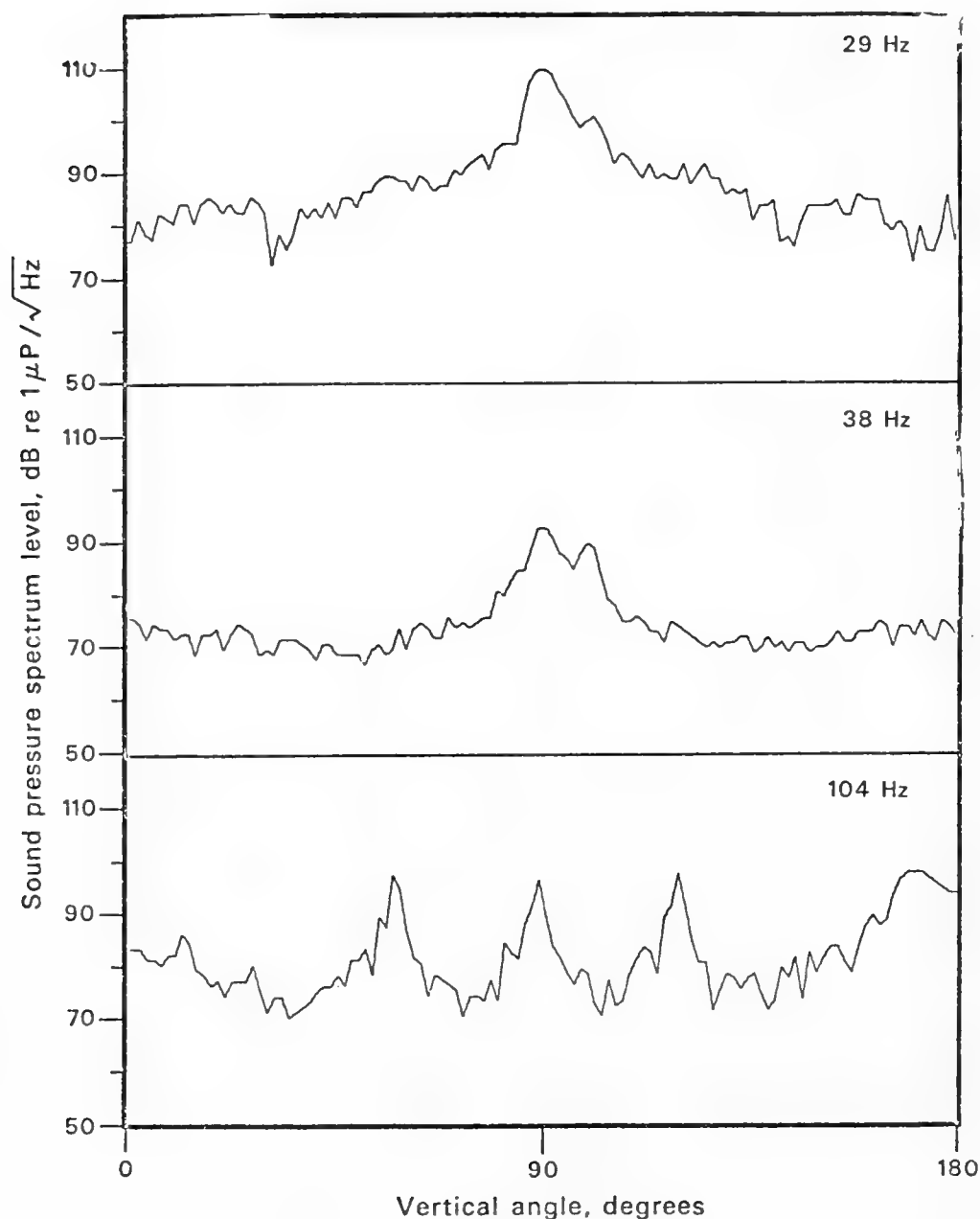


Figure 20. MEASURED BEAM RESPONSE TO NARROWBAND SIGNALS

RESULTS

Figure 21 presents the final interpretation of noise directionality as a function of depth (assuming no significant frequency dependence). The basic technique was to start with the 100 Hertz deep data and, moving shallower, correlate the noise shoulders with the 36 Hertz data. Still shallower, the 36 and 23 Hertz data were correlated to continue the trends. The out-of-band noise associated with the filter characteristics prevented estimates of the noise in the steeper "indeterminate" areas.

These data show a basic increase in noise level and broadening in aperture corresponding to the broader aperture available to long-range paths. For the two deepest receivers, these curves are somewhat tentative since they are pressing the resolution of the system.

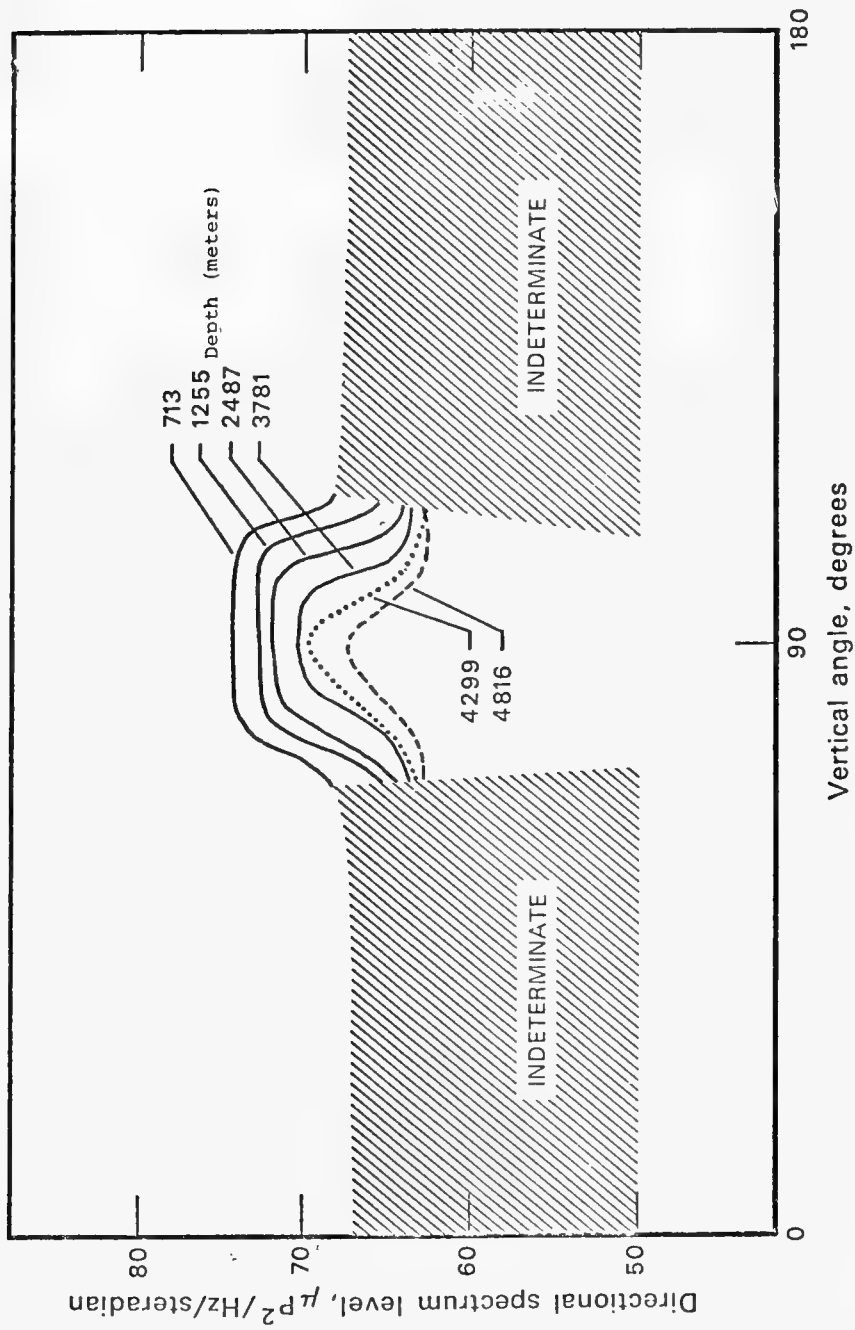


Figure 21. INTERPRETED LOW-FREQUENCY NOISE DIRECTIONALITY AS A FUNCTION OF RECEIVER DEPTH

DISCUSSION

Dr. John Hanna (Office of Naval Research): What exactly is the common mode noise and where does it originate?

Dr. Anderson: I wish we could say what it is. It apparently is a broadband noise that was introduced on all channels coherently, and it is associated with the interface between the array electronics and the beamformer electronics. It has an analog interface between the two.

On board FLIP there must have been some noise picked up in that region, and it seemed to have a fairly uniform spectrum. If you look at the levels of noise that appear at the three frequencies they are within a couple of dB of the same level. If you look at the peak of those responses and correct it for the pre-processing filters, the signal-conditioning filters that are ahead of the beamformer, there seems to be just broadband noise arriving in phase on all elements.

Dr. Gordon Raisbeck (Arthur D. Little, Inc.): We did some analysis of ambient noise measurements made with an ITASS array and found the same phenomenon. There is no way to make a uniform, consistent graphical presentation of the average noise level on each beam without having the broadside beam stick out like a sore thumb. No matter how often you calibrate and recalibrate that, there is always a residual amount of energy which seems to be several times as great in linear units than the energy in the adjacent beams.

Mr. R. L. Martin (New London Laboratory, Naval Underwater Systems Center): Is there no way of getting rid of that type of energy adaptively by using an adaptive process?

Dr. Anderson: We looked at the possibility of doing that. We gave it up because we found that if we looked at all the data we had,

the level did vary. It seemed there would be a little bit of change from frequency to frequency, from data sample to data sample, and as a result we were afraid that by trying to take it out we would be adding more of an artifact than by leaving it in. We had no baseline reference to say how much it really was.

Dr. A. O. Sykes (Office of Naval Research): Was the ship's frequency 60 Hz?

Dr. Anderson: Yes, 60 Hertz.

Dr. Sykes: In some of the early experiments with fitted arrays we had that problem. We gave up and we used DC and it went away.

Dr. Anderson: It could very well be associated with the generator. None of these, however, were 60 Hertz lines. We didn't have any strong 60 Hertz itself. But any ship's generator is pretty noisy and has a lot of broadband noise associated with it. It could very well be that.

The problem is we didn't recognize this until after the fact, because it doesn't appear on a single channel. It's only when you put the array gain on it that you see it show up. It was only at the very low noise conditions that it showed up.

DIRECTIONAL NOISE AMBIGUITY
RESOLUTION WITH LINEAR ARRAYS

Gordon Raisbeck

Reprinted from U.S. Navy Journal of Underwater Acoustics
Vol. 25, No. 3, July 1975

DIRECTIONAL NOISE AMBIGUITY RESOLUTION WITH LINEAR ARRAYS*

Gordon Raisbeck
Arthur D. Little, Inc.
Cambridge, Massachusetts 02140
(Received 8 October 1974)

ABSTRACT

Often the most convenient tool with which to measure the azimuthal distribution of underwater noise is a horizontal linear array. Unfortunately, a linear array cannot distinguish right from left, and measurements made with it are ambiguous. The ambiguities can be reduced by making measurements with the array pointed in two or more directions. The choice of number and alignment of array directions and of method of reducing the data depends on the criteria for weighting errors, which in turn depends on the use to be made of the results. No one scheme is optimal for all applications. The merits and weaknesses of several which have been used are compared.

INTRODUCTION

In surveillance and many other practical detection problems, phenomena are differentiated *a priori* into interesting events, which we may call *targets*, and uninteresting events, which we may call *noise* and *interference*. The technical interest in the detection problem comes from the fact that the information available to the decision maker only partly specifies the type of event. Given only incomplete information, we must judge as reliably as we can whether the event was a target or not.

It often happens that most of the packets of information, which we shall call *signals*, that we receive about target events share a common characteristic which is absent from the signals from nontarget events. One effective detection tool is to sort or match signals according to the presence of absence of such characteristics. To apply this technique, we must know something about the characteristics of signals from target events and from nontarget events. It is not sufficient to have information on particular signals: we must have some information about the range and distributions of all possible signals, and direct our attention to those characteristics which effectively discriminate between targets and nontargets.

No ship or submarine can operate at sea without converting some of its mechanical energy into low-frequency acoustic energy. Furthermore, acoustic energy is propagated long distances in the ocean with only moderate loss. Therefore, the unavoidable acoustic emissions from ships and submarines can be measured far away. Unfortunately, the ocean is quite noisy. Therefore, the primary problem in passive acoustic submarine detection and classification is not one of making a sufficiently sensitive acoustic measuring instrument, but rather one of distinguishing an amply loud acoustic signal from a submarine from the even louder ambient noises and interference.

One of the ways in which signals are distinguished from noise is by their spatial distribution. Under most conditions, most of the acoustic energy from a target will arrive at a receiver along either one or only a few propagation paths, presenting wavefronts at the receiver which are locally nearly plane. Ambient noise, on the other hand, has a vastly different spatial distribution. If the acoustic energy at the receiver is represented as the sum of incoming plane waves (and with some restrictions of little

*This paper is based on a presentation of the same title delivered at the LRAPP Review of Mid-Water Acoustic Measurement Systems at the Woods Hole Oceanographic Institution on 7 June 1974.

practical significance this is always possible), many or even a continuum of, arrival directions will be required to account for most of the ambient noise energy. Thus discrimination between targets and non-targets on the basis of spatial distribution of the arriving signal is practical and useful.

Such discrimination is performed in many passive sonar systems by the use of directional arrays and beam-formers.

To make full use of the power of directional discrimination, one must know the directional distribution of ambient noise. This knowledge can be acquired by cut-and-try—i.e., by trying out various beam forming methods to see which gives the greatest enhancement of the signal-to-noise ratio—or by controlled experiments to measure particular qualities of ambient noise directionality which we know, *a priori*, are significant. Neither method is indisputably superior to the other, and both are being used at present.

A significant amount of effort is being expended to measure ambient noise directionality in the deep ocean with horizontal linear arrays. Characteristically, all of the measurements fall far short of telling all about ambient noise directionality that an analyst might think it reasonable to ask. Some compromise between simplicity and completeness of measurement is needed. This paper is a tutorial analysis of some of the mathematics of directionality measurement with linear arrays, and is intended to help the reader answer the following questions:

- How can one make requests for ambient noise directionality data which are both useful and easy to fulfill?
- How can one design better ambient noise directionality measurement techniques, analyses, and model validations?
- How can one make more effective use of existing ambient noise directionality data and results?

SCOPE

All of my experience is limited to the use of linear arrays of omnidirectional receivers at low frequencies (in the range from 10 to 300 Hz), and so will be this discussion. This band of frequencies is of great practical interest in surveillance. It includes the frequencies where surface shipping guarantees that noise from this source will be highly anisotropic. To gain useful information about directionality, we must make coherent measurements with sensors spaced many wavelengths apart. At these frequencies, spacings of a few hundred feet are required; spacings of several thousand feet are preferable, if possible. A rigid multidimensional structure of this size is almost unthinkable as a deployable measurement tool for occasional use, but a flexible linear array straightened by static force or dynamic tension is quite practical.

For the purpose of this discussion, elevation angle will be ignored, and all sound will be treated as though it arrived approximately horizontally. (Some of the consequences of this assumption are discussed in Ref. 1.) The assumption is without general validity; however, it simplifies the specific points I have to make without detracting from their validity. The receiving elements need not be omnidirectional (in fact, in the seismic array they are not),² but this generalization will not be considered, nor will the effect of side lobes and of the finite width and non-ideal shape of main beams. Methods for handling these departures from the ideal are well-known, and will not be discussed further here.

¹G. Raisbeck, D. Sullivan, and G. Miller, "Ambient Noise Directionality in the EASTLANT II Exercise Little, Inc., ADL Report No. 4630274 (Feb. 1974)

Arthur D.

²R. Gardner and W. H. Luehrmann, "EASTLANT II Project Clear Preliminary Report Seismic Engineering Company, Houston, Texas 77027, (3 Jan. 1973)

In this discussion I make various *ad hoc* assumptions about *a priori* statistics, measurement errors, etc. to produce tractable illustrative examples, but these assumptions should not be construed as being my opinions of the behavior of actual signals and noise.

One implicit assumption is that the distribution of noise intensity in azimuth is stationary, and especially, that its expected value is independent of when the measurement is made. While this may be nearly true over a short time interval, it is certainly not true for longer periods. Inasmuch as directionality measurements with linear arrays normally must be sequential, attempts to improve ultimate results by increasing the number of measurements inevitably extend the observation period and increasingly violate the implicit stationarity assumption. The consequences of this dilemma will not be explored.

AMBIGUITY IN A LINEAR ARRAY

Observations with a Single Array Heading

Suppose we have a linear horizontal array of omnidirection sensors and two plane waves with the same wave shape arriving from horizontal directions of different azimuths. If the two azimuths are equally spaced in opposite senses from the axis of the array, the signals received at the receiving elements will be identical. Given only the sensor outputs, there is no signal processing whatsoever that would distinguish one of these plane waves from the other.

Suppose that the signals from the sensors are combined in a beam former which produces a narrow main lobe beam response and low side lobes. Inevitably, the total array response pattern is symmetric with respect to the axis of the array. Therefore, for any steering angle other than end fire, each main beam will have a twin symmetrically displaced to the opposite side of the axis.

Suppose we are given a stationary two-dimensional sound intensity field where the sound intensity received in any direction characterized by the angle θ is $I(\theta)$ (Fig. 1). Suppose, furthermore, that this field is examined with a linear array having a beam former which produces (symmetrically paired) beams of negligible width with negligible side lobes. What is actually measured with such an instrument?

The easiest way to answer that question is to divide the function $I(\theta)$, representing the field, into a symmetric and an antisymmetric component. Let us define the symmetric part (Fig. 2).

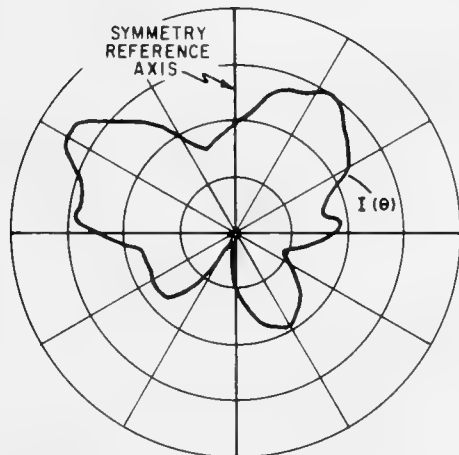


Fig. 1. Example of a two-dimensional angular intensity distribution $I(\theta)$

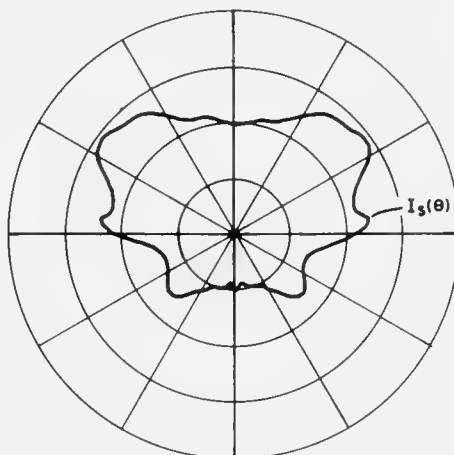


Fig. 2. The symmetric part $I_s(\theta)$ of $I(\theta)$

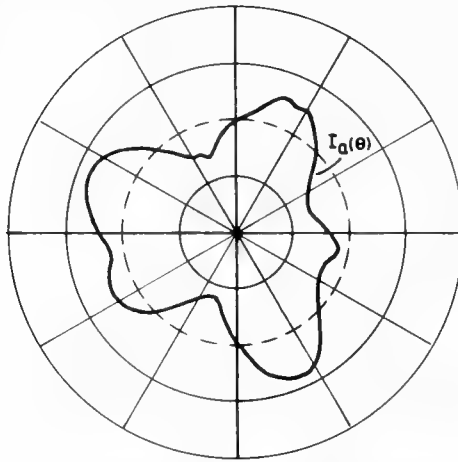


Fig. 3. The anti-symmetric part $I_a(\theta)$ of $I(\theta)$. Zero has been displaced outward to the dashed circle to avoid plotting negative values.

$$I_s(\theta) = \frac{I(\theta) + I(-\theta)}{2} \quad (1)$$

and the anti-symmetric part (Fig. 3).

$$I_a(\theta) = \frac{I(\theta) - I(-\theta)}{2} . \quad (2)$$

Obviously, the function $I(\theta)$ is the sum of its anti-symmetric and symmetric part:

$$I(\theta) = I_s(\theta) + I_a(\theta). \quad (3)$$

Inasmuch as we shall be considering linear space processors, it will be worthwhile to expand the intensity distribution, $I(\theta)$, over an orthogonal basis. Inasmuch as $I(\theta)$ is a periodic function of θ with period 2π , the natural expansion is in a Fourier series:

$$I(\theta) = \frac{a_0}{2} + \sum_{n=1}^{\infty} (a_n \cos n\theta + b_n \sin n\theta). \quad (4)$$

In terms of the Fourier coefficients, the symmetric and anti-symmetric part are, respectively,

$$I_s(\theta) = \frac{a_0}{2} + \sum_{n=1}^{\infty} a_n \cos n\theta \quad (5)$$

and

$$I_a(\theta) = \sum_{n=1}^{\infty} b_n \sin n\theta. \quad (6)$$

With this dissection it is easy to see that the linear array responds only to the symmetric part of the field, $I_s(\theta)$, and is totally insensitive to the anti-symmetric portion of the field, $I_a(\theta)$, where θ is the angle measured with respect to the axis of the array.

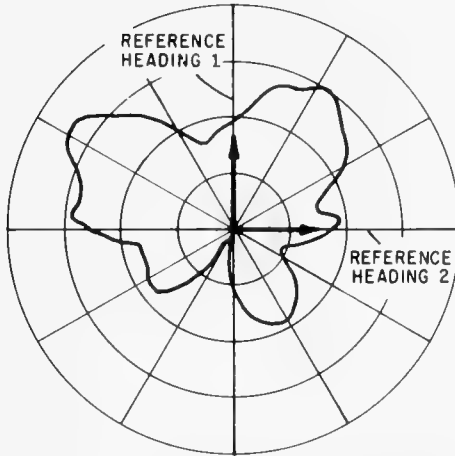


Fig. 4. $I(\theta)$ and two mutually perpendicular reference lines

Two Perpendicular Headings

Suppose we take the same intensity field, $I(\theta)$, and measure it twice with a linear array, once with the array pointed North/South and once with the array pointed East/West (or any arbitrary pair of perpendicular headings) (See Fig. 4). We can dissect field $I(\theta)$ exactly as before into two components, I_s and I_a , which are, respectively, symmetric and anti-symmetric with respect to the North/South axis.

$$I(\theta) = I_s(\theta) + I_a(\theta). \quad (7)$$

Now we can take both of these components and dissect each one of them into two components with respect to the second (East/West) axis, thus:

$$\begin{aligned} I_s(\theta) &= I_{ss}(\theta) + I_{sa}(\theta) \\ I_a(\theta) &= I_{as}(\theta) + I_{aa}(\theta). \end{aligned} \quad (8)$$

Because of the perpendicularity of the two measurement axes, the two components I_{ss} and I_{sa} both retain their symmetry with respect to the North/South axis, and the two components I_{as} and I_{aa} both retain their anti-symmetry with respect to the North/South axis. We have thus dissected the field into four components, i.e.,

$$I(\theta) = I_{ss}(\theta) + I_{sa}(\theta) + I_{as}(\theta) + I_{aa}(\theta) \quad (9)$$

such that each of the four components is either symmetric or anti-symmetric with respect to each of the measurement axes.

Now, when we place the array parallel to the North/South axis, we measure

$$M_1(\theta) = I_{ss}(\theta) + I_{sa}(\theta). \quad (10)$$

Similarly, when we place the array in an East/West orientation, we measure

$$M_2(\theta) = I_{ss}(\theta) + I_{as}(\theta). \quad (11)$$

We can combine these measurements to get

$$M_1(\theta) + M_2(\theta) = 2I_{ss}(\theta) + I_{sa}(\theta) + I_{as}(\theta). \quad (12)$$

If we could find the doubly symmetric component, I_{ss} , we could find the value of

$$M_1(\theta) + M_2(\theta) - I_{ss}(\theta) = I_{ss}(\theta) + I_{sa}(\theta) + I_{as}(\theta). \quad (13)$$

In fact, the value of the doubly symmetric component, I_{ss} , is implicit in either of the sets of measurements, M_1 or M_2 , thus:

$$\begin{aligned} 4I_{ss}(\theta) &= 2M_1(\theta) + 2M_1(\pi - \theta) = 2M_2(\theta) + 2M_2(-\theta) \\ &= M_1(\theta) + M_1(\pi - \theta) + M_2(\theta) + M_2(-\theta). \end{aligned} \quad (14)$$

Equation (13) is the closest we can ever come to a reconstruction of the original intensity field, $I(\theta)$, since, as shown in Eqs. (10) and (11), neither measurement set $M_1(\theta)$ or $M_2(\theta)$ contains any information whatsoever about the doubly anti-symmetric component, I_{aa} . This missing term represents an irreducible bias in any estimate of field $I(\theta)$ reconstructed from these measurements. Any claim to do better without additional information is an exaggeration, for the characteristics of the component I_{aa} are totally unrelated to the data, either deterministically or statistically.

Six Equally Spaced Headings

The same technique can be carried out with any number of equally spaced array headings, but symmetry and anti-symmetry arguments are not very helpful. It is easier to revert to the formulation in Fourier components of Eq. (4). Let us suppose that the array headings with respect to an arbitrary reference direction are $0, \pi/6, 2\pi/6, \dots, m\pi/6$, where m takes on the values 0-5, inclusive. Then we may set

$$\theta = \phi + \frac{m\pi}{6}, \quad (15)$$

where θ is the angle with respect to the original reference system and ϕ is the angle with respect to the array axis. With this substitution, we can rewrite $I(\theta)$ as

$$\begin{aligned} I(\theta) &= \frac{a_0}{2} + \sum_{n=1}^{\infty} \left[a_n \cos n\phi \cos \frac{mn\pi}{6} - a_n \sin n\phi \sin \frac{mn\pi}{6} \right. \\ &\quad \left. + b_n \cos n\phi \sin \frac{mn\pi}{6} + b_n \sin n\phi \cos \frac{mn\pi}{6} \right]. \end{aligned} \quad (16)$$

The array oriented in the direction $m\pi/6$ measures

$$M_m(\theta) = \frac{a_0}{2} + \sum_{n=1}^{\infty} \cos n\phi \left(a_n \cos \frac{mn\pi}{6} + b_n \sin \frac{mn\pi}{6} \right). \quad (17)$$

When n is a multiple of 6, $\sin mn\pi/6$ is identically zero, and the term containing b_n vanishes identically, regardless of the value of m which characterizes the steering angle.

Using the methods described in Appendix A of Ref. 1, we can reconstruct from the measurements the following function (the hat or circumflex $\hat{\cdot}$ signifying an estimating function):

$$\begin{aligned}
\hat{I}(\theta) = & \frac{a_0}{2} + a_1 \cos \theta + b_1 \sin \theta + a_2 \cos 2\theta + b_2 \sin 2\theta \\
& + a_3 \cos 3\theta + b_3 \sin 3\theta + a_4 \cos 4\theta + b_4 \sin 4\theta \\
& + a_5 \cos 5\theta + b_5 \sin 5\theta + a_6 \cos 6\theta + 0 \\
& + a_7 \cos 7\theta + b_7 \sin 7\theta + \dots
\end{aligned} \tag{18}$$

The estimator is the precise analog, under sixfold symmetry conditions, of expression (13) with the last form of expression (14) substituted. This function has all of the terms of the Fourier expansion of $I(\theta)$ except that it lacks the terms in sine of $n\theta$ whenever n is a multiple of 6. The difference between \hat{I} and I is

$$I(\theta) - \hat{I}(\theta) = b_6 \sin(6\theta) + b_{12} \sin(12\theta) + b_{18} \sin(18\theta) + \dots \tag{19}$$

This error represents an irreducible bias. It is irreducible for the same reason as before, i.e., as shown in Eq. (17), all six of measurement sets M_0, M_1, M_2, M_3, M_4 , and M_5 are entirely independent of the values of the coefficients b_6, b_{12} etc.

ESTIMATION TO MINIMIZE ERROR

Error Criteria

For simplicity, suppose the quantity we are trying to measure has a true value X . Suppose that the variable that we observe is not quantity X , but another quantity, Y , which is a function of X . Our measurement is then a measurement of Y with, possibly, some measurement error or noise, i.e.,

$$\text{measurement} = Y + \text{noise} = f(X) + \text{noise}. \tag{20}$$

Out of measurement Y we try to extract and estimate \hat{X} which in some sense matches the true value X .

One criterion which we may invoke is to minimize the bias in the estimate. The bias is defined as the average value of the difference between the estimate and the true value, supposing that repeated measurements are made keeping the true value X constant, i.e., minimize

$$\text{bias} = E\{\hat{X} - X\}. \tag{21}$$

Only rarely does minimization of the bias unambiguously define a processor. Whether it does or not, it is a legitimate criterion of merit.

A much more common criterion is to minimize the mean-square error between the true value of X and the estimated \hat{X} , measured in the metric of the source X , i.e., minimize

$$\text{mean-square error (in source space)} = E\{(\hat{X} - X)^2\}. \tag{22}$$

Another commonly invoked criterion is to choose the estimate which minimizes the mean-square deviation between the actual observations ($Y + \text{noise}$) and what noise- and error-free observations Y would have been, measured in the metric of the observations Y , i.e., minimize

$$\text{mean-square error (in observation space)} = E\{[f(\hat{X}) - (Y + \text{noise})]^2\}. \tag{23}$$

These two are often confused, and each is called "minimizing the mean-square error." The confusion arises because often the quantity $Y = f(X)$ which is observed is the same or nearly the same as X . However, in our case, they are quite different. The quantity we are trying to measure is distribution $I(\theta)$,

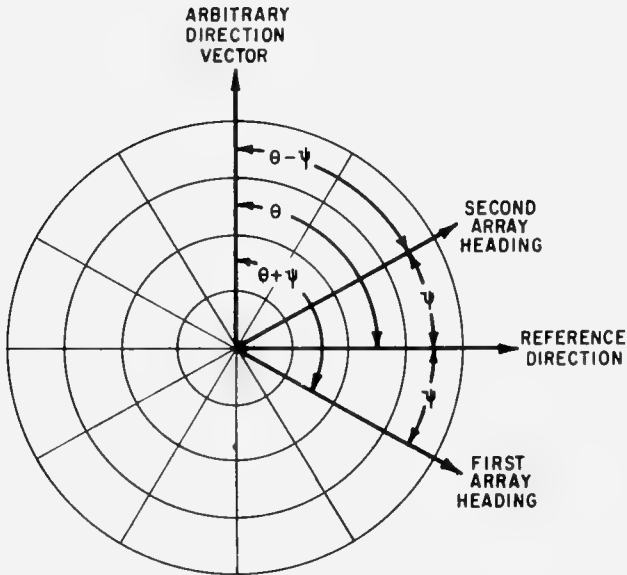


Fig. 5. Relations among array headings, assumed reference direction, and an arbitrary direction vector

and the quantity we can observe is the part, $I_s(\theta)$, which is symmetric with respect to the array axis. Under these circumstances expressions (22) and (23) are quite different, and the signal processor which minimizes one cannot be expected to minimize the other.

In many cases, the bias (Eq. 21) can be reduced to zero or to a provable irreducible minimum without exhausting all the degrees of freedom available in the estimation process. Under such a circumstance, we may have a constrained criterion of error, such as minimize the mean-square error (Eq. 22) subject to the constraint that the bias (Eq. 21) is zero or at the irreducible minimum. Another type of constraint which is relevant to the measurement of the intrinsically positive noise intensity distribution, $I(\theta)$, is to require that estimator $\hat{I}(\theta)$ be greater than or equal to zero for all values of θ , for as shown in Ref. 1, the irreducible-bias minimum-mean-square-error estimator based on real observations may have negative values.

Measurements Made with Two Arbitrary Array Headings

Let us suppose, as in Fig. 5, that we measure an arbitrary intensity field, $I(\theta)$, twice with linear arrays. For convenience, the reference array for angular measurement is chosen halfway between the two array headings, the true azimuth is represented by θ , and the directions of the two array headings are, respectively, $+ \phi$ and $- \phi$. This results in the angular relationships shown in Fig. 5. If the true field is given in Eq. (4), then the fields observed are those given in Eq. (25)

$$I' = \frac{c_0}{2} + \sum c_n \cos n(\theta + \phi) \quad (24)$$

and

$$I'' = \frac{d_0}{2} + \sum d_n \cos(\theta - \phi), \quad (25)$$

where the single prime indicates observations with respect to the first array heading and the double prime indicates observations with respect to the second array heading. For the time being we shall consider only the Fourier components of order n , for if we can determine each Fourier coefficient separately we can determine the function which they collectively represent, and vice versa. Let us call the measured values c and d , where:

$$\begin{aligned} c &= c_n + n_1 \\ d &= d_n + n_2, \end{aligned} \quad (26)$$

where c_n and d_n are true values and n_1 and n_2 are noises or measurement errors. For convenience, we shall assume that n_1 and n_2 are mutually independent Gaussian variables with zero mean and variance $(\sigma_2)^2$.

The components of order n of the true field are characterized by the two coefficients, a_n and b_n . If *a priori* estimates of the distributions of these coefficients are needed, we will assume that the n th order component of the field has the form

$$a_n \cos n\theta + b_n \sin n\theta = A \cos(n\theta - \delta), \quad (27)$$

where A has a Raleigh distribution with variance $2\sigma_1^2$ and δ is uniformly distributed from zero to 2π and independent of A . This seemingly capricious choice of distributions has the quality of making a_n and b_n independent Gaussian variables with zero mean and a common variance σ_1^2 relative to an angular coordinate system with any reference direction whatsoever.

It is easy to work out the deterministic relationships among these n th order coefficients, as follows:

$$c_n = a_n \cos n\phi - b_n \sin n\phi \quad (28)$$

$$d_n = a_n \cos n\phi + b_n \sin n\phi \quad (29)$$

$$a_n = \frac{c_n + d_n}{2 \cos n\phi} \quad (30)$$

$$b_n = \frac{-c_n + d_n}{2 \sin n\phi}. \quad (31)$$

Noise-Free Measurements

Suppose that noises n_1 and n_2 (Eq. (26)) are identically zero, i.e., that the measurements of the observed field are exact. Then Equations (30) and (31) can be used to generate the following estimates:

$$\hat{a} = \frac{c + d}{2 \cos n\phi} = a_n \quad (32)$$

and

$$\hat{b} = \frac{-c + d}{2 \sin n\phi} = b_n. \quad (33)$$

These estimates are exact and free from any error or bias.

Minimum Bias Estimate

Suppose that noise terms n_1 and n_2 are not identically zero, but nevertheless we attempt to minimize the biases

$$E\{\hat{a} - a\} \quad (34)$$

and

$$E\{\hat{b} - b\}. \quad (35)$$

In this case, we use Eqs. (30) and (31) again to form the estimates

$$\hat{a} = \frac{c + d}{2 \cos n\phi} = a_n + \frac{n_1 + n_2}{2 \cos n\phi} \quad (36)$$

and

$$\hat{b} = \frac{-c + d}{2 \sin n\phi} = b_n + \frac{-n_1 + n_2}{2 \sin n\phi}. \quad (37)$$

It is easy to show that the biases (Eqs. (34) and (35)) are both identically zero. The mean-square errors in the estimate are

$$E\{(\hat{a} - a_n)^2\}_m = \frac{\sigma_2^2}{2 \cos^2 n\phi} \quad (38)$$

and

$$E\{(\hat{b} - b_n)^2\} = \frac{\sigma_2^2}{2 \sin^2 n\phi}. \quad (39)$$

This procedure only works if neither $\cos n\phi$ nor $\sin n\phi$ is zero. In the event that one of these factors is zero, one of the estimated components is undetermined. This, however, is not the worst: If one of those factors is *nearly* zero, the estimation process can be carried out as in Eqs. (36) and (37), but one of the errors (Equation (38) or (39)) is necessarily extremely large.

Minimum Mean-Square Error Estimate

The estimate leading to a minimum mean-square error is more subtle. We resort to a general theorem that when the *a priori* distributions of the signals (a_n and b_n) and noises (n_1 and n_2) are Gaussian, the processor leading to the minimum mean-square error estimate is a linear processor (Ref. 3, pp. 286 ff, pp. 335 ff). With that fact, we can write an expression for the mean-square error, differentiate with respect to the linear coefficients, and determine that the estimators are the following:

³Harry L. Van Trees, *Detection, Estimation and Modulation Theory, Part I. Detection, Estimation and Linear Modulation Theory*, (Wiley, New York, 1968).

$$\begin{aligned}\hat{a} &= \frac{c+d}{2 \cos n\phi} \left(\frac{2\sigma_1^2 \cos^2 n\phi}{2\sigma_1^2 \cos^2 n\phi + \sigma_2^2} \right) \\ &= a_n \left(1 - \frac{\sigma_2^2}{2\sigma_1^2 \cos^2 n\phi + \sigma_2^2} \right)\end{aligned}\quad (40)$$

and

$$\begin{aligned}\hat{b} &= \frac{-c+d}{2 \sin n\phi} \left(\frac{2\sigma_1^2 \sin^2 n\phi}{2\sigma_1^2 \sin^2 n\phi + \sigma_2^2} \right) \\ &= b_n \left(1 - \frac{\sigma_2^2}{2\sigma_1^2 \sin^2 n\phi + \sigma_2^2} \right).\end{aligned}\quad (41)$$

The mean-square errors are

$$E\{(\hat{a} - a)^2\} = \frac{\sigma_2^2}{2 \cos^2 n\phi + \frac{\sigma_2^2}{\sigma_1^2}} \quad (42)$$

and

$$E\{(\hat{b} - b)^2\} = \frac{\sigma_2^2}{2 \sin^2 n\phi + \frac{\sigma_2^2}{\sigma_1^2}}. \quad (43)$$

It is easy to see that these are in fact smaller than the quantities in Eqs. (38) and (39), respectively. This improvement is achieved, however, only at the expense of introducing biases, in general nonzero:

$$E\{\hat{a} - a_n\} = a_n \frac{-\sigma_2^2}{2\sigma_1^2 \cos^2 n\phi + \sigma_2^2} \quad (44)$$

and

$$E\{\hat{b} - b_n\} = b_n \frac{-\sigma_2^2}{2\sigma_1^2 \sin^2 n\phi + \sigma_2^2}. \quad (45)$$

It is interesting to see what happens in this case if cosine of $n\phi$ approaches zero. Looking at Eq. 40, we see that the estimator approaches zero independent of the data. Looking at Eq. 42, we see that the mean-square error approaches σ_1^2 , independent of σ_2 . The bias, given in Eq. 44, approaches $-a_n$. The optimum processing according to this error criterion in effect ignores the measurement and gives back the *a priori* estimate.

Minimum-Bias Estimate with the Least Mean-Square Error

In the present example of two measurements made with two array headings, specifying minimum bias fully determines the processor. When more observations are made, there are many possible minimum-bias estimates, and we can further specify the one with the least mean-square error. That is the approach adopted in Ref. 1, and the estimator is the analog of Eq. (13). Reference 1 proves that the estimator given has minimum biases, and only claims, without proof, that among minimum bias estimators it has the least-square error.

Estimate Giving Best Mean-Square Fit to the Measured Values

Rather than to minimize each component of the error separately, let us attempt to minimize the sum of the squares, by choosing estimate a and b which minimizes

$$E\{[c - (\hat{a} \cos n\phi - \hat{b} \sin n\phi)]^2 + [d - (\hat{a} \cos n\phi + \hat{b} \sin n\phi)]^2\}. \quad (46)$$

This is the criterion adopted in Ref. 4.

The minimum is achieved if

$$\hat{a} = \frac{c + d}{2 \cos n\phi} \quad (47)$$

and

$$\hat{b} = \frac{-c + d}{2 \sin n\phi}, \quad (48)$$

provided that neither $\cos n\phi$ nor $\sin n\phi$ equals zero. Furthermore, the error as defined in Eq. (46) is identically zero. If either $\cos n\phi$ or $\sin n\phi$ is zero, then one or the other of the two estimates is indeterminate, and the error is finite and is equal to $2\sigma_2^2$.

This example can be used to illustrate a real danger in this error criterion. The same danger is illustrated by an old anecdote about a light sleeper who had a clock which chimed the hours. On many occasions he woke up during the night hearing the clock chiming. On looking at his watch, he observed that the hour was invariably one hour later than the number of chimes he counted. From this he inferred that the first chime served to wake him from his slumbers, but faded before he was consciously aware of it. He also formed the further inference that if he woke up suddenly during the night and heard nothing, the hour was 1:00 a.m. Although this estimate fits the observation perfectly, there is a danger that the estimate may fail to be related to the true value in any causal sense. The same is true of one of the estimators of Eqs. (47) and (48) if one of the factors cosine $n\phi$ or sine $n\phi$ is nearly zero. This form of processing generates a very large and spurious value for one or the other of the terms \hat{a} or \hat{b} in such a way that the observations fit the estimate perfectly, but reference to Eqs. (38) and (39) shows that the estimator diverges from the true value of the quantity which it purports to estimate.

In homelier words, "the observations fit the estimate" and "the estimate fits the true value" are not necessarily equivalent statements, and, as just seen, it is possible for the observations to fit the estimate perfectly while the estimate fits the true value extremely badly. We try to avoid such a pathologic situation, but in measuring the intensity distribution, $I(\theta)$, with a linear array it cannot be avoided completely. No matter what observation angles are chosen, there are always some values of n for which $\cos n\phi$ and

⁴E. M. Wilson, Directional Noise Measurements with Line Arrays
England (June 1973).

Admiralty Research Laboratory, Teddington,

$\sin n\phi$ are very small. Using more than two sets of observations ameliorates the problem, but cannot eliminate it completely.

A Constrained Estimate

The minimum-bias estimator having the least mean-square error of Ref. 1 is actually the zero-bias estimator of expression 18. Unfortunately, expression 18 may be negative for some values of θ . One way to relieve the implausibility of the resulting solution is to add an arbitrary function of the form of Eq. (19), but with coefficients b_6, b_{12} , etc., chosen to minimize the negative excursions of the estimator. This is done in Ref. 1. Wagstaff, in Ref. 5, rightly criticizes the remedy as ineffectual. The resulting solution "looks" nicer, but it is no better an approximation to the true distribution in several examples. There are analogous instances in signal detection where invoking similar constraints results in a real improvement, but Ref. 1 fails to show any reason why improvement should result in the present case, and Ref. 5 shows examples where it does not.

OTHER USEFUL ESTIMATORS

References 6 and 7 describe two other analytical methods of resolving ambiguities in noise fields which are not easily described in terms of the minimization of some error functions. These are, respectively, the *hot-spot* method and the *BAR* method. Both of these are defined by algorithms rather than by minimization processes, and both of them are nonlinear. Inasmuch as they are nonlinear, analyses in terms of Fourier components of the spatial distribution are not appropriate.

Hot Spot Analysis

To a first approximation, the *hot-spot* method matches the observations as well as possible with plane waves arriving from a small number of points or directions (called hot-spots, from which the algorithm gets its name). The fit with the observations is improved by having more and more hot-spots of progressively lower intensities. Within the limits of consistency of multiple observations, the fit can be made arbitrarily good, for any field whatsoever can be represented by a continuum of plane waves.

The *hot-spot* solution suffers from two potential disadvantages. First, the criterion of fit is to match the measured values, and as indicated, it may be possible to match the measurements very closely with an estimator which is very far from the true field. Second, the solution is sometimes used to justify the assumption that noise comes from a small number of hot-spots. Such an argument is circular and must be validated with additional observations.

The *hot-spot* method was originally designed for use under circumstances where observations were made with an array at two or more geographic locations, with the possibility of a different array heading at each location. This is different from the situation postulated in this paper, where all observations are made at the same location but possibly different array heading angles. When different positions are available for observation, the *hot-spot* method applied to a large number of observations should give not only an unambiguous resolution of direction, but an unambiguous distribution of noise sources in two dimensions. However, that is beyond the scope of this discussion.

⁵R. A. Wagstaff, A discussion and comparison of five methods utilizing the Towed Array to Assess the Azimuthal Directionality of Ambient Noise Naval Underseas Center Report TP-374, (Jan. 1974)

⁶J. P. Holland, T. F. Cannan, Jr., J. J. Hanrahan, and J. B. Bairstow, Preliminary Results of Azimuth Directionality Measurements of Ambient Noise Observed During EASTLANT II, 6-14 August 1972 NUSC Technical Report 4431 (27 Sept. 1972)

⁷J. P. Holland, T. F. Cannan, Jr., J. B. Bairstow, and F. E. Rembetski, EASTLANT II Ambient Noise Study, Vols. 1 and 2 NUSC Technical Reports 4487-1 and 4487-2, (1 Jan. 1973) and (13 Aug. 1973)

BAR Analysis

The BAR method is an alternative to the hot-spot method. The BAR data reduction method is also described by an algorithm rather than by an optimization process. The geometry of directional beams where lower-than average received noise is observed defines directions where high-intensity noise cannot originate. These constraints, applied to the observations of higher-than-average received intensity, in most cases, tell which of the two ambiguous directions the bulk of the noise must have come from. The rest, usually a small part of the total, is spread around rather than attributed to a unique direction as in the hot-spot method. (The reader seeking more detailed information should consult Ref. 5, as well as Refs. 6 and 7.)

DISCUSSION

All linear processing methods are easily generalized from a single component of n th order to a complete Fourier series. This, in turn, is sufficient to characterize an arbitrary field. If more than two sets of observations are made, the solution will be overspecified when the measurements are totally free from error. In the presence of finite error, the redundant measurements can be used to reduce the expected error in the estimates. All of these analytic methods use assumptions about the field to be measured and the kind of measurement errors which will be encountered. These assumptions may be verifiable facts, but they may be chosen for simplicity and plausibility or they may simply be wishful thinking.

We have proceeded stubbornly on the assumption that it is necessary to make an estimate of function $I(\theta)$ which describes the distribution of noise in azimuth. But this may not be necessary. For example, suppose the task at hand is to validate a model of ambient noise distribution. If the model yields a computed value of $I(\theta)$, it is extremely simple to calculate the symmetric part of the model prediction by Eq. (1). An eminently satisfactory way of validating the model is to compare observations with a symmetrical part of the prediction. If the symmetric part of the prediction is matched by a number of independent observations made with the array pointing in arbitrarily assigned directions, this will result in a convincing model validation.

Similarly, experimental studies to support the need for narrower search beams or for adaptive beam forming can be framed in such a way that it is not necessary to determine the noise field distribution unambiguously.

On the other hand, for most kinds of linear array design studies and many kinds of surveillance system performance studies, an approximation to the ambient noise field in all directions is necessary, and some general estimator like that in Eq. (18) is highly desirable.

Choice of error criteria depends on end use. If many measurements will be made, and the reduced estimates may be averaged, smoothed, or interpolated among, then a bias-free estimate is desirable, because averaging reduces the error below the bias. On the other hand, if only one measurement will be made, the minimization of error independent of bias may be appropriate. But why the mean-square-error Eq. (22)? Admittedly it is a simple and plausible error criterion, but the true value or criterion of performance of some system under investigation may be more closely represented as error weighting other than the square.

As shown in the references, it is difficult and expensive to attempt to completely describe the distribution of ambient noise, and we suspect it may be unnecessary. On the other hand, raw data from a linear array is ambiguous and may be of limited utility. A compromise is needed between the qualities of ambient noise directionality specification useful in a particular application and the cost and complexity of measurement and analysis.

Most of the ambiguity in ambient noise directionality measurement can be removed with reasonable amounts of measurement and analysis. However, as residual ambiguity is reduced, improvement gets more and more difficult. Also, the lower bounds of random errors in the results, as distinguished from

bias due to ambiguity, are set by the instruments and techniques of measurement. The kind of residual ambiguity which can be tolerated, that is the criterion of goodness of an ambient noise directionality measurement, must be related to and partly determined by the use. The choice of criterion of goodness sensitively affects both measurement and analysis methods. A simple corollary is that there is no way to measure ambient noise directionality which is best for all applications.

The variety of criteria of goodness which have already been used shows that there is no obvious unique best choice. Unfortunately, some of the sources cited in this paper fail to state and all fail to justify their choices of goodness criteria, even for the particular applications they have in mind. It should not be inferred that their selections are poor or irrelevant, for responsible and experienced scientists and engineers can be counted on to do most things right even when they do not defend each decision explicitly. However, their lack of comment on their choices of criteria makes it difficult to compare them or to decide which among them is most suitable for a particular application.

The validity of the assumptions which make any of the several error optimizations realizable is doubtful and would be extremely hard to verify. A direct comparison among the methods, using real data, is probably the best approach to try next. Reference 5 shows the way to make such comparisons, but does not go far enough, for it does not objectively match the merits and deficiencies of each method to the requirements of the applications.

ACKNOWLEDGMENT

My remarks are stimulated mostly by experience with the LRAPP-sponsored EASTLANT II exercise (Refs. 1, 2, 6, 7, and 8) and SQUARE DEAL Exercise (Refs. 9 and 10). This has involved me intimately with ITASS (Refs. 1, 6, and 7), less intimately with a long seismic array originally developed for geo-physical exploration (Refs. 2, 9, and 10), and to a lesser extent with an experimental directional towed array, STELLA (Refs. 9 and 10), developed in the United Kingdom. I must also acknowledge a debt to Messrs. Pastore, Elyash, and Nuttall at NUSC, Messrs. Wagstaff and Gardner at NUC, Messrs. Gill and Wilson at ARL in Teddington, England, Mr. Sullivan at ADL, and many others whose verbal and written communications I have profited from.

Most of this work was carried out under contract NOOO-14-72-C-0173 with the Office of Naval Research under the Technical Monitorship of Dr. Roy Gaul, Manager, LRAPP, whose guidance is acknowledged with thanks.

⁸ EASTLANT II Acoustics Exercise Plan MC Plan 07, Long Range Acoustic Propagation Project (July 1972)
⁹ SQUARE DEAL Exercise Plan, MC Plan 012 Long Range Acoustic Propagation Project (1973)
¹⁰ D. Sullivan, G. E. Miller, and G. Raisbeck, SQUARE DEAL Synopsis Report MC Report 0015, Long Range Acoustic Propagation Project, (Feb. 1974)

